Experiments on Gas Phase Chemistry with High Sensitivity Laser Spectroscopy

Thesis by
Laura Anna Mertens

In Partial Fulfillment of the Requirements
for the Degree of
Doctor of Philosophy

California Institute of Technology
Pasadena, California
2017
(Defended September 29, 2016)

Acknowledgements

I was fortunate enough to have a lot of support from some really amazing people during my time at Caltech.

I would like to thank my advisor Mitchio Okumura. He always cared about his students and really believed in me during my time at Caltech. His faith in me, his encouragement, and (of course) his scientific expertise were key to my success. He always tried to make time on Fridays to make sure my project on track and to make sure I was doing well. I would also like to thank Stan Sander, who was a great second advisor. Along with Mitchio, he always provided great advice on my project. I would also like to thank my committee: Rudy Marcus, Long Cai, Paul Wennberg, and Jack Beauchamp.

I would also like to thank the Okumura group. Of special note are all the people that I've been fortunate enough to share 17 Noyes with. Matt Sprague was generous enough to train me and show me the ropes of 17 Noyes. A lot of my success at Caltech is thanks to his work my first summer here working with Matt. He was also generous enough to help show me his application for the NIST postdoctoral fellowship when I was applying for mine, and answering all of my questions about it. There a few older students that left soon after I came to Caltech, but who I looked to when I first arrived and showed me the ropes of how to do research at Caltech: Nathan Eddingsas, Kathryn Perez, and Kana Takemastu. I would like to thank Hannah Allen and Fred Winniberg for being a great time with me when we took all the data for the HO_2 + NO work. I would like to thank Joey Messinger, who worked with me my last few months at Caltech and has helped me greatly obtain the OH + NO_2 data. I know he's learned a lot in these last few months, and I can feel good leaving 17 Noyes to someone who is excited to do experiments there. Good luck with QOOH! I was also helped by a number of undergraduates and post-docs who worked in 17 Noyes with me: Marissa Weichman, Luiz Gomez, Heather Gold, Sandy

Wong, and Damien Amedro. I would also like to thank a few friends in the Okumura group who provided me with support during my time at Caltech, especially Aileen Hui and Matt Smarte. Matt was always ready to lend me equipment and talk about pulsed-CRDS with me. I want to thank Aileen for being a good friend and staying up practically all night with me during that one conference in Asilomar.

Thanks to David Robichaud for LabView programing in 17 Noyes and to Ralph Page for optimization of the spectrometer optics.

I would like to thank Paul Wennberg, who almost dual-advised me at Caltech, and his group. Although I never really did research with Paul's group, they were welcoming and invited me to some nice parties. I feel that if my project worked out like I originally planned, I would have had a great second group to support me at Caltech.

I would like to thank Boaqing Zhang, Ian Finneran, and Linhan Shen for TAing with me my first year. I would secondly like to thank Ian Finneran for doing problem sets with me during stat mech and TAing spectroscopy with me.

I would like to thank all the support staff at Caltech who made this thesis possible. There were many great secretaries, including Monica Brito, Agnes Tong, and Anne Penny. Raquel Rodriguez helped me navigate my fellowships. Thanks to Mike Roy for machining the temperature controlled cell and Rick Gerhart for glassblowing (and fixing all the glassware I broke). Elisa Brink and Steve Gould ordered lab equipment and chemicals. Joe Drew and the safety office always made sure my laboratory was safe. There are many more people at Caltech, including people in shipping and receiving and in the central warehouse, who made sure I had what I needed to do science.

I also was fortunate enough to be adopted into the Département Physique Moléculaire at the Université de Rennes 1 in Rennes, France during my 7 month stay my last year of graduate school. I would like to thank Ian Sims for welcoming into his group and guiding me during my work in Rennes. I have been fortunate to be advised by not one, but three great scientists during my graduate work: Mitchio, Stan and Ian. I would like to thank Martin Fournier and Hamza Labiad for welcoming into their lab and teaching me the ropes of the CRESU B. Their hardwork I would also thank everyone else in the department, who were all very welcoming and generous to me. They also were patient with my French and enjoyed teaching me this second language.

I had a lot of other great friends at Caltech. First and foremost, I would like to thank Noah for being an outstanding roommate and really being there for me and being a great friend throughout our time at Caltech. I would like to thank Victoria for enjoying doing puzzles with me and sharing the stress of Caltech together. I would like to thank Kate for having lunch with me and Victoria and again sharing the stress of Caltech with us. I would like to thank Andrew and Julie for being great people that invited me over to dinner multiple times and for lending me their dog, Cyd. I would like to thank Cyd the Dog for being adorable and loving and for being really enthusiastic about catching Frisbees. I would like to thank Nancy Sulahian and the rest of the Caltech Glee club and Chamber Singers for making me a more balanced person during my time at Caltech and supporting me artistically in a fairly un-artistic institute. I would also like to thank them for allowing me to sing at Caltech's annual holiday Gala, which earned me brownie points with Mitchio.

I would like to thank my wonderful boyfriend Bill for all the support he gave me during my last two years at Caltech. He has really shared a lot of the stress of this thesis with me. I

have enjoyed his tasty cooking, and I am so happy that he visited me not once, but twice, in France!

Finally, I always had good support from my family. I would like to thank my mom for always being there to talk on the phone if I was stressed at work. I would also thank her for some wonderful trips together, including exploring Big Sur and the San Diego zoo together. I would like to thank my Dad for always loving to go hiking with me and exploring the mountains of California with me. He also helped me a lot dealing with my migraines and headaches. I have two great brothers, Bobby and Richie, both of which visited me in California. Bobby, his wife (then girlfriend) Sarah, and I had many great times when they stayed with me in California and when we went to France and Germany together. I would like to thank their unborn fetus, whose existence made me happier when I was really stressed and taking tons of exams. I also have two loving grandparents who are always excited to see me when I go home to St. Louis.

Without all these people, my life during the past five years would have not been as good. In their own way, they all provided the support I needed to complete my Ph.D.

Finally, I have been fortunate enough to have received many fellowships during my time at Caltech. NSF GRFP, PEO, AAUW, Chateaubriand, and Rennes Metropole all funded me during my Ph.D.

Abstract

Gas phase chemistry is important to many environments on Earth and beyond. The Earth's atmosphere is dominated by free radical reactions that, when perturbed by pollution, can lead to serious environmental problems like stratospheric ozone depletion and urban smog.[1] Outside Earth, many other planetary atmospheres[2] are affected by gas phase, radical chemistry, including the atmosphere of Saturn's Moon Titan.[3] Gas phase chemistry in interstellar clouds can synthesize the molecular building blocks of our universe.[4] Studying gas phase chemistry has also led to basic chemical knowledge of how chemical reactions proceed and how intermolecular forces work.[5]

This work is dedicated to studying gas phase chemical reactions with high-sensitivity laser spectroscopy. Laser spectroscopy can be a sensitive and selective way to detect gas phase species. Since laser pulses can both create reactants and detect the products, laser techniques allow the study of chemical kinetics in real time. Consequently, many different laser techniques have been developed to study gas phase chemistry.[6,7]

This thesis is divided into two sections: a longer first section on my work at the California Institute of Technology in Pasadena, CA and a smaller second section based on my work at the Université de Rennes 1 in Rennes, France. These two sections, while on different topics – atmospheric chemical reactions and collisional rotational energy transfer at ultra-low temperatures – are united by their study of gas phase with laser spectroscopy, which shows the breadth of this experimental approach. This thesis will both look at kinetics (the rate of chemical reactions) and product yield of chemical reactions, both key pieces of information to modeling gas phase reactions.

The first part of this work outlines my work at the California Institute of Technology, studying atmospheric radical chemistry with cavity-ringdown spectroscopy (CRDS). Chapter 1 put this work in a broader picture of current scientific work on Earth's atmosphere. Chapter 2 provides a detailed description of our cavity-ringdown spectrometer and temperature-controlled flow cell. Next, I discuss work on three important atmospheric reactions: the isomerization of simple alkoxy radicals (Chapter 3), the reaction of HO_2 with NO (Chapter 4), and the reaction of OH with NO_2 (Chapter 5).

The second, and smaller, part of this work, contains one chapter – chapter 6 – on work done at the Université de Rennes 1, which describes work on the rotational energy transfer in collisions between CO and Ar at temperatures from 293 to 30 K with infrared-vacuum ultraviolet double resonance CRESU experiments

(1) Seinfeld, J. H.; Pandis, S. N. *Atmospheric Chemistry and Physics: From Air Pollution to Climate Change*.

(2) Moses, J. I. *Philos. Trans. R. Soc. A-Math. Phys. Eng. Sci.* **2014**, *372*.

(3) Waite, J. H.; Young, D. T.; Cravens, T. E.; Coates, A. J.; Crary, F. J.; Magee, B.; Westlake, J. *Science* **2007**, *316*, 870.

(4) Ferriere, K. M. *Rev. Mod. Phys.* **2001**, *73*, 1031.

(5) Havenith, M.; Schwaab, G. W. *Z. Phys. Chemie-Int. J. Res. Phys. Chem. Chem. Phys.* **2005**, *219*, 1053.

(6) Hodgkinson, J.; Tatam, R. P. *Meas. Sci. Technol.* **2013**, *24*.

(7) Heard, D. E.; Pilling, M. J. *Chemical Reviews* **2003**, *103*, 5163.

Published Content and Contributions

Sprague, M. K.; Mertens, L. A.; Widgren, H. N.; Okumura, M.; Sander, S. P.; McCoy, A. B. *The Journal of Physical Chemistry A.* **2013**, *117*, 10006-10017. DOI: 10.1021/jp400390y

L.A.M. participating in collection of spectrum and calibration of frequency axis of spectra.

Sprague, M. K.; Garland, E. R.; Mollner, A. K.; Bloss, C.; Bean, B. D.; Weichman, M. L.; Mertens, L. A.; Okumura, M.; Sander, S. P. *The Journal of Physical Chemistry A.* **2012**, *116*, 6327-6340. DOI: 10.1021/jp212136r

L.A.M. participated synthesis of precursors used to produce radicals studied and participating in taking all spectra published in this work.

Table of Contents

List of Figures

Chapter 1

Chapter 2

Chapter 3

Chapter 4

Chapter 5

Chapter 6

List of Tables

Chapter 2

Chapter 3

Chapter 4

Chapter 5

Chapter 6

Chapter 1 – Introduction: Radical Chemistry in Earth's Atmosphere

Atmospheric chemistry affects air quality on a local and global level. Free radicals – molecules with an unpaired electron – form when UV and visible light from the sun split apart chemical bonds (Figure 1). While dilute, these radicals are highly reactive and undergo chain reactions that change the composition of the atmosphere and effect air quality. Anthropogenic emissions (cars, factories, etc.) interact with these radicals in ways that can be harmful to environmental and human health. For example, chloroforocarbon refrigerants photolyze in the stratosphere to produce chlorine and bromine radicals which catalyze ozone destruction, leading to the ozone hole in the southern hemisphere and exposing humans and other organisms on Earth's surface to harmful UV radiation. NO_x (NO and NO_2) emissions from combustions, especially from vehicle exhaust, interact with hydrocarbons in the troposphere, to produce urban smog – air with added ozone and particulate matter that poses a significant risk to human health.[1,2]

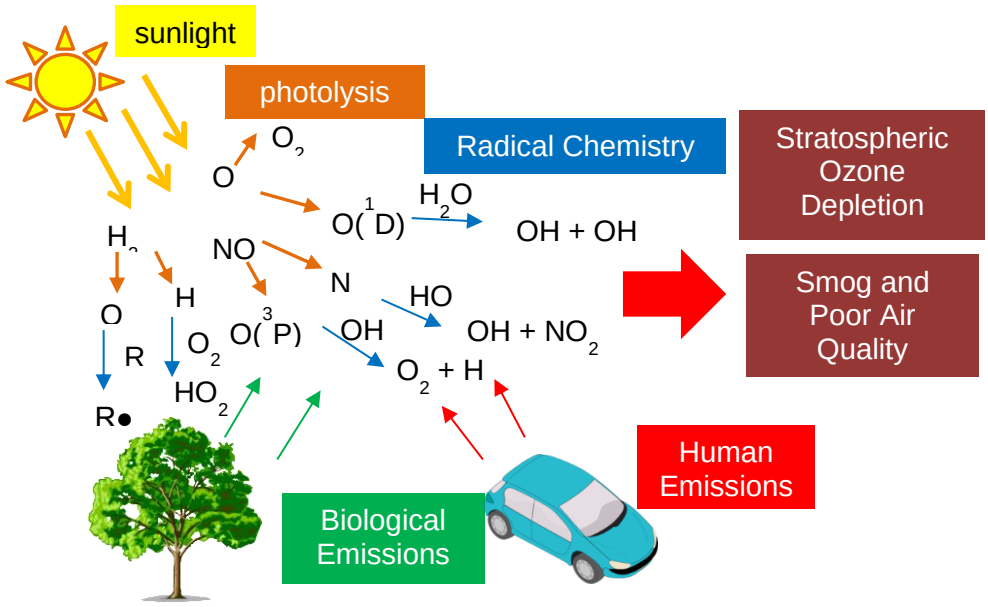

Figure 1. Schematic of how human emissions interacts with pre-existing radical chemistry to cause pollution hazardous to human and environmental health.

HO_x (OH and HO_2) and NO_x radicals catalyze chemistry throughout the atmosphere. They are key reagents in both the troposphere (the lowest, most dense part of the atmosphere that spans from the ground to about 10 km high. The troposphere is characterized by turbulent mixing which causes weather, and its chemistry is characterized by the oxidation of hydrocarbons emitted from plants and humans) and the stratosphere (the layer above the troposphere, which is relatively calm and static. Higher energy UV rays photolyze O_2 in the stratosphere to create the ozone layer).

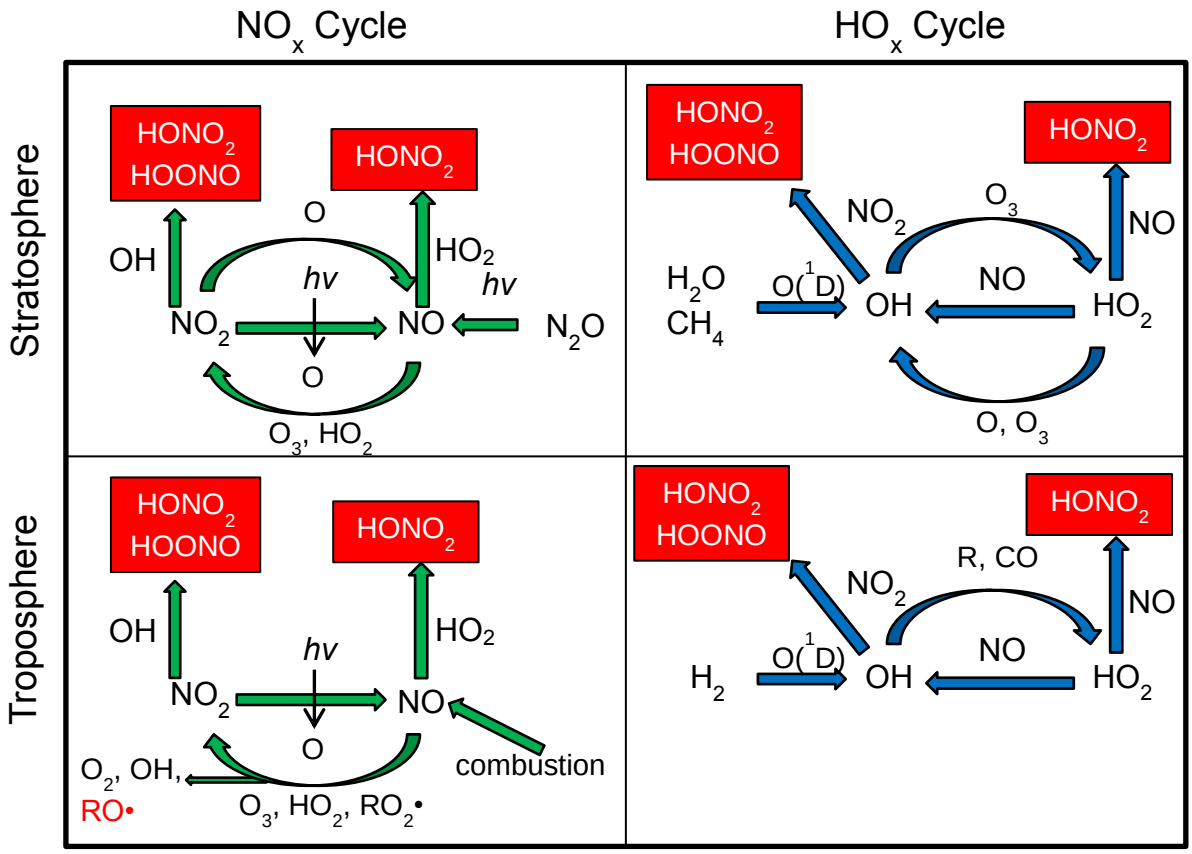

Figure 2. Schematic of the HO_x and the NO_x cycles in the troposphere and stratosphere.

The top two panels of Figure 2 show the HO_x and NO_x cycles in the stratosphere. These cycles do not include any hydrocarbons, since OH reacts with the vast majority of hydrocarbons emitted in the troposphere, eventually oxidizing them to CO_2 before they can reach the stratosphere. NO and OH – produced from the photolysis of H_2O, CH_4 and N_2O – react with O

or O_3 radicals to produce HO_2 and NO_2, respectively. These radicals then react with O_3 or O, and the cycle continues, destroying a molecule of ozone in each reaction. The HO_x and NO_x cycles are tempered by the photolysis of NO_2, which creates oxygen radicals that reaction with molecular oxygen (O_2) to reform ozone.[1,2] The chain reactions are ended by radical terminating reactions, notably the reaction of OH with NO_2 to form nitric acid ($HONO_2$) or peroxynitrous acid (HOONO).[3,4] Butkovskaya *et al*.[5-7] also propose the reaction of HO_2 with NO to form $HONO_2$ as a potential radical terminating reaction, especially important in the colder temperatures of the upper troposphere and lower stratosphere.

In the troposphere (bottom two panels of Figure 2) these cycles catalyze the oxidation of hydrocarbons (denoted by R) emitted from plants and human sources. The first step of hydrocarbon oxidation is reaction with OH to form alkyl radicals, R●. Alkyl radicals react with O_2, which is 21% of the atmosphere, to form peroxy radicals.

$$R + OH \rightarrow R\bullet \quad (R1)$$

$$R\bullet + O_2 \rightarrow RO_2\bullet \quad (R2)$$

In urban areas characterized by high NO_x, which is emitted from human combustion of fossil fuels, the RO_2● radicals will react with NO to form alkoxy radicals.

$$RO_2 + NO \rightarrow RO\bullet + NO_2 \quad (R3)$$

This reaction leads to higher levels of ozone in urban areas, since NO_2 from R3 photolyzes to produce oxygen atoms.

$$NO_2 + h\nu\ (+O_2) \rightarrow NO + O_3 \quad (R4)$$

The ozone produced can pose a substantial threat to human and environmental health, since increased ozone concentrations in the troposphere have been linked to respiratory illness.[8]

The reaction of peroxy radicals ($RO_2\bullet$) with NO produce alkoxy radicals, which can either reaction with O_2, isomerize or decompose. The relative yields of these reactions determine if long hydrocarbon chains oxidized via reaction with O_2 or isomerization to form low-volatility species that can condense to form secondary organic aerosols – particulate matter can also be a hazard to human health[8] – or is broken apart to eventually form CO_2 via decomposition.[9,10]

Scientific Approach to solving Atmospheric Pollutions

A scientific understanding of radical chemistry is essential to addressing the problems of stratospheric ozone depletion and urban smog. Since the HO_x and NO_x cycles are key catalyst to both processes, HO_x and NO_x chemistry needs to be thoroughly understood in order create accurate chemical models of the atmosphere. Additionally, the reactions of hydrocarbons and hydrocarbon-derived radicals are essential to models of the troposphere. Scientists have used a variety of approaches to understand and model this radical chemistry:

1. Performing laboratory experiments to study the rates and product distribution of atmospheric reactions
2. Creating mathematical models that use inputs from experimental data that will predict concentrations of atmospheric species based on theoretical or future emission profiles.
3. Directly measuring the concentrations of atmospheric species in the field and comparing measured values to modeled values to ensure the accuracy of the models.

When these models are created and refined, policy makers can use them to pinpoint the causes of pollution and make pollution controls that work. This approach has already been used to model stratospheric ozone destruction from chloroflurocarbons, which led to the Montreal Protocol that prohibited these compounds and stop the decrease in stratospheric ozone.[1] It has also been used to show that NO_x compounds are responsible for increased ozone and particulate

matter in urban environments.[1] Of course, atmospheric models need to be applicable to a variety of situations and areas of the atmosphere, and significant errors still exist in the model.

Section 1 (Chapter 1 – 5) of the thesis outline laboratory experiments that I have performed at the California Institute of Technology that will provide better inputs to atmospheric models, including data that addresses some of the largest uncertainties in current atmospheric models. In Chapter 3, I will discuss direct rate determinations for *n*-butoxy radicals, the first direct kinetics found for an alkoxy isomerization. In chapter 4, I will describe upper limits on the amount of $HONO_2$ and HOONO from the reaction of HO_2 + NO. While small, any yield of this reaction could have large environmental impacts, due to the importance of HO_x and NO_x chemistry and the number of times atmospheric radicals cycle through the HO_x and NO_x cycles. The $HONO_2$ yield from HO_2 + NO is currently the largest uncertainty in the total modeled NO_x column due to gas phase chemistry, leading to uncertainties as large as a factor of 2 over the tropics.[11] In Chapter 5, I will present data on the reaction of OH + NO_2, one of the most important radical terminating reactions in both the atmosphere, quantifying the branching ratio of $HONO_2$ and HOONO. A lack of temperature dependence for this reaction is currently one of the largest uncertainties in predicting ozone concentrations in urban areas.[4]

References

(1) Seinfeld, J. H.; Pandis, S. N. *Atmospheric Chemistry and Physics: From Air Pollution to Climate Change*.

(2) Jacob, D. J.; Princeton University Press: 1999.

(3) Mollner, A. K.; Valluvadasan, S.; Feng, L.; Sprague, M. K.; Okumura, M.; Milligan, D. B.; Bloss, W. J.; Sander, S. P.; Martien, P. T.; Harley, R. A.; McCoy, A. B.; Carter, W. P. L. *Science*, *330*, 646.

(4) " Predicting smoggiest days: Experiments improve accuracy of ozone predictions in air-quality models." In *ScienceDaily.* 2010. <www.sciencedaily.com/releases/2010/10/101028143946.htm>

(5) Butkovskaya, N.; Kukui, A.; Le Bras, G. *The Journal of Physical Chemistry A* **2007**, *111*, 9047.

(6) Butkovskaya, N.; Rayez, M.-T.; Rayez, J.-C.; Kukui, A.; Le Bras, G. *The Journal of Physical Chemistry A* **2009**, *113*, 11327.

(7) Butkovskaya, N. I.; Kukui, A.; Pouvesle, N.; Le Bras, G. *The Journal of Physical Chemistry A* **2005**, *109*, 6509.

(8) Wardlaw, A. J. *Clin. Exp. Allergy* **1993**, *23*, 81.

(9) Orlando, J. J.; Tyndall, G. S.; Wallington, T. J. *Chemical Reviews* **2003**, *103*, 4657.

(10) Atkinson, R. *Int. J. Chem. Kinet.* **1997**, *29*, 99.

(11) Stavrakou, T.; Müller, J. F.; Boersma, K. F.; van der A, R. J.; Kurokawa, J.; Ohara, T.; Zhang, Q. *Atmos. Chem. Phys.* **2013**, *13*, 9057.

Cavity Ring-Down Spectroscopy in a Temperature Controlled Flow Cell

Cavity ring-down spectroscopy (CRDS) is ideal for studying atmospheric radicals, which, due to their high reactivity, cannot be isolated in large quantities,[1] and consequently, the Okumura group has used it extensively to find spectra of atmospheric compounds[2-4] and kinetics of atmospheric reactions.[4-6] With our pulsed CRD spectrometer, we can detect radical concentrations down to about 10^{-12} cm^{-3} and record spectra of weak transitions, like the Peroxy X←A transition in the near-IR.[7] Although this transition is very weak, it is a bound transition, which means that it is generally a structured, isolated transition. We used the A←X transition in the near-IR to study the kinetics of alkoxy isomerization (Chapter 3). Our pulsed-CRD spectrometer is also operates in the mid-IR OH stretch region (3200 – 3750 cm^{-1}). While many species absorb strongly in this region, the sensitivity of CRDS allows detection of small concentrations of common atmospheric species. This sensitivity was essential to our work in chapter 4 looking for a small branching ratio of $HONO_2$ from the reaction of HO_2 + NO. Since CRDS is a spectroscopic technique we can easily distinguish isomers, like $HONO_2$ and HOONO, because they absorb at different frequencies. This was important for determining the branching ratio of these compounds both from HO_2 + NO (Chapter 4) and from OH + NO_2 (Chapter 5).

We couple CRDS with pulses laser photolysis (PLP), which allows us to detect short lived radicals and measure kinetics in real time. In this technique, an excimer pulse creates radicals by photolyzing precursor molecules and the CRDS probes the resulting radical chemistry. Kinetics are normally found by changing the delay between the excimer and CRDS pulse, so that radical chemistry can be observed in real time. For faster reactions, those in which the timescale of the reaction is near the timescale of the ring-down time (discussed below), we

used the simultaneous kinetics and ring-down method (SKaR) first developed by Brown et al.[8] This method will be discussed in greater detail in Chapter 3.

We also have designed and built a temperature controlled flow cell for use with our CRD spectrometer. This flow cell allows measurement of the temperature dependent kinetics of atmospheric radical reactions, reaching temperatures between -20 and 80 °C and pressures between 0 and 1 atm.

This chapter outlines the basics of CRDS and describes our instrument in detail. This spectrometer was used to obtain all data in Chapters 3-5, which includes direct kinetics of alkoxy isomerization, the branching ratio of $HONO_2$ and HOONO from the reactions of HO_2 with NO and the branching ratios of $HONO_2$ and HOONO from the reaction of OH and NO_2.

The Basics of Cavity Ring-Down Spectroscopy

CRDS uses an optical cavity to increase effective pathlength and therefore sensitivity, allowing detection of weakly absorbing and dilute species.[9-12] While many CRDS techniques use continuous wave lasers,[13] all experiments chapters 3-5 were performed with pulsed-CRDS. In pulsed-CRDS, a pulse from a nanosecond laser is injected into an optical cavity formed from two highly reflective mirrors (Figure 1). While not completely accurate (as discussed below in the section on non-exponential ring-downs), the laser beam can be imaged to bounce back and forth between the two mirrors, allowing the beam to traverse the sample billions of times and increasing the absorption of light.

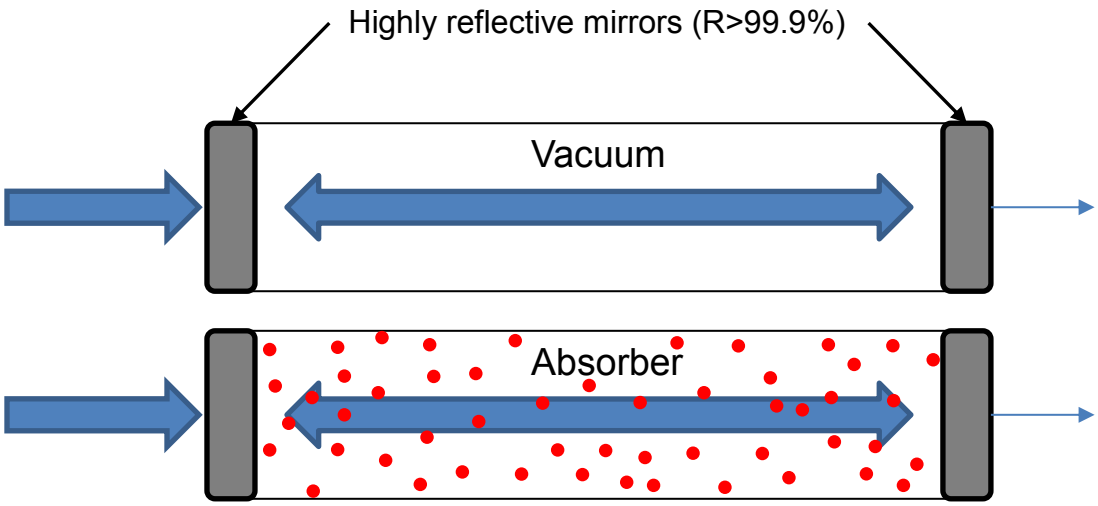

Figure 1. Schematic of CRDS. Light is injected into an optical cavity which increases the pathlength to several kilometers. When an absorber is present, it causes an increase decay rate of light intensity in the cavity.

When there is no absorber present, the only loss of light out of the cavity is when the light hits the mirrors. Since mirrors are typically >99.98% reflective, only about 0.02% or less of the light is lost each time the laser pulse is reflected. This small percentage of light "leaks" out of the cavity can be measured with a fast detector (we typically record a 25 megasamples-per-second), and will exponentially decrease with time, due to the exponential decay of light out of the cavity:

$$I = I_0 \exp\left(\frac{-t}{\tau}\right) \quad (1)$$

where I_0 is the initial intensity of light injected into the cavity, I is the intensity of light at time t, and τ is the characteristic ring-down time.[9] If there is no absorber present (blue trace in Figure 2) τ is determined exclusively by the reflectivity of the mirrors:

$$\tau_0 = \frac{L_{opt}}{c(1-R)} \quad (2)$$

where τ_0 is the ring-down time under vacuum, c is the speed of light, R is the reflectivity of the mirrors, and L_{opt} is the optical pathlength (the distance between the two mirrors).

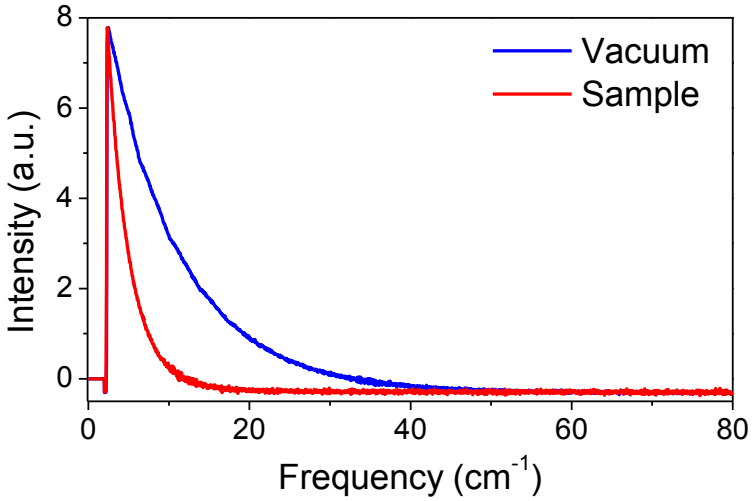

Figure 2. A ring-down taken under vacuum (blue) and with $HONO_2$ from OH + NO_2 in the cell (red) at 3550 cm^{-1}.

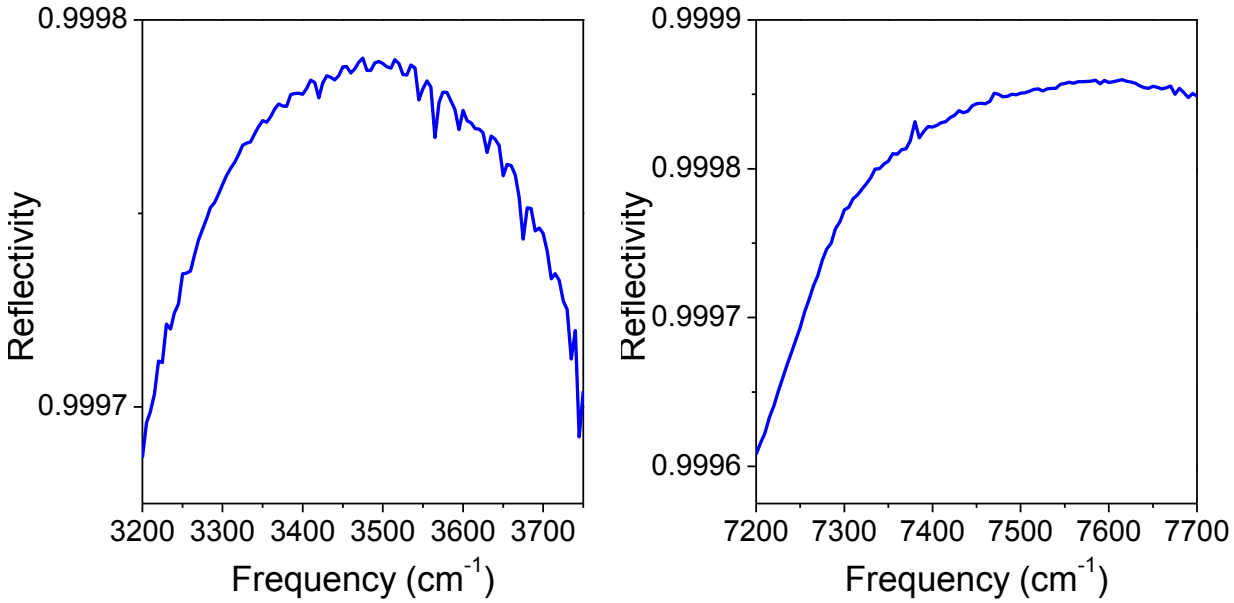

Figure 3. Mirror Reflectivity of (a) LGR 2.8 micron mirrors (6 m radius of curvature, 1" diameter) for the mid-IR and (b) LGR 1.32 micron mirrors (1" diamter, 1" ROC) for the near-IR.

If τ_0 is found by fitting the exponential decay of light under vacuum (equation 1), the reflectivity of the mirrors is given with equation 2. Figure 3 shows the measured reflectivity of the mirrors that we used in our experiments in the mid-IR (a) and the near-IR (b).

When an absorber is placed in the middle of the cavity, there is loss of light both from leakage through the mirrors and the absorbance of the sample, which leads to an exponential decay with a shorter ring-down time, τ (the red decay in Figure 2). The ring-down time, τ is now described by:

$$\frac{1}{\tau} = \frac{1}{\tau_0} + \frac{Ac}{L_{opt}} \quad (3)$$

where τ_0 is the ring-down time without the absorber present and A is the absorbance of the sample.[9] A is described by the Beer-Lambert law:

$$A = \ln\left(\frac{I_0}{I}\right) = \sigma L_{abs} N \quad (4)$$

where I is the initial intensity of light before traveling through the sample, I_0 is the light after the sample, σ is the absorbance cross section of the absorber L_{abs} is the absorbance pathlength of the absorber, and N is the number density of the absorber. Since we purge the ring-down mirrors with dry nitrogen during a typical experiment, the distance between the two mirrors, the optical pathlength, L_{opt}, is not the same as the distance the beam passes through the same during roundtrip through the cavity, L_{abs}. Combining equations 3 and 4, we find that the absorbance of the sample is given by:

$$A = \frac{L_{opt}}{c}\left(\frac{1}{\tau} - \frac{1}{\tau_0}\right) \quad (5)$$

This equation does not depend on the initial intensity of the laser beam, which is another advantage of CRDS, since the experiment is insensitive to power fluctuations of the lasers.[10,11]

The minimum absorbance of our instrument is found by taking several ring-downs (at least 20) at one wavelength without the absorber. The standard deviation, $\Delta\tau$, divided by the ring-down time τ gives $\Delta\tau/\tau$, the relative standard deviation which is not dependent on wavelength. The minimal detectable absorbance is then defined as any absorbance that would lead to ring-down times that are shorter than τ_0 by $\Delta\tau/\tau$. Given equation 5, A_{min} the minimum detectable absorbance (1σ) is:

$$A_{\min} = \frac{L_{opt}}{c}\left(\frac{\Delta\tau}{\tau}\right)\frac{1}{\tau_0} \quad (6)$$

The sensitivity of our spectrometer can be found by multiplying equation 6 by the square-root of time it takes to acquire one ring-down:

$$\text{sensitivity} = \frac{1}{c}\left(\frac{\Delta\tau}{\tau}\right)\frac{1}{\tau_0}\sqrt{N} \quad (7)$$

The factor of $\sqrt{N}$ reflects that the signal-to-noise ratio decreases as $1/\sqrt{N}$. Generally, we average 16 shots of a 10 Hz laser, so N is 1.6 s. We also divided equation 6 by L_{opt} to yield equation 7, so that the measure of sensitivity is independent of pathlength. This equation shows that the sensitivity is improved as τ_0 – or in other words the reflectivity of the mirrors – increases. Consequently, we want the highest reflectivity mirrors available, given that our laser pulses are intense enough that we can still measure the small leakage through the mirrors. In the mid-IR, we typically have ring-down times of 9.5 μs at the center of the 2.8 micron mirrors, values of $\Delta\tau/\tau$ of 0.3%, and an optical pathlength of 0.57 m, leading to a minimum detectable absorbance of 1.2 ppm (2σ, equation 6) and a sensitivity of 2.7×10^{-8} cm^{-1} $Hz^{-1/2}$ (2σ, equation 7). In the near-IR, we typically have ring-down times of 14 μs at the center of the 1.32 micron mirrors, values of $\Delta\tau/\tau$ of 0.1%, and an optical pathlength of 0.53 m, leading to a minimum detectable absorbance of 0.25 ppm (2σ, equation 6) and a sensitivity of 6.0×10^{-9} cm^{-1} $Hz^{-1/2}$ (2σ, equation 7).

Non-exponential Ring-downs

While we generally fit our ring-downs to an exponential model, there are several instances where we cannot assume a pure exponential function. Non-exponential ring-downs can occur when: (1) when the length of the laser pulse is long enough that the laser pulse overlaps with itself, creating interference patterns, (2) when the concentration of the absorber changes on the same time scale as the ring-down (3) the bandwidth of the laser is large when compared to the full-full-width half-max of spectral feature.

(1) Although we like to imagine pulsed-CRDS as a laser pulsed bouncing back and forth between the mirrors, since our pulses are a few nanoseconds long (our Nd:YAG laser has pulses that are 4-6 ns long), their pulse width is actually longer than the time it takes to make a roundtrip though the cavity (if the cavity is 50 cm long, the time of one roundtrip is about 2 ns). Since each laser pulse contains multiple modes, only some of which couple into the cavity, these modes can create interference patterns visible in the ring-downs as shown in Figure 4.[14] In our spectrometer, we typically see these beating patterns if the cavity is misaligned or if the output of the cavity is not focused properly on the detector (i.e. the detector is not measuring the entire beam). Generally, if the whole laser beam is captured by the detector, the multiple beating patterns from multiple modes wash out to create an almost perfect exponential. Even if we experience slight interference patterns, like in Figure 4, we can still fit to an exponential to get an accurate, consistent ring-down time if the beats are small and regular.

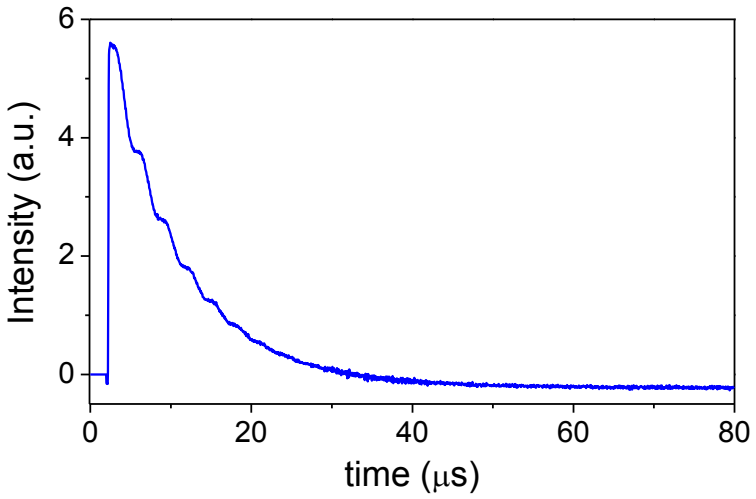

Figure 4. Example of a Ring-down (3400 cm^{-1}, 10 torr) with beating patterns.

(2) Since the decay time depends on the absorbance of a sample (equation 3), if the concentration of the absorber changes during a ring-down, the ring-down time will change accordingly. We experience non-exponential ring-downs if there is fast chemistry occurring in our cell, and we can record the kinetics of fast reactions by measuring how τ changes with time during a single ring-down.[8] This will be discussed further in Chapter 3 where we find the rate of alkoxy isomerization (which is on the timescale of 10 μs) with the SKaR method.[8]

(3) If the bandwidth of the laser pulse is larger than the width of the absorbance peak, different wavelengths in the laser beam will decay at different rates.[14-16] Water, which is generally present in our system due to small leaks or impurities in our gas cylinders, has many sharp absorbances in the mid and near-IR. Figure 5 shows a ring-down at 10 torr and 3730 cm^{-1} (1 cm^{-1} bandwidth of the mid-IR beam) in which there is a sharp initial absorption of the wavelengths absorbed by water followed by a much slower decay of other wavelengths. Since absorbing wavelengths decay much faster than the other wavelengths, an exponential fit will be biased towards non-absorbing wavelengths. Consequently, the apparent absorbance will be artificially small, and the Beer-Lambert law can no longer be used to derive accurate

concentrations. This effect is more prominent the sharper the peak and the higher the absorbance.[14-16] Chapters 4 and 5 discuss this problem in more detail and discuss methods for extracting real concentrations under these conditions.

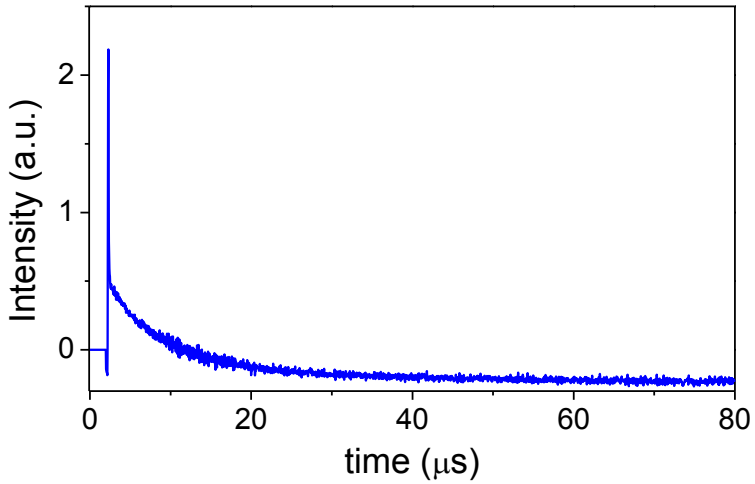

Figure 5. Example of a multiexponential ring-down (3730 cm^{-1}, 10 torr) with a first sharp decay of wavelengths absorbed by water.

Overview of our CRD Spectrometer

A schematic of the experimental apparatus is shown in Figure **6** and Figure **7**, and details of our experimental method have previously been described by Sprague *et al*. (2012 and 2013).[3,6] Matt Sprague also gives a detailed descriptions of the CRD spectrometer and laser set-up in his thesis.[17] Gas mixtures flow through a small (~10 cm^3) slow flow tube (~3000 sccm, ~50 ms residence time) into a vacuum (Leybold Trivac D65B, 65 m^3/h pumping rate). This temperature controlled flow cell will be described later in this chapter. Chemistry is initiated by 351 nm UV pulses (10 Hz) from an excimer laser (XeF, Lambda Physick LPX) focused (4.1 cm × 1.0 cm area) on the flow cell. After chemistry has been initiated, a digital delay generator (DDG) triggers a tunable IR probe, also at 10Hz, which is sent through the flow cell perpendicular the UV beam. IR light is generated via two methods: a H_2 Raman shifter to produce near-IR light

(Figure **6**) to detect the A←X transition (7200-7700 cm^{-1}) of peroxy radicals (Chapter 3) and an OPA to produce mid-IR light (Figure **7**) to measure absorptions in the OH stretch region (3200-3750 cm^{-1}, Chapters 4 and 5). Two highly reflective mirrors (R>99.97%, purchased from Los Gatos Research) placed at the ends of the flow cell and form an optical cavity for the IR pulse. The resulting ring-down (Figure **2**) is detected with either an InSb (mid-IR) or InGaAs (near-IR) detector and recorded by a 25Hz Gageboard PC oscilloscope and processed by a LabVIEW program. The pressure of the cell (measured with a 1000 torr MKS Barton) and the gas flows (measured with Omega or Edwards flow meters) are also recorded on LabVIEW via an A/D board.

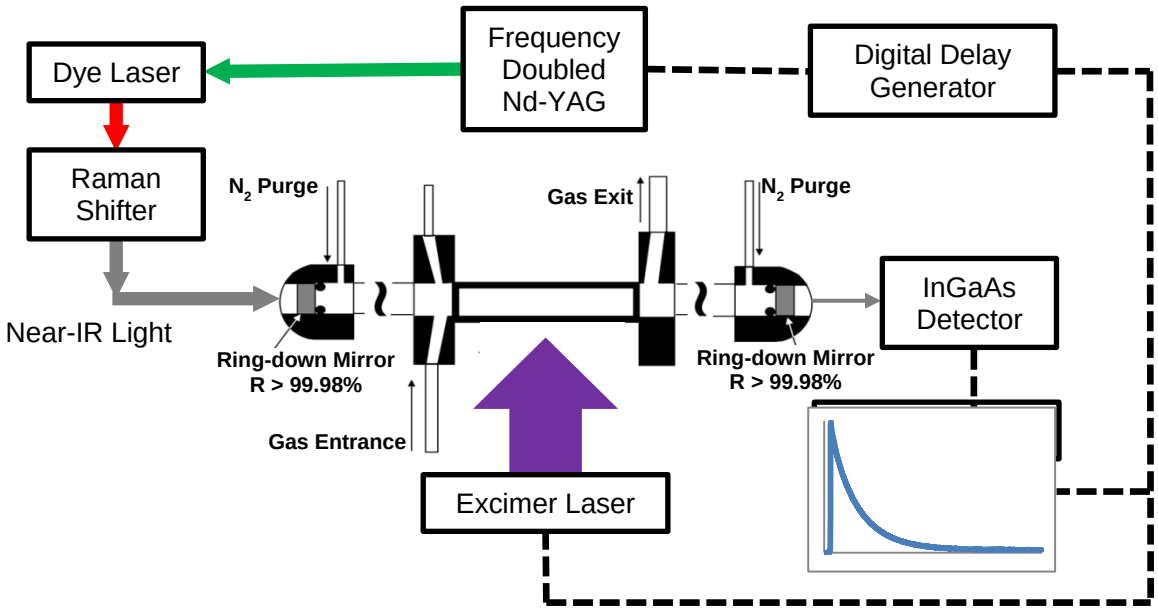

Figure 6. Schematic of Near-IR CRDS experiments.

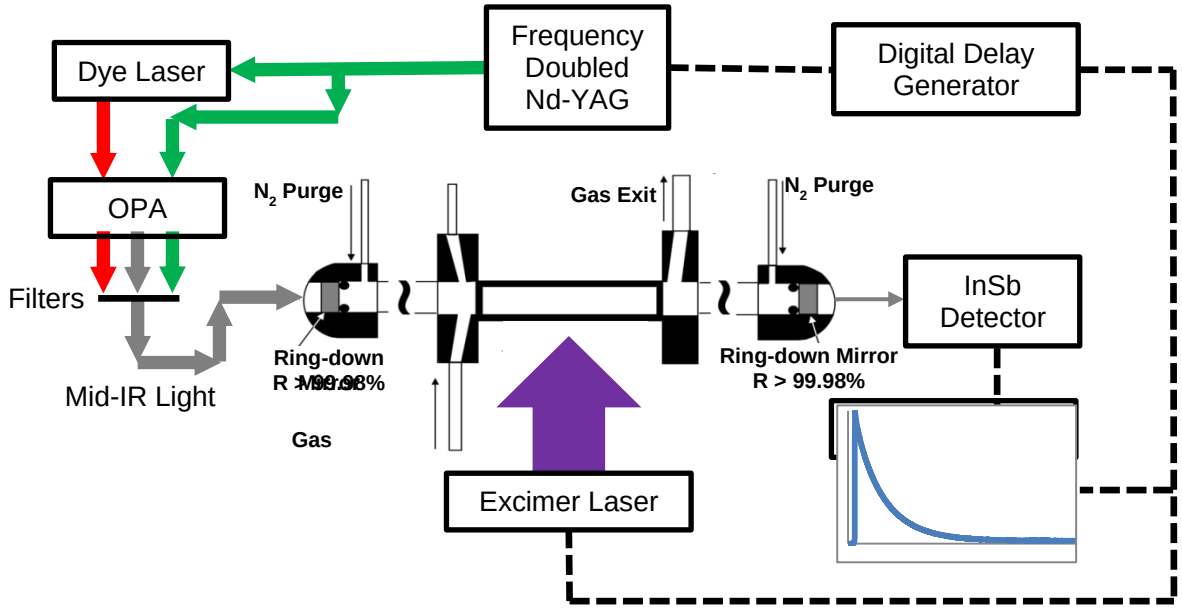

Figure 7. Schematic of Mid-IR CRDS experiments.

Temperature Controlled Flow Cell

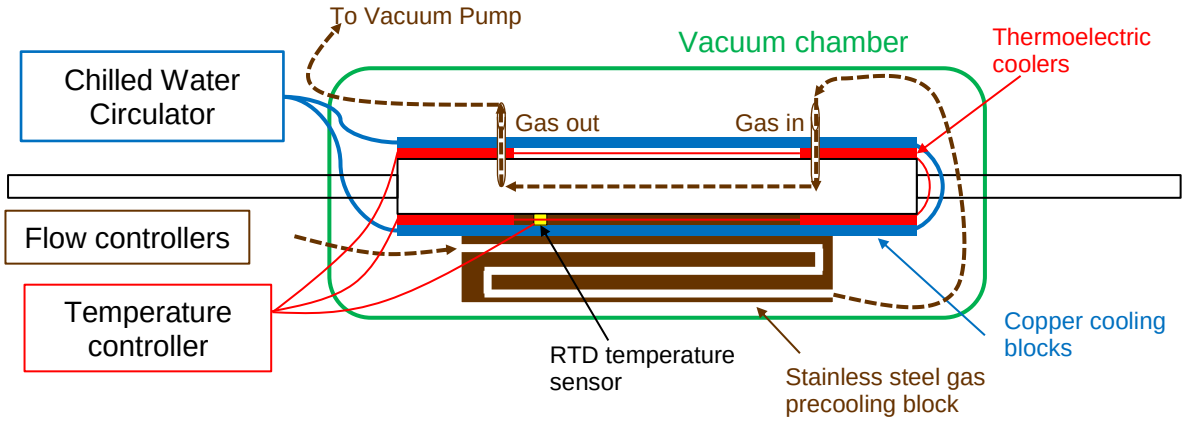

Figure 8. Schematic of the temperature controlled flow cell. The water circulation system is shown in blue, the electronic temperature control with TECs is shown in red, the vacuum in shown in green, and the path of the gases is shown in brown.

To study temperature dependent reactions and to find rate constants applicable to cooler parts of the atmosphere, we built a temperature controlled flow reactor. A schematic of this flow cell is shown in Figure 8. The original design on SolidWorks made by Luiz Gomez is shown in

Figure 9. A Picture of the cell with labels of the alignment of the laser beams during a typical experiment is shown in Figure 10.

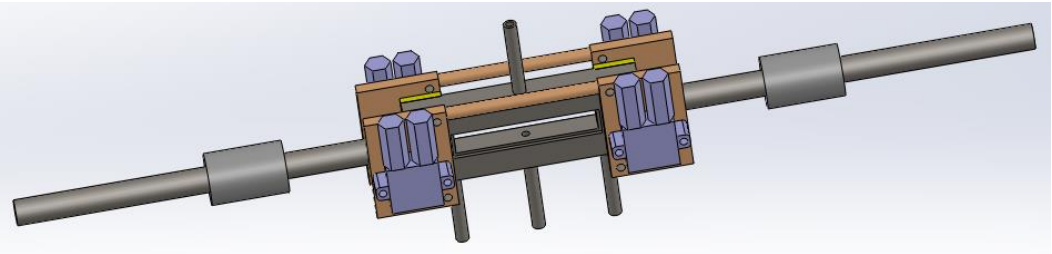

Figure 9. Original SolidWorks design of the temperature controlled cell. The cooling block is in copper and purple and the TECs are shown in yellow.

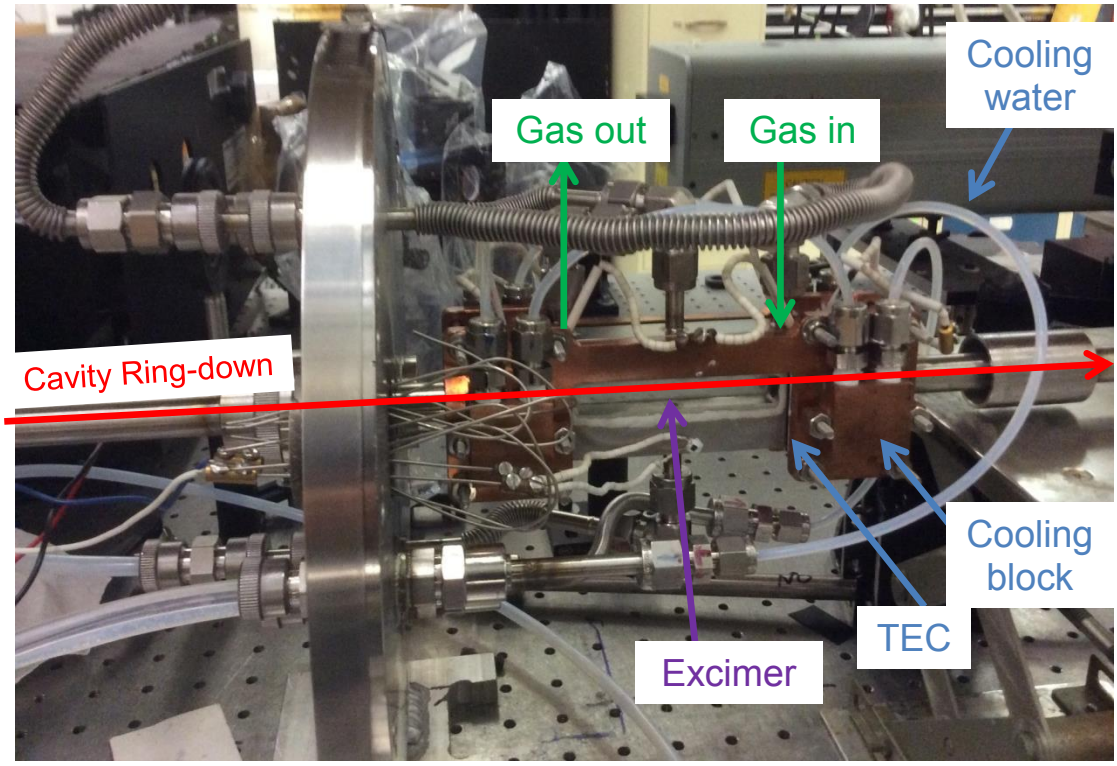

Figure 10. Picture of the temperature controlled cell outside the vacuum chamber. Later, we modified the cell by adding a precooling block placed underneath the cell.

Lower temperatures were achieved by flowing chilled water through a copper cooling block which cools thermoelectric coolers (TEC) in thermal contact with the flow cell. TECs are electronic elements that become hot on one side and cold on the other when current is passed through them. Four 2.0 × 4.0 cm TECs (TE Technologies TE-63-1.4-1.15) were placed on the surface of the stainless steel flow cell with a 7.0 × 1.0 cm UV fused silica window on the front and back of the cell epoxied to the cell with Torr Seal vacuum epoxy to allow passage of the excimer beam. The current through these four TECs was controlled with the temperature controller (ILX Lightwave LDT-5948) which used a PID algorithm to ensure that the temperature remained constant during experiments. The temperature was measured by the temperature controlled with a resistance temperature detector (RTD) attached to the front of the cell just below the excimer window with more Torr Seal epoxy. The resistance across the RTD is directly proportional to the temperature:

$$T = \frac{R - 100}{0.385}$$

where T is the temperature in °C and R is the resistance in ohms. A copper cooling block was attached to the TECs to remove heat from the hot side and to add rough temperature control. Chilled or heated water was sent through the copper cooling block with a Neslab coolflow CFT-33 refrigerated water circulator capable of temperatures between 10 and 40 °C. With the TECs we can reach temperatures between -20 and 100 °C. The assembly was placed in a vacuum chamber to prevent condensation on the excimer windows and provide insulation. The pressure of the vacuum chamber was measured with a thermocouple gauge and held below a torr during all experiments. Two 7.25 × 1.35 cm UV fused silica windows are attached to the vacuum chamber to allow passage of the excimer beam.

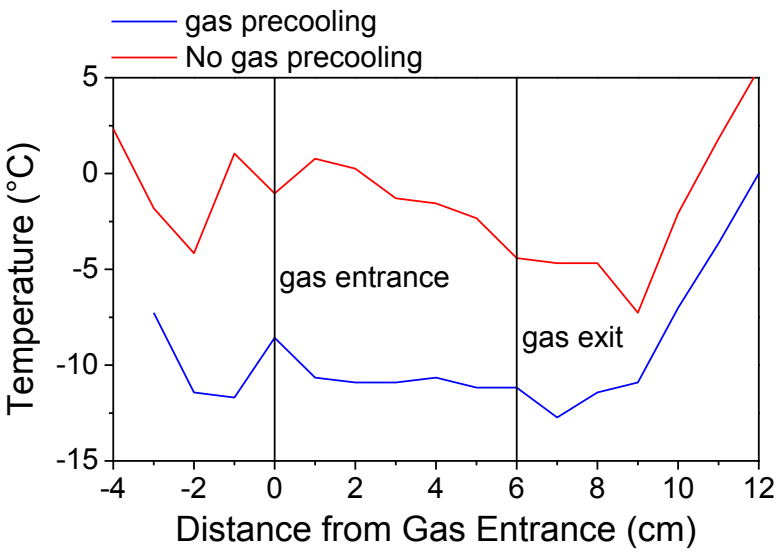

Figure 11. Measured temperature gradients in the cell with nitrogen gas flow and purges (5000 sccm total flow) at 700 torr and the temperature controller set to -10 °C with (blue) and without (red) the gas precooling block. The gases entered the cell at 0 cm and exited the cell at 6 cm. The excimer beam traveled through the cell between 1 and 5 cm. The temperature between 1 and 5 cm was (-1.4 ± 2.6) °C without precooling and (-10.6 ± 0.4) °C with precooling (2σ errors).

A stainless steel precooling block is placed in thermal contact with the flow cell to precool the gases to ensure uniform temperature. Gases travel 12 cm through this block, which is at the same temperature as the flow cell, before entering the cell for experiments. The gases traveled about 10 cm through the flow cell along the IR-CRDS laser axis before exiting to the vacuum. The excimer beam, focused to a 4.1 × 1.0 cm crosses the cell perpendicular through the cell. A dry, room temperature N_2 purge is used to prevent condensation on the mirrors and to ensure the mirrors remain clean during an experiment. We measured the temperature of the cell as a function of length along the CRDS axis with an RTD attached to a Garolite (G10) tube under flow rates and pressures of a typical experiment (Figure 11). G10 was chosen because it is expected to only minimally perturb the temperature of the gases. Figure 11 shows that the

precooling is effective in ensuring uniform temperature of the gases in the area of the excimer beam. When there is no precooling of gases, the temperature in the 4 cm where the excimer beam is typically focused was (-1.4 ± 2.6) °C at 700 torr and the temperature controller set to -10 °C. With the cooling block the temperature was (-10.6 ± 0.4) °C. All errors are 2σ standard deviation.

Currently, the cell is capable of temperature between -20 and 100 °C. The upper limit is set to ensure that the Torr Seal epoxy that glues on the excimer window does not become detached from the cell. The lower limit is determined first by the temperature range of the water chiller, the cooling power of the TECs, and alignment problems that only happen at cold temperatures. The alignment problem occurs only at cold temperatures 5 °C or less and worsens with higher pressures. It is not due to condensation on the ring-down mirrors, since increasing the purge does not mitigate the problem. It is unlikely due to aerosol formation, because the problem still occurs when the only gases flowing is dry N_2, purified with molecular sieve 13x and filtered through a particle filter. If this problem is solved, lower temperatures can be reached by replacing the water chiller with a chiller that uses other solvents, like methanol, that have lower melting points.

Other possible improvements of the cell include replacing the Torr Seal connection on the excimer windows with a different seal method, perhaps a Teflon o-ring. Torr Seal is only capable of holding vacuum, but with the vacuum chamber the cell is usually at higher pressure than the outside. This has caused several leaks in the windows. When the Torr Seal does leak, it must be taken off using a heat gun or oven to bake the Torr Seal off and a new coat of Torr Seal is applied and left overnight to dry. This process is time consuming and potentially damaging to the windows, making the frequent small leaks very difficult to fix. Additionally, the custom

ordered UV fused silica windows are easily destroyed if the excimer beam accidently hits the Torr Seal. This mistake can easily occur, since the vacuum chamber blocks sight of the excimer alignment through the flow cell, but it can be mitigated by using as low of power on the excimer beam as possible. To improve the cell, a different seal should be used for the windows that is capable of holding pressure or is easier reseal. The copper cooling block could also be improved by replacing the 1/8" tubing currently in the cell with 1/4" tubing to allow more efficient cooling and to prevent clogs.

Production of Tunable Near-IR Light

A schematic of the Near-IR laser set-up is given in Figure 6. 1064 nm light from a 10 Hz Continuum Surelite III Nd:YAG laser is frequency doubled by a KD*P second harmonic generator (SHG) to produce 532 nm light. The laser power was adjusted by changing the Q-switch delay (the delay between the voltage to the flashlamp and the voltage to the Q-switch). The maximum power was (~700 mJ/pulse) was at a 240 μs delay, but we typically ran experiments at much lower powers, a 180 μs delay. Typical laser powers for the Near-IR are given in Table 1. Light exciting the YAG is linearly[L1] polarized and converted to circularly polarization light needed for the SHG. The resulting 532 nm (linearly polarized) beam is used to pump a Quantum Ray PDL-3 dye laser to produce tunable red light (DCM dye, in methanol, 620 – 670 nm, Table 2) which is transversely pumped where the 532 beam pumps the amplifier perpendicular to the red beam from the pre-amplifier. This method of pumping was chosen, because although it does not protect the mode quality of the beam, it results in the maximum power.

Table 1. Typical laser powers in the Near-IR at a Q-switch delay of at a Q-switch of 180 μs.

Laser	Wavelength (nm)	Typical Power (mJ/pulse)
YAG before SHG	1064	367
YAG after SHG	532	140
Dye laser	647	16.3

Table 2. DCM dye concentration (in HPLC grade methanol) used for all experiments.

Dye	DCM dye concentration (mg/L)
Oscillator	270
Amplifier, transverse pumping	90
Amplifier, longitudinal pumping	27

The red beam was then converted to tunable near-IR light with a double pass hydrogen Raman shifter (214psi). A detailed description of the Raman shifter can be seen in Matt Sprague's thesis.[17] The second stokes shift of hydrogen, a shift of 8310.4 cm^{-1} produces several μJ of near-IR light (7000-7800 cm^{-1}). At a max Q-switch delay of 240 μs, Matt Sprague measured 90 μJ per pulse of near-IR light.[17] The bandwidth of the resulting near-IR beam was 0.1 cm^{-1}, the bandwidth of the dye laser. 1.32 micron mirrors were used in the Near-IR; their mirror reflectivity curve is shown in Figure 3b. Light exiting the cavity was focused on an InGaAs photodiode (Thorlabs PDA10CS, 17 MHz) with a built-in amplifier.

Productions of Tunable Mid-IR Light

A schematic of the Near-IR laser set-up is given in Figure 7. The 532nm YAG beam and the red beam from the dye laser (as described above) are passed through two KTP optical parametric amplifier (OPA) crystals to produce tunable IR light. As described by Reid and Tang,[18] the OPA converts 532 nm photons (pump) into a 620 – 670 nm photon of red (signal) and a mid-IR photon (2660-3870 cm^{-1}). Before the dye laser, the green beam is divided with a beam splitter so that about 1/3 of the green beam enters the dye laser and 2/3 is preserved for the

OPA. For the mid-IR, the amplifier of the dye laser is longitudinally pumped, to preserve the model quality of the beam, which is necessary for the OPA. The incident 532 nm and red beams must be linearly polarized (one horizontal and one vertical). Telescoping lenses in front of the OPA focus the beams through the two KTP crystals.

Table 3. Typical laser powers in the mid-IR at a Q-switch delay of at a Q-switch of 200 μs.

Laser	Wavelength (nm)	Typical Power at a Q-switch of 200 μs (mJ/pulse)
YAG before SHG	1064	467
YAG after SHG	532	195
Dye laser	647.5	6.0
Dye laser beam after OPA (no 532 beam)	647.5	3.9
Dye laser beam after OPA (with 532 beam)	647.5	14.4
IR	3345.5	~0.5-1

The near-IR instrument is shown in the bottom panel of Figure 3. The beam from the dye laser is sent through a pressurized hydrogen Raman shifter (214psi), where near-IR light is produced from the second Stokes shift of hydrogen (8310.5 cm^{-1}). In the near-IR the wavelength is calibrated by tuning the dye laser to the atomic emissions of Ne gas with an optogalvanic cell. The wavelength of the resulting IR pulse was then compared to the absorbance of water at 7000-7400 cm^{-1}. The bandwidth of the resulting near-IR beam was 1 cm^{-1}, the bandwidth of the dye laser. The large bandwidth can lead to significantly non-exponential ring-downs, since many species, including H_2O, CO_2 and $HONO_2$ can have linewidths much narrower than 1 cm^{-1}. The wavelength calibration from the mid-IR was checked with position of water (3500-3800cm^{-1}) or other standard compounds, including methanol and $HONO_2$. 1.32 micron mirrors were used in the Near-IR; their mirror reflectivity curve is shown in Figure 3a. Light exiting the cavity was focused on an InSb photodiode (Judson J10D-M204-R500U-60) with a transimpedance amplifier (Analog Modules 351-A-1-50-NI) for HO_2 + NO experiments. For OH + NO_2 experiments, the

InSb detected was from Infrared Associates Inc. (IS-0.50) with a custom built transimpedance amplifier made by George Perry.

Excimer

A Lambda Physik LPX210i excimer laser was used to initiate chemistry. XeF (351 nm) was used to photolyze butyl nitrite to create an *n*-butoxy radical (Chapter 3) and to photolyze Cl_2 in the presence of methanol to create HO_2 in the HO_2 + NO experiments (Chapter 4). KrF (248 nm) was used to photolyze O_3 the presence of H_2 to create OH for the OH + NO_2 experiments. Gas concentrations are shown in Table 4. While the excimer is capable of higher powers, especially for KrF, we typically ran with powers of 700 mJ/pulse or 0.15 W/cm^2 at the entrance of the flow cell. The profile of the excimer beam was measured with a joule meter with a small slit placed in from of it. As shown by Figure 12, the excimer beam was not entirely uniform, meaning that concentrations of species from photolysis chemistry are likely non-uniform as well.

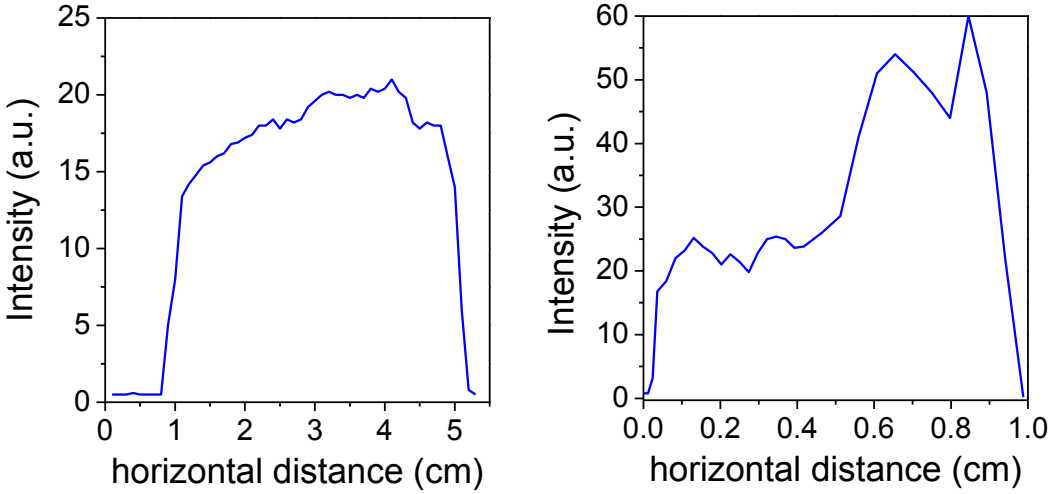

Figure 12. (a) Horizontal and (b) vertical profile of the excimer beam right before the cell. Profile was taken by placing a piece of cardboard with a small slit in front of the joule meter and moving the slit to measure different areas of the beam.

Table 4. Gas concentrations in excimer for KrF and XeF.

Gas	Pressure added for KrF (mb)	Pressure added for XeF (mb)
Rare gas (100% Kr or 100% Xe)	80	150
5% F_2 in He	120	10
75% Ne in He	2000	2800

Data Acquisition and Processing

The output of the InSb and InGaAs detectors was inputed into a GageScope CS1450 digital oscilloscope and the ring-down was recorded with LabView software (National Instruments). Each ring-down trace was collected for 80-100 μs at a rate of 25 MHz and traces were averaged for 16 shots (1.6 s). Ring-down traces were fit to a simple exponential model using the Levenberg-Marquardt algorithm after he first 1/8 of the initial lifetime was discarded to remove signal from scattered light.

LabView also controlled movement of the grating on the dye laser and stepper motors that adjust the alignment of the OPA with wavelength. Readings on flow meters (Omega 1700 series) were inputted into a A/D board connected to the computer, and flow rates were recorded on LabView. The flows and pressure in the cell are controlled manually with needle valves after each gas line and before the vacuum. A 1000 torr MKS Baratron (626A13TDD) monitored the pressure in the reaction cell, which was also recorded on LabView via the A/D board.

References

(1) Brown, S. S. *Chemical Reviews* **2003**, *103*, 5219.

(2) Takematsu, K.; Eddingsaas, N. C.; Robichaud, D. J.; Okumura, M. *Chemical Physics Letters* **2013**, *555*, 57.

(3) Sprague, M. K.; Mertens, L. A.; Widgren, H. N.; Okumura, M.; Sander, S. P.; McCoy, A. B. *The Journal of Physical Chemistry A* **2013**.

(4) Bean, B. D.; Mollner, A. K.; Nizkorodov, S. A.; Nair, G.; Okumura, M.; Sander, S. P.; Peterson, K. A.; Francisco, J. S. *The Journal of Physical Chemistry A* **2003**, *107*, 6974.

(5) Mollner, A. K.; Valluvadasan, S.; Feng, L.; Sprague, M. K.; Okumura, M.; Milligan, D. B.; Bloss, W. J.; Sander, S. P.; Martien, P. T.; Harley, R. A.; McCoy, A. B.; Carter, W. P. L. *Science* **2010**, *330*, 646.

(6) Sprague, M. K.; Garland, E. R.; Mollner, A. K.; Bloss, C.; Bean, B. D.; Weichman, M. L.; Mertens, L. A.; Okumura, M.; Sander, S. P. *The Journal of Physical Chemistry A* **2012**, *116*, 6327.

(7) Sharp, E. N.; Rupper, P.; Miller, T. A. *Physical Chemistry Chemical Physics* **2008**, *10*, 3955.

(8) Brown, S. S.; Ravishankara, A. R.; Stark, H. *The Journal of Physical Chemistry A* **2000**, *104*, 7044.

(9) *Cavity-Ringdown Spectroscopy: An Ultratrace-Absorption Measurement Technique*; Busch, K. W.; Busch, M. A., Eds.; ACS Publications: Washington, DC, 1999; Vol. 720.

(10) Ball, S. M.; Jones, R. L. *Chemical Reviews* **2003**, *103*, 5239.

(11) Berden, G.; Peeters, R.; Meijer, G. *Int. Rev. Phys. Chem.* **2000**, *19*, 565.

(12) Vallance, C. *New Journal of Chemistry* **2005**, *29*, 867.

(13) Hodgkinson, J.; Tatam, R. P. *Meas. Sci. Technol.* **2013**, *24*.

(14) Hodges, J. T.; Looney, J. P.; Zee, R. D. v. *The Journal of Chemical Physics* **1996**, *105*, 10278.

(15) Hodges, J. T.; Looney, J. P.; van Zee, R. D. *Appl. Opt.* **1996**, *35*, 4112.

(16) Yalin, A. P.; Zare, R. N. *Laser Phys.* **2002**, *12*, 1065.

(17) Sprague, M. K. **2011**. Ph.D Thesis.

(18) Reid, S. A.; Tang, Y. *Appl. Opt.* **1996**, *35*, 1473.

Appendix A – List of equipment in 17 Noyes and Their Manuals.

Piece of equipment	Model/Serial number	Stats	Link to website or manual
Nd:YAG laser	Continuum Surelite III	1064nm 10 Hz Max power = 7.6 watts at q-sw 240µs 4-6ns pulses power = 3.5 watts at q-sw 180µs	Stats: http://www.continuumlasers.com/products/pdfs/Surelite%20Rev%20F%20LR.pdf manual: http://www.doylegroup.harvard.edu/wiki/images/a/a0/996-0207_Rev_Q_Surelite_Manual.pdf
SHG	Inrad KD*P type II SHG crystals	Typical 532 powers: 1.2 watts at s-qw of 180 µs	Data sheet: http://www.inradoptics.com/pdfs/KDP_KD*P_DataSheet.pdf
Pulsed Dye Laser	Quanta-Ray PDL-3	Depends on the dye see dye table below.	Manual only in lab. Cannot find manual online.
Excimer	Lambda Physik LPX210i	Max frequency 60Hz, but we run it at 10Hz 351nm (XeF, 10mbar Xe, 160mbar %5 F_2 in He, 75% Ne/He buffer).	Online manual: http://cer.ucsd.edu/LMI/MANUALS/LPX240i.pdf The one in the lab is better, though.
Vacuum pump	Leybold-Trivac D65B	Pumping rate: 65 m^3/h <2 x 20^{-3} mbar	Stats: https://leyboldproducts.oerlikon.com/products/produktkatalog_03.aspx?cid=10_20_10_60 We have a copy of the manual in the lab.
Near IR detector InGaAs	PDA10CS from Thorlabs	700-1800nm (14,000-5550cm^{-1}) Peak response: 1500nm Output voltage: 50Ω	Manual and spec sheet: http://www.thorlabs.com/Thorcat/13000/PDA10CS-SpecSheet.pdf http://www.thorlabs.com/Thorcat/13000/PDA10CS-EC-Manual.pdf
Mid IR detector	Infrared Associates Inc. IS-0.50	1-5.5 microns (10,000-1818 cm^{-1})	spec sheet: http://irassociates.com/index.php?page=ln2-cooled Manual should be in lab.
Gage board	CS1450	Two channels	http://www.egmont.com.pl/gage/instruk

		25 MHz of 50 MHz	cje/CS1450.pdf
DDGs	Stanford Research Systems DG535		http://www.thinksrs.com/downloads/PDFs/Manuals/DG535m.pdf
Mass flow meter	Omega 1700 series		http://www.omega.com/manuals/manualpdf/M1680.pdf
Mass flow meter	Edwards		Hard to find stuff on, because Edwards no longer makes flow meters
Baratron (connected to flow cell)	MKS 626A13TDD	0.1-1000 torr Baratron (check)	Information on model 626B, which replaced 626A http://www.mksinst.com/docs/UR/622B_623B-626B-DS.pdf
Board the turns the motor for the grating on the dye laser	National Instruments CB-50LP		http://www.ni.com/pdf/products/us/4daqsc381-384.pdf

Mirror	Center Wavelength	R_{max}	Range (cm^{-1})**	Diameter (in.)	Radius of Curvature (m)
LGR 1400nm	7315cm^{-1}	99.99%	6950-7300	1	1? (from CRD optics website)
LGR 1320nm	7575cm^{-1}	99.987%	7250-7800	1	1?
LGR 1200nm	8357cm^{-1}	99.993%	7800-8500	0.8	6? I think it's different than the ROC of the other NIR mirrors
LGR 2800nm	3570 cm^{-1}	99.978%	3100-3800	0.8	6
CRD optics 2900 nm	3420 cm^{-1}	99.974%	3200-3700	1	1

**As of now, these numbers might be biased by the dye. Most of these are the usual range that we take the mirror reflectivity curve.

Dye	Oscillator concentration (mg/L)	Amplifier concentration (mg/L)	Center wavelength	Power @ center wavelength (W)	range
DCM (NIR, transverse)	270	90	640nm counter = 25,600	0.45 (q-sw 240μs) 0.1-0.2 (q-sw 180-190 μs)	620-655nm 7000-7800 cm^{-1}
DCM (MIR, longitudinal)	270	27	640nm Counter= 25600	0.03 (q-sw 180 μs) w/out OPA	“
Rh640	203	108	613nm Counter = 24500	0.53 (q-sw 240μs) 0.1-0.15 (q-sw 180 μs)	601-630nm
Rh640+Rh610	640: 23 610:39	640: 12 610:19	598.5 Counter = 23947.8	0.13 (q-sw 180 μs)	590-612 nm

Appendix B – Detailed Drawings of Optics and Lasers.

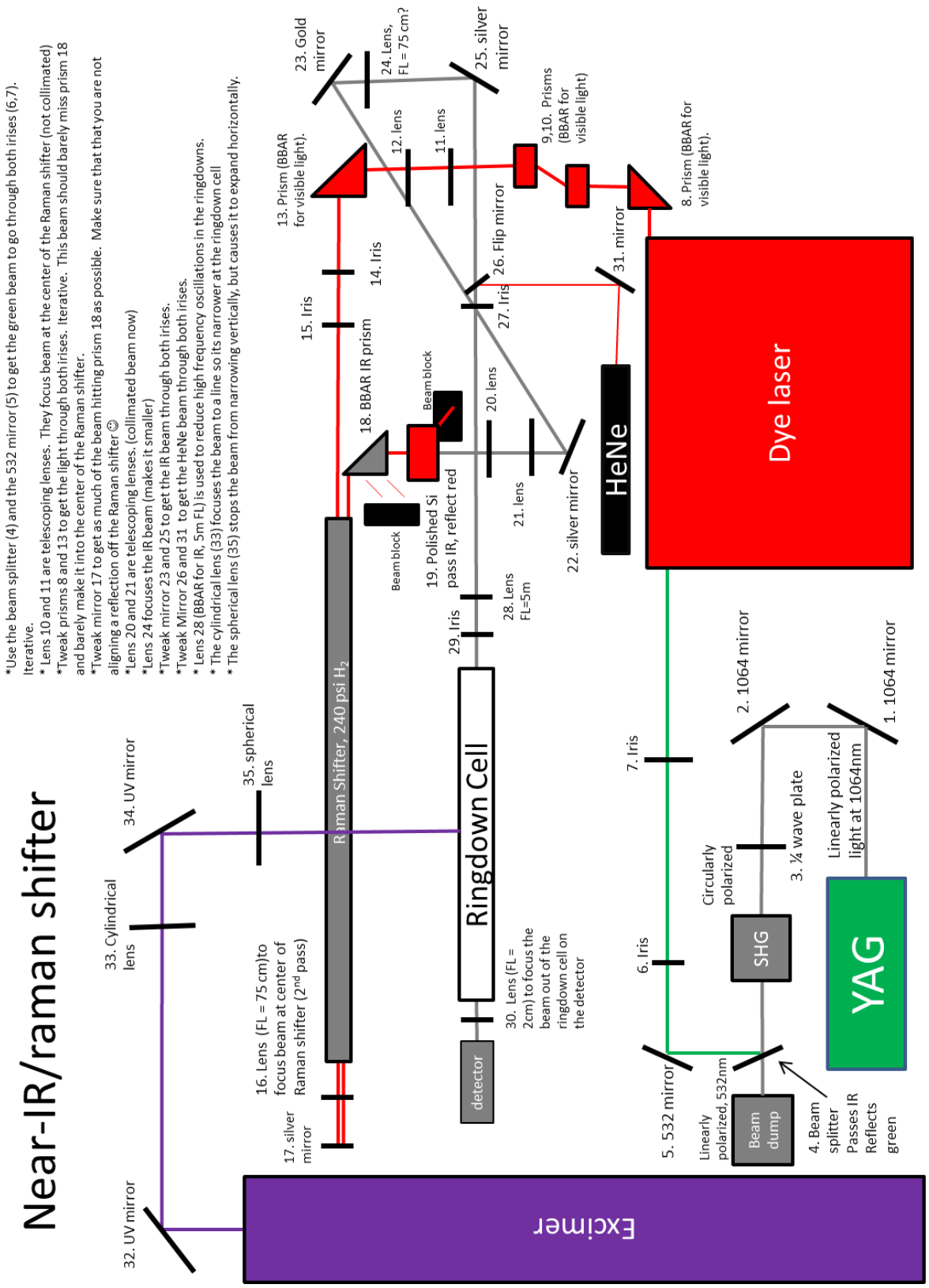

Mid-IR/OPA

*Use the beam splitter (4) and the 532 mirror (5) to get the green beam to go through both irises (6,7). Iterative.
* The ½ wave plate (11) is needed because the red and green beam need to be polarized perpendicular to each other (linearly polarized)
Lens 12 and 14 and lenses 18 and 19 are telescoping lenses to focus the beam more when it goes through the OPA crystals.
* Align the green beam with mirror 9 and 10 to get it go through both irises (13,16). Make sure that it's going through the center of the crystals (if it's not, then align it so it's going through the center of both crystals and move the irises).
* Align the red beam after the green beam. Align it first through iris 16 with the exit prism. Then align it so that the red dot on beam dump 1 overlaps with the green dot on beam dump 1 with beam splitter 15.
* We have on gold mirror (23) which is ideal for IR. Most mirrors are silver, because silver is cheaper.
*Tweak mirror 23 and 25 to get the IR beam through both irises.
*Tweak Mirror 26 and 31 to get the HeNe beam through both irises.
* The cylindrical lens (33) focuses the beam to a line so its narrower at the ringdown cell
* The spherical lens (35) stops the beam from narrowing vertically, but causes it to expand horizontally.

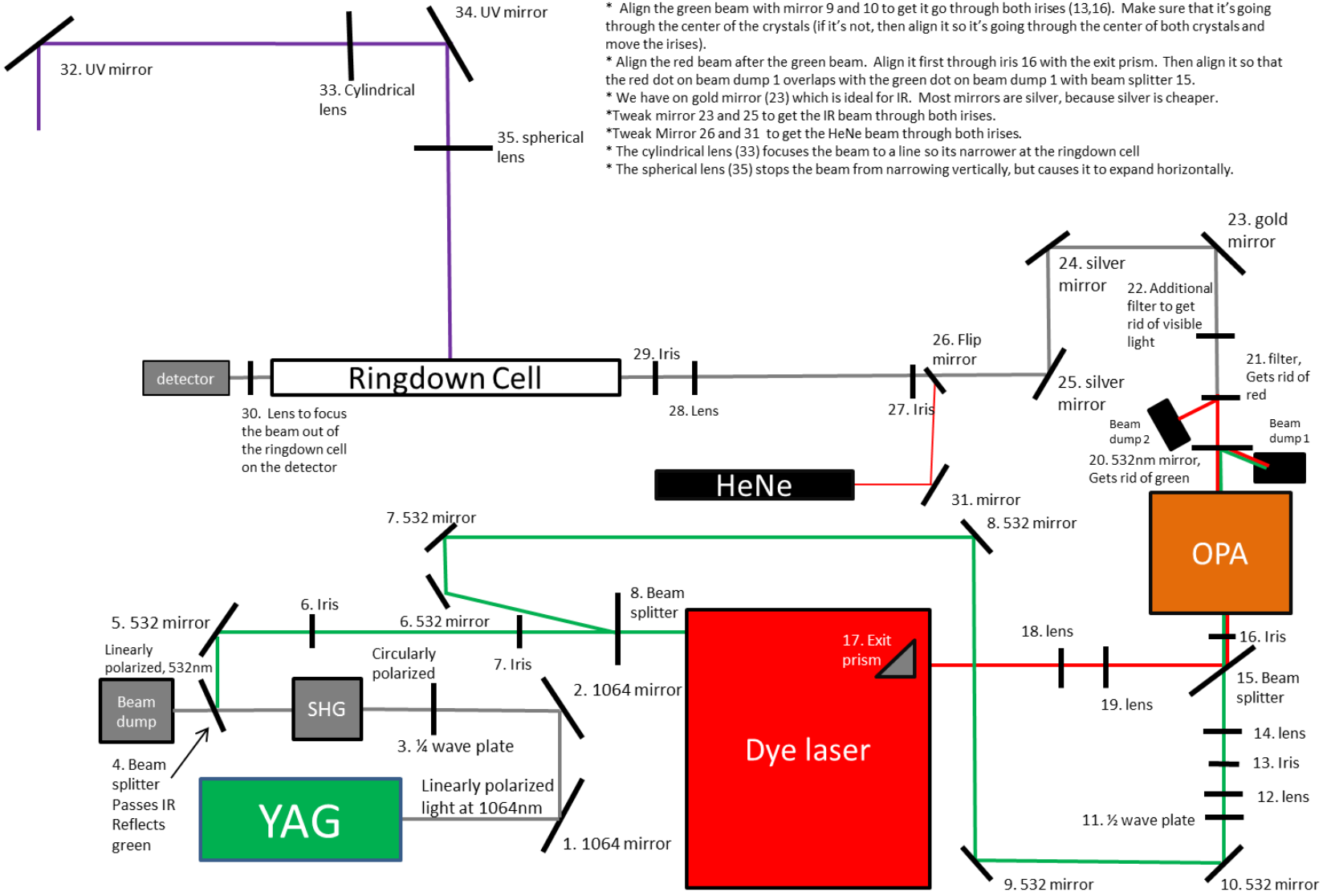

Chapter 3: Absolute and Relative Kinetics of *n*-Butoxy Isomerization using Cavity Ring-down Detection of the Direct Isomerization Products with the First A←X Electronic Spectrum of δ-Hydroxy-Butyl-Peroxy

Abstract

Alkoxy radicals are important atmospheric intermediates in high-NO_x environments, and the branching ratios for alkoxy chemistry determine the fate of hydrocarbon oxidation in the polluted troposphere. We use pulsed cavity ring-down spectroscopy (CRDS) to study the kinetics of *n*-butoxy 1,5-H shift isomerization. We have characterized the isomerization products with the first A←X electronic spectrum of δ-hydroxy-butyl-peroxy (δ-$HOC_4H_8OO\bullet$), produced from the isomerization of *n*-butoxy, and used this spectrum to find direct and relative kinetics of *n*-butoxy isomerization and direct kinetics for *n*-butoxy-d_9 isomerization. Direct kinetics were found using the simultaneous kinetics and ring-down method (SKaR) in which the reaction rate is found by tracking the change in ring-down decay constant, τ, as a function of time. At 630 ± 5 torr and 294 ± 1 K, we found k_{isom} to be (1.7 ± 0.2) × 10^5 s^{-1} for *n*-butoxy; at 590 ± 5 torr and 294 ± 1 K, we found k_{isom} to be (6.2 ± 0.3) × 10^4 s^{-1} for *n*-butoxy-d_9. To our knowledge, this is the first direct rate constant determination for an alkoxy isomerization. We also found the rate of isomerization relative to the rate of reaction with O_2, $k_{isom}/k_{O2,}$ for *n*-butoxy at 595 ± 5 torr and 294 ± 1 K: (2.02 ± 0.14) × 10^{19} molecules cm^{-3}. Given our direct rate constant for isomerization, k_{O2} is (8.6 ± 1.1) × 10^{-15} cm^3 $molecules^{-1}$ s^{-1}. This value agrees with previous literature values for similar alkoxy radicals.

Introduction

Tropospheric oxidation of volatile organic compounds, from both biogenic and anthropogenic sources, affects atmospheric chemistry on a local and global scale.[1] For alkanes, unfunctionalized, unsaturated volatile organic compounds, OH starts the oxidation process by abstracting a hydrogen to produce an alkyl radical, which quickly reacts with O_2 to form a peroxy radical (reactions R1 and R2). In highly polluted high-NO_x environments, such as Los Angeles, this alkyl peroxy will react with NO to form an alkoxy radical. Since NO_2 will photolyze to produce O_3, reaction R3 causes elevated concentrations of O_3, a key constituent of air pollution that causes to respiratory disease in humans.[1-4]

$$R + OH \rightarrow \bullet R \qquad (R1)$$

$$\bullet R + O_2 \rightarrow RO_2\bullet \qquad (R2)$$

$$RO_2\bullet + NO \rightarrow RO\bullet + NO_2 \qquad (R3)$$

Alkoxy radicals can undergo one of three different reactions: decomposition, reaction with O_2, or isomerization (Figure 1). The branching ratios between these reactions – which change based on the structure of the alkoxy radical – determine the end products of hydrocarbon oxidation in polluted areas of the troposphere.[2-4] Unlike decomposition, reaction with O_2 and isomerization maintain the original carbon-chain, potentially leading to lower volatility products that could condense into the aerosol phase. Several of the products, such as HO_2 and peroxy (RO_2) radicals, further increase ozone concentration by reaction with NO (reaction R3) to produce NO_2.

While obtaining accurate kinetics and branching ratios for alkoxy reactions is needed to understand and model ozone chemistry and secondary aerosol formation in polluted environments, this system has proven challenging to study because the alkoxy and many of its products are transient radical species, making them difficult to isolate and detect in the

laboratory. Isomerization and decomposition compete with reaction with O_2, which, under atmospheric conditions, occurs within 20 μs, and the speed of this chemistry causes further challenges and complicates measurement of direct kinetics.

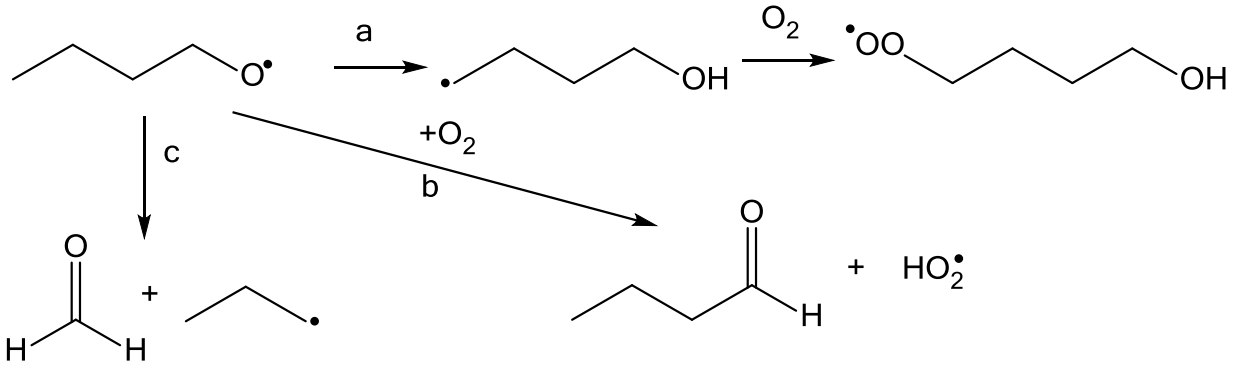

Figure 1. Possible reactions of n-butoxy (a) isomerization, followed by reaction with O_2 to form δ-hydroxy-butyl-peroxy (b) reaction with O_2 and (c) decomposition.

Previous work on the isomerization of simple alkoxy radicals has dealt with these complications by measuring the products of reaction with O_2 or the stable end products of the isomerization channel, which are formed after a second isomerization.[5-13] Most previous experimental work on the isomerization of simple alkoxy molecules have only produced indirect kinetics, *i.e.*, the ratio between the rate of isomerization and rate of reaction with O_2 (k_{isom}/k_{O2}).[6-12,14]

Isomerization of simple alkoxy radicals have been studied extensively with quantum and RRKM calculations. Somnitz and Zellner modeled the decomposition and isomerization of a variety of different alkoxy radicals and found theoretical isomerization rates for n-butoxy, 1.3×10^5 s^{-1} at atmospheric pressure.[15,16] Mereau *et al*. performed similar calculations that yielded an isomerization rate of 1.93×10^5 s^{-1}.[17] These studies both found barrier heights of 7 to 10 kcal/mol for n-butoxy isomerization.[16-18] Although these earlier theoretical studied ignored tunneling, later theoretical work on n-buroxy isomerization has centered on estimated rate

constants given hydrogen tunneling.[17,19-23] The tunneling coefficient is the factor by which tunneling enhances isomerization. Literature estimates of the tunneling coefficient of n-butoxy range from 2.7-120, although most values are closer to 2.7-15.[17,19-23] The most recent estimate by Xu *et al*. predicts a tunneling coefficient assuming small curvature tunneling of 11 and a tunneling coefficient of 3.3 assuming zero curvature tunneling.[23] While much theoretical work has dealt with hydrogen tunneling, there is currently no experimental evidence on the effect of hydrogen tunneling or kinetic isotope effects on alkoxy isomerization.

The only absolute experimental kinetics measurements of n-butoxy chemistry were made by Hein *et al*., who monitored OH and NO_2 concentrations with UV absorption spectroscopy and laser induced fluorescence, respectively, in the presence of *n*-butoxy radicals. They then fit the time profiles of OH and NO_2 to calculate the rates of n-butoxy isomerization and reaction with O_2. The isomerization rate constant was found at a pressure of 37.5 torr, significantly lower than atmospheric pressure and the high pressure limit.[24] Hein *et al.* also give the only available experimental value of k_{O2} of *n*-butoxy, $(1.4\pm0.7) \times 10^{-14}$ cm^3 $molecules^{-1}$ s^{-1}, which is needed to calculate an absolute isomerization rate from $k_{isom}/k_{O2.}$

Rate constants of reaction of alkoxy with O_2 are often found by measuring the alkoxy radical concentration with laser induced-fluorescence (LIF) spectroscopy and tracking its decay in the presence of oxygen and are all within a factor of two of 1×10^{-14} cm^3 $molecules^{-1}$ s^{-1}.[24-35] Most studies find little pressure dependence for k_{O2}.[25,26,28-32,35] Few values are available for rates of reaction with O_2 for alkoxy radicals that can isomerize, because the decay of the alkoxy radical will be complicated by the addition of a second reaction pathway, isomerization, whose rate constant is poorly known. In order to find rates of both isomerization and reaction with O_2,

there needs to be ways of detecting not only the alkoxy reactants, but the products of these channels in real time.

While previous work from our lab detected the isomerization products, δ-C_4H_8● and δ-C_4H_8OO●, using the ν_1 OH stretch,[14] the products of *n*-butoxy also contain a peroxy group which can be characterized by its A←X electronic transition. The A←X transition of peroxy radicals provides a selective measurement of peroxy radicals.[36] Unlike the ν_1 OH stretch region, where a number of secondary products can interfere with the spectra, few secondary species absorb in the A←X region. Because the A←X is a forbidden transition, a highly sensitive technique, like cavity ring-down spectroscopy CRDS, is required to measure it. Cavity ring-down spectroscopy uses a high-finesse optical cavity to increase sensitivity, allowing for detection of trace species.[37-40] When combined with pulsed-laser-photolysis, CRDS allows the detection of transient radical species 1 μs or sooner after photolysis, ideal for deriving direct rate constants for quick radical reactions, like those of alkoxy radicals[14,41]

Here, we present the first spectra of the A←X origin of δ-C_4H_8OO●, produced from the isomerization of *n*-butoxy, with pulsed Near-IR CRDS (7100 – 770 cm^{-1}). We report, to our knowledge, the first direct measurement of the kinetics of *n*-butoxy and *n*-butoxy-d_9 isomerization by monitoring the A←X electronic origin of δ-C_4H_8OO● or δ-C_4D_8OO● and using the Simultaneous Kinetics and Ring-down (SKaR) method first described by Brown *et al*. to a time resolution of <1 μs.[42] Deuterating the sample should greatly reduce hydrogen tunneling as well as introducing a traditional kinetic isotope effect, so deuterating the sample gives qualitative experimental evidence for how much tunneling affects isomerization. We have found new relative rate constants between reaction with O_2 and isomerization using the A←X transition, which combined with our values of k_{isom} yield a rate constant for reaction of *n*-butoxy

with O_2. We've included a re-analysis of previous relative kinetics data for *n*-butoxy and 2-pentoxy published by Sprague *et al.*(2012).[14]

Experimental

Our pulsed-laser photolysis cavity ring-down spectrometer and flow cell has been described previously,[14,41] and the set-up is shown in Figure **2**. Precursor gases traveled 6 cm through a laminar flow cell situated in the middle of an optical cavity with an optical pathlength of 50 cm. The flushtime of the cell was about 70 ms. Chemistry was initiated by an excimer laser (Lambda Physik LPX 210i, 10 Hz, 0.5 W/cm^2) at 351 nm (XeF) focused to a 4 × 0.3 cm beam at the fused silica window of the cell. A beam of tunable Near-IR beam (1.1 – 1.4 μm) was sent perpendicular to the photolysis beam to probe the reaction. As described by Sprague *et al.* (2013), this near-IR light was produced from the stimulated Raman scattering of the output of a 10Hz Nd:YAG (Continuum Surelite III) pumped dye laser (Spectra Physics PDL-3). To produce about 100 μJ of near-IR light, the output of the dye laser was sent through double-pass cell of high pressure H_2 gas. The resulting light was sent through the 53 cm optical cavity formed from two highly reflective mirrors (R=99.99%, Los Gatos Research, peak reflectivity at 1.35 μm). The exponential decay of light exciting the cavity (the "ring-down") was focused on an InGaAs photodiode (ThorLabs PDA10CS) with an internal amplifier, which was connected to a GageScope CS1450 digital oscilloscope. Each ring-down trace was collected for 100 μs at a rate of 25 MHz. Each ring-down trace was averaged for 16 shots or 1.6 s.

For spectra and relative kinetics, the ring-down traces were fit to a simple exponential model using the Levenberg-Marquardt algorithm. To remove scattered light, the first 1/8 of the initial lifetime was cut out and the ring-down trace was fit to a simple exponential. Analysis of the ring-down traces for the direct kinetics will be discussed in the following section. A typical

vacuum ring-down lifetime was 14 μs at the center of the mirrors with about 0.1% shot-to-shot noise. This yields a minimum detectable absorbance of 0.25 ppm per each scan (16 shots averaged at 10 Hz).

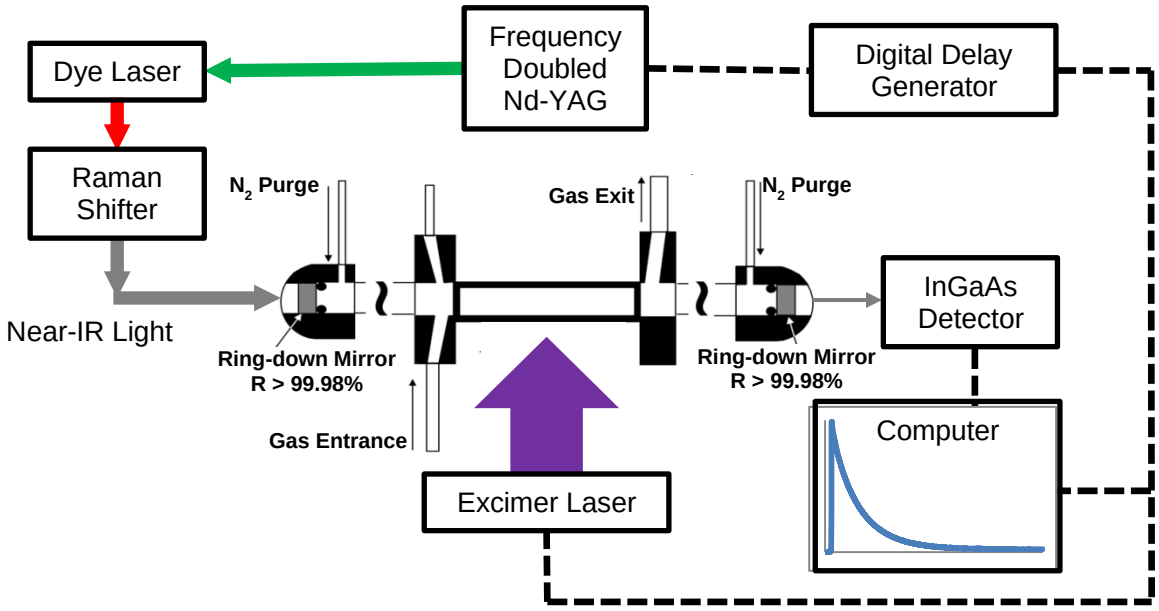

Figure 2. Schematic of cavity ring-down spectrometer and flow cell.

The experimental conditions and chemistry in our flow has been described in detail by Sprague *et al.* (2012).[14] Briefly, *n*-butoxy radicals ($C_4H_9O\bullet$) were formed from the photolysis of *n*-butyl nitrite at 351 nm:

$$C_4H_9ONO + h\nu \rightarrow C_4H_9O\bullet + NO \qquad \text{(R4)}$$

Commercial butyl nitrite was purchased from Sigma Aldrich (Saint Louis, MO) and stored in a freezer at 273 K. Fully deuterated butyl nitrite was synthesized from butanol-d_{10} (Sigma Aldrich) and sodium nitrite as described in *Organic Syntheses*.[43] The product was vacuum distilled to remove extra water and leftover butanol. The deuterated butyl nitrite was stored in an inert atmosphere of N_2 at 195 K to preserve the expensive sample. The identity of the synthesis product was confirmed to be fully deuterated butyl nitrite with deuterium NMR. Samples were freeze-pumped for at least three cycles to remove higher volatility impurities. Nitrogen gas was

bubbled through the nitrite to carry it to the flow cell. The sample was then diluted by N_2 and O_2 gas to a total pressure of about 600 torr. The pressure was kept at 600 torr to prevent pressure instability that occurred above 700 torr. Assuming that the N_2 that was bubbled through the butyl nitrite was fully saturated with the sample, the cell had about 1×10^{16} molecules $cm^{-3}$of butyl nitrite. The power of the excimer at its brightest part was measured to be 0.5 W/cm^2 at the laser's aperture. Assuming butyl nitrite has a cross section of 1×10^{-19} cm^2/molecule at 351 nm[44] and a quantum yield of one, about 1.5% of the butyl nitrite will be photolyzed, leading $[C_4H_9O\bullet]$ = 2×10^{14} molecules cm^{-3}. This number should only be considered as an upper limit to our radical concentration, because it assumes that the entire excimer beam has a uniform energy of 0.5 W/cm^2 and none of the beam is lost between the aperture of the laser and the inside of the flow cell.

Direct Kinetics with SKaR

Direct kinetics were found using the SKaR method first described by Brown *et al.*[42] This method is used to find kinetics of reactions that occur at times on the same order of magnitude as the ring-down time. Under these conditions, the ring-down in not a single exponential decay and kinetics can be derived by tracking the change in the ring-own decay constant, τ, over time.

If it is assumed that the ring-down time, τ, can change as a function of time, t, each ring-down trace can be modeled by:

$$I = I_0 e^{-\frac{t}{\tau(t)}} \qquad \text{(E1)}$$

where I_0 is the initial intensity of light in the cavity and I is the intensity of light in the cavity at time t. For ring-downs where the excimer didn't fire, no reaction is occurring, and τ is a constant (denoted τ_0). If you divide a ring-down where the excimer fires by a reference one in which the excimer didn't fire you get:

$$ratio = \frac{ExON}{ExOFF} = \frac{I_{ON}}{I_{OFF}} \exp\left[-\left(\frac{1}{\tau(t)} - \frac{1}{\tau_0} \right) t \right] \qquad \text{(E2)}$$

where I_{ON} is the intensity of the IR beam for the excimer on ring-down and I_{OFF} is the intensity of the IR beam for the excimer off trace.

In cavity ring-down, the absorbance of a sample is given by:

$$A = \frac{L_{opt}}{c}\left(\frac{1}{\tau} - \frac{1}{\tau_0} \right) \qquad \text{(E3)}$$

By simplifying equation E2 with a Taylor expansion and substituting equation E3, equation E2 becomes:

$$ratio \cong \frac{I_{ON}}{I_{OFF}}\left(1 - \frac{A(t)c}{L_{opt}} t \right) \qquad \text{(E4)}$$

where *A(t)* is the absorbance of the species as a function of time, and can be modeled with the kinetics of reaction of interest. For alkoxy isomerization, the concentration of the product, *[P]*, which is proportional to *A(t)*, is related to the initial concentration of the reactant, $[R_0]$ by:

$$[P] = [R_0]\left(1 - e^{-k_{rxn}t} \right) \qquad \text{(E5)}$$

where k_{rxn} is the first order rate constant. Substituting equation E5 into equation E4 and combing variables so that $c = I_{on}/I_{OFF}$ and $a' = I_{ON}cA_{final}/(I_{OFF}L_{opt})$ yields:

$$ratio = c - a't(1 - e^{-k_{rxn}t}) \qquad \text{(E5)}$$

In order to combine all the data from one trace, each trace was scaled so that its intercept, c, was equal to 1, to remove differences between the IR intensity of each shot and to allow averaging of multiple shots. This gives the final equation:

$$ratio = 1 - at(1 - e^{-k_{rxn}t}) \qquad \text{(E6)}$$

where $a = cA_{final}/L_{opt.}$ If the chemistry includes a first order formation reaction followed by a first order (or pseudo first order) loss reaction equation,

$$[P] = \frac{[R_0]k_{rxn}}{k_{loss} - k_{krxn}}\left(e^{-k_{rxn}t} - e^{-k_{loss}t}\right) \qquad \text{(E7)}$$

where k_{loss} is the rate constants for the first order loss of the product, equation E4 becomes:

$$ratio = 1 + at\left(e^{-k_{loss}t} - e^{-k_{rxn}t}\right) \qquad \text{(E8)}$$

where now $a = A_{max}k_{rxn}/(L_{opt}(k_{loss}-k_{rxn}))$ and the intercept has been scaled to 1. In both equation E6 and E8, *a* is proportional to absorbance, and the slope at long times can be used to find the final absorbance of the sample after the first order reaction is complete.

Chemistry

At low oxygen concentrations (~1×10^{18} molecules cm^{-3} or less) most *n*-butoxy of will isomerize to form δ-hydroxy-butyl (δ-HOC_4H_8●):

$$C_4H_9O\bullet \rightarrow \delta\text{-}HOC_4H_8\bullet \qquad \text{(R5)}$$

Some "hot" alkoxy radicals with excess energy from photolysis might promptly isomerize. Prompt isomerization is more thoroughly discussed in the supplemental information. If any O_2 is present, δ-HOC_4H_8● will react with O_2 to form δ-HOC_4H_8OO●:

$$\delta\text{-}HOC_4H_8\bullet + O_2 \rightarrow \delta\text{-}HOC_4H_8OO\bullet \qquad \text{(R6)}$$

Assuming that O_2 has the same rate constant with δ-HOC_4H_8● as it does the butyl radical (7.5×10^{-12} cm^3 $molecules^{-1}$ s^{-1})[45] and an oxygen concentration of only 1×10^{17} molecules cm^{-3}, the δ-HOC_4H_8● will be converted to δ-HOC_4H_8OO● in about 1 μs.[45] Even for our lowest oxygen concentrations (1.5×10^{17} molecules/cm^3), δ-HOC_4H_8● will react almost instantly with O_2 to form δ-HOC_4H_8OO●. At higher oxygen concentrations, a significant portion of alkoxy radical will react with O_2:

$$C_4H_9O\bullet + O_2 \rightarrow HO_2 + R'CHO \qquad (R7)$$

While most alkoxy radicals can, in theory, decompose,

$$C_4H_9O\bullet \rightarrow HCHO + C_3H_7\bullet \qquad (R8)$$

the approximate rate constant for decomposition is on the order of magnitude to 10^2 s^{-1},[15,46,47] 2-3 orders of magnitude slower than reaction with O_2 and isomerization. Sprague *et al.* (2012) showed that at photolysis at 351 nm, decomposition was negligible for *n*-butoxy, because no HCHO was observed in the mid-IR region. This set an upper limit for decomposition of 10% based on the noise of our spectrometer.[14]

Secondary chemistry (especially alkoxy self-reaction) has little effect since alkoxy concentration was kept so low (< 2×10^{14} molecules cm^{-3}), and secondary chemistry of the peroxy radical with itself and with HO_2 produced from reaction R7 was negligible. The main loss pathway of δ-$C_4H_8OO\bullet$ in our cell was reaction with NO to form a hydroxy-alkoxy radical (δ-$C_4H_8O\bullet$):

$$HO\ C_4H_8OO\bullet + NO \rightarrow HO\ C_4H_8O\bullet + NO_2 \qquad (R9)$$

The experimental lifetime of δ-$C_4H_8OO\bullet$ was about 450 μs for *n*-butoxy and about 2.5 ms for deuterated n-butoxy due to the higher purity of the deuterated sample. This alkoxy radical will undergo a second isomerization, and then form an aldehyde after reaction with O_2 followed by HO_2 elimination:[48]

$$HOC_4H_8O\bullet \rightarrow \bullet CH(OH)CH_2CH_2CH_2OH \qquad (R10)$$

$$\bullet CH(OH)CH_2CH_2CH_2OH + O_2 \rightarrow HCOCH_2CH_2CH_2OH + HO_2 \qquad (R11)$$

Since the second isomerization does not produce another peroxy radical, reaction with NO only decreases the concentration of isomerization product over time and does not contribute to spectral interferences in the near-IR region.

Results

A←X Electronic Spectrum of δ-C_4H_8OO●

The A←X spectrum δ-C_4H_8OO● was found by photolyzing ≈6×10^{14} molecules/cm^3 of butyl nitrite in the presence of 2.0×10^{17} molecules/cm^3 and taking the spectrum between 7150 – 7700 cm^{-1}. This spectrum had a step size of 1 cm^{-1} and includes 6.4 s of averaging for points from 7150-7400 cm^{-1} and 24 s of averaging for points from 7150-7400 cm^{-1}. To eliminate the possibility of secondary reactions, the spectrum was taken only 10 μs after photolysis. The spectrum features a broad absorbance from about 7200-7700 cm^{-1} with the main peak at 7556 cm^{-1} and a smaller peak at 7355 cm^{-1}. This peak is attributed to stable photolysis products, and not to alkyl peroxys, including HOC_4H_8OO•. Since O_2 was kept very low (2×10^{17} molecules cm^{-3}), we expect isomerization will be about 100 times faster than the next most favorable reaction, reaction with O_2. No rotational lines can be observed, likely due to the presence of multiple molecular conformers. As observed in other alkyl peroxy studies,[36,49,50] a large absorption at 7190 cm^{-1} is observed, attributed to other unknown, stable photolysis products.

Our A←X spectrum of δ-C_4H_8OO● shows spectral features similar to the spectra of other primary peroxy radicals, especially the Glover *et al.*'s spectrum of *n*-butyl peroxy produced from the photolysis of butyl bromide in the presence of oxygen.[50] The A←X origin of *n*-butyl peroxy features a large broad peak at 7591 cm^{-1} and a small broad peak at 7355 cm^{-1}, which Glover *et al.* assign to the A←X origin of different conformers of the *n*-butyl peroxy. These two peaks compare with to the large peak at 7556 cm^{-1} and the small peak at 7355 cm^{-1} that we observed for δ-HOC_4H_8OO●.

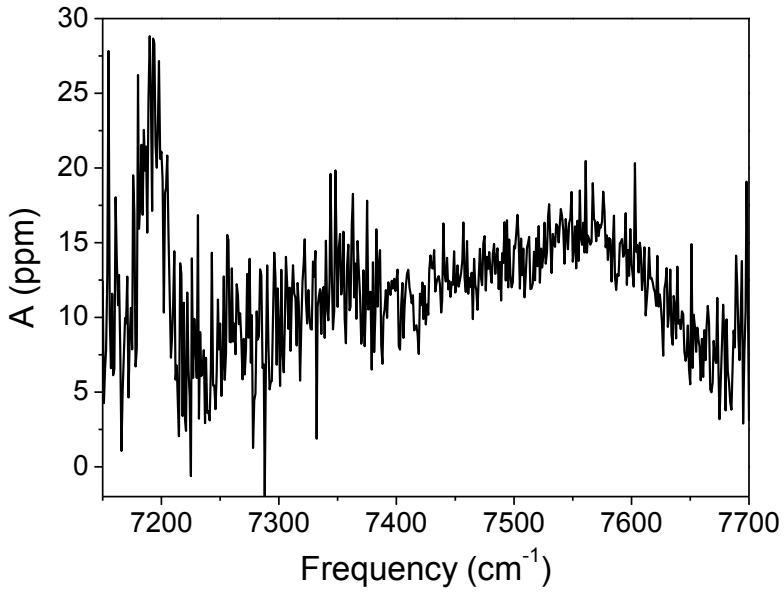

Figure 3. Spectrum of A←X electronic origin of δ-hydroxy-butyl-peroxy (HOROO●) produced from the isomerization of n-butoxy taken at 295 K and 300 torr ($[O_2]$ =2.0×10^{17} molecules/cm^3, RONO≈6×10^{14} molecules/cm^3). The spectrum was taken from 7150-7700 cm^{-1} 10 μs after photolysis with 6.4-24s averaging per point. δ-Hydroxy-butyl-peroxy absorbs from 7200-7700cm^{-1} with a peak at 7556cm^{-1} and a shoulder at 7500cm^{-1}.

While we attempted to find the OO stretch vibronic transition, expected to be near 8500 cm^{-1} based on the vibronic spectra of similar peroxy radicals[36,50], we could not observe this transition due to a large background absorbance, likely from *n*-butyl nitrite, that decreased our signal-to-noise.

Direct Kinetics and n-Butoxy-d_9 isomerization

Figure 4 and Figure 5 show the ratio between the sample and the reference ring-down vs. time after photolysis for *n*-butoxy and *n*-butoxy-d_9 isomerization, respectably. Rate constants were found by taking ring-downs at a large variety of excimer delays (from -50 μs to 200 μs) at 630 ± 5 torr and 293 ± 1 K. The wavelength was held constant at 7575cm^{-1}, near the center of the absorbance of δ-C_4H_8OO●, for all ring-downs. The last 80 μs of each 100 μs ring-down was

fit to a single exponential model ($a+b\times\exp[-t/\tau]$), and the baseline, *a*, was subtracted out. The ratio between the sample and the reference ring-downs is plotted in Figure 4 and Figure 5. Since the noise in this ratio increased dramatically as the sample ring-down (denominator) near zero, only the first 50 μs of each ring-down was considered in the data analysis. Each trace was scaled so that its y-intercept was 1 to account for differences in laser power between the sample and reference ring-downs.

The *n*-butoxy data (Figure 4) was fitted to equation E8, which yielded a value of k_{isom} of $(1.7 \pm 0.2)\times10^{5}$ s^{-1} (2σ). Equation E8 includes both the first order formation of products and a loss reaction, because significant amounts of δ-C_4H_8● were lost due subsequent chemistry, likely reaction with NO (Reaction R9). The fit to equation E8 yielded a value of k_{loss} of δ-C_4H_8OO● of $\sim2.4\times10^{3}$ s^{-1} which agrees well with our measurements of the lifetime of the δ-C_4H_8OO● in our cell, 450 μs. Assuming pseudo-first order kinetics where [NO]>>[δ-C_4H_8OO●] and a rate constant similar to the reaction of other simple peroxy radicals with NO ($\sim9\times10^{-12}$ cm^3 $molecules^{-1}$ s^{-1})[45], our cell had $\sim2.5\times10^{14}$ molecules cm^{-3} of NO, more than our absolute upper value for the *n*-butoxy concentration of 2×10^{14} molecules cm^{-3}. This is likely because there were NO impurities in the butyl nitrite sample. Since 2×10^{14} molecules cm^{-3} is an overestimation of radical concentration, first order loss kinetics are likely valid under our experimental conditions.

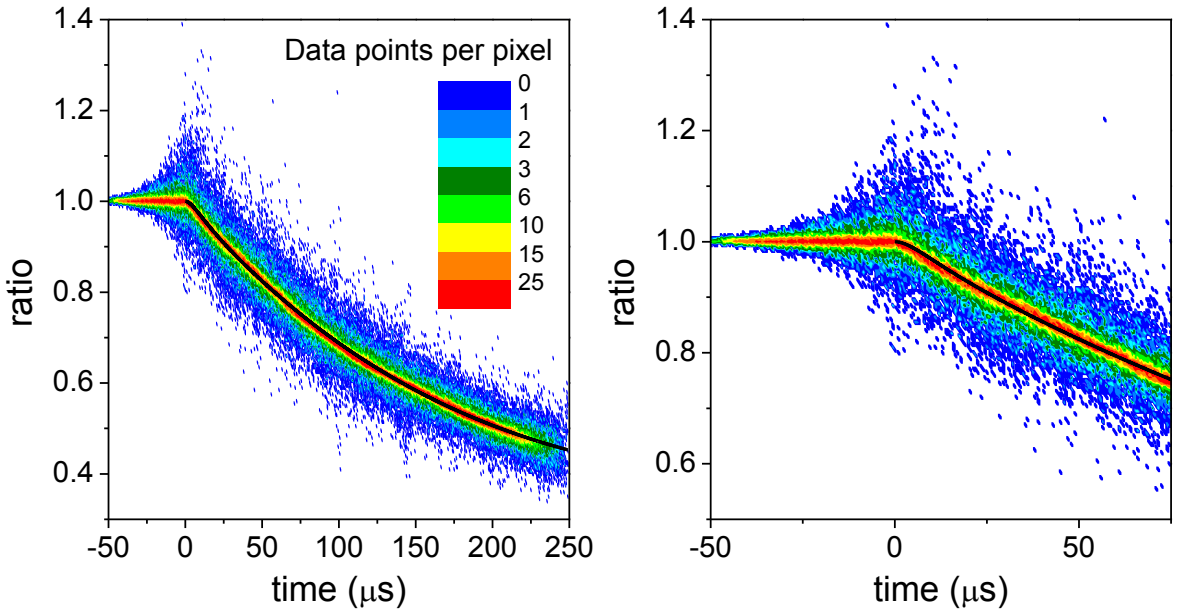

Figure 4. Experimental ratio of ring-downs with excimer photolysis to ring-downs without photolysis vs. time after photolysis for the isomerization of *n*-butoxy to δ-C_4H_8OO● (which is detected at 7575 cm^{-1}) at 590 ± 5 torr, 293 ± 1 K and $[O_2] = 7\times10^{17}$ molecules cm^{-3} (black). Ring-down traces were taken at excimer delay times ranging from -50 μs to 200 μs, and only the first 50 μs of each trace was taken (giving a total of n=105,084 individual points). Each individual ratio trace was scaled so that the intercept at time=0 μs was equal to 1. This experimental data was fit equation E6 (black line) to get a value for k_{isom} of (1.7 ± 0.2) × 10^5 s^{-1}. The decrease in absorbance at longer times is most likely due to reaction of the δ-C_4H_8OO● with NO. Given a rate constant for reaction of NO[45] of ~1 × 10^{11} cm^3 $molecules^{-1}$ s^{-1} and our experimental fit, [NO] ≈ 2 × 10^{14} molecules cm^{-3}.

The *n*-butoxy-d_9 data (Figure 5) was fitted to equation E6, yielding a value of k_{isom} of (6.2 ± 0.3) × 10^4 s^{-1}. Substituting hydrogen for deuterium slows down isomerization by a factor of 2.8 ± 0.3. The absorbance of the n-butoxy-d_9 was constant up to 100 μs, as indicated by the constant slope in Figure 5, because very little hydroxy-butyl-peroxy was lost due to subsequent chemistry in 100 μs. While the deuterated butyl nitrite precursor was stored under an inert

atmosphere of N_2 at 195 K to preserve the expensive sample, the nondeuterated butyl nitrite was stored in air at 273K, likely leading to large amounts of decomposition to form NO in the nondeuterated sample only. This excess NO, likely lead to much higher NO concentrations in the nondeuterated sample compared to the deuterated sample, and therefore the lifetime of the hydroxy-butyl peroxy was much lower in the nondeuterated data, only 2.5 ms. If this is all due to reaction with NO, there was an NO concentration of 2.5×10^{13} molecules/cm^3, an order of magnitude lower than that of the nondeuterated sample. This further justifies ignoring reaction with NO for the direct deuterated alkoxy isomerization kinetics.

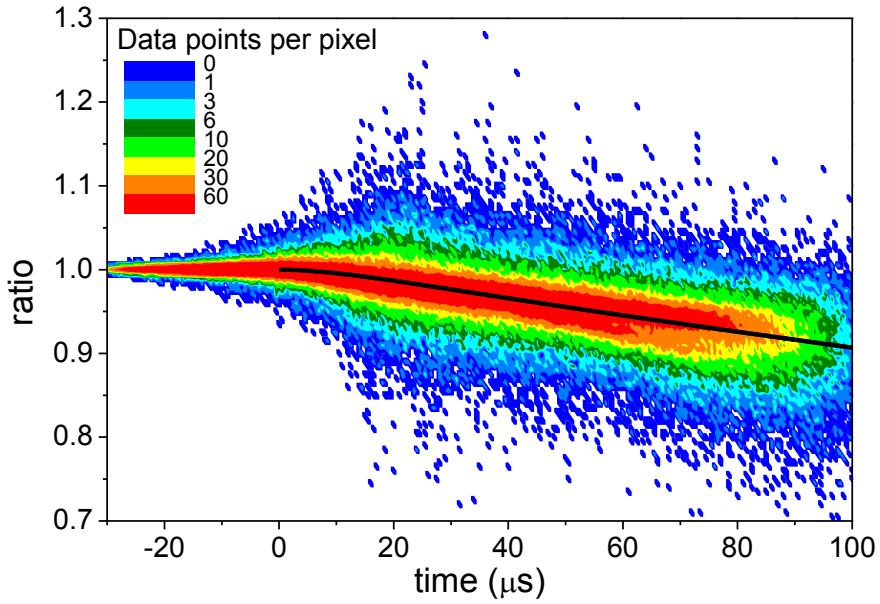

Figure 5. Experimental ratio of ring-downs taken at 7575 cm^{-1} with the excimer on to ring-downs with the excimer off for the isomerization of *n*-butoxy-d_9 at at 630 ± 5 torr, 293 ± 1 K and $[O_2] = 1 \times 10^{17}$ molecules cm^{-3}. The excimer was fired at time=0 μs. Ring-downs were taken at excimer delay times ranging from -30 μs to 51 μs, and only the first 50 μs of each trace was taken (giving a total of n=261,459 individual points). Each individual ratio trace was scaled so that the intercept at time=0 μs was equal to 1. This experimental data was fit equation E8 (black line) to get a value for k_{isom} of $(6.2 \pm 0.3) \times 10^4$ s^{-1}.

Relative Kinetics using Cavity Ring-down Detection of the A←X Origin

Relative kinetics at 595 ± 5 torr and 293 ± 1 K were found by observing the change in absorbance of the isomerization product δ-C_4H_8OO● with oxygen concentration (Figure **6**). Assuming that all *n*-butoxy radicals will either isomerize or react with O_2, we can find the relative kinetics with the following equation:

$$\left(\frac{A_0}{A}\right) = \frac{k_{O_2}}{k_{isom}}[O_2] + 1 \qquad \text{(E9)}$$

where A is the absorbance of the sample at a given $[O_2]$ and A_0 is the absorbance of the sample at very low $[O_2]$ so that 100% of the sample isomerizes. A was found by integrating the A←X spectrum of δ-C_4H_8OO● (taken at a 10 μs excimer delay) produced from the isomerization of *n*-butoxy from 7400-7700 cm^{-1}. By taking a linear regression of this data (Figure **6**), we found that k_{isom}/k_{O2} = (2.02±0.14) × 10^{19} molecules cm^{-3}. Points that were taken with O_2 concentration below 1×10^{17} molecules cm^{-3} were excluded from this fit, because at very low oxygen concentrations, the rate of reaction R6 is slow enough that not all δ-C_4H_8● will be converted to δ-C_4H_8OO● by 10 μs. Given our value of k_{isom}/k_{O2} and k_{isom}, k_{O2} for *n*-butoxy should be (8.6±1.1) × 10^{-15} cm^3 $molecules^{-1}$.

For our relative kinetics, we assumed that all the alkoxy radical in our cell either reacted with O_2 or thermally isomerized. The supplemental information discusses of why we feel justified ignoring side chemistry. We especially consider prompt isomerization, where *n*-butoxy radicals with excess energy after photolysis isomerize virtually instantly after isomerization. This would lead to unwanted nonlinearities in our data and invalidate our use of equation E9, but as shown in the supplemental information, we detected no nonlinearities in our data, suggesting negligible prompt isomerization.

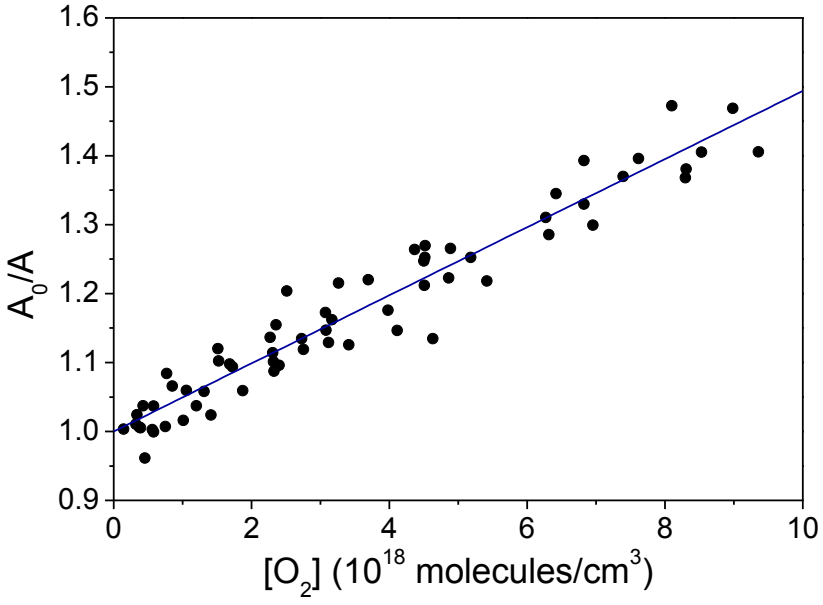

Figure 6. Plot of A_o/A (A is absorbance, and A_0 is absorbance at $[O_2]=0$) vs. oxygen concentration used to find relative kinetics of *n*-butoxy isomerization using cavity ring-down detection of the A←X origin of δ-C_4H_8OO● at 595 ± 5 torr and 293 ± 1 K. Each point was found by integrating the absorbance of δ-C_4H_8OO● from 7450-7765 cm^{-1}. The blue line is the best linear fit to all points over 1×10^{17} molecules/cm^3, and has a slope of $(4.94 \pm 0.17) \times 10^{-20}$ cm^3 $molecules^{-1}$ and intercept of 0.998 ± 0.007. This yields a value of k_{isom}/k_{O2} of $(2.02 \pm 0.14) \times 10^{19}$ molecules cm^{-3} according to equation E9.

Relative Kinetics using Cavity Ring-down Detection of the v_1 OH stretch

Figure 7 show previously reported, but re-analyzed, data previously published by Sprague *et al.* on the relative kinetics, k_{isom}/k_{O2}, of *n*-butoxy and 2-pentoxy.[14] Previous data miscalculated the O_2 concentration by about 10%, and the data presented here corrects these errors. Using equation E9, k_{isom}/k_{O2} is $(2.09 \pm 0.16) \times 10^{19}$ molecules cm^{-3} and $(4.2 \pm 0.6) \times 10^{19}$ molecules cm^{-3} for n-butoxy and 2-pentoxy, respectively. These values are significantly higher than those previous reported: $(1.7 \pm 0.1) \times 10^{19}$ molecules cm^{-3} and $(3.4 \pm 0.4) \times 10^{19}$ molecules

cm^{-3} for *n*-butoxy and 2-pentoxy, respectively. While much of this discrepancy is due to the difference in O_2 concentration, it also arises because the previous analysis included corrections prompt isomerization and other secondary reactions while we do not. See supplemental information for our complete explanation for why we chose to ignore this side reaction. Briefly, we felt that alkoxy decomposition and reaction with NO were negligible, given that their rate constants are believed to be at least two orders of magnitude less than isomerization. We ignored prompt isomerization because we detected no nonlinearities in the data.

Using the OH stretch relative kinetics and our previous value of k_{isom}, for *n*-butoxy, k_{O2} is calculated to be $(8.6 \pm 1.1) \times 10^{-15}$ cm^3 $molecules^{-1}$. If 2-pentoxy reacts with O_2 at the same rate as *n*-butoxy, its isomerization rate is calculated to be $\approx 3.6 \times 10^5$ s^{-1}.

Analysis of the Effect of Unwanted chemistry on Relative Kinetics

We investigated three different side reactions that might affect our relative n-butoxy and 2-pentoxy relative kinetics: reaction with NO, decomposition, and prompt isomerization. Each of these reactions could, in theory, change the final concentration of δ-hydroxy-butyl-peroxy that we measured to characterize the relative kinetics. While prompt decomposition might occur, it cannot affect the relative kinetics because it would only lead to a slightly lower amount of alkoxy radicals being produced after photolysis.

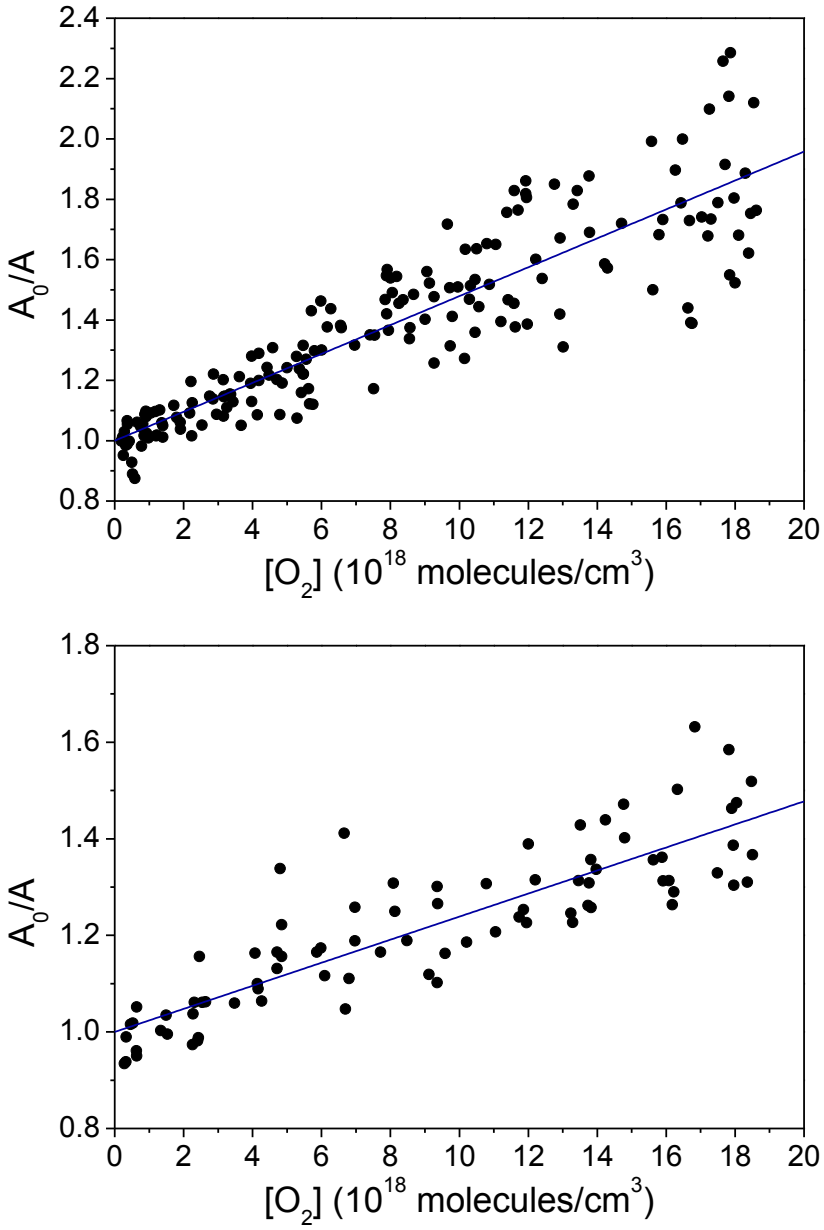

Figure 7. Plot of A_o/A (A is absorbance, and A_0 is absorbance at $[O_2]=0$) vs. oxygen concentration used to reanalyze the relative kinetics of *n*-butoxy (top panel) and 2-pentoxy (bottom panel) isomerization using cavity ring-down detection of the v_1 OH stretch of OHROO●. Data are those reported by Sprague *et al*. but with recalculated oxygen concentrations. A linear fit to the data (blue line) yielding values of k_{isom}/k_{O2} of $(2.09 \pm 0.16) \times 10^{19}$ molecules/cm^3 (n-butoxy) and $(4.19 \pm 0.53) \times 10^{19}$ molecules/cm^3 (2-pentoxy) according to equation E9.

Reaction with NO and Decomposition

We claim, given the concentration of NO in our cell and literature estimates of k_{NO} and k_{decomp}, that only negligible amount of alkoxy will reaction via one of these pathways. Based on the experimental lifetime of the δ-hydroxy-butyl-peroxy radical, the amount of NO in the cell is about 2.5×10^{14} molecules/cm^3. Given the literature values for the reaction of peroxy radicals with NO ($\approx 1 \times 10^{-11}$ cm^3 molecules^{-1} s^{-1})[45] , the pseudo-first order rate constant for reaction with NO, k_{NO}[NO], should be $\approx 2 \times 10^3$ s^{-1}, two orders of magnitude lower than the isomerization rate constant, $(1.7 \pm 0.2) \times 10^5$ s^{-1}. As stated in the chemistry section: the approximate rate constant for decomposition is on the order of magnitude to 10^2 s^{-1},[15,46,47] 2-3 orders of magnitude slower than reaction with O_2 and isomerization. Sprague *et al.* (2012) showed that at photolysis at 351 nm, decomposition was negligible for n-butoxy, because none of the decomposition was observed in the mid-IR region. This set an upper limit for decomposition of 10% based on the noise of our spectrometer,[14] even though all theoretical estimates predict decomposition to be much less favorable than 10%. Thus, only ≈1% of the alkoxy radicals is expected to undergo decomposition or reaction with NO, and these side reactions can be ignored.

Prompt Isomerization

Previous work by our group investigated how the kinetics might deviate from equation E9 due to reaction with NO (reaction R9), decomposition (reaction R8), prompt decomposition and isomerization.[14] Prompt isomerization is particularly troubling because it would lead to a higher concentration of the isomerization products, which we detect, than would be expected given fully thermalized products. This effect would have very little influence on low oxygen concentrations where most of the *n*-butoxy will isomerize without or without prompt isomerization, but would become more pronounced at higher O_2, possibly leading to negative

curvature in Figures 5 and 6. The presence of prompt chemistry can therefore be tested if the calculated value of k_{isom}/k_{O2} decreases as points taken at higher $[O_2]$ are excluded.

For the relative kinetics using the A←X transition, all values of k_{isom}/k_{O2} are within error of the value of (2.02 ± 0.14) × 10^{19} molecules/cm^3 found using the full range no matter what fitting window was used for the linear regression. The value of k_{isom}/k_{O2} using points taken at less than 5 × 10^{18} molecules/cm^3 of oxygen was (1.9 ± 0.2) × 10^{19} molecules/cm^3, which is indistinguishable within error of the value of k_{isom}/k_{O2} found using points taken at more than 5 × 10^{18} molecules/cm^3, (2.0 ± 0.7) × 10^{19} molecules/cm^3. Additionally, equation E9 was changed so that a fraction of the n-butoxy radical promptly isomerized (ϕ_{PI}):

$$\frac{A_0}{A} = \left(\phi_{PI} + (1+\phi_{PI}) \left(\frac{k_{isom}}{k_{isom} + [O_2] k_{O_2}} \right) \right)^{-1} \qquad \text{(E10)}$$

An estimate for ϕ_{PI} was found by assuming k_{isom}=1.7 × 10^5 s^{-1} and k_{isom}/k_{O2} = 2 × 10^{19} molecules/cm^3 and fitting the data to equation E10 using a Levenberg-Marquardt algorithm. For the *n*-butoxy A←X kinetics, ϕ_{PI} was found to be (0.4 ± 3)%. The data was then fitted again to equation E10, this time not assuming any value for k_{isom}/k_{O2}. This analysis again yielded a value of ϕ_{PI} indistinguishable from zero, (8 ± 36)%. Unfortunately, these fit had high errors on ϕ_{PI}, indicating that likely equation E10 is not a good for to the data or there is too much experimental scatter to get a reasonable estimates of ϕ_{PI}. Since, no significant nonlinearities were found in the data and all fitted values of ϕ_{PI} were indistinguishable from zero, we choose to ignore prompt isomerization.

The relative kinetics calculated using the absorbance of the OH stretch was analyzed and fit to equation E10, and again yielded values of ϕ_{PI} within error of zero. When the data was fit to equation E10, assuming previously calculated values of k_{isom} and k_{isom}/k_{O2}, ϕ_{PI} was found to be

(0.2 ± 3)% and (-0.2 ± 5)% for *n*-butoxy and 2-pentoxy, respectively. For 2-pentoxy, k_{O2} was assumed to be the same as that of *n*-butoxy (8.6×10^{15} cm^{-3} molecules^{-1} s^{-1}), and k_{isom} was calculated given k_{O2} and k_{isom}/k_{O2}. When the data was refitted to equation E10 only assuming previously calculated values of k_{isom}, ϕ_{PI} was found to be (10 ± 38)% and (27 ± 168)% for *n*-butoxy and 2-pentoxy, respectively. Because these values are within error of zero, we chose to ignore prompt isomerization prompt isomerization for the OH stretch relative kinetics as well as the A←X relative kinetics.

Discussion

In the results section, we presented the A←X spectrum of δ-C_4H_8OO● (Figure 3) with broad peaks at 7355 and 7556 cm^{-1}. The spectrum features broad peaks without rotational structure due to a number of molecular conformers present. The spectrum compares to the spectrum of C_4H_8OO● taken by Glover *et al.*[50] who found peaks at 7355 cm^{-1} and 7591 cm^{-1}. The small shifts in peak positions are likely due to energy shifts in the valence orbitals from interactions between the OH and OO• groups, similar to the $HOCH_2OO$• vs CH_3OO• transition discussed by Sprague *et al.* (2013).[41]

Table 1 compares our values of k_{isom}/k_{O2} for *n*-butoxy and 2-pentoxy to those from the literature. It shows that our value for of k_{isom}/k_{O2} taken with using the OH stretch at 670 torr, $(2.09 \pm 0.16) \times 10^{19}$ molecules cm^{-3}, is within error to that found using the A←X transition at 595 torr, $(2.02\pm 0.14) \times 10^{19}$ molecules cm^{-3}. This suggests that isomerization is near the high pressure limit at 595 torr. This was confirmed by re-taking the A←X relative kinetics data at 700 torr, getting the value of $(1.90 \pm 0.22) \times 10^{19}$ molecules cm^{-3}, which is in error of the value found at 595 torr. The 700 torr data was complicated by unstable pressure in our flow cell, leading to higher noise and possible systematic errors. Multiple theoretical studies have

concluded that the rate constant for isomerization is near the high pressure limit at atmospheric pressure.[15,47,51] Using the pressure dependence of Somnitz and Zellner,[15] the rate constant at 760 torr is expected to be only 1.03 times larger than the rate constant at 595 torr, an insignificant correction given our experimental error. Thus, any of our kinetics data can be directly compared to previous data taken at atmospheric pressure.

Table 1. List of previous literature values of k_{isom}/k_{O2} for n-butoxy and 2-pentoxy at room temperature a pressure of 600-760 torr.

Compound	kisom/k_{O2} ($\times 10^{19}$ molecules cm^{-3})
n-butoxy	**1.6[13]**
	1.9±0.4[6]
	1.5±0.5[7]
	1.8±0.6[9]
	2.1±0.5[12]
	1.8±1.1[12]
	1.95±0.4[11]
	1.7±0.1[14]
	2.09±0.16 (this work, OH str)
	2.02±0.14 (this work, A←X)
2-pentoxy	**0.17[52]**
	3.1[8] (factor of 2 error)
	5.2±2.1[10]
	3.4±0.4[14]
	4.2±0.5 (this work, OH str)

Table 1 shows that our values of k_{isom}/k_{O2} compare well with previous literature values. In particular, our value is within error of the value, $(1.95 \pm 0.4) \times 10^{19}$ molecules cm^{-3}, found in the most recent *n*-butoxy relative kinetics paper by Cassanelii *et al.*[11], who measured k_{isom}/k_{O2} by quantifying both the butanal produced from reaction with O_2 and δ-hydroxy-butanal produced after a second isomerization (reactions R9-R11) with FT-IR spectroscopy. Cassanelli *et al.* claim that no prompt isomerization occurred when they photolyzed n-butyl nitrite at 370 nm because isomerization products were not seen at very high [O_2] concentrations. While earlier work using GC-FID detection did claim that a small percentage of alkoxy radicals promptly

isomerized (≈10%) when photolyzed at 370 nm because the yield of butanal, produced from reaction with O_2, was found to be less than one even at very high [O_2].[12] This study still found a value of k_{isom}/k_{O2} close to the present study, (2.1 ± 0.5) × 10^{19} molecules cm^{-3} for their data taken using butyl nitrite photolysis to create the *n*-butoxy radicals.

Our recommended values for k_{isom}/k_{O2} are slightly, but significantly higher than those published by in our previous paper by Sprague *et al.* (2012).[14] While some of this discrepancy is due to previous miscalculation of [O_2] in our cell, some of it is also how we treated prompt isomerization. We chose to ignore prompt isomerization, while Sprague *et al.* (2012) assumed a few percent (3-4%) of alkoxy radicals promptly isomerized.[14] While we have no evidence that prompt isomerization is occurring, a small percentage of prompt isomerization could be affecting our data. Assuming 10% prompt isomerization would only reduce our value of k_{isom}/k_{O2} for n-butoxy from 2 × 10^{19} molecules $cm^{-3}$to about 1.8 × 10^{19} molecules cm^{-3}.

There are few literature values in which to compare our value of k_{isom}, (1.7 ± 0.2)×10^5 s^{-1}. Estimates have been made based on modeling the end-products of chamber experiments.[5,53] Baldwin *et al.* estimated k_{isom} to be ≈6.2 × 10^5 s^{-1},[5] and Atkinson and Aschmann estimate k_{isom} to be ≈1.3 × 10^5 s^{-1}.[8] Morabito and Heicklen found k_{isom} by measuring the rate constant for reaction with NO, k_{NO}, and then measuring k_{NO}/k_{isom}. They found that k_{isom} ≈ 2.5 × 10^5 s^{-1}.[54] Heiss and Sahetchian found the k_{isom} to be 1 × 10^5 s^{-1}, but this value is calculated from Arrhenius parameters from high temperature experimental data (350K and higher).[55] Hein *et al.* found that k_{isom} = (3.5 ± 2) × 10^4 s^{-1} at 37.5 torr. At this pressure, which is well below any pressures found in the troposphere, isomerization is well into its fall-off region.[15,47,51] Xu *et al*. extrapolate their rate constant to 1 atm and get a value of 1.1 × 10^5 s^{-1}.[23] Our value is on the same order of magnitude as the rate constants found by these previous studies, but is the only measurement of

alkoxy isomerization that was found by measuring the immediate isomerization products in real time, and consequently contains much less uncertainty.

Table 2. List of rate constants for the reaction of alkoxy radicals with O_2 at room temperature

Compound	k_{O2} at room temperature ($\times 10^{-15}$ cm^3 $molecules^{-1}$ s^{-1})
ethoxy	**8.1**[25] **8.0**[26] **14**[27] **11**[28] **8.2**[4]
n-propoxy	**14**[25] **9.8**[29]
2-propoxy	**6.6**[25] **6.8**[29] **7.8**[30] **8.7**[31]
n-butoxy	**14±7**[24] **8.6±1.1 (this work)**
2-butoxy	**12**[31] **7.7**[32] **6.5±2**[33] **9±2**[35]
n-pentoxy	**≤100**[24]
2-pentoxy	**≤65**[9]
3-pentoxy	**12**[32] **7.2±3.5**[34]

Table 2 compares our value of k_{O2} rate for *n*-butoxy to literature values of k_{O2} for larger (C_2 or larger) simple alkoxy radicals. Our value, $(8.6 \pm 1.1) \times 10^{-15}$ cm^3 $molecules^{-1}$ s^{-1}, is within error of the previous value given by Hein *et al.*, $(1.4 \pm 0.7) \times 10^{-15}$ cm^3 $molecules^{-1}$ s^{-1},[24] but is more precise than the previous value. Our value of k_{O2} is one of the few values of k_{O2} found for an alkoxy radical that can isomerize. Since our value compares well with the values of k_{O2} found for smaller alkoxy radicals (Table 2), the length of the carbon chain does not seem to have a large effect of the rate of reaction with O_2. This data suggests that larger alkoxy radicals react

with O_2 at about the same rate as smaller alkoxy radicals, whose values of k_{O2} can be more readily obtained with LIF.

Finally, our direct rate constant for the isomerization of deuterated n-butoxy, shows that substituting a deuterium for hydrogen decreases the isomerization rate by a factor of 2.8 ± 0.3. This reduction is likely due to a reduction in hydrogen tunneling due to deuterium's larger mass as well as a traditional isotope effect. Previous theory work predicts that just elimination of hydrogen tunneling should reduce the rate constant by at least this much. Vreecken and Peeters,[19] Mereau *et al.*[17] and Somnitz[20] predict that hydrogen tunneling increases the isomerization rate by a factor of 3. The most recent estimates by Xu *et al.* predict hydrogen tunneling to increase isomerization by a factor of 3.3 (zero-curvature tunneling) or 11 (small-curvature tunneling). Given that we found the total kinetic isotope effect to reduce the isomerization rate by a factor of ≈3, previous theoretical estimates of hydrogen tunneling are likely too high.

Conclusions

We have reported the first spectra of the A←X origin of δ-HOC_4H_8OO● using cavity-ring-down spectroscopy. This spectrum features a broad absorbance with peaks at 7355 and 7556 cm^{-1}, similar to the A←X origin of butyl peroxy found by Glover *et al.*[50] We used these spectra to characterize the kinetics of *n*-butoxy isomerization, as δ-HOC_4H_8OO● is produced from *n*-butoxy isomerization. Absolute rate constants for the isomerization of *n*-butoxy ($[1.7\pm0.2]\times10^5$ s^{-1}) and *n*-butoxy-d_9 ($[6.2 \pm 0.3] \times 10^4$ s^{-1}) were found by monitoring the absorbance of δ-HOC_4H_8OO● in real time. These rate constants are, to our knowledge, the first direct measurements of alkoxy isomerization. We have found the rate of isomerization relative to the rate of reaction with O_2 (k_{isom}/k_{O2}), again using cavity ring-down detection of δ-

$HOC_4H_8OO\bullet$, and our value ([2.02± 0.14] × 10^{19} molecules cm^{-3}) agrees well with previous literature values. We used this value to calculate n-butoxy's rate of reaction with O_2. Our value ([8.6 ± 1.1] × 10^{-15} cm^3 $molecules^{-1}$ s^{-1}) shows that n-butoxy reacts with O_2 at about the same rate as other simple alkoxy radicals.

References

(1) Seinfeld, J. H.; Pandis, S. N. *Atmospheric Chemistry and Physics: From Air Pollution to Climate Change*.

(2) Atkinson, R. *Atmospheric Environment* **2007**, *41*, 8468.

(3) Orlando, J. J.; Tyndall, G. S.; Wallington, T. J. *Chemical Reviews* **2003**, *103*, 4657.

(4) Devolder, P. *Journal of Photochemistry and Photobiology A: Chemistry* **2003**, *157*, 137.

(5) Baldwin, A. C.; Barker, J. R.; Golden, D. M.; Hendry, D. G. *The Journal of Physical Chemistry* **1977**, *81*, 2483.

(6) Niki, H.; Maker, P. D.; Savage, C. M.; Breitenbach, L. P. *The Journal of Physical Chemistry* **1981**, *85*, 2698.

(7) Cox, R. A.; Patrick, K. F.; Chant, S. A. *Environmental Science & Technology* **1981**, *15*, 587.

(8) Atkinson, R.; Kwok, E. S. C.; Arey, J.; Aschmann, S. M. *Faraday Discussions* **1995**, *100*, 23.

(9) Geiger, H.; Barnes, I.; Becker, K.; Bohn, B.; Brauers, T.; Donner, B.; Dorn, H.-P.; Elend, M.; Freitas Dinis, C.; Grossmann, D.; Hass, H.; Hein, H.; Hoffmann, A.; Hoppe, L.; Hülsemann, F.; Kley, D.; Klotz, B.; Libuda, H.; Maurer, T.; Mihelcic, D.; Moortgat, G.; Olariu,

R.; Neeb, P.; Poppe, D.; Ruppert, L.; Sauer, C.; Shestakov, O.; Somnitz, H.; Stockwell, W.; Thüner, L.; Wahner, A.; Wiesen, P.; Zabel, F.; Zellner, R.; Zetzsch, C. *Journal of Atmospheric Chemistry* **2002**, *42*, 323.

(10) Johnson, D.; Cassanelli, P.; Cox, R. A. *The Journal of Physical Chemistry A* **2004**, *108*, 519.

(11) Cassanelli, P.; Cox, R. A.; Orlando, J. J.; Tyndall, G. S. *Journal of Photochemistry and Photobiology A: Chemistry* **2006**, *177*, 109.

(12) Cassanelli, P.; Johnson, D.; Anthony Cox, R. *Physical Chemistry Chemical Physics* **2005**, *7*, 3702.

(13) Carter, W. P. L.; Lloyd, A. C.; Sprung, J. L.; Pitts, J. N. *Int. J. Chem. Kinet.* **1979**, *11*, 45.

(14) Sprague, M. K.; Garland, E. R.; Mollner, A. K.; Bloss, C.; Bean, B. D.; Weichman, M. L.; Mertens, L. A.; Okumura, M.; Sander, S. P. *The Journal of Physical Chemistry A* **2012**, *116*, 6327.

(15) Somnitz, H.; Zellner, R. *Physical Chemistry Chemical Physics* **2000**, *2*, 1907.

(16) Somnitz, H.; Zellner, R. *Physical Chemistry Chemical Physics* **2000**, *2*, 1899.

(17) Mereau, R.; Rayez, M.-T.; Caralp, F.; Rayez, J.-C. *Physical Chemistry Chemical Physics* **2003**, *5*, 4828.

(18) Mereau, R.; Rayez, M. T.; Caralp, F.; Rayez, J. C. *Physical Chemistry Chemical Physics* **2000**, *2*, 1919.

(19) Vereecken, L.; Peeters, J. *J. Chem. Phys.* **2003**, *119*, 5159.

(20) Somnitz, H. *Physical Chemistry Chemical Physics* **2008**, *10*, 965.

(21) Zheng, J.; Truhlar, D. G. *Physical Chemistry Chemical Physics* **2010**, *12*, 7782.

(22) Davis, A. C.; Francisco, J. S. *Journal of the American Chemical Society* **2011**, *133*, 18208.

(23) Xu, X.; Papajak, E.; Zheng, J.; Truhlar, D. G. *Physical Chemistry Chemical Physics* **2012**, *14*, 4204.

(24) Hein, H.; Hoffmann, A.; Zellner, R. *Physical Chemistry Chemical Physics* **1999**, *1*, 3743.

(25) Fittschen, C.; Frenzel, A.; Imrik, K.; Devolder, P. *Int. J. Chem. Kinet.* **1999**, *31*, 860.

(26) Gutman, D.; Sanders, N.; Butler, J. E. *The Journal of Physical Chemistry* **1982**, *86*, 66.

(27) Zabarnick, S.; Heicklen, J. *Int. J. Chem. Kinet.* **1985**, *17*, 455.

(28) Hartmann, D.; Karthäuser, J.; Sawerysyn, J. P.; Zellner, R. *Berichte der Bunsengesellschaft für physikalische Chemie* **1990**, *94*, 639.

(29) Mund, C.; Fockenberg, C.; Zellner, R. *Berichte der Bunsengesellschaft für physikalische Chemie* **1998**, *102*, 709.

(30) Balla, R. J.; Nelson, H. H.; McDonald, J. R. *Chemical Physics* **1985**, *99*, 323.

(31) Deng, W.; Wang, C.; Katz, D. R.; Gawinski, G. R.; Davis, A. J.; Dibble, T. S. *Chemical Physics Letters* **2000**, *330*, 541.

(32) Deng, W.; Davis, A. J.; Zhang, L.; Katz, D. R.; Dibble, T. S. *The Journal of Physical Chemistry A* **2001**, *105*, 8985.

(33) Hein, H.; Hoffmann, A.; Zellner, R. *Berichte der Bunsengesellschaft für physikalische Chemie* **1998**, *102*, 1840.

(34) Hein, H.; Somnitz, H.; Hoffmann, A.; Zellner, R. *Zeitschrift für Physikalische Chemie* **2000**, *214*, 449.

(35) Falgayrac, G.; Caralp, F.; Sokolowski-Gomez, N.; Devolder, P.; Fittschen, C. *Physical Chemistry Chemical Physics* **2004**, *6*, 4127.

(36) Sharp, E. N.; Rupper, P.; Miller, T. A. *Physical Chemistry Chemical Physics* **2008**, *10*, 3955.

(37) Ball, S. M.; Jones, R. L. *Chemical Reviews* **2003**, *103*, 5239.

(38) Berden, G.; Peeters, R.; Meijer, G. *Int. Rev. Phys. Chem.* **2000**, *19*, 565.

(39) Brown, S. S. *Chemical Reviews* **2003**, *103*, 5219.

(40) Vallance, C. *New Journal of Chemistry* **2005**, *29*, 867.

(41) Sprague, M. K.; Mertens, L. A.; Widgren, H. N.; Okumura, M.; Sander, S. P.; McCoy, A. B. *The Journal of Physical Chemistry A* **2013**.

(42) Brown, S. S.; Ravishankara, A. R.; Stark, H. *The Journal of Physical Chemistry A* **2000**, *104*, 7044.

(43) Noyes, W. A. *Organic Syntheses* **1943**, *Collect. Vol. 2*, 108.

(44) Heicklen, J. In *Advances in Photochemistry*; John Wiley & Sons, Inc.: 2007, p 177.

(45) Atkinson, R.; Baulch, D. L.; Cox, R. A.; Crowley, J. N.; Hampson, R. F.; Hynes, R. G.; Jenkin, M. E.; Rossi, M. J.; Troe, J.; Subcommittee, I. *Atmos. Chem. Phys.* **2006**, *6*, 3625.

(46) Curran, H. J. *Int. J. Chem. Kinet.* **2006**, *38*, 250.

(47) Mereau, R.; Rayez, M.-T.; Caralp, F.; Rayez, J.-C. *Physical Chemistry Chemical Physics* **2000**, *2*, 3765.

(48) Jungkamp, T. P. W.; Smith, J. N.; Seinfeld, J. H. *The Journal of Physical Chemistry A* **1997**, *101*, 4392.

(49) Chen, M. W.; Just, G. M. P.; Codd, T.; Miller, T. A. *J. Chem. Phys.* **2011**, *135*.

(50) Glover, B. G.; Miller, T. A. *The Journal of Physical Chemistry A* **2005**, *109*, 11191.

(51) Lendvay, G.; Viskolcz, B. *The Journal of Physical Chemistry A* **1998**, *102*, 10777.

(52) Dóbé, S.; Bérces, T.; Márta, F. *Int. J. Chem. Kinet.* **1986**, *18*, 329.

(53) Atkinson, R.; Aschmann, S. M. *Environmental Science & Technology* **1995**, *29*, 528.

(54) Morabito, P.; Heicklen, J. *Bulletin of the Chemical Society of Japan* **1987**, *60*, 2641.

(55) Heiss, A.; Sahetchian, K. *Int. J. Chem. Kinet.* **1996**, *28*, 531.

Chapter 4: Upper Limits on the Yields of $HONO_2$ and HOONO from the Reaction of HO_2 and NO using Pulsed Laser Photolysis and Mid-IR Cavity Ring-down Spectroscopy

Abstract

HO_x (HO_2 and OH) and NO_x (NO_2 and NO) radicals are key intermediates in the chemistry of Earth's atmosphere; the HO_x and NO_x cycles catalyze ozone depletion in the stratosphere and ozone and photochemical smog production in the troposphere. Interconversion within the HO_x and NO_x families happens continuously, partially through the reaction of HO_2 and NO to form OH and NO_2. Since these radicals are continually recycled, even a small branching yield of nitric acid ($HONO_2$) from the reaction of HO_2 with NO will impact radical concentrations predicted in the troposphere and stratosphere, by cumulatively sequestering radicals in a stable reservoir species. Butkovskaya *et al*. measured a small yield of $HONO_2$ from the reaction of HO_2 with NO (0.5±0.2% at 700 Torr and 298 K) in a turbulent flow reactor with Chemical-Ionization Mass Spectrometry (CIMS) detection.[1-3] This yield increased with pressure and humidity and decreased with temperature. We investigated this reaction by an alternative method: directly detecting the $HONO_2$ in the mid-IR – as well as its weakly bound isomer HOONO – with Pulsed-Cavity Ring-down spectroscopy. HO_2 radicals were produced by Pulsed Laser Photolysis of Cl_2 in a slow flow cell, in the presence of methanol (CH_3OH). Addition of 700 Torr of CO prevented unwanted $HONO_2$ formation from the reaction of OH and NO_2 and recycled HO_2. This experiment allowed detection of products spectroscopically on short time-scales (2.5 ms) in the absence of any wall reactions. We found no evidence for the formation of either $HONO_2$ or HOONO from the reaction of HO_2 and NO. At (700 ± 14) Torr and (300 ± 3) K, we place an upper limit of 0.2% on the yield of $HONO_2$ and 0.1% on the yield of HOONO. The upper limit of $HONO_2$ decreases to 0.1% when the amount of $HONO_2$ from OH side chemistry is taken into account using a comprehensive chemical model. Reducing the

temperature to 278 K did not result in a detectable amount of $HONO_2$ from reaction of HO_2 with NO. These upper limits are significantly lower than the yield of $HONO_2$ measured by Butkovskaya *et al*.

Introduction

Hydrogen radicals (HO_x, OH and HO_2) and nitrogen radicals (NO_x, NO and NO_2) catalyze chemistry throughout the troposphere and stratosphere.[4] Consequently, an accurate understanding of HO_x and NO_x chemistry is essential to solving problems from stratospheric ozone destruction to urban smog. These radicals are continuously recycled in the HO_x and NO_x cycles, which are coupled via the reaction of HO_2 with NO to form OH and NO_2 (R1a).[4,5]

$$HO_2 + NO \rightarrow OH + NO_2 \quad (R1a)$$

This reaction has long been known to be one of the most important radical recycling channels in the atmosphere,[4,6] and it affects the concentrations many important atmospheric compounds, including HO_x, NO_x, $HONO_2$, and O_3,[7] throughout the stratosphere and troposphere.

For decades, R1a was believed to be the only pathway for the reaction of HO_2 with NO, but in principle, there could be association channels leading to the formation of either nitric acid ($HONO_2$) or its more weakly bound isomer, peroxynitrous acid (HOONO):

$$HO_2 + NO \rightarrow HONO_2 \quad (R1b)$$
$$HO_2 + NO \rightarrow HOONO \quad (R1c)$$

While there is strong experimental evidence that HO_2 could react with NO in the solution phase to form $HONO_2$,[8] experimental evidence suggested that this reaction does not occur in the gas phase.[6,9,10] In 1979, Howard measured lower limits for the rate constants for channels R1b and R1c in a laminar flow reactor using laser magnetic resonance detection of OH and HO_2 and determined that ≥99.88% of the reaction was radical propagating at pressures $p \leq 3$ Torr.[9] The rate coefficient has a strong negative temperature dependence, suggesting that the reaction

proceeds through a bound intermediate, HOONO,[9-13] but the absence of any strong pressure below 750 Torr,[10,12,13] indicates that intermediate does not last long enough to experience collisional stabilization needed for the radical termination channels (R1b and R1c).

It is well established that peroxy radicals (RO_2) undergo a reaction equivalent to R1b to form nitrates ($RONO_2$).[14,15] The larger the carbon chain, the higher the nitrate branching ratio; if we consider HO_2 as the smallest possible peroxy radical, it should be the least likely to isomerize to the nitrate ($HONO_2$ in this case).[14,15] Theoretical calculations by Lohr *et al*. investigated nitrate formation in a number of peroxy radicals, and found a 38 kcal/mol barrier to HOONO → $HONO_2$ isomerization – too large for any $HONO_2$ formation. Yet they came to the same conclusion for the larger peroxy radicals, which are well known to form a small amount of nitrate,[15] and in 2004 Zhang *et al*. suggested that quantum theory was not good enough to theoretically quantify nitrate formation.[16] In 2008, Dibble discussed the limitations in current theoretical work on these reactions, and noted that many studies suffered from misuse of spin-restricted wavefunctions and acknowledged the difficulties in finding an accurate transition state for HOONO → $HONO_2$ isomerization.[17] Vereecken and Francisco highlighted this difficulty in finding an accurate transition state and said that these difficulties prevented quantitative $RONO_2$ yields.[18]

Multiple theoretical studies have assessed the possibility of a radical terminating channel from the reaction of HO_2 with NO and have formed no consensus on the existence of R1b.[2,15,16,19-27] Most recent sources have a potential energy surface similar to Figure 1, but with disagreement about the energies and structures of the HOONO → $HONO_2$ transition states. HO_2 and NO are approximately 9 kcal/mol higher in energy than OH and NO_2 and approximately 18 kcal/mol higher in energy than the reaction intermediate, HOONO. HOONO exists as one of

two isomers, of which *cis-cis* is more stable by approximately 2 - 4 kcal/mol[2,28] – the less stable *trans-perp* HOONO rapidly isomerizes to form *cis-cis* HOONO near room temperature.[29] From the reaction of HO_2 + NO (R1), most of the chemically activated HOONO formed will break apart to OH and NO_2. To form $HONO_2$, (1) HOONO must isomerize to $HONO_2$ and (2) the excited $HONO_2$ must be collisionally stabilized before it can break apart to form OH and NO_2. The most likely pathway to $HONO_2$ is through a weakly bound adduct of OH and NO_2 (WB in Figure 1). TS2 leads from this weakly bound complex to $HONO_2$ and is structurally very close to OH and NO_2 with the oxygen from OH loosely interacting with the nitrogen of NO_2.[2,22] Studies that only considered TS1 in Figure 1 predicted no isomerization from HOONO to $HONO_2$, since the energy of TS1 was consistently calculated to be above the energy of OH and NO_2.[15,21,23] With TS2, Chen *et al.* predicted, with density functional theory (B3LYP/6-311G(d,p)) and quasiclassical trajectory calculations, a high pressure limit of the yield of R1b of 1.4% at 300 K, which agreed with previous experiments by Butkovskaya *et al.*[1,30] Yet, theoretical calculations are currently unable to quantify the amount of $HONO_2$ from R1b to the within 1% accuracy needed for atmospheric chemical models due to problems finding an accurate potential energy surface and modeling the spin of TS2.[17,18]

Butkovskaya *et al.* measured a small (<1%) yield of $HONO_2$ from the reaction of HO_2 and NO (R1b) with a turbulent flow tube and Chemical Ionization Mass Spectrometry (CIMS) detection.[1-3] While this work disagreed with previous conclusions in the literature about reaction yields of R1b,[9-13] it is currently the only published work that uses a method capable of directly measuring small $HONO_2$ yields from R1b at pressures near 1 atm. They report a (0.50 ± 0.20) % $HONO_2$ yield at room temperature and 700 Torr and found that the yield increased with pressure, decreased with temperature, and increased with water vapor concentration.[1-3] While small, this

pathway could have major impacts in the atmosphere. Since HO_x and NO_x radicals are continuously recycled in the atmosphere, a <1% yield R1b would lead to large amounts of radicals sequestered as $HONO_2$.

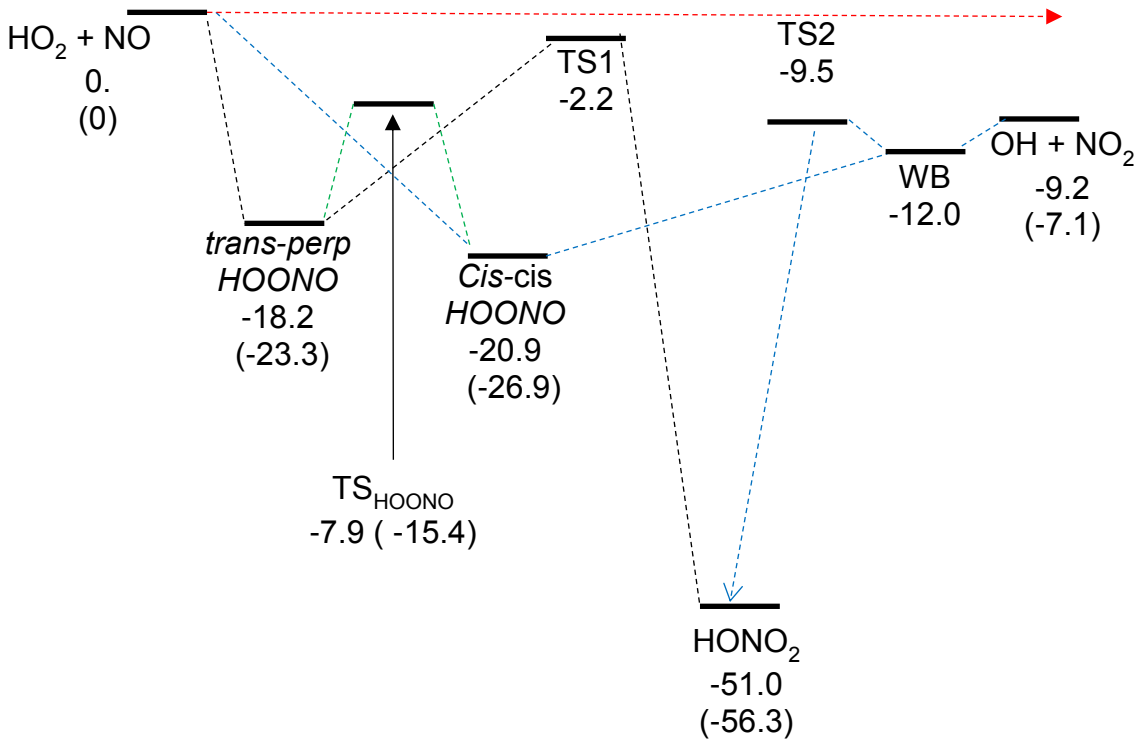

Figure 1. Potential energy surface of the HO_2 + NO reaction with energies (in kcal/mol) from Butkovskaya *et al* (DFT-UB3LYP/6-311++G(d,p), includes zero-point vibrational corrections).[2] Energies in the parenthesis are experimental values of ΔH_f^{o}[31-34] or E_a[29] in the case of the HOONO isomerization barrier. The dominant pathway (red) is HO_2 and NO directly forming OH and NO_2 via excited HOONO. Isomerization between *trans-perp* HOONO and $HONO_2$ (black) is believed to be highly unfavorable due to the barrier of TS1.[2,15,23] The most likely pathway to form $HONO_2$ (blue) goes through a weakly bound adduct of OH and NO_2 (WB) which isomerizes to $HONO_2$ via TS2 (which is structurally close to OH + NO_2, except for a weak interaction between the O of OH and the N of NO_2).

While Butkovskaya *et al*. first published their results in 2005,[3] to the best of our knowledge there has been no verification of their results, leading to considerable uncertainties in atmospheric models.[7,35-41] The JPL data evaluation[42,43] does not currently recommend a nonzero value of the $HONO_2$ yield (they do report Butkovskaya *et al*. in footnotes), and most modelers do not include this yield. However, many modelers have studies the impact of R1b on the concentrations of many atmospheric species. Cariolle *et al.* showed that addition of R1b into a chemical transport model (CTM) changed the concentrations of NO_x, OH, and $HONO_2$ throughout the atmosphere (for example, OH decreased by more than 20% near the tropopause), making the output of the model disagree with field measurements.[7] Sovde *et al.* found that addition of R1b into an atmospheric model, decreased [NO_x] by ~50% and [O_3] by ~18% at the tropopause.[38] Gottschadlt *et al.* found addition of R1b to their model resulted in a 20% decrease in OH, a 40% decrease in NO_x, a 25% decrease in O_3 and a 50% increase in $HONO_2$ near the tropopause. Unlike Cariolle *et al.*, these latter two studies were in better agreement with field measurements after addition of R1b, but they contend that there is too much uncertainty in the current models confirms the existence of R1b.[36,38] Boxe *et al.* found that addition of R1b into their photochemical box model of the South Pole caused better agreement between model [OH] and field measurements but worse agreement between model O_3 and $HONO_2$ and field measurements.[39] Stavrakou *et al*. calculated which reactions contribute the most to uncertainties in NO_x loss throughout the atmosphere with a CTM, and found that the yield of R1b is currently the largest gas phase uncertainty in atmospheric NO_x loss.[37] Righi *et al.* also found that addition of Butkovskaya *et al.*'s yield of R1b had the largest effect on the total ozone column than any other model parameter they tested.[40]

Since its addition into models causes severe changes to HO_x, NO_x, O_3 and $HONO_2$ concentrations, the accuracy of current atmospheric models hinges on properly quantifying the yield of R1b. To eliminate these uncertainties, the yield of R1b needs to be re-measured with complementary experimental techniques, but this system poses several experimental challenges. Firstly, unwanted side chemistry, especially the reaction of OH with NO_2 (R2a), readily produces $HONO_2$, interfering with results.

$$OH + NO_2 \rightarrow HONO_2 \text{ (R2a)}$$
$$OH + NO_2 \rightarrow HOONO \text{ (R2b)}$$

Second, heterogeneous chemistry can produce $HONO_2$ on the walls of reactions chambers, often leading to large $HONO_2$ backgrounds and unwanted $HONO_2$ signal from "wall" reactions. Finally, the branching ratios of $HONO_2$ or HOONO from R1b or R1c are likely very small, necessitating highly sensitive detection methods, such as mid-IR Cavity Ring-down spectroscopy (CRDS), a sensitive means of detecting primary products of free radical reactions in real time during flow cell experiments. In previous work, we used this method to detect $HONO_2$ and HOONO formed from the reaction of OH and NO_2 and quantified their absolute yields.[44]

To verify the results of Butkovskaya *et al.*,[1-3] we investigated the reaction of HO_2 with NO in a pulsed-laser photolysis (PLP) flow cell experiment using mid-IR CRDS to detect both $HONO_2$ and HOONO products by their ν_1 OH stretch at 300, 500, and 700 Torr and 300 and 278 K. Mid-IR spectroscopy in the 3200-3750 cm^{-1} region allows us to detect a number of other species, including the HO_2 reactant and secondary products CO_2, peroxynitric acid (HO_2NO_2), nitrous acid (HONO), and ClNO. PLP experiments allow us to detect these products on a 10 μs to 10 ms timescale. On these timescales, this technique only probes reactions occurring in the center of the cell, and diffusion rates are slow enough that wall reactions do not significantly contribute to the observed products. While the IR-CRDS instrument is more sensitive than most traditional

spectroscopy techniques, it is less sensitive than CIMS. To compensate, we need higher initial radical concentrations (10^{13} - 10^{14} cm^{-3}) and a chemical amplification scheme with carbon monoxide (CO) to both suppress unwanted $HONO_2$ from R2a and to enhance final $HONO_2$ concentrations. With PLP and the CO chemical amplification scheme, we can ensure that any $HONO_2$ detected is from the gas phase reaction of HO_2 with NO and not unwanted gas phase or heterogeneous side chemistry.

Experimental

Cavity Ring-down Spectroscopy with Pulsed Laser Photolysis

The pulsed-laser photolysis cavity ring-down spectrometer (CDRS) and flow cell (Figure 2) have been described previously.[44-46] We flowed a gas mixture, usually $N_2/O_2/CO/Cl_2/CH_3OH/NO$, through a slow flow cell situated in the middle of a mid-IR optical cavity. Chemistry was initiated by an excimer laser (Lambda Physik LPX 210i, 10 Hz) at 351 nm (XeF). Initial radicals, intermediates, and precursors were detected by CRDS in the 3200-3750 cm^{-1} spectral region, with a time resolution of 10 μs.

The experiments were performed in a flow cell (58-cm long with a square 1 cm × 1 cm cross section) that was temperature controlled to ± 1 K and could reach temperatures as low as 273 K. The reaction gas mixture entered via a (0.6 cm diameter) side port, traveled through 12 cm of cooled stainless steel (~0.6 diameter, in thermal contact with the reaction cell) and finally flowed through the center 7 cm of the reaction cell before being pumped out. A 4.1 × 0.5 cm excimer beam passed through the gases via two 5 × 1 cm quartz windows on the sides of the cell. Purge gas (N_2 at 10% of the reagent gas flow rate) passed over the mirrors and entered the cell at either end of the reaction region. Chilled water (Neslab Coolflow CFT-33) circulated around a cooling block in contact with thermoelectric coolers (TE Technology, Inc. TE-63-1.4-1.15) attached to

the cell and controlled by an ILX Lightwave LDT-5948 Precision Temperature Controller. A resistance temperature detector (RTD) monitored the cell's temperature. The assembly was placed in a vacuum chamber to insulate the cell and prevent water condensation.

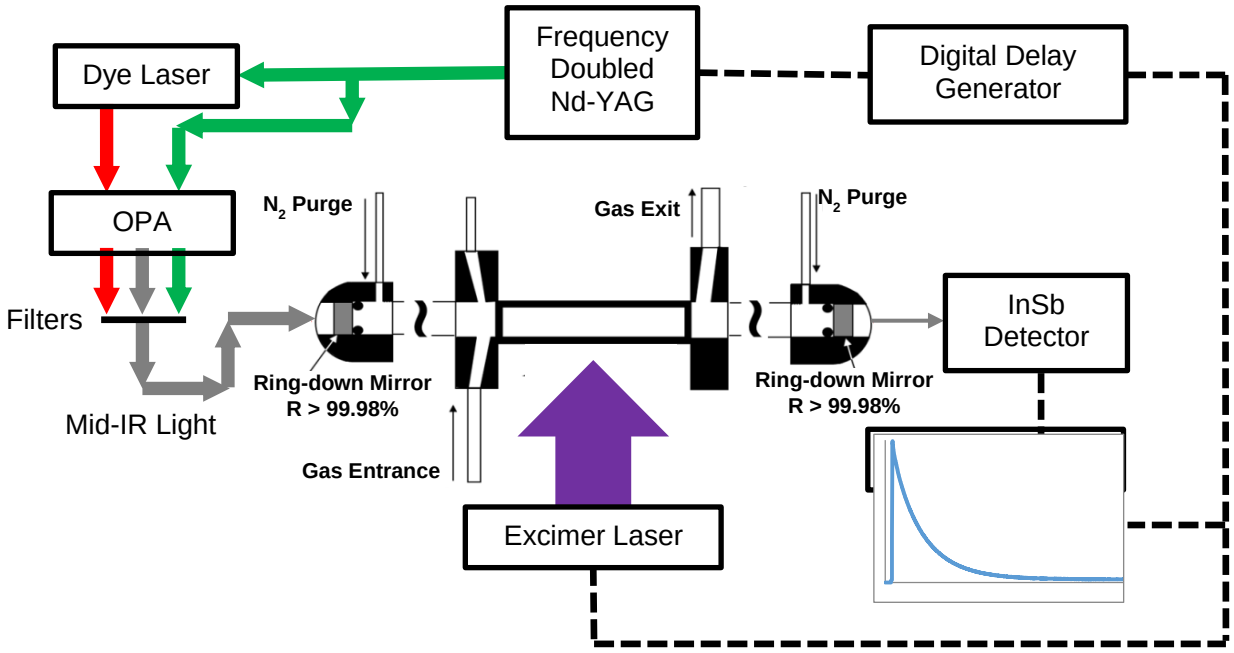

Figure 2. Schematic of PLP-CRDS spectrometer and flow cell. Cooling system not shown.

The residence time of gases in the flow cell was typically 30 - 40 ms. Gas flows were monitored with gas flow meters (Omega Engineering). N_2 (Air Liquide, typically $2 – 3 \times 10^{18}$ cm^{-3}), O_2 (Air Liquide, typically $2 – 3 \times 10^{18}$ cm^{-3}) and CO (UHP, Matheson, typically $1.7 – 1.8 \times 10^{19}$ cm^{-3}) were purified with molecular sieve 13X (Alfa Aesar) before they entered the cell. 2% NO in N_2 (Airgas, typically $1 – 10 \times 10^{15}$ cm^{-3} of NO) was purified with ascarite II (Thomas Scientific) to reduce unwanted NO_2 and then with molecular sieve 13X (Alfa Aesar) to remove water. 3.5% Cl_2 in He (Matheson, typically $2 - 8 \times 10^{15}$ cm^{-3} of Cl_2) was flowed directly into the cell. CH_3OH (HPLC grade, >99.8% purity, J.T. Barker) was purified with three freeze-pump thaw cycles and then introduced into the cell by bubbling N_2 carrier gas through the CH_3OH sample. The methanol concentration in the cell, typically $5 – 6.5 \times 10^{15}$ cm^{-3}, was

spectroscopically quantified by measuring the intensity of its ν_1 OH stretch band (3600 – 3750 cm^{-1}).

As described by Sprague *et al.* (2012)[45], the mid-IR CRDS probe beam (~500 μJ) was produced from an optical parametric amplifier as described by Reid and Tang[47] that used the output of a 10 Hz Nd:YAG (Continuum Surelite III) and a YAG pumped dye laser (Spectra Physics PDL-3, DCM dye from Exciton). The resulting mid-IR light was sent through the optical cavity formed from two highly reflective mirrors (R=99.98%, Los Gatos Research, peak reflectivity at 2.8 μm). Light exiting the cavity was focused on an InSb photodiode (Judson J10D-M204-R500U-60) with an external amplifier (Analog Modules 351-A-1-50-NI), which was connected to a GageScope CS1450 digital oscilloscope. Each ring-down trace was collected for 80 μs at a rate of 25 MHz and traces were averaged for 16 shots (1.6 s). Ring-down traces were fit to a simple exponential model using the Levenberg-Marquardt algorithm after he first 1/8 of the initial lifetime was discarded to remove signal from scattered light. A typical ring-down lifetime under experimental conditions was 6.5 μs at 3475 cm^{-1} with about 0.4 - 0.5% shot-to-shot noise. This yields a minimum detectable absorbance of 2.6 ppm per trace (16 shots averaged at 10 Hz) or a sensitivity of 3.2×10^{-6} $Hz^{-1/2}$.

Spectra were fitted manually with a linear least-squared fit using reference cross sections either from the PNNL spectral database[48] ($HONO_2$, HONO, HCHO, H_2O, and CH_3OH. PNNL reports <10% error for all compounds used and 1% for $HONO_2$, specifically) or experimentally determined in our cell (CO_2, ClNO, and HO_2NO_2). All errors are reported as two standard deviations (2σ).

Kinetics Model

Numerical simulation of the chemistry was used alongside the experimental data to provide a guideline for what the products and kinetics of the chemistry should be and to account for any $HONO_2$ produced from side chemistry (R2a). The comprehensive chemical kinetics model was constructed using predominantly recommended rate coefficients from JPL[38] and IUPAC[49] data evaluations; the supplemental information contains a full list of all reactions and rates included. Table 1 displays the most important reactions used and their respective rate coefficients. Chemical simulations were conducted in the Kintecus numerical integration package.[50] Modelled $HONO_2$ yields from R1b were estimated using our kinetics model with a Monte-Carlo-type simulation. Chosen initial concentrations and rate coefficients were varied "randomly" according to a normal distribution about the chosen mean value using uncertainties presented in the literature.

Table 1. Key Reactions used in the kinetics model. All listed rate constants are from the JPL data evaluation.[38]

Reaction		Rate / $cm^3\ s^{-1}$
	Initiation	
R4	$Cl + CH_3OH \rightarrow CH_2OH + HCl$	5.5×10^{-11}
R5	$CH_2OH + O_2 \rightarrow HO_2 + HCHO$	9.1×10^{-12}
	Propagation	
R1a	$HO_2 + NO \rightarrow OH + NO_2$	8.2×10^{-12}
R6	$OH + CO\ (+O_2) \rightarrow HO_2 + CO_2$	2.3×10^{-13}
	Termination	
R7	$Cl + NO \rightarrow ClNO$	1.8×10^{-12}
R8	$OH + NO \rightarrow HONO$	7.1×10^{-12}
R2a	$OH + NO_2 \rightarrow HONO_2$	1.0×10^{-11}
R2b	$OH + NO_2 \rightarrow HOONO$	1.7×10^{-12}
R9	$HO_2 + NO_2 \rightarrow HO_2NO_2$	1.1×10^{-12}

Table 2 shows the parameters varied and their respective uncertainties. Parameters were chosen based rate constant uncertainties reported in the rate constants in the JPL[38] and IUPAC[49] databases and experimental uncertainties in initial gas concentrations. Each experiment was modelled 1000 times and the resulting distributions of simulated values of HONO2 yields were plotted as a frequency histogram. The mean and 2σ uncertainty were taken from a Gaussian fit to the histogram distribution.

Table 2. Parameters varied during the Monte Carlo simulation of uncertainties in the kinetics model.

Parameter	Uncertainty
$[NO_2]_0$	2.00
$k_{HO2+HO2}$	1.20
k_{R1}	1.15
k_{R4}	1.20
k_{R3a}	1.30
k_{R3b}	1.50
k_{R2}	1.10

Results

Chemistry

Figure 3 shows the output of the kinetics model under conditions of a typical experiment and Table 1 lists the key reactions in our cell. HO_2 was created by photolyzing Cl_2 at 351 nm in the presence of CH_3OH:

$$Cl_2 + h\nu \rightarrow Cl + Cl \text{ (R3)}$$
$$Cl + CH_3OH \rightarrow HCl + CH_2OH \text{ (R4)}$$
$$CH_2OH + O_2 \rightarrow HO_2 + HCHO \text{ (R5)}$$

HO_2 reacted with an excess of NO ($1 - 10 \times 10^{15}$ cm^{-3}) to produce OH and NO_2 (R1a). We added an extreme excess of CO (1.8×10^{19} cm^{-3}) to convert OH back to HO_2 via R6 (>99% of OH reacts with CO).

$$OH + CO (+O_2) \rightarrow HO_2 + CO_2 \text{ (R6)}$$

This chemical amplification scheme, also used by Butkovskaya *et al.*,[1-3] prevented unwanted OH side chemistry (especially from the reaction of OH with NO_2, R2a) and increased any $HONO_2$ signal from R1b by over a factor of 20.

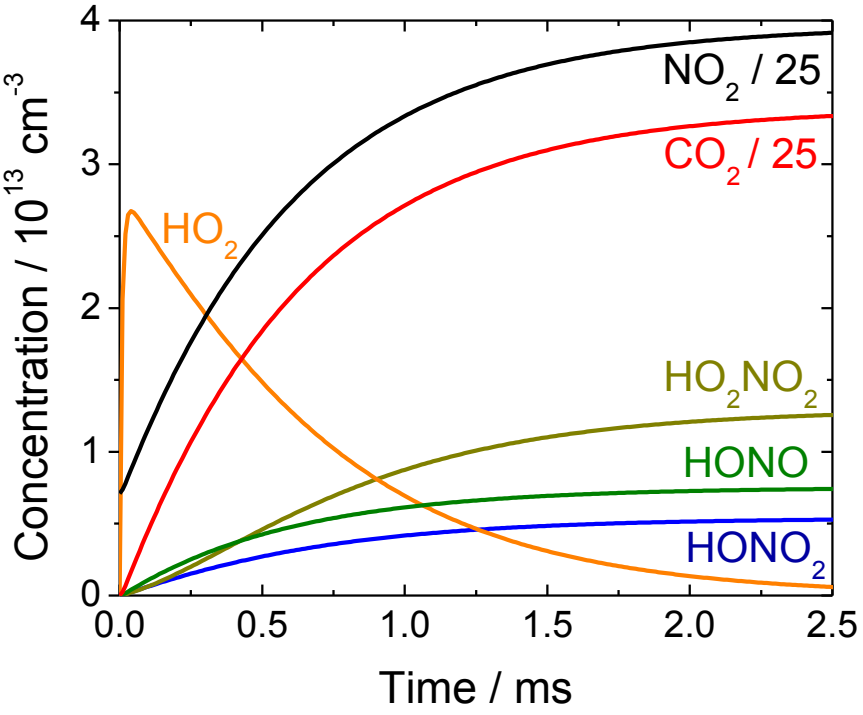

Figure 3. Kinetics model output assuming no $HONO_2$ from R1b. Input concentrations were the same as those of trial 1 on Table 3.

We quantified the amount of chemical amplification cycles based on the resulting [CO_2], since a molecule of CO was catalytically converted to CO_2 each cycle (R6). Our kinetics model predicts that the [CO_2] will agree with the number of times an HO_2 radical reacted with NO (R1a) to within 0.3% accuracy. If no other reaction produces $HONO_2$, the yield of $HONO_2$ from R1b is given by [$HONO_2$]/[CO_2].

There other chain terminating reactions include

$$Cl + NO \rightarrow ClNO \text{ (R7)}$$

$$OH + NO \rightarrow HONO \quad (R8)$$
$$HO_2 + NO_2 \rightarrow HO_2NO_2 \quad (R9)$$

The reaction of Cl with NO (R7) prevents reaction of Cl with CH_3OH to produce HO_2, slightly reducing $[HO_2]_0$. The reaction of OH with NO (R8) both terminates radical chemistry and scavenges OH radicals.

While NO_2 was not deliberately added to the cell, NO_2 chemistry is important since our chemical amplification scheme catalytically converts NO to NO_2. At room temperature and 760 Torr, the reaction of OH with NO_2 will form $HONO_2$ (87 ± 11) % of the time (R2a),[44] meaning that the $[HONO_2]$:$[CO_2]$ ratio could potentially over-estimate the amount of $HONO_2$ from R1b. In our experiments, we observed significant $HONO_2$ under conditions conducive to OH side-chemistry: high $[HO_2]_0$ and low [CO]. We dealt with this issue by (1) adding as much CO as possible to the cell to scavenge the OH radicals before they reacted with NO_2 (2) decreasing the radical concentration as much as possible (given our sensitivity) and (3) referring to our kinetics model to estimate the amount of $HONO_2$ produced from R2a and using this value to correct the experimental $[HONO_2]$:$[CO_2]$.

Below we discuss in greater detail the spectral quantification and chemistry of each compound observed in our spectra: HO_2, $HONO_2$ (from R1b and R2a), CO_2, HONO, HO_2NO_2 and ClNO.

HO_2 Detection

We detected HO_2 with its ν_1 OH stretch (3300 - 3500 cm^{-1}), a series of sharp peaks spaced ~40 cm^{-1} apart (Figure 4). The spectrum was taken 10 μs after Cl_2 photolysis (before much HO_2 reacted with NO) under typical conditions of our HO_2 + NO experiments (trial 1 on Table 3). Also in the spectrum is HCHO, which is a co-product of HO_2 from R4 and R5.

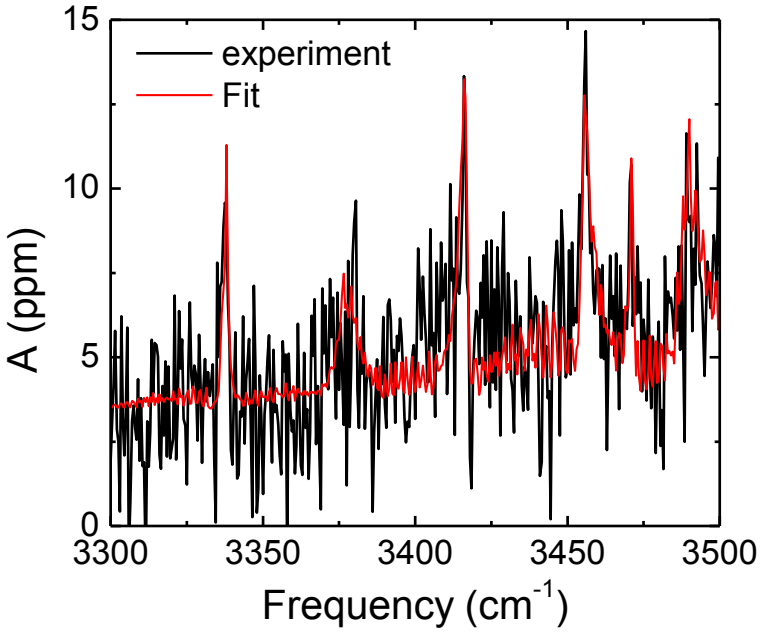

Figure 4. Spectrum of initial HO_2 at (710 ± 14) Torr and (300 ± 3) K. Gas concentrations were identical to those of trial 1 on Table 3. The experimental spectrum (black) was taken 10 μs after photolysis between 3300 - 3500 cm^{-1} with a 0.5 cm^{-1} step size and 96 shots averaged per point. The fitted spectrum (red) includes only HO_2 (3337, 3376, 3416, 3456, and 3490 cm^{-1})[55] and HCHO (Q-branch at 3471 cm^{-1}).[48]

Before every experiment, we quantified the initial radical concentration with the kinetics of the HO_2 self-reaction. Without NO in the cell, HO_2 will react with itself according to R10:

$$HO_2 + HO_2 \rightarrow H_2O_2 \quad \text{(R10)}$$

Figure 5 shows typical HO_2 self-reaction kinetics (at 3416 cm^{-1}) measured with a background of N_2 (blue) or CO (red) at (700 ± 14) Torr and (300 ± 3) K. Since the rate constant for the HO_2 self-reaction is well known,[38] $[HO_2]_0$ can be directly obtained from these kinetics by fitting the experimental data with a rate equation for a second-order reaction. We corrected for the removal of gases from our cell through the vacuum during the reaction, which was modeled as a first order exponential decay of the HO_2 out of the cell; the time constant (typically about 35 ms) for this decay was determined experimentally by measuring the absorbance of a stable compound,

HONO, as it was pumped out. Figure 5 also shows that the $[HO_2]_0$ from the HO_2 self-reaction in a background of CO ($[HO_2]_0 = (1.1 \pm 0.3) \times 10^{14}$ cm^{-3}) is within 2σ error of the $[HO_2]_0$ from the HO_2 self-reaction in a background of N_2 ($[HO_2]_0 = (1.4 \pm 0.4) \times 10^{14}$ cm^{-3}), confirming that the HO_2 self-reaction chemistry was not affected by ~1 atm of CO. While CH_3OH can increase the rate of HO_2 self-reaction with a chaperone mechanism, leading to inaccurately calculated $[HO_2]_0$, given the rate constants from Christensen *et al.*,[51] we expect the CH_3OH to affect our measured HO_2 concentrations by less than 0.5%. To reduce unwanted side chemistry (mainly from R2a), we kept the $[HO_2]_0$ as low as possible and quantified the radical concentration before every experiment.

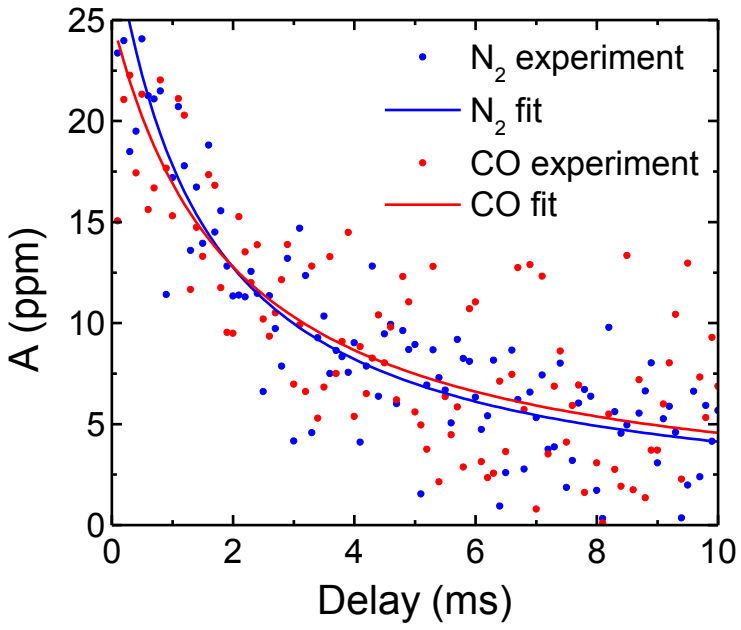

Figure 5. HO_2 self-reaction with $[HO_2]_0 = (1.1 \pm 0.3) \times 10^{14}$ cm^{-3} at (700 ± 14) Torr and (300 ± 3) K in a background of N_2 (blue points) or in a background of CO (red points). HO_2 absorbance was taken at 3416 cm^{-1} with 16 shots averaged per point (blue) or 32 shots averaged per point (red). Fits to 2nd order kinetics (corrected for the pumpout of gases out of the cell) are shown as solid red or blue lines.

$HONO_2$ and HOONO Detection

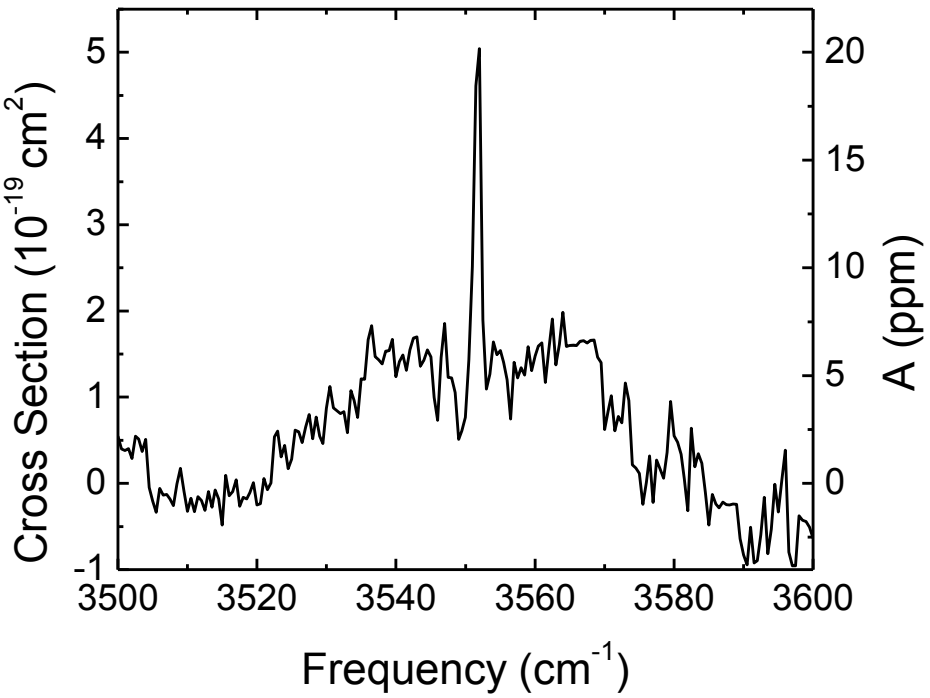

Figure 6. Spectrum of pure $HONO_2$ (4.0×10^{12} cm^{-3}) at room temperature. $HONO_2$ was purified by vacuum distilling a mixture of $HONO_2$ (70% in water) and concentrated H_2SO_4 and added to the cell with (87 ± 2) Torr of N_2. The spectrum was taken from 3500 – 3600 cm^{-1} with a 0.5 cm^{-1} step size, 16 shots averaged per point with a concentration of 9.7×10^{12} cm^{-3} of $HONO_2$ and a pathlength of 4.1 cm.

Given the cross section of the $HONO_2$ Q-branch at 3551 cm^{-1} (4×10^{19} cm^2)[48], our 4.1 cm photolysis pathlength and our typical sensitivity of 3.2×10^{-6} Hz$^{-1/2}$, we can detect a [$HONO_2$] of 1.6×10^{12} cm^{-3} after just one scan. Under typical experimental conditions, we predict 4.1×10^{12} cm^{-3} of $HONO_2$ if the branching ratio of R1b = 0.5%; this concentration is double our minimum detectable absorbance. We tested our ability to quantify [$HONO_2$], by adding pure $HONO_2$ (purified by vacuum distilling 70% $HONO_2$ in water (EMD) dissolved in double the amount of concentrated H_2SO_4 (Macron)) into our CRDS cell. We quantified the amount $HONO_2$ entering the CRDS cell by UV absorption at 214 nm (cross section = 4.4×10^{-19} cm^2)[38] in a 1 m flow cell

with a Zn Pen-Ray source (UVP) and photomultiplier tube detector positioned after a monochromater. Figure 6 shows a spectrum of pure $HONO_2$ taken with our spectrometer and demonstrates that a [$HONO_2$] of 9.7×10^{12} cm^{-3} at a 4.1 cm pathlength is several times higher than our detection limit. For all [$HONO_2$] investigated ($1 - 12 \times 10^{13}$ cm^{-3}), the concentration from the Mid-IR spectrum (fitted to a reference spectrum from the PNNL spectral database. PNNL reported an error of 2.5% for the ν_1 OH stretch cross section of $HONO_2$) agreed with concentration from the UV absorption measurements.[48]

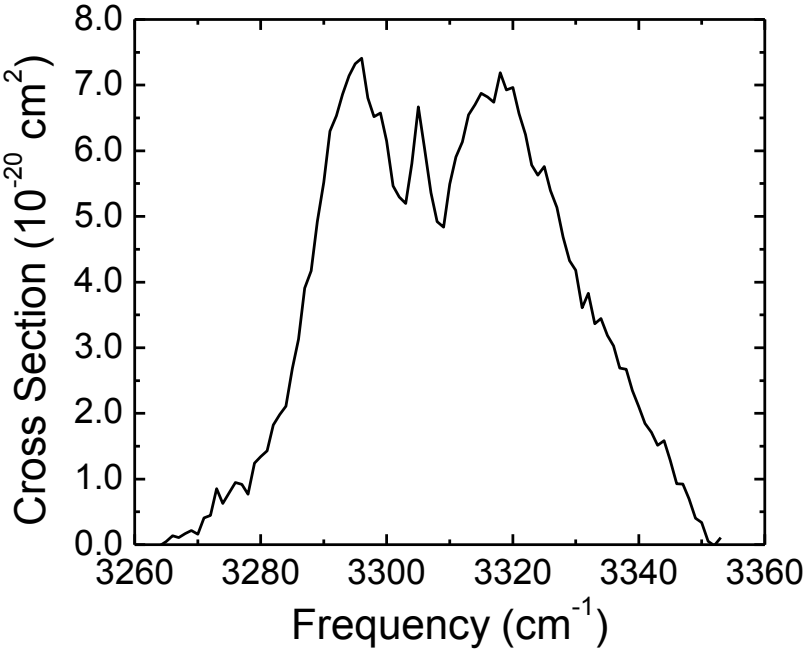

Figure 7. Spectrum of *cis-cis* HOONO taken from Mollner *et al*.[44]

The spectrum of *cis-cis* HOONO has been studied previously,[52-55] and the cross section of the ν_1 OH stretch *cis*-HOONO, which absorbs from 3280 - 3320 cm^{-1} were taken from Mollner *et al.* (Figure 7).[44] Due to hydrogen-bonding, the frequency of the ν_1 OH stretch of *cis-cis* HOONO is redshifted compared to the ν_1 OH stretch of $HONO_2$, making it easily distinguishable from $HONO_2$. We expect all HOONO to be present as a *cis-cis* isomer; while HOONO can exist in a higher energy *trans-perp* isomer (Figure 1), at room temperature *trans-perp* HOONO is expected

to isomerize to *cis-cis* HOONO within 0.35 ms at 300 K,[55] and Fry *et al*. found no evidence for *trans-perp* HOONO at room temperature.[29] Once formed HOONO is stable at room temperature; Bean *et al*. report a HOONO lifetime of more than 500 ms after it was produced from R2b.[55]

CO_2 Detection

CO_2 was a tracer for the amount of chemical amplification and the yield of R1b was based on the ratio of $[HONO_2]$:$[CO_2]$. We quantified $[CO_2]$ based on its $2\nu_2 + \nu_3$ band absorption between 3580 - 3640 cm^{-1}. Quantification of CO_2 was complicated by systematic errors due to multiexponential ring-downs as previously described by Yalin and Zare[56] and Hodges *et al*.[57] If the bandwidth of the laser is larger than the linewidth of a spectral line, different wavelengths within the laser pulse will decay at different rates, leading to a multiexponential decay of light out of the cavity. Wavelengths absorbed strongly by the sample will decay faster than others, causing the exponential fit to be biased against these wavelengths and resulting in underestimation of the absorbance. This effect is more pronounced with sharp spectral lines and the large the absorbances, both seen in our CO_2 spectra (Figure 8). To account for this effect, we took spectra of multiple concentrations of CO_2, ((0.6 - 4.5) × 10^{15} cm^{-3}, with a pathlength of gases in our flow cell of (7.4 ± 1.2) cm) to calibrate the change in effective cross section of CO_2 as a function of $[CO_2]$. The calibration was performed at (700 ± 14) Torr and (300 ± 3) K with a 5 × 10^{15} cm^{-3} CH_3OH background, similar to the spectral background of the actual experiment. An external CO_2 analyzer (LI-COR LI-7000 CO_2/H_2O Analyzer) verified the $[CO_2]$. With this calibration, we were able to determine $[CO_2]$ in our cell to within 15% uncertainty (2σ), including errors in our pathlength and spectrometer noise. Figure 8 plots the integrated

absorbance of CO_2 from 3590 – 3630 cm^{-1} determined by this calibration, and CO_2 absorbance is not linear with concentration, with the slope decreasing for higher [CO_2]

We also mathematically simulated the multiexponential ring-downs of CO_2 using a method described by Yalin and Zare.[56] With Matlab,[58] we modeled our laser bandwidth as a Gaussian beam of 1 cm^{-1} FWHM (according to the specs of our YAG laser) and calculated how each wavelength would decay given a certain concentration of CO_2 with a background of CH_3OH. Reference CO_2 spectra were taken from the PNNL[48] and Hitran[59] spectroscopic databases. The end-product was a theoretical multi-exponential ring-down that we could fit and compare to the experimental results (Figure 8). After the excellent agreement between the measured and modeled CO_2 spectra at (700 ± 14) Torr and (300 ± 3) K, we relied on the theoretical calculation method to account for multiexponential ring-down decays at lower temperatures and pressures.

Since the $HONO_2$ absorbance was much less than the CO_2 absorbance during our experiments, $HONO_2$ absorbance did not suffer from reduced absorbance due to multiexponential ring-downs. This assumption was checked with additional simulations that predicted distortions in the $HONO_2$ absorbance by <1% and with the UV absorption measurements of $HONO_2$ described above.

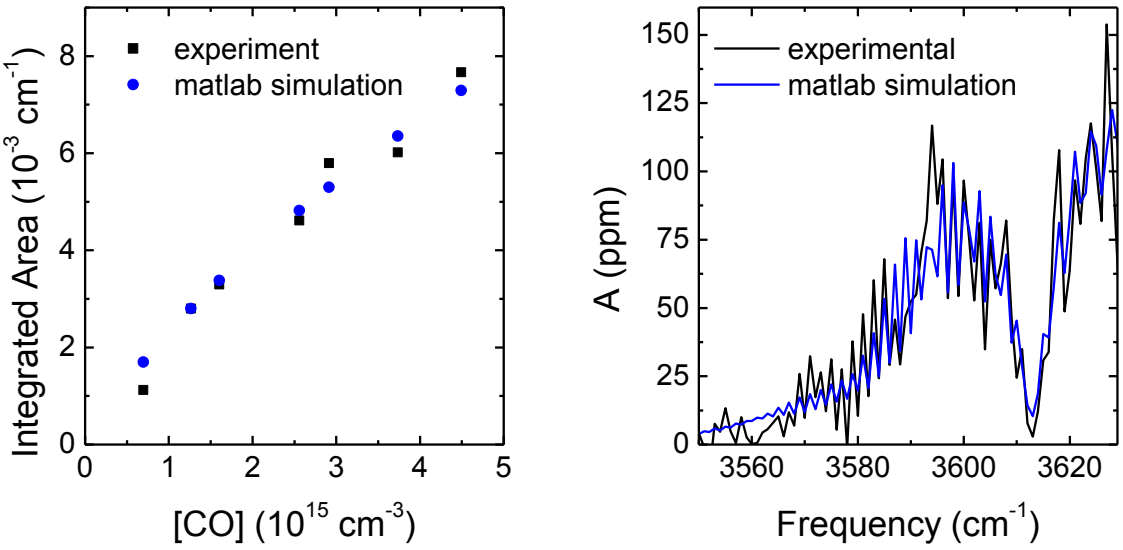

(a) (b)

Figure 8. (a) Total integrated area of the CO_2 spectrum from 3590 – 3630 cm^{-1} from our CO calibration (black) and predicted with our matlab simulation (blue) for [CO] = 0.7 – 4.7 × 10^{15} cm^{-3} (b) comparison of a modeled CO_2 spectrum (blue) with an experimental CO_2 spectrum (black) of the same concentration (1.2 × 10^{15} cm^{-3}).

HONO Detection

Figure 9 shows the spectrum of HONO from R8 (3500 - 3650 cm^{-1}, Q-branch at 3590 cm^{-1}). This spectrum was taken under typical experimental conditions but with N_2, instead of CO, as the bath gas. Under these conditions, the OH from R1a reacted with the excess NO to form HONO (R8). Since the kinetics model predicts >90% conversion of Cl to HONO (without any CO added to the flow cell) the amount of HONO is approximately equal to $[HO_2]_0$. Radical concentrations found by measuring the ν_1 OH spectrum of HONO agreed within 2σ error of the $[HO_2]$ from the HO_2 self-reaction.

The spectrum of HONO overlaps significantly with that of CO_2 (Figure 8 and Figure 9), possibly leading to systematic errors in $[CO_2]$. Underestimation of [HONO] could cause an overestimation of $[CO_2]$, leading to upper limits of R1b and R1c that are too low. We put an

upper limit on the [HONO] (1.5×10^{13} cm^{-3}) by quantifying the weakly absorbing *cis*-HONO isomer in the 3286 - 3332 cm^{-1} region, which is free from spectral interference. Since the experimental fits for the R1b yield included [HONO] near this upper limit, we assumed no underestimation of [HONO].

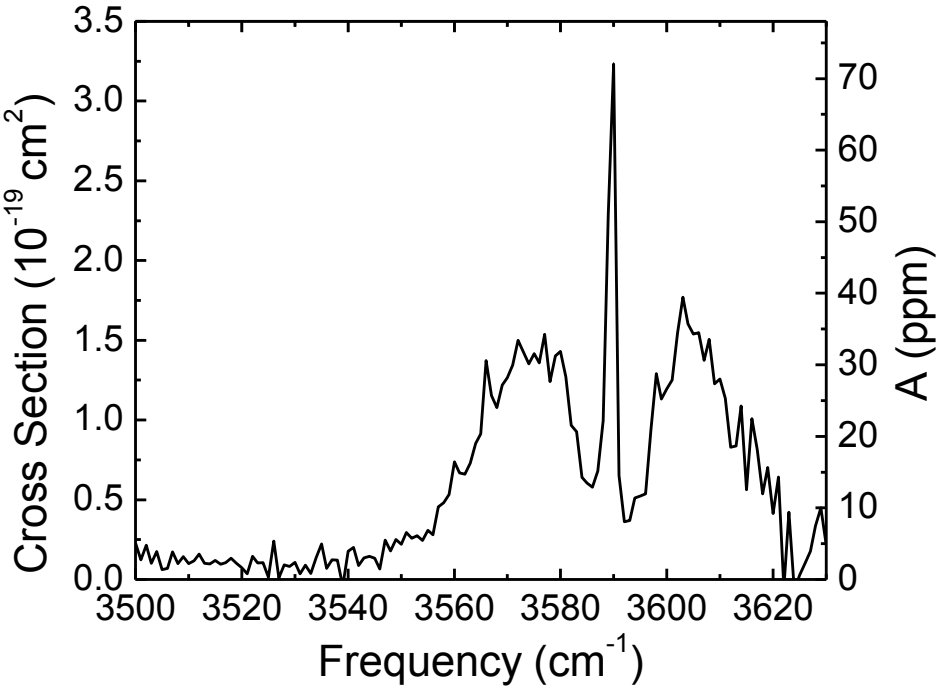

Figure 9. Spectrum of HONO at (710 ± 14) Torr and (300 ± 3) K. HONO (Q-branch at 3590 cm^{-1}) was from OH from R1a reacting with an excess of NO. Gas concentrations were: (5.3 ± 1.5) $\times 10^{13}$ Cl, 6×10^{15} cm^{-3} of NO, 2.4×10^{18} cm^{-3} of O_2, 4.2×10^{15} cm^{-3} of Cl_2, and 5.5×10^{15} cm^{-3} of CH_3OH in a background of N_2. Spectrum was taken 1 ms after photolysis from 3500 - 3630 cm^{-1} with a 1 cm^{-1} step size and 16 shots averaged per point.

HO_2NO_2 Detection

We observed HO_2NO_2 from the reaction of HO_2 with NO_2 (R9) in almost every experiment and used it to quantify [NO_2] in our cell. Figure 10 shows a spectrum of HO_2NO_2

produced from reacting of HO_2 (from R4) with NO_2 (R9). The HO_2NO_2 Q-branch (3540 cm^{-1}) absorbs just to the red of the Q-branch of $HONO_2$ (3551 cm^{-1}).

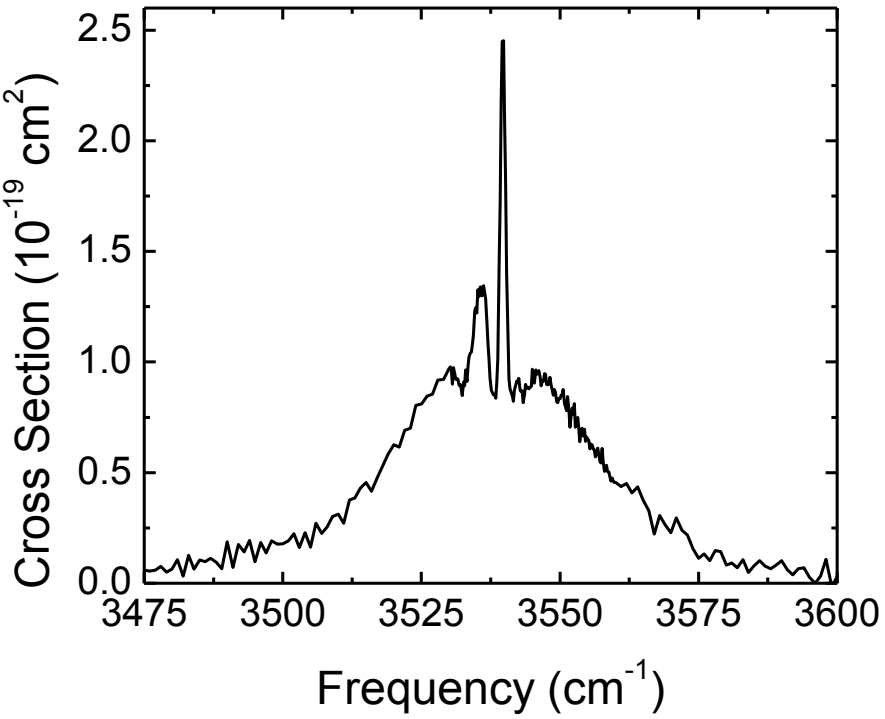

Figure 10. Spectrum of HO_2NO_2 at (710 ± 14) Torr and (300 ± 3) K. HO_2NO_2 (Q-branch at 3540 cm^{-1}) was created from reaction of HO_2 (from Cl and CH_3OH) reacting with NO_2 (4% in N_2, Matheson). Gas concentrations were: (1.1 ± 0.3) $\times 10^{14}$ Cl, 2.3 $\times$ 10^{15} cm^{-3} of NO_2, 2.1 $\times 10^{18}$ cm^{-3} of O_2, 1.2 $\times$ 10^{16} cm^{-3} of Cl_2, and 6 $\times$ 10^{15} cm^{-3} of CH_3OH in a background of N_2. Spectrum was taken 1 ms after photolysis from 3475 - 3600 cm^{-1} (1 cm^{-1} step size) and 3530 - 3560 cm^{-1} (0.2 cm^{-1} step size) and 48 shots averaged per point.

ClNO Detection

The reaction of Cl with NO (R7) produces ClNO which has a broad absorbance from 3540 - 3600 cm^{-1} and overlaps with $HONO_2$, but has no sharp features near the $HONO_2$ Q-branch. The ClNO spectrum, produced by reacting (1.3 ± 0.3) $\times 10^{14}$ cm^{-3} of Cl with 8.7 $\times$ 10^{15}

cm^{-3} of NO at 712 Torr, is shown in Figure 11, and agrees within 2σ error with the cross section from PNNL.[48] This reaction reduces the $[HO_2]_0$ (typically by ~20%), and ClNO is stable during the time scale of our experiments.

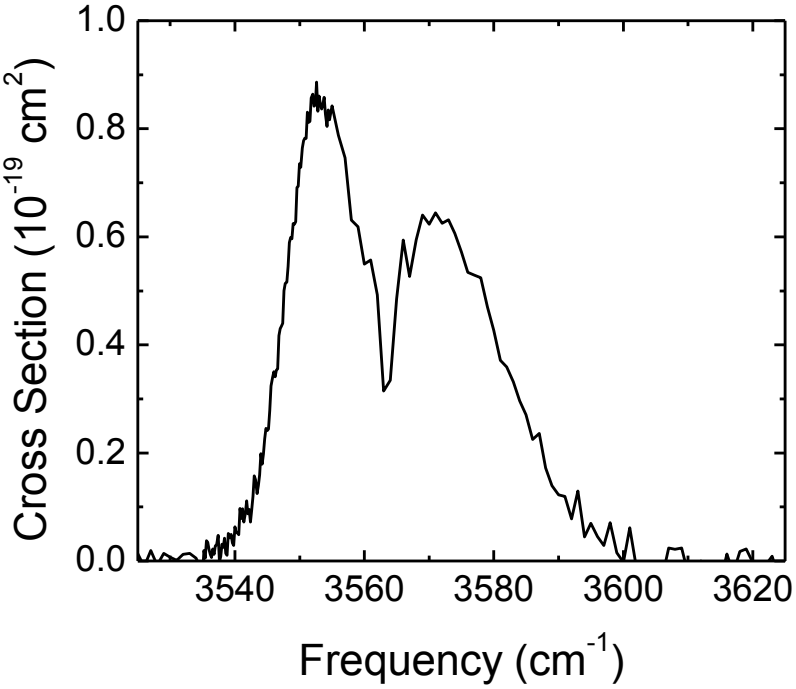

Figure 11. Spectrum of ClNO at (712 ± 14) Torr and (300 ± 3) K. ClNO was created from reaction of Cl reacting with NO. Gas concentrations were: (1.3 ± 0.3) $\times 10^{14}$ Cl, 8.7 $\times$ 10^{15} cm^{-3} of NO, 3.2 $\times 10^{18}$ cm^{-3} of O_2, and 1.0 $\times$ 10^{16} cm^{-3} of Cl_2 in a background of N_2. Spectrum was taken 1 ms after photolysis from 3475 - 3630 cm^{-1} (1 cm^{-1} step size) and 3535 – 3555 cm^{-1} (0.2 cm^{-1} step size) and 36 shots averaged per point.

Experimental Approach and Chemical Amplification

During a typical experiment, we first quantified the radical concentration with the HO_2 self-reaction, with Cl_2, CH_3OH in the cell with a background of N_2. Then NO was added to the cell and a spectrum of HONO from 3500 - 3630 cm^{-1} (Figure 9), to double check the radical concentration (since under these conditions all HO_2 should be converted to HONO via R1a

followed by R8). Finally, the N_2 bath gas was replaced by CO, and a spectrum was taken from 3500 – 3630 cm^{-1} to quantify the amount of CO_2 and $HONO_2$ produced from the chemical amplification scheme. We repeated the experiment at different NO, CO, Cl concentrations and at pressures down to 300 Torr to test the robustness of our experiments and the agreement with the kinetics model. Table 3 gives a summary of all of our trials. The upper limit of HOONO was found under the conditions of trial 3 on Table 3 by searching for its absorbance from 3280 – 3380 cm^{-1}.

Table 3. Summary of the trials of our HO_2 + NO experiment. All errors are 2σ. [CH_3OH] was typically 5-6.5 × 10^{15} cm^{-3} and [O_2] was 2-3 × 10^{18} cm^{-3}.

Trial	[NO] (× 10^{15} cm^{-3})	[CO] (× 10^{19} cm^{-3})	[Cl] (× 10^{13} cm^{-3})	T (K)	p (Torr)	[$HONO_2$]:[CO_2] Experiment	[$HONO_2$]:[CO_2] Kinetics Model
1	6	1.8	5.3 ± 1.3	300 ± 3	710 ± 14	0.13 ± 0.15	0.18 ± 0.07
2	5.7	0.33	5.2 ± 2.0	300 ± 3	701 ± 14	0.63 ± 0.41	0.64 ± 0.27
3	5.5	1.7	11 ± 3.5	300 ± 3	697 ± 14	0.18 ± 0.34	0.24 ± 0.10
4	5.2	0.51	10 ± 3	300 ± 3	710 ± 14	0.78 ± 0.18	0.65 ± 0.24
5	5.5	0.54	12 ± 3	300 ± 3	501 ± 10	0.92 ± 0.24	0.61 ± 0.23
6	5.4	0.53	12 ± 3	300 ± 3	302 ± 6	0.89 ± 0.21	0.65 ± 0.23
7	5.4	1.0	4.2 ± 1.7	300 ± 3	711 ± 14	0.13 ± 0.17	0.27 ± 0.10
8	10	1.8	4.2 ± 1.7	300 ± 3	717 ± 14	0.06 ± 0.35	0.21 ± 0.08
9	1.2	1.8	4.2 ± 1.7	300 ± 3	708 ± 14	0.07 ± 0.77	0.05 ± 0.02
10	5.9	1.8	3.0 ± 1.0	300 ± 3	712 ± 14	0.13 ± 0.08	0.15 ± 0.06
11	5.3	0.1	10.5 ± 3	300 ± 3	301 ± 6	1.68 ± 0.93	1.61 ± 0.61
12	5.3	0.26	10.5 ± 3	300 ± 3	299 ± 6	0.94 ± 0.47	0.93 ± 0.33
13	4.8	0.46	10.5 ± 3	300 ± 3	303 ± 6	0.91 ± 0.35	0.67 ± 0.23
14	9.5	0.49	10.5 ± 3	300 ± 3	304 ± 6	0.65 ± 0.31	0.77 ± 0.26
15	4.8	0.42	9.0 ± 2.3	300 ± 3	305 ± 6	0.56 ±1.45	0.64 ± 0.23
16	6.2	1.8	4.7 ± 2.8	278 ± 2	718 ± 14	0.23 ± 0.30	0.18 ± 0.07

Figure 12 shows a typical background (scans taken without the excimer firing); the only compounds seen were CH_3OH and H_2O. This shows that our experiment was not affected by a large background signal from $HONO_2$ and that all $HONO_2$ in our spectra was from photolysis chemistry only.

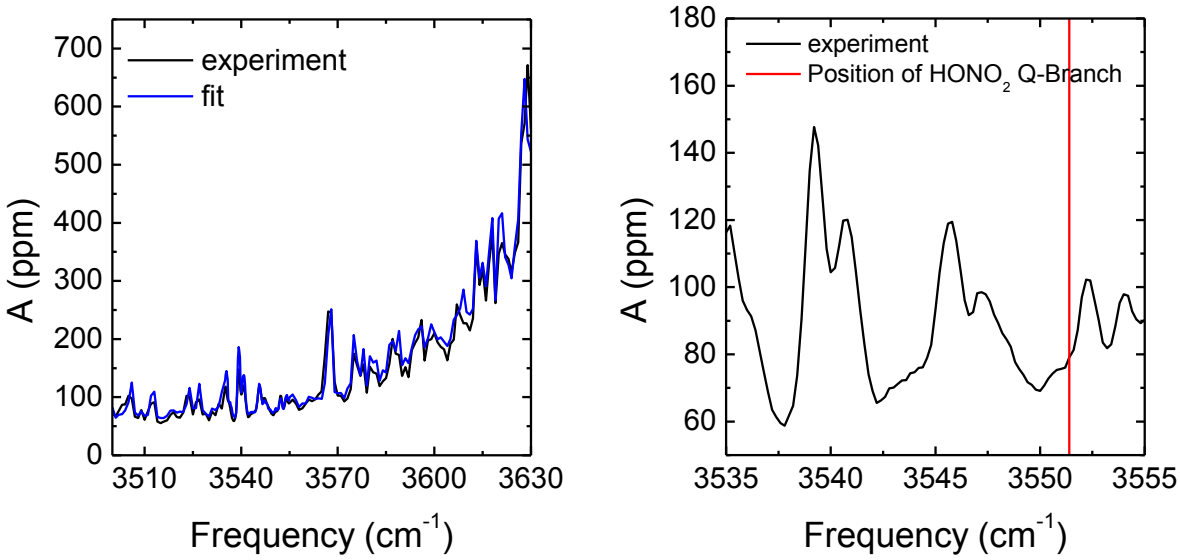

(a) (b)

Figure 12. Background (excimer off) from spectrum in Figure 15 (trial 10 on Table 3). (a) The background (black) compared to the best fit (blue) which includes only CH_3OH (from the bubbler, 5.5×10^{15} cm^{-3}) and H_2O (impurity, 2×10^{13} cm^{-3}). (b) The experimental spectrum (black) which shows no trace of the Q-branch of $HONO_2$, which absorbs at 3551.4 cm^{-1} (marked by the red line).

We ensured that our chemical amplification scheme (R1a and R6) worked properly by looking at the kinetics of HO_2 and CO_2 in our system. Figure 13 shows the effect of [CO] on the HO_2 lifetime in our cell. Solid lines represent the output of our kinetics model, and the points with error are the integration of an HO_2 peak from 3333 - 3341 cm^{-1}. In the absence of any CO, the OH radicals produced from R1a quickly reacted with the excess NO in the cell to form HONO. This happened in fewer than 100 μs with a 1/e HO_2 decay time of 32 μs (black curve in Figure 13). When 3×10^{18} cm^{-3} of CO was added to the cell, the HO_2 decay time increased to 350 μs (red curve in Figure 13). Finally, at 1.8×10^{19} cm^{-3} of CO, the HO_2 decay time increased to 740 μs (blue curve on Figure 13). We observed good agreement between the model and the measurements. Figure 14 shows the kinetics of CO_2 in our cell with 1.7×10^{19} cm^{-3} of CO.

Since the absolute experimental [CO_2] contains uncertainty from the initial radical concentration and the pathlength, the experimental data and output from the kinetics model were scaled to so that [CO_2] = 1 at 2.5 ms to highlight the kinetics. Based on our experimental measurements of [HO_2]$_0$ and the amount of CO_2, there were 23 ± 7 chemical amplification cycles; this value is within error the number predicted by the kinetics model: 27 ± 3 cycles.

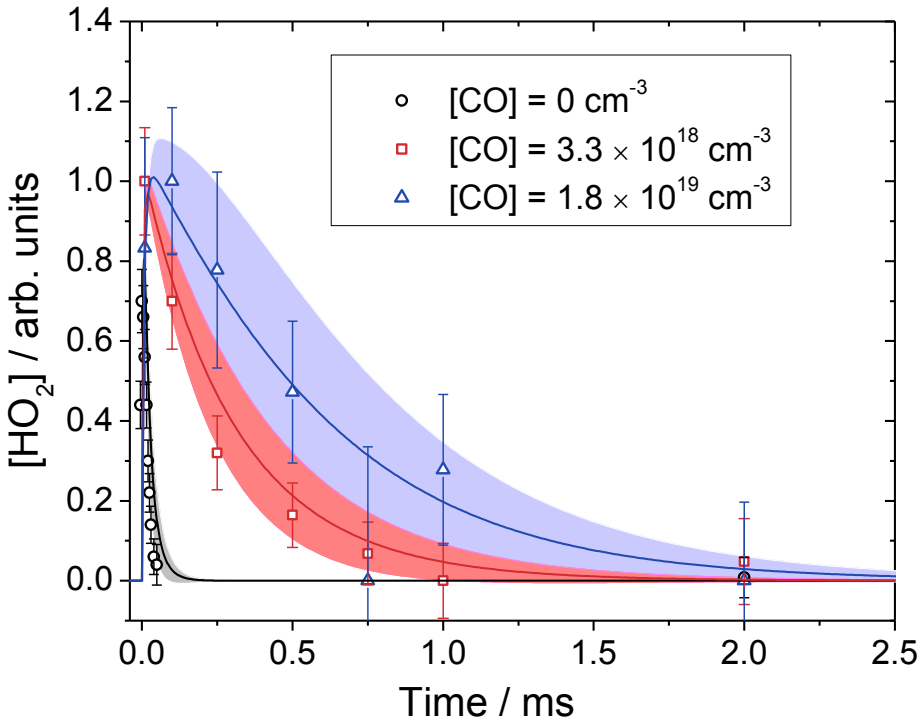

Figure 13. HO_2 decay curves at three different [CO]: 0 cm^{-3} (black), 3.3 × 10^{18} cm^{-3} (red), and 1.8 × 10^{19} cm^{-3} (blue) at (700 ± 14) Torr and (300 ± 3) K. Gas concentrations were: (5 ± 2) × 10^{13} cm^{-3} of Cl = [HO_2]$_0$, 6 × 10^{15} cm^{-3} of NO, 3 × 10^{18} cm^{-3} of O_2, 5 × 10^{15} cm^{-3} of Cl_2, and 6 × 10^{15} cm^{-3} of CH_3OH. Each point was found by integrating an experimental spectrum from 3333-3341 cm^{-1} (0.5 cm^{-1} step size), and error bars are 2σ. Red and blue lines are the expected HO_2 decays based on the kinetics model with errors shown as the red and blue shaded regions.

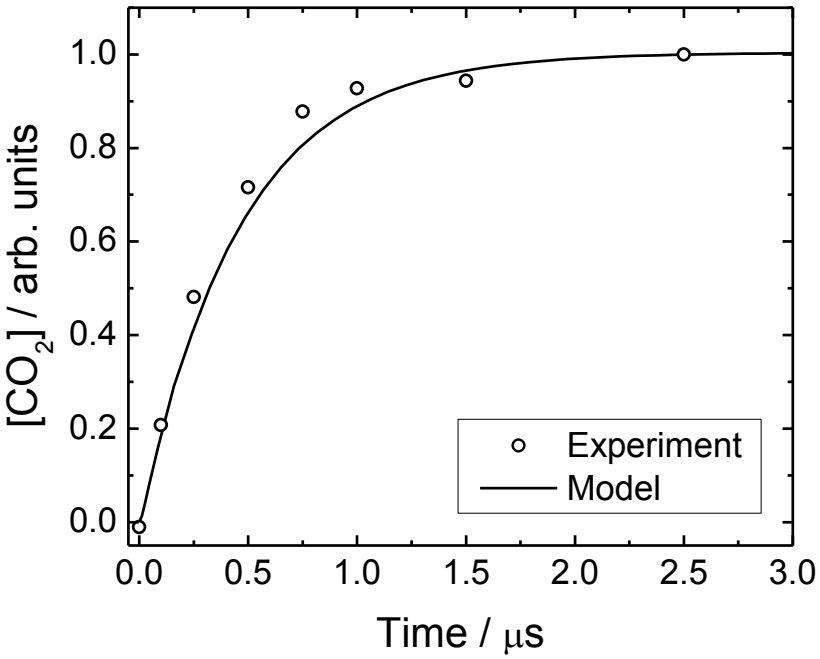

Figure 14. $[CO_2]$ vs. time taken with the same conditions as trial 1 on Table 1. Both the experimental and kinetics model were scaled so that $[CO_2]$ at 2.5 ms = 1. Each point (open circles) was found by fitting the experimental CO_2 spectrum (3550-3650 cm^{-1} with a 1 cm^{-1} step size and 16 shots averaged per point) and error bars represent the uncertainty in the fit to 2σ. The solid line with blue uncertainty is the CO_2 time trace from the kinetics model assuming (3 ± 3)% of NO was initially converted to NO_2 via R11. Based on the $[CO_2]$ produced from our chemical amplifier, there are 23 ± 7 cycles; this is within error of the number of cycles from the kinetics model: 27 ± 3 cycles (2σ).

The amounts of $HONO_2$ and HOONO produced each chemical amplification cycle were found by fitting the spectra to quantify $HONO_2$, HOONO, CO_2, HONO, HO_2NO_2, and ClNO and then calculating the $[HONO_2]$:$[CO_2]$ and [HOONO]:$[CO_2]$ ratios. Upper limits on $[HONO_2]$ and [HOONO] were determined by calculating the amount of $HONO_2$ or HOONO that would lead to an absorbance equal to two times the standard deviation of the baseline. To account for the spectral overlap in experiments, only the Q-branch of $HONO_2$ was used in determining the

[$HONO_2$]. Although HONO, ClNO, and HO_2NO_2 all absorb in the same region as $HONO_2$, none have a sharp absorption near the $HONO_2$ Q-branch at 3551 cm^{-1}.

The error in the $HONO_2$ yield measurements comes from two main sources: (1) background noise in the spectrum and (2) systematic errors in quantifying [CO_2] due to multiexponential ring-downs. Since we only used five points on the Q-branch to quantify the [$HONO_2$], the spectral noise near the Q-branch of $HONO_2$ was the largest source of error in our experiment, and made up 80% of the error in our values of [$HONO_2$]:[CO_2]. The other 20% of the error was from error in the CO_2 cross section; the error in the $HONO_2$ cross section from PNNL[48] accounted for less than 1% of the reported errors. Since CO_2 has a very intense absorbance, the spectral noise underneath the spectrum of CO_2 made up less than 1% of the reported error as well.

Based on the amount of HO_2NO_2 produced during a typical experiment, we believe that there was a small impurity of NO_2 at time = 0, likely from NO reacting with O_2 (R11) when the gases were mixed before entering the cell.

$$2NO + O_2 \rightarrow 2NO_2 \text{ (R11)}$$

From the observed [HO_2NO_2] we estimated (3 ± 3)% conversion of NO to NO_2, which was incorporated into the kinetics model. Similarly, based on the residence time of the gases in the tubing before they enter the photolysis cell (~14 s) and the rate of R11 (3.95×10^{-38} cm^{-6} s^{-1})[49], ~2% of NO should be converted to NO_2. The kinetics model included this small NO_2 impurity; the $[NO_2]_0$ was varied based on (3 ± 3)% of the $[NO]_0$ so that the corrected initial NO used for each model run was $[NO]_{corr} = [NO]_0 - [NO_2]_0$. Since extra NO_2 would increase measured [$HONO_2$]:[CO_2], a small NO_2 impurity would not lead to underestimation of our upper limits.

Upper Limits of $HONO_2$ from HO_2 + NO at Room Temperature

We place an upper limit on the amount of $HONO_2$ from the reaction of HO_2 with NO of 0.21%. Figure 15 shows the spectrum of the observed products 2.5 ms after photolysis taken at (712 ± 14) Torr and (300 ± 3) K, and the concentrations from our fit in Figure 15 are compared to those predicted by the kinetics model in Table 4.

The spectrum in Figure 15 was taken at our lowest radical concentration ($(3 \pm 1) \times 10^{15}$ cm^{-3} Cl) and with a bath gas of CO (1.8×10^{19} cm^{-3}). The main product observed was CO_2, produced from the chemical amplification (R1a + R6), which gave a direct measure of the HO_2 recycling in our cell: (27.0 ± 9.5) cycles. Other products included 1.1×10^{13} cm^{-3} of HO_2NO_2 (Q-branch at 3540 cm^{-1}), 1.3×10^{13} cm^{-3} of HONO (Q-branch at 3590 cm^{-1}, which is mostly overshadowed by the large CO_2 absorption), and 6×10^{12} cm^{-3} of ClNO (3545 - 3565 cm^{-1}). Our best fit, included ~1×10^{12} cm^{-3} of $HONO_2$, leading to a $[HONO_2]$:$[CO_2]$ of (0.13 ± 0.08)%. This yielded an experimentally determined upper limit of 0.21% for R1b. Our kinetics model predicted an impurity of $HONO_2$ from the reaction of OH with NO_2 (R2a) of (0.15 ± 0.06) %, which suggests that all of the $HONO_2$ observed can be explained exclusively by OH + NO_2 (R2a). If the modelled $[HONO_2]$:$[CO_2]$ is subtracted from the experimental yield, the amount of $HONO_2$ produced from R1b becomes (0.0 ± 0.1) %.

Table 4. Best fit concentrations (cm^{-3}) to the experimental spectrum in Figure 15 Reaction (trial 10) compared to those expected based on the kinetics model (with and without R1b).

	Experimental (Trial 10)	Kinetics model (yield R1b = 0)	Kinetics model (yield R1b = 0.5%)
$HONO_2$	1.0×10^{12}	1.3×10^{12}	5.7×10^{12}
HONO	1.2×10^{13}	9.5×10^{12}	8.5×10^{12}
HO_2NO_2	1.1×10^{13}	1.3×10^{13}	1.1×10^{13}
ClNO	6×10^{12}	1.2×10^{12}	1.2×10^{12}
CO_2	8.0×10^{14}	1.0×10^{15}	9.3×10^{14}
$HONO_2$: CO_2	(0.13 ± 0.08)%	0.12%	0.61%

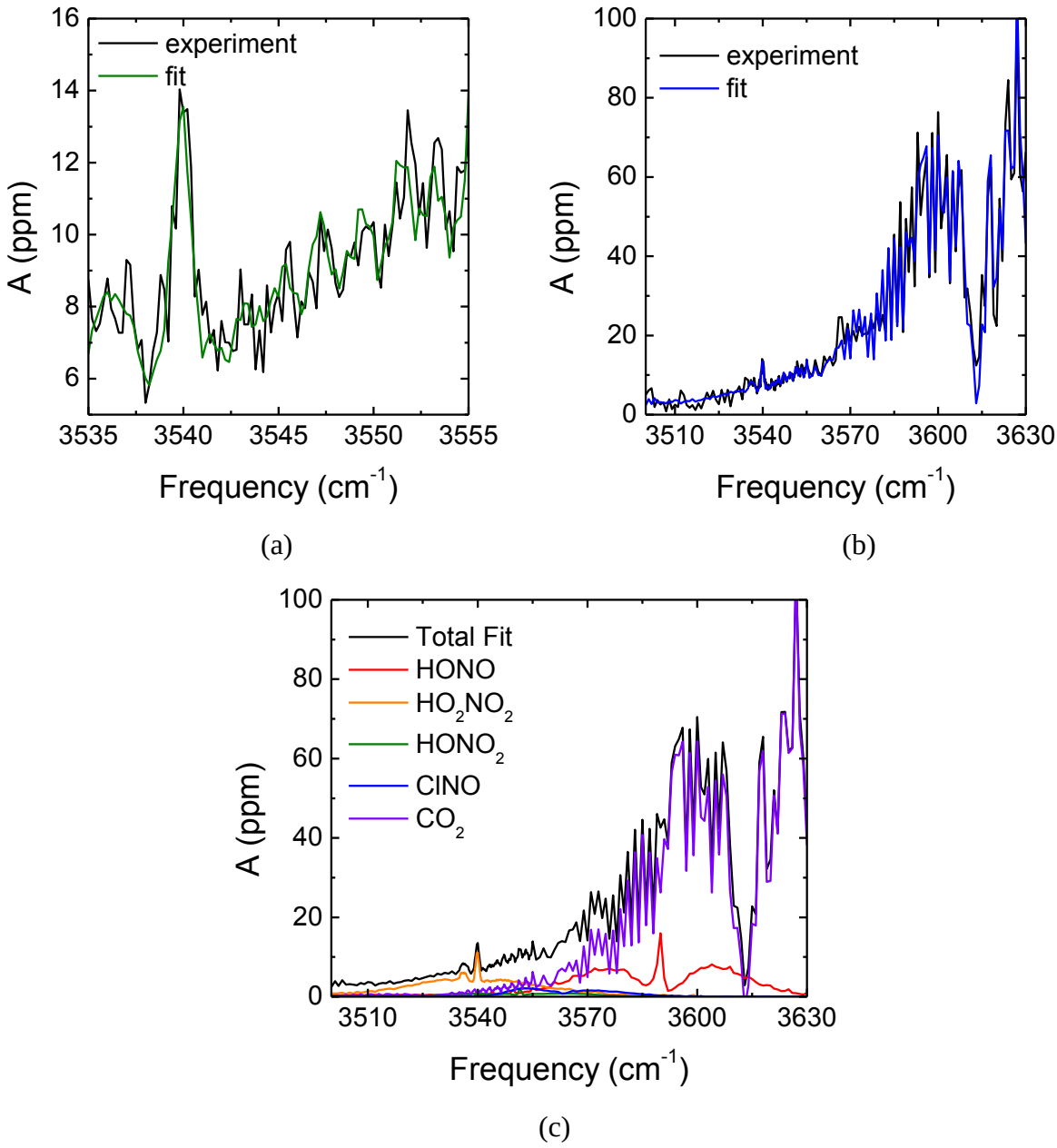

Figure 15. Spectrum from trial 10 on Table 1 which shows the products of the HO_2 + NO chemistry with HO_2 recycling at (710 ± 14) Torr and (300 ± 3) K. Spectrum was taken 2.5 ms after photolysis (a) from 3535 – 3555 cm^{-1} with a step size of 0.2 cm^{-1} and 496 shots averaged per point and (b) from 3500 - 3630 cm^{-1} with a 1 cm^{-1} step size and 128 shots averaged per point. For (a) and (b), the experimental spectrum is black and the best fit is green (a) or blue (b). Panel (c) shows the fit spectrum split into its individual components.

We observed $HONO_2$ whenever we changed the conditions to favor OH + NO_2 chemistry – increasing initial [HO_2] and decreasing [CO]. For example, Figure 16 was taken with a [Cl] of 1 × 10^{14} and a [CO] of 5 × 10^{18} cm^{-3}. In this figure, the Q-branch of $HONO_2$ is almost as prominent as the Q-branch of HO_2NO_2. As shown in Table 3, the amount of $HONO_2$ decreases with increasing [CO], which suggests OH chemistry (R2a) as the source of any observed $HONO_2$; if $HONO_2$ was produced from HO_2 with NO, we would expect the [$HONO_2$] to increase with [CO] due to increased chemical amplification. Additionally, Table 3 shows that all of the experimental [$HONO_2$]:[CO_2] ratios are within error of those predicted by this kinetics model without channel R1b. In our system, any $HONO_2$ detected can be explained entirely by R2a.

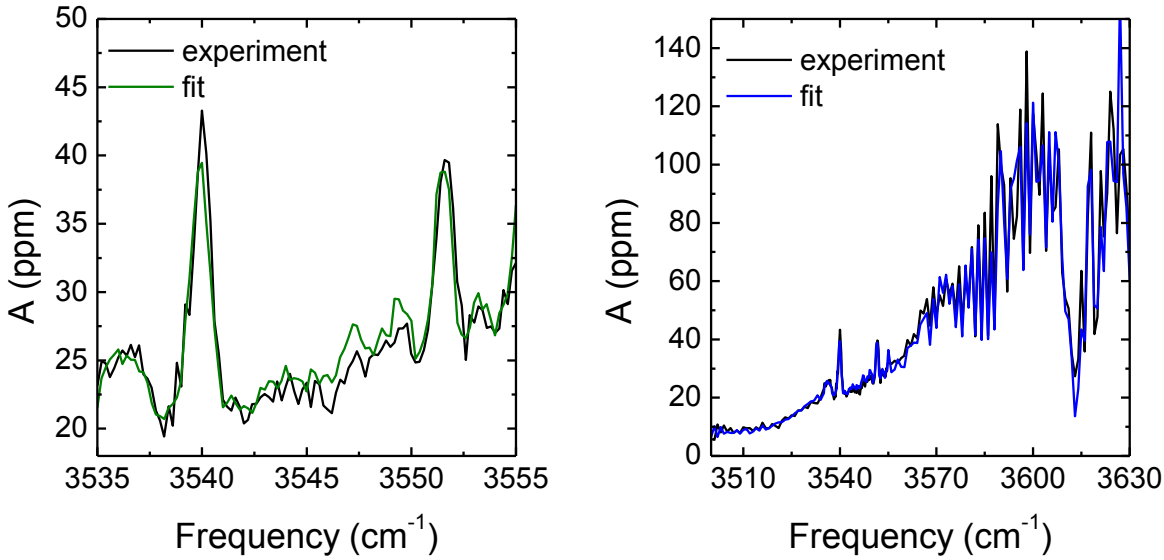

Figure 16. Spectrum from trial 4 on Table 3 which shows the products of the HO_2 + NO chemistry with low [CO] at (710 ± 14) Torr and (300 ± 3) K. Spectrum was taken 2.5 ms after photolysis (a) from 3535 – 3555 cm^{-1} with a step size of 0.2 cm^{-1} and 48 shots averaged per point and (b) from 3500 - 3630 cm^{-1} with a 1 cm^{-1} step size and 32 shots averaged per point. The experimental spectrum is black and the best fit is green (a) or blue (b).

Upper Limits of HOONO from HO_2 + NO at Room Temperature

We found no evidence of HOONO produced from the reaction of HO_2 with NO and place an upper limit on its yield of 0.1% at 700 Torr and 300 K. Figure 17 shows the spectrum in the region where *cis-cis* HOONO absorbs 2.5 ms after photolysis at (697 ± 14) Torr and (300 ± 3) K. As shown in Figure 17, no HOONO absorbance was found, yielding an upper limit of HOONO (the red spectrum in Figure 17) of 0.1%. Since the yield of HOONO from OH + NO_2 (R2b) is about 10 times lower than the yield of $HONO_2$ from OH + NO_2 (R2a),[44] we observed no measurable HOONO from R2a.

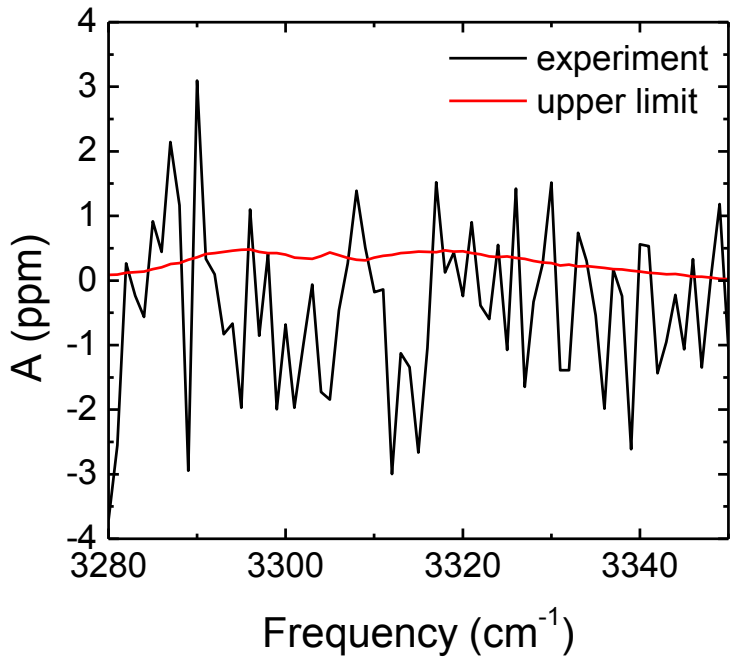

Figure 17. Upper limit of HOONO from R1c at (679 ± 14) Torr and (300 ± 3) K. Gas concentrations were the same as trial 3 on Table 3. The spectrum was taken 2.5 ms after photolysis from 3280 - 3380 cm^{-1} with a 1 cm^{-1} step size and 128 shots averaged per point. The black is the experimental spectrum; red is the [HOONO] that is 2σ above the noise (1.6×10^{12} cm^{-3}, or 0.1% branching ratio of R1c).

Upper Limits of $HONO_2$ from HO_2 + NO at 278 K

Since Butkovskaya *et al.* reported that the yield of R1b increases at lower temperatures,[1] we repeated the experiment at 278 K, as shown in Figure 18. The experimental upper limit of $HONO_2$ from R1b of 0.53% at (278 ± 2) K and (718 ± 14) Torr. We measured a $HONO_2$ concentration, (1.6 ± 2.1) × 10^{12} cm^{-3}, within error of 0 cm^{-3}. The [$HONO_2$]:[CO_2] was (0.23 ± 0.30)%, within error of the yield of $HONO_2$ from R2a predicted by the kinetics model (0.18 ± 0.07)%. Subtracting the predicted amount of $HONO_2$ from OH + NO_2, from the experiment ratio leads to a corrected yield of R1b of (0.05 ± 0.31) % and a corrected upper limit of 0.36%.

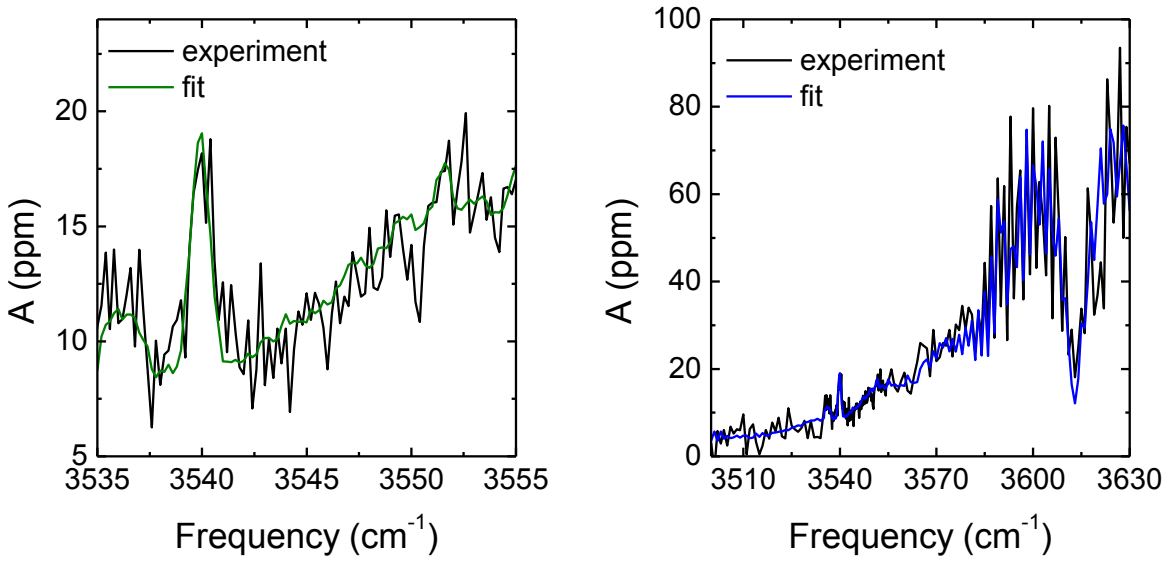

(a) (b)

Figure 18. Spectrum from trial 16 on Table 3 which shows the products of the HO_2 + NO chemistry at (718 ± 14) Torr and (278 ± 2) K. Spectrum was taken 2.5 ms after photolysis (a) from 3535 – 3555 cm^{-1} with a step size of 0.2 cm^{-1} and 624 shots averaged per point and (b) from 3500 - 3630 cm^{-1} with a 1 cm^{-1} step size and 128 shots averaged per point. The experimental spectrum is black and the best fit is green (a) or blue (b).

Summary of Results

Table 5 summarizes our upper limits of R1b and R1c. We found no evidence of either $HONO_2$ or HOONO from the reaction of HO_2 with NO in our experiments. We put an upper limit on the $HONO_2$ yield from reaction R1b of 0.2%, assuming all observed $HONO_2$ was from R1b, and a corrected upper limit of 0.1%, assuming a small amount of OH side chemistry (R2a) as predicted by the kinetics model. Decreasing the temperature to 278 K did not lead to a detectable amount of $HONO_2$ from R1b. We put an upper limit on the amount of HOONO from HO_2 + NO of 0.1%. We predict that the branching ratio of R1a will be $\geq$0.997 at room temperature and 700 Torr.

Table 5. Summary of Upper Limits of $HONO_2$ and HOONO from HO_2 + NO

	Experimental Yield of R1b	Experimental Upper limit of R1b	Corrected yield of R1b	Predicted value of R1b (Butkovskaya *et al.*)
$HONO_2$ (300 K)	(0.13 ± 0.08)%	0.21%	(0.00 ± 0.10)%	(0.50 ± 0.20)%
$HONO_2$ (278 K)	(0.23 ± 0.30)%	0.53%	(0.05 ± 0.31)%	(0.63 ± 0.20)%
HOONO	(0.00 ± 0.10)%	0.1%	n/a	n/a

Discussion

An advantage of mid-IR CRDS is its ability to quantify a number of products from the chemistry in our cell by their absorptions between 3200 – 3750 cm^{-1}. Firstly, by looking at the [CO_2] we had a direct measurement of chemical amplification in our system. Secondly, we were sensitive to both HNO_3 isomers: HOONO and $HONO_2$, which allowed quantification of upper limits for all possible radical terminating channels of HO_2 + NO. The ν_1 OH stretches of these two isomers are approximately 250 cm^{-1} apart, making them easily distinguishable. Finally, we could detect many other species, including HO_2NO_2 and HO_2, to ensure that our chemical amplification scheme worked as expected.

Another advantage of our method was the insensitivity of our experiment to heterogeneous chemistry on the walls of the flow cell. With pulsed laser photolysis, compounds created by radical reactions on the walls of the flow cell did not have enough time to diffuse into the center before the gas phase products were measured only 2.5 ms after the excimer fired. Furthermore, $HONO_2$ was not observed in the background spectra (excimer off, Figure 12), ensuring that any detected $HONO_2$ was not an artifact from a large background signal.

CRDS is less sensitive than CIMS in detecting $HONO_2$, which means that we needed to use much higher radical concentrations than Butkovskaya *et al.* Our $[HO_2]_0$ was $(3 \pm 1) \times 10^{13}$ cm^{-3}, while their typical $[HO_2]$ were two orders of magnitude lower: $(2 - 5) \times 10^{11}$ cm^{-3}.[1-3] An increase in radical concentration would likely only lead to more $HONO_2$ from R2a. Yet, due to high radical concentration, our experiment was susceptible to unexpected, and possibly unknown, side-chemistry which could have interfered with our results. We are additionally susceptible to unknown side-chemistry, because unlike Butkovskaya *et al.*,[1-3] we report results with only one HO_2 production scheme: photolysis of Cl_2 in the presence of CH_3OH. Yet, to our knowledge, there are no radicals in our cell that would readily react with $HONO_2$, except OH. Given the rate constants of OH reaction with $HONO_2$ (1.5×10^{-13} cm^3 s^{-1} at 700 Torr and 300 K),[44] only 0.005% of $HONO_2$ will be destroyed through reaction with OH.

We performed many checks to ensure unknown chemistry is not affecting our experiments. The kinetics models predicts that 96% of the Cl radicals will react with CH_3OH, with the remaining 4% of Cl radicals reacting with NO and NO_2 (to form ClNO and ClONO). Only 0.4% of the Cl_2 will react with radicals, the majority of which reacts with H radicals (an intermediate in R6) to reform Cl with an HCl coproduct. Once produced, 99.7% of HO_2 will react with either NO or NO_2, and 99.7% of OH will react with either CO or NO. While this

doesn't exclude the possibility of secondary reactions, it does suggest that, if present, such chemistry is not listed or wrong in the JPL[38] and IUPAC[49] data evaluations. As shown in Figure 13 and Figure 14, the kinetics of the main reactants and products agrees with our kinetics model, so any unknown side chemistry would have to lead to HO_2 lifetimes and CO_2 production kinetics almost identical to that of the expected chemical amplification scheme. Except for larger than expected [ClNO], the end products agree very well with what is predicted by the kinetics model (Table 4). It is unlikely if our experiments were plagued by obstructing side chemistry, that this chemistry wouldn't either produce products detectable in the mid-IR spectra or prevent formation of the expected products. In summary we believe that obstructing side chemistry is unlikely because it would have to (1) be unlisted in the JPL and IUPAC data evaluations, (2) lead to CO_2 production rates almost exactly the same as the expected chemical amplification scheme (3) lead to HO_2 lifetimes almost exactly the same as the expected chemical amplification scheme and (4) produce almost exactly the same products as the expected chemical amplification scheme, including HO_2NO_2 and large amounts of CO_2.

Another consequence of our high $[HO_2]_0$ was that we had to use extremely high [CO] (1.8×10^{19} cm^{-3}). Our kinetics model and data analysis assumed that replacing CO for N_2 would not affect the reaction rates. We checked that CO wasn't affecting the chemical kinetics by measuring the HO_2 self-reaction with and without CO (Figure 5), and the calculated $[HO_2]_0$ and $k_{HO2 + HO2}$ were within the uncertainty of the fit based on the noise of the spectrometer, suggesting that the collision efficiency of CO is close to that of N_2. As shown in Table 3, we performed different experiments with different [CO], and found no unexpected $[HONO_2]$ between scans with high [CO] and low [CO].

Our upper limits for $HONO_2$ from R1b are lower than the values given by Butkovskaya *et al.*[1-3] At room temperature and 700 Torr, they predict a (0.50 ± 0.2)% yield of $HONO_2$ from R1b,[1] which is more than twice our upper limit (0.21% experimental upper limit and 0.1% corrected upper limit). Figure 19 shows a fit that assumes a yield of $HONO_2$ expected based on the work by Butkovskaya *et al.* and demonstrates that our data are inconsistent with their measured yield of R1b. At 700 Torr and 278 K, they predicted (0.63 ± 0.20)% $HONO_2$ from R1b,[1] which is within error of experimental upper limit, (0.23 ± 0.30)%, not within error of the corrected upper limit, (0.05 ± 0.31)%. Our measured $HONO_2$, even with possible side chemistry from R2a, is only a third of what was predicted by Butkovskaya *et al.*[1]

Unlike our system, the turbulent flow cell that Butkovskaya *et al*. used was sensitive to heterogeneous chemistry, which could be the cause of their higher $HONO_2$ yields. Butkovskaya *et al*. describe the thorough process to ensure that the measured $HONO_2$ was not from wall reactions, including measuring diffusion rates of their flow cell and checking for heterogeneous chemistry during initial mixing of reagent gases and during the microwave discharge.[1-3] They also note that their yield of R1b shows a positive linear pressure dependence, which is uncharacteristic of heterogeneous chemistry, suggesting that gas phase chemistry is responsible for at least part of their measured $HONO_2$.[2,3] They do mention that there was a non-zero intercept of the pressure dependence of the branching ratio of R1b, which is characteristic of heterogonous chemistry.[2] Despite their extensive checks to rule out heterogeneous chemistry, the experimental technique that they use is inherently susceptible to chemistry on the walls of the flow tube, unlike our pulsed laser photolysis experiments.

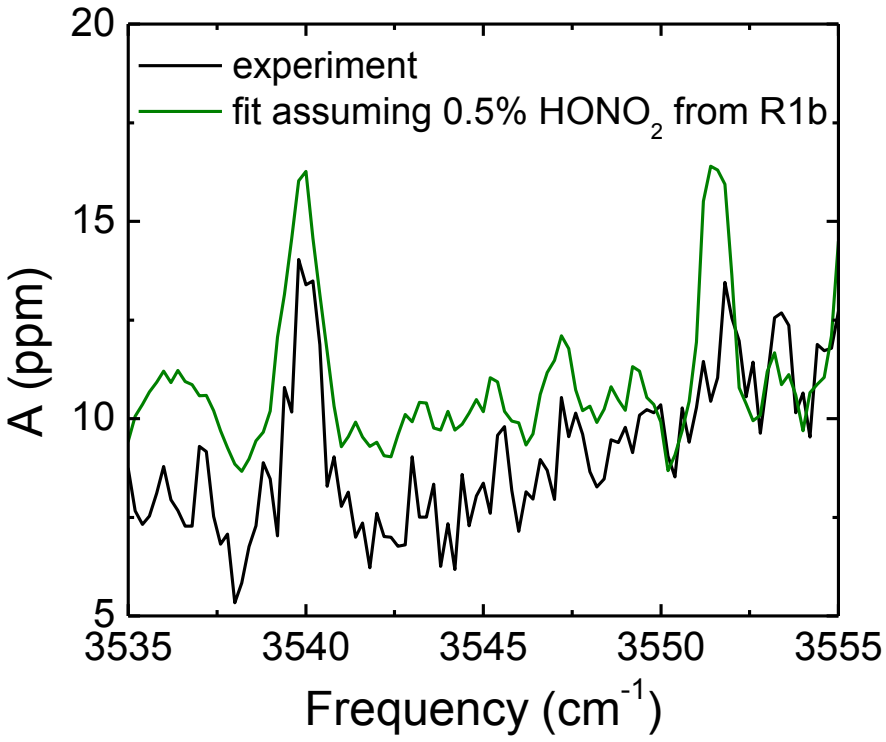

Figure 19. Experimental spectra shown in Figure 15 (black, trial 10 in Table 3) compared to a fit (green) that assumes a branching ratio of R1b given by Butkovskaya et al. (0.50%).

Since we have limited temperature, pressure and [H_2O] dependence, our data does not suggest that the reaction of HO_2 + NO never produces any $HONO_2$. Butkovskaya *et al*. saw this branching ratio increased at low temperatures, high pressures, and with added water vapor. Thus, increasing pressure and decreasing pressure will, theoretically, lead to $HONO_2$ formation, although it is unclear what pressures and temperatures are necessary. To reduce H_2O absorbance in the background of our spectra we performed all experiments under dry conditions (0.003% relative humidity or ~2×10^{13} cm^{-3} of H_2O), conditions inapplicable to Earth's atmosphere. For these reasons, the $HONO_2$ of the reaction of HO_2 with NO_2 needs to be confirmed at higher water concentrations, lower temperatures, and higher pressures.

Conclusions

We used mid-IR CRDS to measure $HONO_2$ and HOONO yields from the reaction of HO_2 with NO using CO to scavenge OH radicals and reform HO_2 to increase the signal. There was no evidence of either $HONO_2$ or HOONO from the reaction of HO_2 with NO.

Table ***5*** shows our upper limits for the branching ratio of R1b and R1c. The absolute upper limit of the $HONO_2$ branching ratio at room temperature and 700 Torr is 0.2%, and 0.1% considering the amount of $HONO_2$ predicted from R2a. These upper limits disagree with the previous work of Butkovskaya *et al.*[1-3] Since our experiments were performed in dry conditions (0.003% relative humidity) and only to temperatures down to 278 K, these results do not exclude the possibility of $HONO_2$ produced from R1b at lower temperatures or in the presence of water vapor, and future work is needed to verify Butkovskaya's work under these conditions.

References

(1) Butkovskaya, N.; Kukui, A.; Le Bras, G. *The Journal of Physical Chemistry A* **2007**, *111*, 9047.

(2) Butkovskaya, N.; Rayez, M.-T.; Rayez, J.-C.; Kukui, A.; Le Bras, G. *The Journal of Physical Chemistry A* **2009**, *113*, 11327.

(3) Butkovskaya, N. I.; Kukui, A.; Pouvesle, N.; Le Bras, G. *The Journal of Physical Chemistry A* **2005**, *109*, 6509.

(4) Seinfeld, J. H.; Pandis, S. N. *Atmospheric Chemistry and Physics: From Air Pollution to Climate Change*; John Wiley & Sons, Inc.: Hoboken, NJ, 2006.

(5) Cox, R. A.; Derwent, R. G. *Journal of Photochemistry* **1975**, *4*, 139.

(6) Howard, C. J.; Evenson, K. M. *Geophysical Research Letters* **1977**, *4*, 437.

(7) Cariolle, D.; Evans, M. J.; Chipperfield, M. P.; Butkovskaya, N.; Kukui, A.; Le Bras, G. *Atmos. Chem. Phys.* **2008**, *8*, 4061.

(8) Koppenol, W. H.; Moreno, J. J.; Pryor, W. A.; Ischiropoulos, H.; Beckman, J. S. *Chemical Research in Toxicology* **1992**, *5*, 834.

(9) Howard, C. J. *The Journal of Chemical Physics* **1979**, *71*, 2352.

(10) Bohn, B.; Zetzsch, C. *The Journal of Physical Chemistry A* **1997**, *101*, 1488.

(11) Leu, M. T. *The Journal of Chemical Physics* **1979**, *70*, 1662.

(12) Seeley, J. V.; Meads, R. F.; Elrod, M. J.; Molina, M. J. *The Journal of Physical Chemistry* **1996**, *100*, 4026.

(13) Bardwell, M. W.; Bacak, A.; Teresa Raventos, M.; Percival, C. J.; Sanchez-Reyna, G.; Shallcross, D. E. *Physical Chemistry Chemical Physics* **2003**, *5*, 2381.

(14) Orlando, J. J.; Tyndall, G. S. *Chemical Society Reviews* **2012**, *41*, 6294.

(15) Lohr, L. L.; Barker, J. R.; Shroll, R. M. *The Journal of Physical Chemistry A* **2003**, *107*, 7429.

(16) Zhang, J.; Dransfield, T.; Donahue, N. M. *The Journal of Physical Chemistry A* **2004**, *108*, 9082.

(17) Dibble, T. S. *Atmospheric Environment* **2008**, *42*, 5837.

(18) Vereecken, L.; Francisco, J. S. *Chemical Society Reviews* **2012**, *41*, 6259.

(19) Cameron, D. R.; Borrajo, A. M. P.; Thatcher, G. R. J.; Bennett, B. M. *Canadian Journal of Chemistry* **1995**, *73*, 1627.

(20) Houk, K. N.; Condroski, K. R.; Pryor, W. A. *Journal of the American Chemical Society* **1996**, *118*, 13002.

(21) Sumathi, R.; Peyerimhoff, S. D. *The Journal of Chemical Physics* **1997**, *107*, 1872.

(22) Dixon, D. A.; Feller, D.; Zhan, C.-G.; Francisco, J. S. *The Journal of Physical Chemistry A* **2002**, *106*, 3191.

(23) Zhu, R. S.; Lin, M. C. *The Journal of Chemical Physics* **2003**, *119*, 10667.

(24) Barker, J. R.; Lohr, L. L.; Shroll, R. M.; Reading, S. *The Journal of Physical Chemistry A* **2003**, *107*, 7434.

(25) Zhao, Y.; Houk, K. N.; Olson, L. P. *The Journal of Physical Chemistry A* **2004**, *108*, 5864.

(26) Zhang, J.; Donahue, N. M. *The Journal of Physical Chemistry A* **2006**, *110*, 6898.

(27) Contreras, R.; Galván, M.; Oliva, M.; Safont, V. S.; Andrés, J.; Guerra, D.; Aizman, A. *Chemical Physics Letters* **2008**, *457*, 216.

(28) Golden, D. M.; Barker, J. R.; Lohr, L. L. *The Journal of Physical Chemistry A* **2003**, *107*, 11057.

(29) Fry, J. L.; Nizkorodov, S. A.; Okumura, M.; Roehl, C. M.; Francisco, J. S.; Wennberg, P. O. *The Journal of Chemical Physics* **2004**, *121*, 1432.

(30) Chen, C.; Shepler, B. C.; Braams, B. J.; Bowman, J. M. *Physical Chemistry Chemical Physics* **2009**, *11*, 4722.

(31) *CRC Handbook of Chemistry and Physics*; 88 ed.; Linde, D. R., Ed.; CRC Press: Boca Raton, Fl, 2007.

(32) Hippler, H.; Nasterlack, S.; Striebel, F. *Physical Chemistry Chemical Physics* **2002**, *4*, 2959.

(33) Matthews, J.; Sinha, A. *The Journal of Chemical Physics* **2005**, *122*, 104313.

(34) Konen, I. M.; Pollack, I. B.; Li, E. X. J.; Lester, M. I.; Varner, M. E.; Stanton, J. F. *The Journal of Chemical Physics* **2005**, *122*, 094320.

(35) Brühl, C.; Steil, B.; Stiller, G.; Funke, B.; Jöckel, P. *Atmos. Chem. Phys.* **2007**, *7*, 5585.

(36) Gottschaldt, K.; Voigt, C.; Jöckel, P.; Righi, M.; Deckert, R.; Dietmüller, S. *Atmos. Chem. Phys.* **2013**, *13*, 3003.

(37) Stavrakou, T.; Müller, J. F.; Boersma, K. F.; van der A, R. J.; Kurokawa, J.; Ohara, T.; Zhang, Q. *Atmospheric Chemistry and Physics* **2013**, *13*, 9057.

(38) Søvde, O. A.; Hoyle, C. R.; Myhre, G.; Isaksen, I. S. A. *Atmos. Chem. Phys.* **2011**, *11*, 8929.

(39) Boxe, C. S.; Hamer, P. D.; Ford, W.; Hoffmann, M.; Shallcross, D. E. *Antarctic science* **2012**, *24*, 417.

(40) Righi, M.; Eyring, V.; Gottschaldt, K. D.; Klinger, C.; Frank, F.; Jöckel, P.; Cionni, I. *Geosci. Model Dev.* **2015**, *8*, 733.

(41) Lin, J. T.; Liu, Z.; Zhang, Q.; Liu, H.; Mao, J.; Zhuang, G. *Atmos. Chem. Phys.* **2012**, *12*, 12255.

(42) Sander, S. P., J. Abbatt, J. R. Barker, J. B. Burkholder, R. R. Friedl, D. M. Golden, R. E. Huie, C. E. Kolb, M. J. Kurylo, G. K. Moortgat, V. L. Orkin and P. H. Wine "Chemical Kinetics and Photochemical Data for Use in Atmospheric Studies, Evaluation No. 17," JPL Publication 10-6, Jet Propulsion Laboratory, Pasadena, 2011 http://jpldataeval.jpl.nasa.gov.

(43) J. B. Burkholder, S. P. Sander, J. Abbatt, J. R. Barker, R. E. Huie, C. E. Kolb, M. J. Kurylo, V. L. Orkin, D. M. Wilmouth, and P. H. Wine "Chemical Kinetics and Photochemical

Data for Use in Atmospheric Studies, Evaluation No. 18," JPL Publication 15-10, Jet Propulsion Laboratory, Pasadena, 2015 http://jpldataeval.jpl.nasa.gov.

(44) Mollner, A. K.; Valluvadasan, S.; Feng, L.; Sprague, M. K.; Okumura, M.; Milligan, D. B.; Bloss, W. J.; Sander, S. P.; Martien, P. T.; Harley, R. A.; McCoy, A. B.; Carter, W. P. *Science* **2010**, *330*, 646.

(45) Sprague, M. K.; Garland, E. R.; Mollner, A. K.; Bloss, C.; Bean, B. D.; Weichman, M. L.; Mertens, L. A.; Okumura, M.; Sander, S. P. *The Journal of Physical Chemistry A* **2012**, *116*, 6327.

(46) Sprague, M. K.; Mertens, L. A.; Widgren, H. N.; Okumura, M.; Sander, S. P.; McCoy, A. B. *The Journal of Physical Chemistry A* **2013**, *117*, 10006.

(47) Reid, S. A.; Tang, Y. *Applied Optics* **1996**, *35*, 1473.

(48) Sharpe, S. W.; Johnson, T. J.; Sams, R. L.; Chu, P. M.; Rhoderick, G. C.; Johnson, P. A. *Appl. Spectrosc.* **2004**, *58*, 1452.

(49) Atkinson, R.; Baulch, D. L.; Cox, R. A.; Crowley, J. N.; Hampson, R. F.; Hynes, R. G.; Jenkin, M. E.; Rossi, M. J.; Troe, J. *Atmos. Chem. Phys.* **2004**, *4*, 1461.

(50) Ianni, James C. , "A Comparison of the Bader-Deuflhard and the Cash-Karp Runge-Kutta Integrators for the GRI-MECH 3.0 Model Based on the Chemical Kinetics Code Kintecus", pg.1368-1372, Computational Fluid and Solid Mechanics 2003, K.J. Bathe editor, Elsevier Science Ltd., Oxford, UK., 2003.

(51) Christensen, L. E.; Okumura, M.; Hansen, J. C.; Sander, S. P.; Francisco, J. S. *The Journal of Physical Chemistry A* **2006**, *110*, 6948.

(52) Nizkorodov, S. A.; Wennberg, P. O. *The Journal of Physical Chemistry A* **2002**, *106*, 855.

(53) McCoy, A. B.; Fry, J. L.; Francisco, J. S.; Mollner, A. K.; Okumura, M. *J Chem Phys* **2005**, *122*, 104311.

(54) McCoy, A. B.; Sprague, M. K.; Okumura, M. *The Journal of Physical Chemistry A* **2010**, *114*, 1324.

(55) Bean, B. D.; Mollner, A. K.; Nizkorodov, S. A.; Nair, G.; Okumura, M.; Sander, S. P.; Peterson, K. A.; Francisco, J. S. *The Journal of Physical Chemistry A* **2003**, *107*, 6974.

(56) Yalin, A. P.; Zare, R. N. *Laser Physics* **2002**, *12*, 1065.

(57) Hodges, J. T.; Looney, J. P.; van Zee, R. D. *Applied Optics* **1996**, *35*, 4112.

(58) MATLAB and Statistics Toolbox Release 2012b, The MathWorks, Inc., Natick, Massachusetts, United States.

(59) L.S. Rothman, I.E. Gordon, Y. Babikov, A. Barbe, D. Chris Benner, P.F. Bernath, M. Birk, L. Bizzocchi, V. Boudon, L.R. Brown, A. Campargue, K. Chance, E.A. Cohen, L.H. Coudert, V.M. Devi, B.J. Drouin, A. Fayt, J.-M. Flaud, R.R. Gamache, J.J. Harrison, J.-M. Hartmann, C. Hill, J.T. Hodges, D. Jacquemart, A. Jolly, J. Lamouroux, R.J. Le Roy, G. Li, D.A. Long, O.M. Lyulin, C.J. Mackie, S.T. Massie, S. Mikhailenko, H.S.P. Müller, O.V. Naumenko, A.V. Nikitin, J. Orphal, V. Perevalov, A. Perrin, E.R. Polovtseva, C. Richard, M.A.H. Smith, E. Starikova, K. Sung, S. Tashkun, J. Tennyson, G.C. Toon, Vl.G. Tyuterev, G. Wagner, The HITRAN2012 Molecular Spectroscopic Database // JQSRT 130, 4-50 (2013)

(60) Veyret, B.; Lesclaux, R.; Rayez, M. T.; Rayez, J. C.; Cox, R. A.; Moortgat, G. K. *The Journal of Physical Chemistry* **1989**, *93*, 2368.

Appendix A – Reactions and Rate Constants in HO_2 + NO Kinetics Model

Table 6. List of all Reactions in kinetics models.

Reaction	Rate coefficient	Source
HO_x reactions		
$OH + HO_2 \rightarrow H_2O + O_2$	$4.8 \times 10^{-11} \times \exp(250/T)$	JPL[38]
$OH + OH \rightarrow H_2O + O$	1.8×10^{-12}	JPL[38]
$OH + OH (+M) \rightarrow H_2O_2$	$k_0^{300} = 6.9 \times 10^{-31}$ m = 1, $k_\infty^{300} = 2.6 \times 10^{-11}$ n = 0	JPL[38]
$HO_2 + HO_2 \rightarrow H_2O_2 + O_2$	$3 \times 10^{-13} \times \exp(460/T)$	JPL[38]
$HO_2 + HO_2 (+ M) \rightarrow H_2O_2 + O_2$	$2.1 \times 10^{-33} \times [M] \times \exp(920/T)$	JPL[38]
$H + O_2 (+ M) \rightarrow HO_2$	$k_0^{300} = 4.4 \times 10^{-32}$ m = 1.3, $k_\infty^{300} = 7.5 \times 10^{-11}$ n = -0.2	JPL[38]
$OH + H_2O_2 \rightarrow H_2O + HO_2$	1.8×10^{-12}	JPL[38]
NO_x reactions		
$HO_2 + NO \rightarrow NO_2 + OH$	$3.3 \times 10^{-12} \times \exp(270/T)$	JPL[38]
$HO_2 + NO \rightarrow HONO_2$ $HO_2 + NO \rightarrow HOONO$	varied	Butkovskaya *et al*.
$OH + NO (+ M) \rightarrow HONO$	$k_0^{300} = 7 \times 10^{-31}$ m = 2.6, $k_\infty^{300} = 3.6 \times 10^{-11}$ n = 0.1	JPL[38]
$OH + NO_2 (+ M) \rightarrow HONO_2$	$k_0^{300} = 1.8 \times 10^{-30}$ m = 3, $k_\infty^{300} = 2.8 \times 10^{-11}$ n = -1	JPL[38]
$OH + NO_2 (+ M) \rightleftharpoons HOONO$	$k_0^{300} = 1.8 \times 10^{-30}$ m = 3, $k_\infty^{300} = 2.8 \times 10^{-11}$ n = -1, $K_{eq} = 3.5 \times 10^{-27} \times \exp(10135/T)$	JPL[38]
$HO_2 + NO_2 (+ M) \rightleftharpoons HO_2NO_2$	$k_0^{300} = 2.0 \times 10^{-31}$ m = 3.4, $k_\infty^{300} = 2.9 \times 10^{-21}$ n = 1.1, $K_{eq} = 2.1 \times 10^{-27} \times \exp(10900/T)$	JPL[38]
$OH + HONO \rightarrow NO_2 + H_2O$	$1.8 \times 10^{-11} \times \exp(-390/T)$	JPL[38]
$OH + HONO_2 (+ M) \rightarrow NO_3 + H_2O$	$k_1 + k_2 \times [M] / (1 + k_2 \times [M] / k_3)$ $k_1 = 2.4 \times 10^{-14} \times \exp(460/T)$ $k_2 = 6.5 \times 10^{-34} \times \exp(1335/T)$ $k_3 = 2.7 \times 10^{-17} \times \exp(2199/T)$	JPL[38]
$H + NO_2 \rightarrow OH + NO$	$4 \times 10^{-10} \times \exp(-340/T)$	JPL[38]
$NO_2 + NO_2 (+ M) \rightarrow N2O4$	$k_0 = 1.4 \times 10^{-33} (T/300)^{-3.8} \times [M]$ $k_\infty = 1.0 \times 10^{-12}$ $F_c = 0.6$	IUPAC[49]
$N_2O_4 \rightarrow NO_2 + NO_2$	1.13×10^{5}	IUPAC[49]
$OH + HO_2NO_2 \rightarrow NO_2 + H_2O + O_2$	$4 \times 10^{-12} \times \exp(-380/T)$	JPL[38]
CO Reactions		
$OH + CO (+ M) \rightarrow H + CO_2$	$k_0^{300} = 1.5 \times 10^{-13}$ m = -0.6, $k_\infty^{300} = 2.1 \times 10^{9}$ n = -6.1	JPL[38]
$OH + CO (+ M) \rightarrow HOCO$	$k_0^{300} = 5.9 \times 10^{-33}$ m = 1.4, $k_\infty^{300} = 1.2 \times 10^{-12}$ n = -1.3	JPL[38]
$HOCO + O_2 \rightarrow HO_2 + CO_2$	2×10^{-12}	JPL[38]
Other Cl Chemistry		

$Cl + O_2$ (+ M) ⇌ ClOO	$k_0^{300} = 2.2 \times 10^{-33}$ m = 3.1, $k_\infty^{300} = 1.8 \times 10^{-10}$ n = 0, $K_{eq} = 6.6 \times 10^{-25} \times \exp(-2502/T)$	JPL[38]
$OH + Cl_2 \rightarrow HOCl + Cl$	$2.6 \times 10^{-12} \times \exp(-1100/T)$	JPL[38]
Cl + CO (+ M) ⇌ ClCO	$k_0^{300} = 1.3 \times 10^{-33}$ m = 3.8, $k_\infty^{300} = 1$ $K_{eq} = 3.5 \times 10^{-25} \times \exp(-3730/T)$	JPL[38]
$OH + HCl \rightarrow Cl + H_2O$	$1.8 \times 10^{-12} \times \exp(-250/T)$	JPL[38]
$HO_2 + Cl \rightarrow HCl + O_2$	$1.4 \times 10^{-11} \times \exp(270/T)$	JPL[38]
$HO_2 + Cl \rightarrow OH + ClO$	$3.6 \times 10^{-11} \times \exp(-375/T)$	JPL[38]
Methanol Chemistry		
$Cl + CH_3OH \rightarrow CH_2OH + HCl$	5.5×10^{-11}	JPL[38]
$CH_2OH + O_2 \rightarrow HCHO + HO_2$	9.1×10^{-12}	JPL[38]
$OH + CH_3OH \rightarrow CH_2OH + H_2O$	$2.465 \times 10^{-12} \times \exp(-345/T)$	JPL[38]
$OH + CH_3OH \rightarrow CH_3O + H_2O$	$4.35 \times 10^{-13} \times \exp(-345/T)$	JPL[38]
Formaldehyde Chemistry		
$Cl + HCHO \rightarrow HCl + HCO$	$8.1 \times 10^{-11} \times \exp(-30/T)$	JPL[38]
$HCO + O_2 \rightarrow CO + HO_2$	5.2×10^{-12}	JPL[38]
$HO_2 + HCHO \rightarrow HMP$	$6.7 \times 10^{-15} \times \exp(600/T)$	JPL[38]
$HMP \rightarrow HO_2 + HCHO$	$2 \times 10^{12} \times \exp(-7000/T)$	Veyret 1989[60]
$HMP + NO \rightarrow HMA$	5.6×10^{-12}	IUPAC[49]
$HMA + O_2 \rightarrow HCOOH + HO_2$	$2.4 \times 10^{-14} \times \exp(-325/T)$	IUPAC[49] rate for ethoxy + O_2
$ClO_x + NO_x$		
$Cl + NO_2$ (+ M) → ClONO	$k_0^{300} = 1.3 \times 10^{-30}$ m = 2, $k_\infty^{300} = 1 \times 10^{-10}$ n = 1	JPL[38]
$Cl + NO_2$ (+ M) → $ClNO_2$	$k_0^{300} = 1.8 \times 10^{-31}$ m = 2, $k_\infty^{300} = 1 \times 10^{-11}$ n = 1	JPL[38]
$Cl + NO \rightarrow NOCl$	$6.4 \times 10^{-12} \times (T/300)^{-1.8}$	JPL[38]
$ClO + NO \rightarrow Cl + NO_2$	$6.4 \times 10^{-12} \times \exp(290/T)$	JPL[38]
ClO + NO_2 (+ M) → $ClONO_2$	$k_0^{300} = 1.8 \times 10^{-31}$ m = 3.4, $k_\infty^{300} = 1.5 \times 10^{-11}$ n = 11	JPL[38]
$H + Cl_2 \rightarrow HCl + Cl$	$1.43 \times 10^{-10} \times \exp(-598/T)$	IUPAC[49]
$Cl + H_2O_2 \rightarrow HCl + HO_2$	$1.1 \times 10^{-11} \times \exp(-980/T)$	JPL[38]
O_x reactions		
$O + O_2$ (+M) → O_3	$6 \times 10^{-34} \times [M]$	JPL[38]
$O + O_3 \rightarrow 2O_2$	$8 \times 10^{-12} \times \exp(-2060/T)$	JPL[38]

Appendix B – Copy of Matlab Programs Used To Calculate HO_2 Concentration

pumpout.m

This program takes experimental data that follows the absorbance of a stable species with time (generally from 0 – 89 ms) to watch how quickly it gets "pumped out" in to the vacuum. The code will output the residence time of gases in the cell.

You need to input variable datap. The first column should be time in seconds. The second column should be absorbance.

```
function [fitresult_p, gof_p, k_pumpout, pumpout_error, restime]
= pumpout(datap)

%% Fit: 'residence time'.
%% datap is experimental data that watches how quickly a stable
product is removed from the cavity.
%% The first column should be time in seconds
%% The second colmn is absorbance

%  Output:
%      fitresult : a fit object representing the fit.
%      gof : structure with goodness-of fit info.
%    k_pumpout : the rate constant for gas removal from cell
(s^-1)
%    pumpout_error : 2 sigma error in k_pumpout
%    restime : value and 2 sigma error of residence time of cell
(in s)

xp=datap(:,1);
yp=datap(:,2);
[xData, yData] = prepareCurveData( xp, yp );

% Set up fittype and options.
ft = fittype( 'a*exp(b*x)+c', 'independent', 'x', 'dependent',
'y' );
opts = fitoptions( ft );
opts.Display = 'Off';
opts.Lower = [-Inf -Inf 0];
opts.StartPoint = [50 20 1];
opts.Upper = [Inf Inf Inf];

% Fit model to data.
[fitresult_p, gof_p] = fit( xData, yData, ft, opts );

% Create a figure for the plots.
figure( 'Name', 'residence time' );
```

```
% Plot fit with data.
subplot( 2, 1, 1 );
plot( fitresult_p, xData, yData );
% Label axes
xlabel( 'time (s)' );
ylabel( 'A' );
grid off
legend('hide')

% Plot residuals.
subplot( 2, 1, 2 );
plot( fitresult_p, xData, yData, 'residuals' );
% Label axes
xlabel( 'time (s)' );
ylabel( 'residual' );
grid off
legend('hide')

coeffs_p=coeffvalues(fitresult_p);
int_p=confint(fitresult_p);
k_pumpout=[-1*coeffs_p(2)];
pumpout_error=abs(coeffs_p(2)-int_p(2,2));
restime=[1/k_pumpout,pumpout_error/k_pumpout*(1/k_pumpout)];
```

HO2_conc5_alwaysfloatbaseline.m

This program takes the pumpout and the experimental data for the HO_2 self-reaction to calculate the HO_2 concentration in the cell, assuming second order kinetics and rate constants and errors from the JPL data evaluation.[38] It needs pumpout.m, since it accounts for pumpout of HO_2 in addition to HO_2 self-reaction.

I made another version of this program where I did not float the baseline, but you really should float the baseline.

```
function [fitresult, gof, HO2, fitresult_p, gof_p, k_pumpout,
pumpout_error, restime] = HO2_conc5_alwaysfloatbaseline(datap,
data_ho2, p, T)


%% Fit: 'untitled fit 1'.
%datap is experimental data that watches how quickly a stable
product is removed from the cavity.
%The first column should be time in seconds
% The second colmn is absorbance
% data_ho2 is experimental data of the HO2 self reaction.
```

```
% The first column should be time in seconds
% The second colmn is absorbance of HO2

%  Output:
%      fitresult : a fit object representing the fit.
%      gof : structure with goodness-of fit info.
%    HO2 is the HO2 concentration with 2 sigma error
%   fitresult_p, gof_o, kpumpout, pumpout_error, restime are the
outputs from pumpout.m

x=data_ho2(:,1);
y=data_ho2(:,2);

[fitresult_p,  gof_p,  k_pumpout,  pumpout_error,  restime]  =
pumpout(datap);

%scale according to pumpout
scale=exp(-x.*k_pumpout);
y2=y.*scale;
[xData, yData] = prepareCurveData( x, y2 );

% Set up fittype and options.
ft = fittype( @(a, b, c, x) a./(b*x+1)+c, 'independent', 'x',
'dependent', 'y' );
opts = fitoptions( ft );
opts.Algorithm = 'Levenberg-Marquardt';
opts.Display = 'Off';
opts.Lower = [-Inf -Inf -Inf];
opts.MaxFunEvals = 6000000;
opts.MaxIter = 4000000;
opts.StartPoint = [14 200 0];
opts.TolFun = 1e-10;
opts.TolX = 1e-10;
opts.Upper = [Inf Inf Inf];
% Fit model to data.
[fitresult, gof] = fit( xData, yData, ft, opts );

% Create a figure for the plots.
figure( 'Name', 'HO_2 kinetics' );

% Plot fit with data.
subplot( 2, 1, 1 );
plot( fitresult, xData, yData );
% Label axes
xlabel( 'time (s)' );
ylabel( 'A_H_O_2' );
grid off
```

```
legend('hide')

% Plot residuals.
subplot( 2, 1, 2 );
plot( fitresult, xData, yData, 'residuals' );
% Label axes
xlabel( 'time (s)' );
ylabel( 'residual' );
grid off
legend('hide')

% Calculate the [HO2] rate constants based on T and p
%T is in Kelvin, p is in torr
% from JPL 2011
M=p*2.5e19/760;
k1=3e-13*exp(460/T); %pressure independent
k2=M*2.1e-33*exp(920/T); %pressure dependent
k=k1+k2; %total rate constant
f1=1.15; %error at 298 K for the p independent reaction
f2=1.2; %error at 298 K for the p dependent reaction
g1=100; % temp dependence of f1
g2=200; % temperature dependence of f2
k_error=2*sqrt((k1*(f1*exp(abs(g1*(1/T-1/298)))-
1))^2+(k2*(f2*exp(abs(g2*(1/T-1/298)))-1))^2);

%Calculates HO2 concentration and error from the JPL rate
constant and
%fitting
% The variable "HO2" give HO2 concentration in the first column
and the
% error from both JPL and from the fitting in the second column
(2 std dev)
coeffs = coeffvalues(fitresult);
int=confint(fitresult);
HO2=[coeffs(2)/2/k,sqrt(((int(2,2)-
coeffs(2))/coeffs(2))^2+(k_error/k)^2+(pumpout_error/k_pumpout)^
2)*coeffs(2)/2/k];
```

Chapter 5: Branching Ratios of HOONO and $HONO_2$ from the Reaction of OH with NO_2 at 254 – 333 K and 50 – 700 Torr using Pulsed Laser Photolysis and Mid-IR Cavity Ring-down Spectroscopy

Abstract

The HO_x (HO_2 and OH) and NO_x (NO and NO_2) cycles play major roles in both ozone loss in the stratosphere and pollution from hydrocarbon oxidation in the troposphere. Any reactions between these two classes of radicals that create stable compounds, like the reaction of OH with NO_2 to form $HONO_2$, will greatly decrease radical concentrations throughout the atmosphere. The reaction of OH with NO_2 can also form a less stable isomer of $HONO_2$, HOONO. Since HOONO readily dissociates near room temperature to reform OH and NO_2, this reaction will reduce the ability of the reaction of OH and NO_2 to sequester HO_x and NO_x radicals. Consequently, the branching ratio between HOONO and $HONO_2$ is essential parameter to accurate atmospheric models. While previous measurements from our research group used pulsed-laser-photolysis (PLP) combined with mid-IR cavity ring-down spectroscopy (CRDS) of the products' ν_1 OH stretch quantified this branching ratio at ambient temperature,[1] no one has measured the yields' temperature dependence, an essential parameter to atmospheric models. This deficiency remains the largest uncertainty in current predictions of ozone concentration in urban environments (Fig 1).[2] With a temperature controlled to our flow cell added to the CRD spectrometer, we measured the branching between HOONO and $HONO_2$ from the reaction of OH with NO_2 at a range of atmospheric temperatures and pressures: 254 to 333 K and 50 to 700 Torr. By combining our results with results of collaborators in Stan Sander's group at JPL who used laser-induced fluorescence detection of OH to find the total rate of the reaction of OH with NO_2, we have fit our data to extract the rates of HOONO and $HONO_2$ formation.

Introduction

The reaction of OH with NO_2 (R1) is one of the most important radical terminating reactions in Earth's atmosphere, sequestering both HO_x (HO_2 and OH) and NO_x (NO_2 and NO) radicals into stable nitric acid ($HONO_2$). Since HO_x and NO_x radicals catalyze ozone depletion in the stratosphere and photochemical smog production in the troposphere, R1 impacts radical concentrations and atmospheric pollution globally.[3]

$$OH + NO_2 \rightarrow HONO_2 \text{ (R1a)}$$
$$OH + NO_2 \rightarrow HOONO \text{ (R1b)}$$

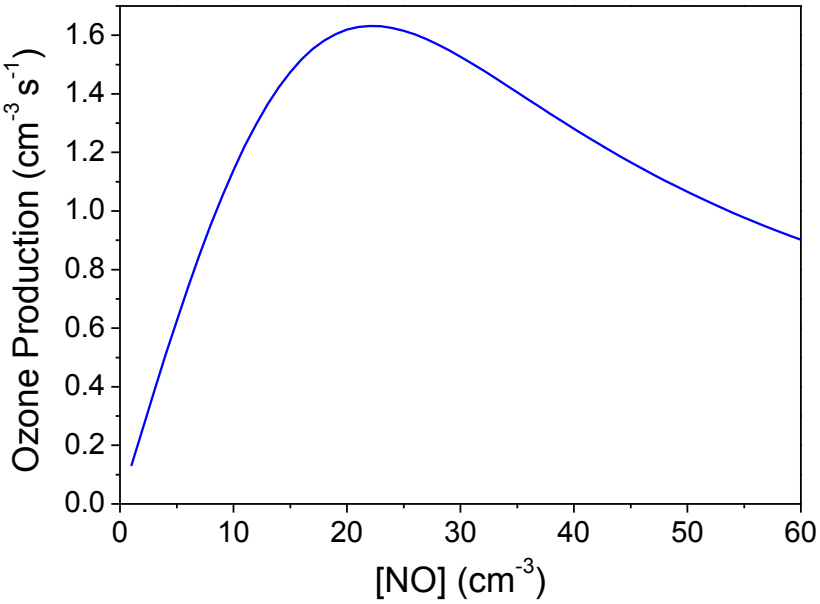

Figure 1. Effect of NO_x concentration on ozone production in the troposphere (p = 1 atm, T = 298 K, HO_x production = 1.5×10^7 cm^{-3} s^{-1}).

In Urban areas (high NO_x environments), this reaction will limit the amount of ozone formed by titrating out radicals from the atmosphere. Figure 1 shows that when NO_x concentration is low, increasing NO_x concentration will lead to higher ozone production, but when NO_x concentration is high, adding more NO_x will increase the rate of R1a, decreasing the ozone produced. Consequently, the rate of R1a is essential to accurately modeling pollution

chemistry, and errors of even ±10% in the rate or yield of $HONO_2$ formation (R1a) would have drastic impacts on atmospheric models (for example, Mollner *et al*. found that a ~10% decrease in this reaction leads to a 10% decrease in ozone over Los Angeles as shown in Figure 2),[1] and much previous work has explored the rate and product yields of this reaction.[1,4,5]

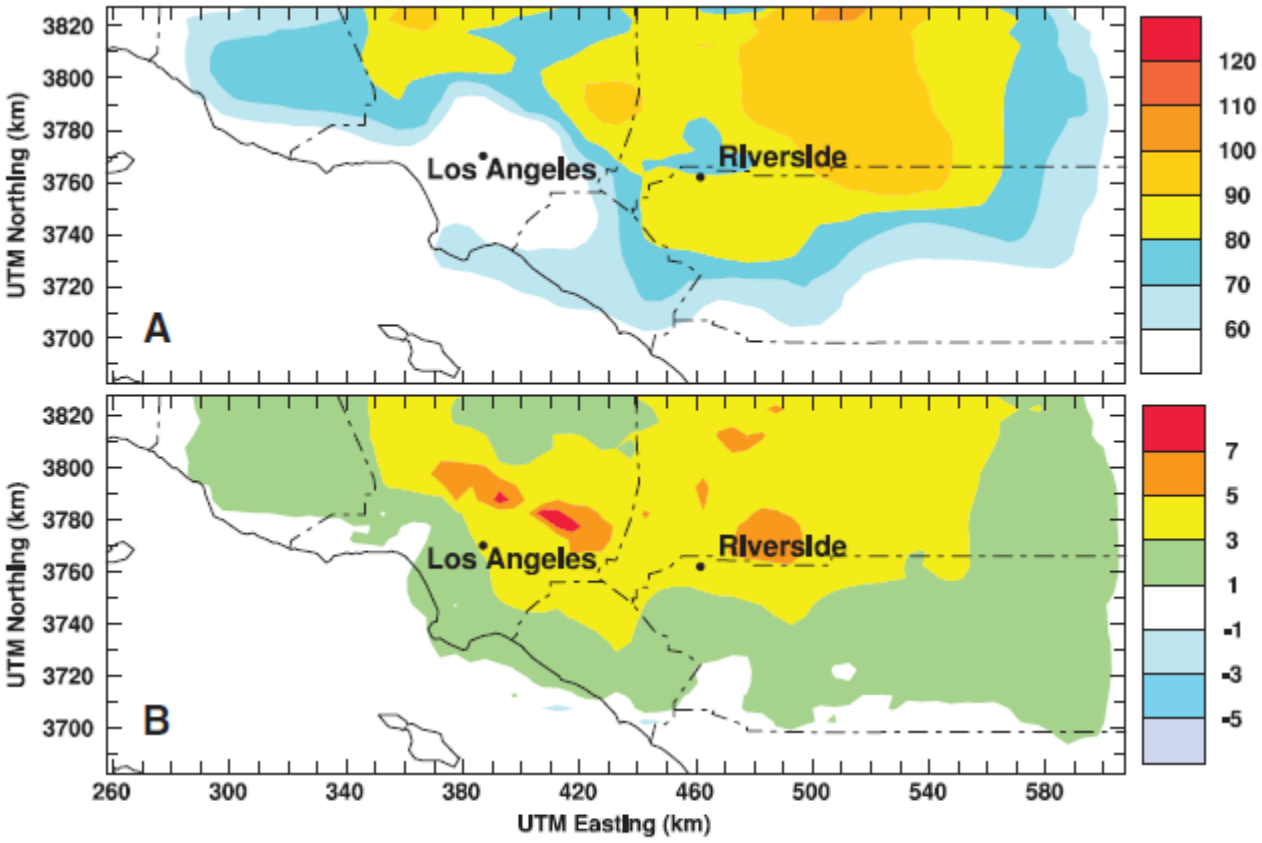

Figure 2. Figure from Mollner *et al*.[1] plotting (a) the concentration of ozone (ppb) (between 12 and 1 pm) over the Los Angeles Basin modeled using 2010 emission inventory estimates and rate constant for R1a, k_{HONO2}, from the 2006 JPL Data Evaluation[6] and (b) the change in the calculated ozone concentration (ppb) calculated when the rate of k_{HONO2} is decrease by 10%.

Atmospheric chemists have identified $HONO_2$ (R1a) as the main product of the reaction of OH + NO_2, and most early papers assumed $HONO_2$ and the only product.[7-17] Subsequent studies proposed formation of another product, HOONO, to explain unexpected fall-off

behavior.[4,5,18-20] The rate of OH + NO_2 does not reach its high pressure limit even at four atm of Ar or CF_4, likely due to increased formation of HOONO at higher pressures.[18] As shown in Figure 3, $HONO_2$ is much more stable than HOONO, so when HOONO* and $HONO_2$* are formed from the reaction of OH + NO_2, $HONO_2$* will have a larger binding energy and therefore a longer lifetime. Since HOONO* has a smaller lifetime, R1b will reach its higher pressure limit at much higher pressures than R1a.[21]

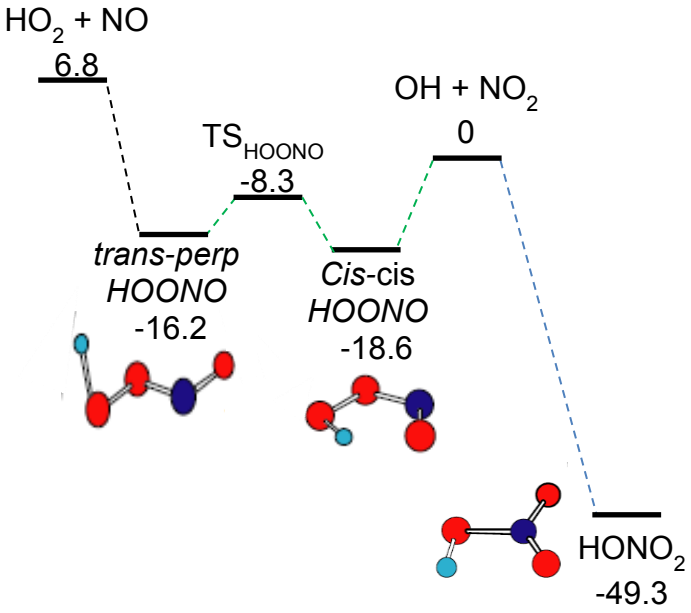

Figure 3. Potential energy surface of the $HONO_2$ and HOONO system, with energies in kcal/mol of $\Delta H_f°$[22-25] or E_a[26] in the case of the HOONO isomerization barrier.

Speculation remained about this minor pathway[17,20,27,28] until, HOONO, created from R1b, was detected in 2002 with vibrational photodissocation action spectroscopy.[29] In our laboratory, the exact branching ratio of HOONO was measured at room temperatures and 25 – 760 torr with Cavity Ring-down spectroscopy;[1,30] at room temperature this branching ratio HOONO ($\alpha = k_{1b}/k_{1a}$, k_{HOONO}/k_{HONO2}) was measured to be 0.035 ± 0.009 at 25 Torr and 0.142 ± 0.004 at 760 Torr (2σ errors)[1] and early experiments showed that the branching ratio increases at lower temperatures.[30]

Ab initio calculations and spectroscopy studies have found two main isomers of HOONO: *cis-cis* and *trans-perp* (Figure 3). *Cis-cis* HOONO is 19.8 kcal/mol more stable than OH and NO_2[23] and 3.6 kcal/mol more stable than *trans-perp* HOONO.[31] While both *trans-perp* and *cis-cis* HOONO are formed from OH and NO_2, *trans-perp* HOONO isomerizes readily to *cis-cis* HOONO with an energy barrier of (7.8 ± 2.8) kcal/mol.[26] Consequently, for the previous branching, our laboratory used the ν_1 OH stretch of *cis-cis* HOONO to measure HOONO concentration.[1,30]

While preliminary measurements on temperature dependence of the branching ratio were made at 20 Torr,[30] no one has measured the temperature dependence of this reaction at a broad range of temperatures and pressures. Since HOONO, especially at high temperatures, will dissociate to reform OH and NO_2, R1b essentially reduces the radical terminating power of the reaction of OH with NO_2. If its branching ratio changes with temperature, this will also change how effect OH + NO_2 is at removing ozone producing radicals from the atmosphere. The lack of temperature dependent branching ratios for R1b remains one of the largest uncertainties in current atmospheric models,[2] preventing accurate predictions of HO_x, NO_x, and ozone concentrations in areas that are not near 295 K.

We have directly measured the branching ratios of HOONO from the reaction of OH with NO_2 (R1b) at pressures between 50 and 700 Torr and temperatures between 254 and 333 K with mid-IR cavity ring-down spectroscopy. As described in Chapter 4, mid-IR CRDS can easily distinguish between HOONO and $HONO_2$ based on their ν_1 OH stretches at 3306 cm^{-1} and 3551 cm^{-1}, respectively. This work relies heavily on the previous work on OH + NO_2 → HOONO described by Bean *et al.*,[30] Mollner *et al.*[1] and Andrew Mollner in his Ph.D. Thesis.[21] This chapter will describe how I combined their previous method with my temperature controlled

flow cell to find the branching ratio of HOONO at a full range of atmospherically relevant temperatures and pressures.

Experimental

This experiment uses the same flow cell and laser set-up as described in Chapter 4. Again, tunable mid-IR light (3200 – 3750 cm^{-1}) is sent through our optical cavity to detect the ν_1 OH stretch of HOONO and $HONO_2$. These differences and specific techniques relevant to our OH + NO_2 experiments are described below. The main differences between the experiments in Chapter 4 on the reaction of HO_2 with NO, are from the different chemistry occurring in the flow cell and how the spectra were fit and analyzed.

Chemistry

Typical gas concentrations are provided in Table 1. OH radicals were produced from the photolysis of ozone at 248 nm (from the excimer with KrF) to make $O(^1D)$.

$$O_3 + h\nu = 248 \text{ nm} \rightarrow O(^1D) + O_2 \quad \text{(R2)}$$

As described by Andrew Mollner in his thesis,[21] ozone was created by flowing oxygen through with a simple UV-lamp ozonizer and in to a U-shaped tube filled with silica gel in a dry ice/acetone trap (-78.5 °C). At these temperatures, the ozone is adsorbed onto the silica gel, allowing storage for later use in experiments. To introduce the trapped O_3 into the ring-down flow cell, N_2 was passed through the U-shaped tube. This O_3-enriched N_2 passed through a 1 m flow cell in which the UV absorbance of the O_3 was measured at 307.6 nm ($\sigma = 1.4 \times 10^{19}$ cm^2) with a Zn lamp (Hamamatsu), Monochromater and PMT, and then into the ring-down cell after being pre-cooled and mixed with the other precursor gases. The U-shaped tube was kept at pressures greater than 850 Torr to limit O_3 de-adsorb from the silica gel and ensure a steady O_3 for up to 10 hours.

Table 1. Typical Concentrations of Precursor Gases.

Gas	Concentration cm^{-3}
O_3	$(5 – 10) \times 10^{15}$
NO_2	$(1 – 10) \times 10^{15}$
H_2	$(5 – 20) \times 10^{18}$

Once formed the $O(^1D)$ can either be quenched to the ground state $O(^3P)$ or react with added H_2 to make OH radicals.

$$O(^1D) + H_2 \rightarrow OH + H \text{ (R3)}$$

An excess of NO_2 is added so that the vast majority of the OH will react with NO_2 to make either $HONO_2$ (R1a) or HOONO (R1b).

$$OH + NO_2 \rightarrow HONO_2 \text{ (R1a)}$$
$$OH + NO_2 \rightarrow HOONO \text{ (R1b)}$$

H atoms are a coproduct of OH produced from R3. If there was oxygen in the cell, H could readily react with O_2 to form HO_2. To prevent HO_2 formation, we did not add any O_2 into the cell. Yet, leaks in the flow cell or impurities from the other gases might lead to chemical interference from O_2 and HO_2. If there was significant HO_2, it would likely react with NO_2 to form HO_2NO_2. We have never spectroscopically observed any HO_2NO_2 (Q-branch at 3540 cm^{-1}) during these experiments, so our results are not likely complicated by significant HO_2 formation.

From the kinetics model (Appendices A and B in Chapter 4, 300 K, 700 Torr, 2.5×10^{15} cm^{-3} NO_2, 1×10^{16} cm^{-3} O_3, 2×10^{14} cm^{-3} $O(^1D)$, 1×10^{18} cm^{-3} H_2), we predict that 48% of the H atoms will react with O_3 to create another OH molecule.

$$H + O_3 \rightarrow OH + O_2 \text{ (R4)}$$

The remaining 52% of H atoms will react with NO_2, again creating an addition molecule of OH.

$$H + NO_2 \rightarrow OH + NO \text{ (R5)}$$

NO from this reaction can combine with the OH in the cell to form HONO. We did see at least 1 × 10^{13} cm^{-1} of HONO in the background of most spectra, but to limit the amount of HONO, NO_2 was kept at fairly high concentrations (1-10 × 10^{15} cm^{-3}, Table 1). HONO does not interfere with the chemistry, and can be accounted for in the spectra, since its spectrum is known.

Especially at higher pressures, the majority of the $O(^1D)$ will be quenched to $O(^3P)$. For this reason, more H_2 was generally added at higher pressures. At 700 Torr and 1 × 10^{18} cm^{-3} H_2, the kinetics model predicts that only 14 % of $O(^1D)$ will react with H_2 (compared to 69% at 50 Torr), while the rest gets quenched to $O(^3P)$ through collisions with the bath N_2. With 2.5 × 10^{15} cm^{-3} of NO_2, one of the lower NO_2 concentrations used, the majority of $O(^3P)$, 96% will react with NO_2 to form NO_3. Most of the NO_3 (>approximately 60%) will react with NO to form two molecules of NO_2, the rest reaching an equilibrium of N_2O_5 with NO_2 (R6).

$$NO_3 + NO \rightarrow 2NO_2 \quad (R5)$$
$$NO_3 + NO_2 \leftrightarrow N_2O_5 \quad (R6)$$

Before the precursor gases enter the cell NO_2 can react with O_3 to Form NO_3.

$$NO_2 + O_3 \rightarrow NO_3 + O_2 \quad (R7)$$

NO_3 will then react with the walls for form $HONO_2$. This reaction results in a significant background absorption of $HONO_2$. While there are some $HONO_2$ impurities from the NO_2 cylinder, the $HONO_2$ background created from R7 is the larger contributor to background $HONO_2$. Mollner *et al.*[1,21] observed a much smaller $HONO_2$ background because they mixed the gases a few centimeters before the flow cell. Since we have to flow our gases through a pre-cooling block, the gases are mixed about 20 cm before the cell, leading to a significant $HONO_2$ background. This background can be reduced by increasing the flow rate and reducing O_3 and NO_2 as much as possible. For this reason, we keep NO_2 lower than Andrew Mollner, who typically had NO_2 concentrations above 1 × 10^{16} cm^{-3}. In later experiments, especially those at

50 and 60 °C, this background was still present but greatly reduced by coating the walls with halocarbon wax.

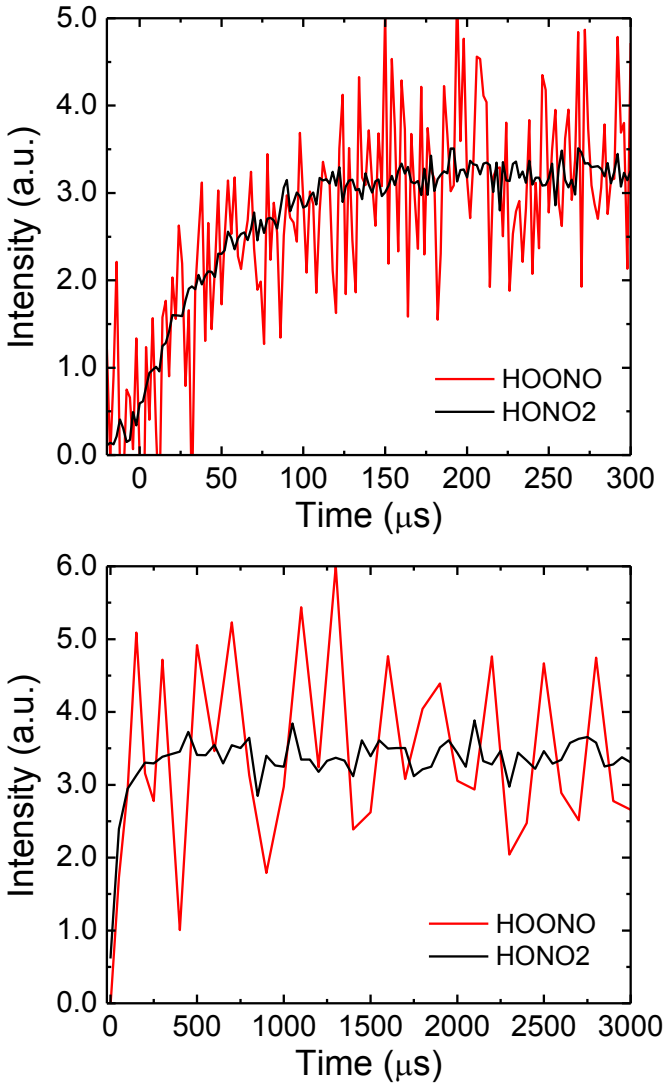

Figure 4. Intensity of the absorbance of HOONO at 3306 cm^{-1} (red) and $HONO_2$ at 3520 cm^{-1} (black) at 60 °C with time during a typical experiment up to 300 μs (top panel) and up to 3 ms (bottom panel).

At the NO_2 concentrations used in the experiment, chemistry was generally complete within a few hundred microseconds. As shown in Figure 4, which follows the formation of both HOONO and $HONO_2$ in our cell, HOONO and $HONO_2$ form at exactly the same rate – what we

would expect from coproducts of the same reaction. After HOONO and $HONO_2$, their concentrations remain essentially constant in our cell up to several milliseconds, even at the highest temperature, 60 °C, where we would expect HOONO to most readily thermally decompose. During experiments, we measured the products at 500 μs after photolysis, well after all chemistry has finished but before there is any decay or removal from pumpout of the products.

"Hot" OH

The reaction of $O(^1D)$ with H_2 to make OH, produces vibrational excited OH. Experiments with time-resolved Fourier transform spectroscopy measured that the initial product distributions, (Pv' = 1:2:3:4) = 0.29:0.32:0.25:0.13, meaning that approximately 99% of the OH starts out in v=1 or higher.[32] While the rate constant for vibrational relaxation of OH with many of the gases in the cell, notably NO_2 ($(2.54\pm0.11) \times 10^{-11}$ $cm^3 s^{-1}$ for vibrational relaxation of v=1, leading to a OH* lifetime of 4 μs, much smaller than the timescales of our reaction which are larger than 100 μs),[33] the vibrational relaxation with the main bath gases, H_2 and N_2 is very low, $\leq 10^{-14}$ for v=2.[34] Andrew Mollner performed multiple experimental tests to ensure that hot OH doesn't affect our results: (1) He added SF_6, a strong quencher that would reduce the lifetime of hot OH, to the flow cell and observed no increase in the HOONO branching ratio, what would be expected if there was significant hot OH without SF_6 and (2) He used CH_4 instead of H_2 to produce OH. Even though $CH_4 + O(^1D)$ is expected to produce less vibrationally excited OH than R2, Mollner, again, observed no significant increase in the HOONO branching ratio with CH_4.[21] Thus, our laboratory has demonstrated with multiple experiments that hot OH is not interfering with our results.

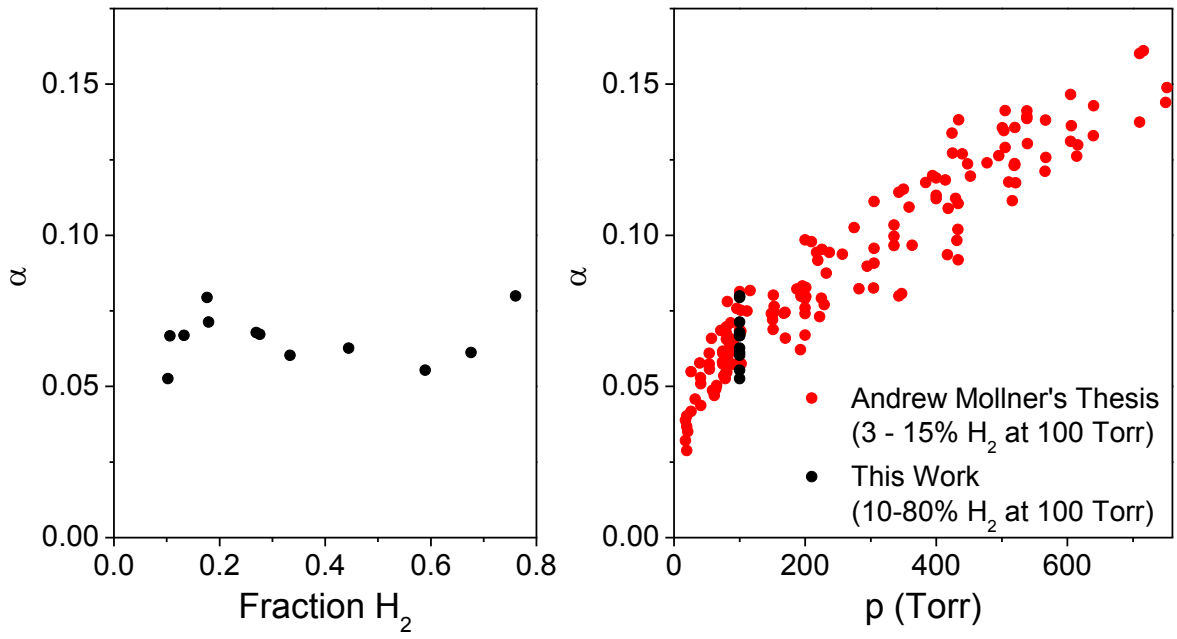

Figure 5. (a) Effect of H_2 background gas on the branching ratio of HOONO. All points taken at 4×10^{15} [NO_2], $3 - 10 \times 10^{15}$ [O_3], 100 Torr, 20 °C and 10 – 80% H_2 (90 – 20% N_2). (b) points from (a) compared to previous results by Andrew Mollner.[21]

Effect of H_2 on the Branching Ratio

Since reaction of $O(^3D)$ with H_2 competes with quenching from the bath gas, we need high concentration of H_2, often over 10^{18} cm^{-3} to create enough OH radicals. At 50 Torr, we routinely use H_2 concentrations that are over 50% of the total pressure in the cell (the rest being N_2 bath gas), but at higher pressures, H_2 is typically 10% or less of the total gases. If the collisional properties of H_2 are significantly different than that of N_2, then our results might not be directly applicable to the atmosphere. We measured the effect of percentage of H_2 in the bath gas on the branching ratio of HOONO from R1b. Figure 5a shows that the branching ratio of HOONO at 100 Torr and 20 °C remains essentially unchanged within typical errors as the percent of H_2 in the cell is changed from mostly N_2 to mostly H_2. Figure 5b plots the data in Figure 5a against the full data set from Andrew Mollner's thesis,[21] and shows that all points,

regardless of H_2 concentration, match the previous data very well. This suggests that our branching ratios are equivalent to branching ratios found in a bath gas of 100% N_2, since the added H_2 does not significantly change the measured values.

Spectroscopy and Spectral Fitting

Figure 6 shows a typical experimental spectra 500 μs after photolysis of O_3 in the presence of H_2 and NO_2. The largest peak at 3551 cm^{-1} is the v_1 OH stretch of $HONO_2$ at 3551 cm^{-1} with two smaller peaks from the v_1 OH stretch of HOONO (3306 cm^{-1}) and the $2v_2$ band of $HONO_2$ (3400 cm^{-1}). There is often impurities of HONO in the spectra at 3275, 3370, and 3590 cm^{-1}. While our fitting procedure is almost identical to that of Mollner *et al.*[1] (this procedure is discussed in detail in Andrew Mollner's thesis[21]), I will briefly outline it here and discuss any changes I've made.

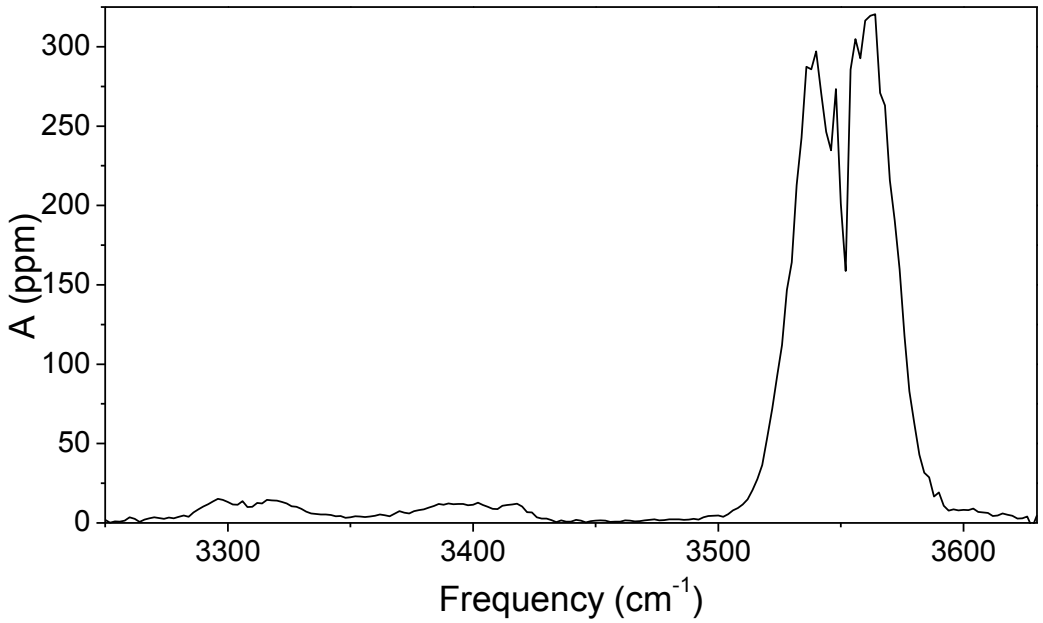

Figure 6. Typical spectra in an OH + NO_2 experiment. Pressure = 296 Torr, Temperature = 10 °C, $[H_2] = 8.6 \times 10^{17}$ cm^{-3}, $[NO_2] = 1.3 \times 10^{16}$ cm^{-3}.

HOONO Spectroscopy

The v_1 OH stretch of HOONO was first published by Bean *et al*.[30] This spectrum, shown in Figure 7 was later used by Mollner *et al*.[1] to find the pressure dependent branching ratio at ambient temperatures. While there is not an experimental measurement of HOONO cross section, Mollner *et al*. calculated the ratio of ν_1 OH stretch of HOONO to the ν_1 OH stretch of $HONO_2$ (2.71, leading to a total integrated cross section of 2.4×10^{-18} cm^2) with high-level *ab initio* calculations (CCSD(T)/ANO). These calculations accurately predicted intensity ratios of other transitions, including the ratio of the v_1 and $2v_2$ OH stretches of $HONO_2$, and the frequencies of $HONO_2$ and HOONO IR transitions to 5%, so this ratio is likely accurate to 5%.[1]

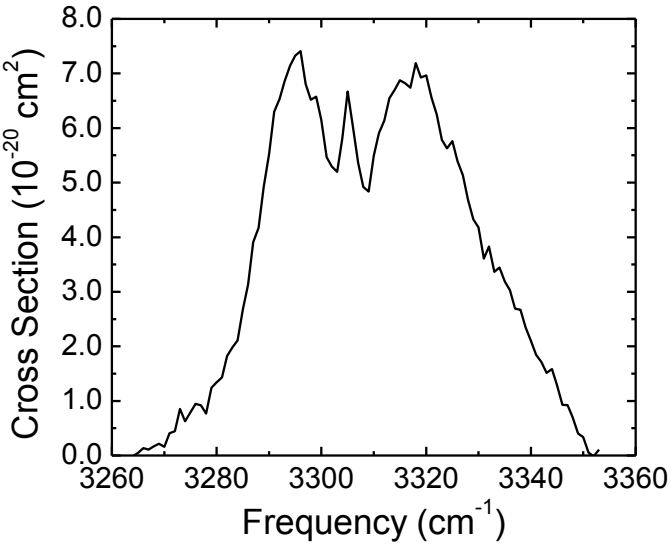

Figure 7. Spectrum of cis-cis HOONO used by Mollner *et al*.[1]

Complicating accurate quantification of HOONO, there is a stretch torsional coupling that blue shifts a significant proportion of the intensity of the OH-stretch even at room temperature. *Cis-cis* HOONO's OH stretch is red shifted due to the hydrogen bond between the terminal H and O (a picture of *cis-cis* HOONO is shown in Figure 3). If we simply fit the peak at 3306 cm^{-1}, we will underestimate the concentration of HOONO, especially at high

temperatures. Like Mollner *et al*.,[1] we added a correction factor to account for the blue-shifter intensity due to the stretch-torsional coupling. This temperature-dependent factor was calculated based on the HOONO torsional potential energy surface calculated by McCoy *et al*.[35] Energies of the torsional modes (v_9 and v_8) in both $v_1 = 0$ and 1 are shown in Table 2. Any of the stretch-torsional modes with a blue shift of less than about 50 wavenumbers will be included in the main peak and thus were not included in our correction factor. For the other modes with significant blue shift, we used a simple calculation based on their Boltzman weights (i.e. the probability that in the ground state HOONO will be at a certain value of v_9 and v_8 at temperatre T). The correction factor, f_{Boltz} which when multiplied by the integrated area of the HOONO peak at 3306 cm^{-1} gives the total absorbance of HOONO given stretch torsional coupling, is given by:

$$f_{Boltz} = \frac{\sum_{includedstates} P_{rel}}{Q} \quad (1)$$

where P_{rel} is the relative probability of finding HOONO is a particular state and Q is the total partition function (sum of all P_{rel}). The sum in this equation includes only state that are included in the peak at 3306 cm^{-1}). This correction factor changes with temperature, since P_{rel} changes with temperature. This calculation is complicated by two peaks $v_9 = (1,0)$ and $v_8 = (1,1)$ which are partially accounted for in the 3006 cm^{-1} but partially not. Andrew Mollner dealt with this by taking a spectrum like that in Figure 6, subtracting out $HONO_2$ and HONO and calculating how much unexplained intensity is not included in the spectra shown in Figure 7. According to this calculation, 19% of these two peaks should be included in the sum of included states in equation 1. The value of f_{Boltz} calculated from equation 1 as a function of temperature is shown in Figure 8. Since more HOONO molecules will start out in high energy torsional vibrational states at higher temperatures, the correction factor increases with temperature.

Table 2. Energies in the ground and first vibrational state for different excitations of HOONO's two tornsional modes (v_9 and v_8) and the expected blue shifts of the v_1 OH stretch.

v_9 n=HOON	v_8 n-OONO	Energy (cm^{-1}) $v_1 = 0$	Energy (cm^{-1}) $v_1 = 0$	Transition frequency (cm^{-1})	blue shift
0	0	2174.19	5546.25	3372.06	0
1	0	2481.65	5897.99	3416.34	44.28
0	1	2659.93	6046.14	3386.21	14.15
2	0	2687.65	6174.41	3486.76	114.7
3	0	2767.79	6314.99	3547.2	175.14
4	0	2827.44	6396.3	3568.86	196.8
5	0	2924.94	6472.36	3547.42	175.36
1	1	2940.52	6358.44	3417.92	45.86
6	0	3022.74	6572.06	3549.32	177.26
2	1	3094.61	6611.61	3517	144.94
0	2	3122.12	6529.22	3407.1	35.04
7	0	3132.87	6679.3	3546.43	174.37
3	1	3163.9	6712.07	3548.17	176.11
3	2	3229.19	6771.08	3541.89	169.83
8	0	3237.3	6794.21	3556.91	184.85

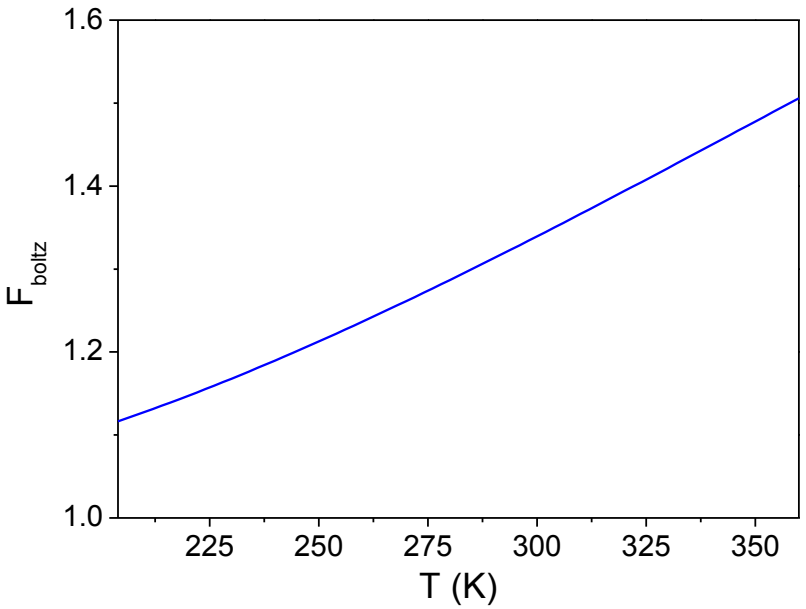

Figure 8. Dependence of calculated f_{boltz} with temperature.

$HONO_2$ Spectroscopy

The largest peak in Figure 6 belongs to the ν_1 OH stretch of $HONO_2$, which is integrated to find the $HONO_2$ yield from R1a. This peak is preferred to the $2\nu_2$ band of $HONO_2$ at 3400 cm^{-1} because it is free from interference from HONO. Yet its large absorption and narrow peaks (if we had better resolution we could see significant rotational structure) lead to multi-exponential ring-downs, and if the peak is simply integrated, we will underestimate the absorbance. To compensate for this, we used the same Matlab program used in Chapter 5 with CO_2 to correct for this effect. The code is described in detail by Andrew Mollner in his thesis,[21] and the programs that make up this code are summarized in Appendix A. The program was checked by extensively by Andrew with measurements of $HONO_2$ and several concentrations and under several pressures, and was found to accurately derive experimental $HONO_2$ from the CRDS spectra.[21]

The code convolutes a Doppler-limited spectra received from Pine and Goldman[36] with a 1 cm^{-1} bandwidth Gaussian laser beam and calculates the resulting ring-down. The theoretical multi-exponential ring-down is then fit to a simple exponential with the first 1/8 of the ring-down time discarded (exactly what we do to process our data) and compared to the unconvoluted absorbance from the original spectra. The correction factor, $f_{multiexp}$ the factor which we can multiply the integrated absorbance of the $HONO_2$ peak by to get the absolute absorbs, is given by:

$$f_{multi\exp}(p,I) = \frac{A_{absolute}}{A_{multi\exp onential}} \quad (2)$$

where p is the pressure, I is the integrated absorbance from 3525 – 3575 cm^{-1}, $A_{absolute}$ is the integrated absorbance from the Doppler-limited spectra, and $A_{multiexponential}$ is the integrated

"absorbance" calculated by fitting the theoretical multiexponential ring-downs on Matlab (again 3525 – 3725 cm^{-1}).

The correction factors used in this experiment are plotted in Figure 9. As with CO_2, the distortion increases with as the linewidth narrows and the absorbance increases, meaning that the correction is largest at the lower pressures, where the $HONO_2$ absorbance lines are narrowest. The integral between 3525 and 3575 cm^{-1} was typically $(1 – 4) \times 10^4$ ppm cm^{-1}, leading to correction factors between 1.5 and 2 at 50 Torr and between 1 and 1.1 at 700 Torr.

Due to the limited wavelength range of the Doppler-limited spectra, we only apply this correction to the most intense part of the $HONO_2$ peak: 3525 – 3575 cm^{-1}. We integrated the experimental spectra from 3476 – 3525 cm^{-1} and 3575 cm^{-1} to capture the wings of the peak, but do not correct these values. This leads to a negligible error, since the small absorbance leads to minimal multi-exponential behavior in the ring-downs.

Since, as described above, we have a larger background than the previous work due the reaction of O_3 with NO_2 to make NO_3, unlike the previous work, we apply the correction factor separately to background spectra and the sample (excimer on) spectra. If there is little or no $HONO_2$ background signal, this procedure is unnecessary, but is essential in our case. The total integrated area of $HONO_2$ is given by:

$$\int A_{HONO_2} = \left[\int_{3476}^{3525} A + f_{multi\exp}(p,I) \int_{3525}^{3575} A + \int_{3575}^{3630} A \right]_{ExOn} - \left[\int_{3476}^{3525} A + f_{multi\exp}(p,I) \int_{3525}^{3575} A + \int_{3575}^{3630} A \right]_{ExOFF} \quad (3)$$

where all integrals represent the integration of the spectra. The first term is the corrected integral for the sample (excimer on) spectra, and the second term in the corrected integral for the background (excimer off) spectra.

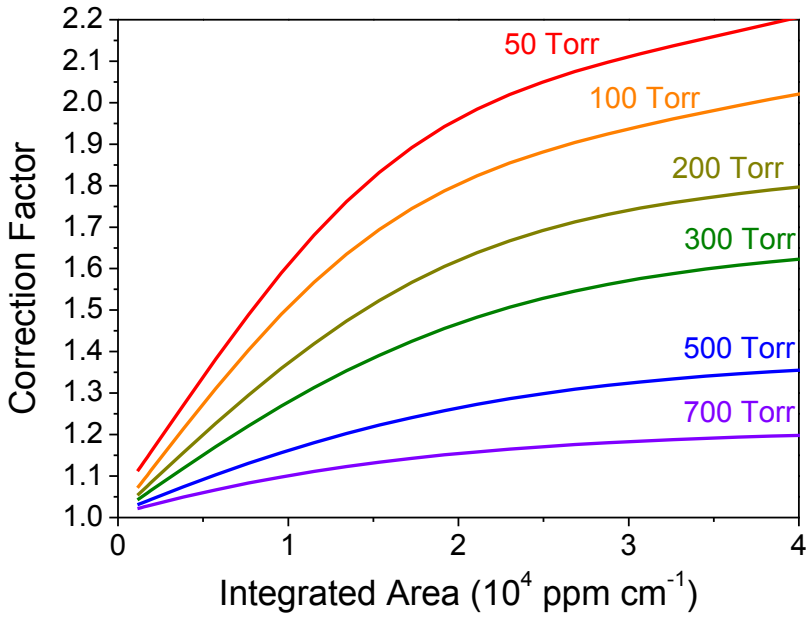

Figure 9. Correction factor vs. the integrated area (3525 – 3575 cm^{-1}) of the ν_1 OH stretch of $HONO_2$ from our matlab program as a function of pressure and integrated area of the peak.

Calculation of Branching Ratio Measurements

To find the branching ratio of R1b, α, we first integrate the ν_1 OH stretch of $HONO_2$ from 3476 – 3630 cm^{-1} and corrected for multiexponential ring-downs as described in the previous section. To find the integral of HOONO, we fit the spectra from 3250 – 3450 cm^{-1} as shown in Figure 10. This is preferable to integrating because there is significant absorption from $HONO_2$ and HONO in this region. The integrated area of HOONO is then found by integrating the HOONO component of the spectra fit and multiplying by f_{Boltz}. The branching ratio is then the integrated area of HOONO divided by the integrated area of $HONO_2$ and multiplying by the ratio of their cross sections:

$$\alpha = \frac{\int A_{HOONO}}{\int A_{HONO_2}} \frac{\sigma_{HONO_2}}{\sigma_{HOONO}} f_{Boltz}(T) \quad (4)$$

As discussed above, the ratio of the cross sections ($\sigma_{HONO2}/\sigma_{HOONO}$) is 2.71, based on quantum calculations.

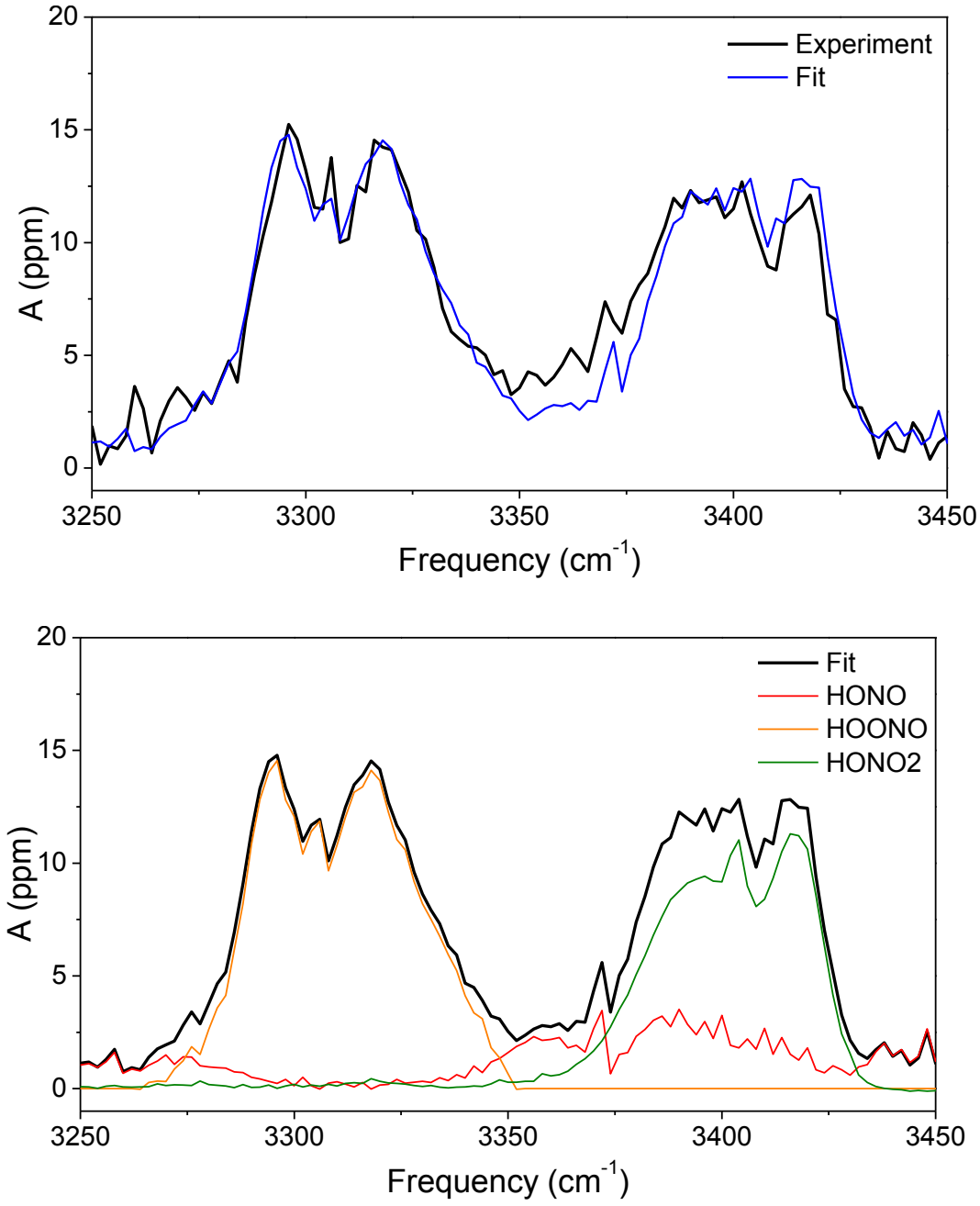

Figure 10. (top panel) a typical fit (blue) to an experimental spectra (black) (Pressure = 296 Torr, Temperature = 10 °C, $[H_2] = 8.6 \times 10^{17}$ cm^{-3}, $[NO_2] = 1.3 \times 10^{16}$ cm^{-3}). (bottom panel) components of the fit (black).

Results

Branching Ratio Measurements

We took spectra from 3250 – 3630 cm^{-1} for six different pressures: 50, 100, 200, 300, 500, and 700 Torr. We repeated these pressures for multiple different temperatures: -19, -8, 1, 10, 20, 30, 40, and 60 °C. The step size for each spectra was fairly large, 2 cm^{-1}, so that only a small amount of time would elapse between taking the spectrum of HOONO at 3306 cm^{-1} and the spectra of $HONO_2$ and 3551 cm^{-1}. Along with monitoring ozone concentration with the UV flow cell, this ensured reasonably constant radical concentration and experimental conditions during a single scan. These spectra were then fit and integrated to find the branching ratio of HOONO, α, according to equations 3 and 4. Figure 11 shows our data at 30 °C compared our data with data from Mollner *et al.*[1], and demonstrates that our data agrees well with the previous work.

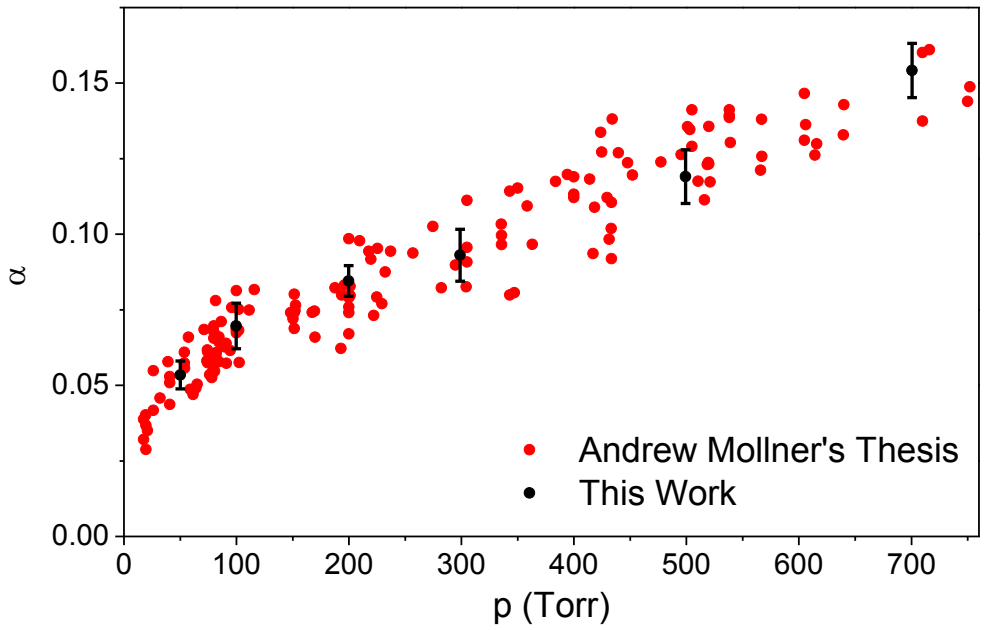

Figure 11. Branching ratio of HOONO (α) at 30 °C (black, 2σ errors) as a function of pressure at room temperature compared to data published in Andrew Mollner's thesis[21] (red).

The only published work on the temperature dependence of this reaction was by Bean *et al.*[30] At 20 Torr of total pressure, they found that the branching ratio, α, changed by (-1.7 ± 2.4) × 10^{-4} K^{-1} (2σ) by simply plotting α as a function of temperature and finding the slope with a linear regression.[30] Performing the same procedure for our data at 50 Torr (our lowest pressure) as shown in Figure **12**, we find a slope of (-2.9 ± 1.4) × 10^{-4} K^{-1} (2σ), within error of the previous measurements.

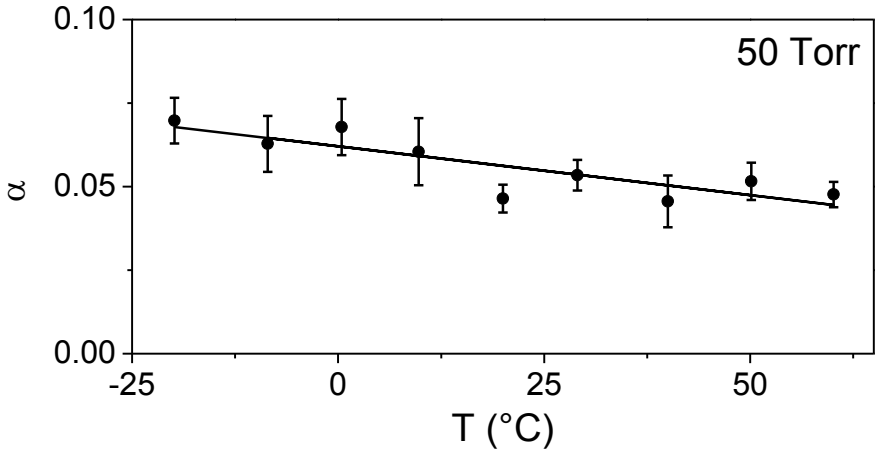

Figure 12. Branching ratio of HOONO (*α)* as a function of temperature at 50 Torr.

This work has found comparable branching ratios and temperature dependence as work of Mollner *et al.*[1] and Bean *et al.*,[30] but expands the temperature range of the previous data. Table 3 shows all of our branching ratio measurements from -19 to 60 °C and 50 to 700 Torr. For each point, several spectra were taken (4 – 7 scans) on at least two different days. The standard error between these scans gave the 2σ reported on Table 3.

Table 3. All values of α used in the fit with 2σ standard errors. At all pressures and temperatures we averaged approximately 4-7 points from at two different days of experiments.

T (°C)	p of N_2 (Torr)	α, Branching Ratio in N_2 (%)	k_{HOONO} in air (10^{-12} cm^{-3} s^{-1})
-19.9	49.9	7.0 ± 0.7	0.20 ± 0.02
-19.0	100.5	7.8 ± 0.5	0.36 ± 0.02
-18.5	200.5	9.7 ± 1.1	0.67 ± 0.08
-18.0	299.6	11.5 ± 0.8	0.97 ± 0.06
-18.6	400.2	14.5 ± 1.5	1.38 ± 0.14
-8.6	50.2	6.3 ± 0.8	0.16 ± 0.02
-8.3	100.1	8.2 ± 0.7	0.34 ± 0.03
-7.9	200.2	9.7 ± 1.0	0.61 ± 0.06
-7.8	300.0	12.1 ± 1.5	0.93 ± 0.12
-8.3	501.6	17.0 ± 0.4	1.64 ± 0.04
0.4	50.3	6.8 ± 0.8	0.16 ± 0.02
1.0	100.0	8.0 ± 1.0	0.30 ± 0.04
0.4	200.1	10.1 ± 0.8	0.59 ± 0.05
1.3	300.3	11.5 ± 0.9	0.83 ± 0.06
2.3	500.5	14.0 ± 0.9	1.28 ± 0.08
9.8	50.1	6.0 ± 1.0	0.13 ± 0.02
9.9	100.1	7.5 ± 1.2	0.26 ± 0.04
10.0	200.0	9.2 ± 1.2	0.50 ± 0.07
9.9	299.3	10.9 ± 0.8	0.74 ± 0.05
10.3	498.9	14.1 ± 1.0	1.21 ± 0.08
10.2	700.3	16.9 ± 1.1	1.67 ± 0.10
20.0	50.5	4.6 ± 0.4	0.09 ± 0.1
20.0	100.0	6.4 ± 0.5	0.21 ± 0.02

20.0	199.1	7.6 ± 0.7	0.39 ± 0.03
20.0	298.2	9.8 ± 0.9	0.62 ± 0.06
20.0	500.0	12.9 ± 0.8	1.04 ± 0.07
20.0	698.9	15.9 ± 0.6	1.48 ± 0.06
29.0	50.1	5.3 ± 0.5	0.09 ± 0.01
28.9	99.7	7.0 ± 0.8	0.20 ± 0.02
28.9	199.7	8.5 ± 0.5	0.40 ± 0.02
28.8	298.9	9.3 ± 0.9	0.55 ± 0.05
28.8	499.3	11.9 ± 0.9	0.91 ± 0.07
28.8	700.5	15.4 ± 0.9	1.36 ± 0.08
40.0	50.6	4.6 ± 0.8	0.07 ± 0.01
40.0	100.1	5.6 ± 0.7	0.15 ± 0.02
40.1	200.2	6.6 ± 0.4	0.29 ± 0.02
40.0	300.4	7.9 ± 0.7	0.44 ± 0.04
40.0	501.1	9.9 ± 0.9	0.72 ± 0.07
40.0	702.8	12.0 ± 0.6	1.01 ± 0.06
50.1	50.0	5.2 ± 0.6	0.07 ± 0.01
50.1	100.0	6.1 ± 0.3	0.15 ± 0.01
49.9	200.1	7.0 ± 0.7	0.28 ± 0.03
49.8	300	7.9 ± 0.6	0.40 ± 0.03
50.1	500.5	10.6 ± 0.9	0.71 ± 0.06
49.9	702	11.2 ± 1.6	0.90 ± 0.13
60.9	50.1	4.8 ± 0.4	0.06 ± 0.01
60.3	100.1	5.4 ± 0.5	0.12 ± 0.01
60.2	200.8	6.6 ± 0.7	0.24 ± 0.03
60.3	299.9	6.9 ± 0.5	0.33 ± 0.02
59.9	501.2	9.7 ± 0.9	0.62 ± 0.06
60.1	702.4	12.0 ± 1.0	0.89 ± 0.07

Rate Constant for HOONO and $HONO_2$ Formation: k_{HOONO} and k_{HONO2}

Combining our data with data from collaborators at JPL who found the total rate constant ($k_{HOONO} + k_{HONO2}$), we can calculate the individual rate constants for R1a (k_{HONO2}) and R1b (k_{HOONO}). This work, performed by Yingdi Liu and Stanley Sander,[37] tracked the decay of OH radicals in the presence of NO_2 using laser-induced fluorescence (LIF). After finding the rate at a range of -43 – 57 °C and 40 – 800 Torr of air they found the total rate constant as a function of temperature, *T*, by fitting their data to the following equation:

$$k(T) = \frac{k_0(T)M}{1+\frac{k_0(T)M}{k_\infty(T)}} \times F_c^{\left(1+\log_{10}\left(\frac{k_0(T)M}{k_\infty(T)}\right)^2\right)^{-1}} \quad (6)$$

where M is the number density in cm^{-3}, $k_0(T)$ is the rate constant in the low pressure limit, $k_\infty(T)$ is the rate constant at the high pressure limit and F_c is a broadening constant, usually 0.6. The temperature dependence of $k_0(T)$ and $k_\infty(T)$ is given by:

$$k_0(T) = k_0^{300}\left(\frac{T}{300}\right)^{-n} \quad (7)$$

and

$$k_\infty(T) = k_\infty^{300}\left(\frac{T}{300}\right)^{-m} \quad (8)$$

where k_0^{300} is the rate constant at the low pressure limit, k_∞^{300} is the rate constant at the high pressure limit at 300 K, and *n* and *m* are fitted constants that give the temperature dependence of the reaction. They found the following constants needed in equations 6-8 to calculate the rate for $k_{total}(T)$:

$$k_0^{300} = (1.63 \pm 0.10) \times 10^{-30}\ cm^6\ s^{-1}$$

$$k_{\infty}^{300} = (3.43 \pm 0.34) \times 10^{-11}\ \mathrm{cm}^3\ \mathrm{s}^{-1}$$

$$n = 2.7 \pm 0.4$$

$$m = 0.4 \pm 0.8$$

$$F_c = 0.6$$

With this rate constant (errors are 2σ) we can convert our branching ratio, to the rate constant for HOONO formation, k_{HOONO} with the follow equations:

$$k_{total}(T) = k_{HOONO}(T) + k_{HONO_2}(T) \quad (9)$$

$$\alpha = \frac{k_{HOONO}(T)}{k_{HONO_2}(T)} \quad (10)$$

Combining equations (9) and (10) we find that:

$$k_{HOONO} = \left(\frac{1}{\alpha} + 1\right)^{-1} \times k_{total} \quad (11)$$

The values for k_{HOONO} are shown in Table 1 and plotted in Figure **13** for all temperatures studies. Figure 11 and Figure 13 show that k_{HOONO} increases with increasing pressure and decreasing temperature. It is also increases very linearly with pressure, which suggests that the reaction is near the low pressure limit. The low pressure rate constant, $k_0(T)$, can consequently be calculated by finding a simple linear regression at each of the temperatures. The slope will be $k_0(T)$, and the intercept should be zero, since the reaction cannot proceed without collisions to stabilize excited HOONO and $HONO_2$ after they're formed from R1. The results of these simple linear fits are shown in Table 4 and plotted as colored lines in Figure 13. As expected, the intercepts are within error of zero. The slope $k_0(T)$, converted to $\mathrm{cm}^6\ \mathrm{s}^{-1}$ in a background of air, ranges from $(8.7 \pm 0.7) \times 10^{-32}\ \mathrm{cm}^6\ \mathrm{s}^{-1}$ at -19 °C to $(4.4 \pm 0.2) \times 10^{-32}\ \mathrm{cm}^6\ \mathrm{s}^{-1}$ at 60 °C. While our data was taken in a background of N_2, air is 79% N_2 and 21% O_2. Air has slightly different

collisional properties, because O_2 is a slightly stronger collisional partner than N_2. We can account for this by scali-ng our N_2 pressures with well-known scaling factors (β_{air}) to convert them to equivalent pressures of air.

$$[air] = \beta_{air} \times [N_2]$$

We used a value of Brown *et al*. of 0.94.[38] Mollner *et al*. found a similar value of 0.92.[1]

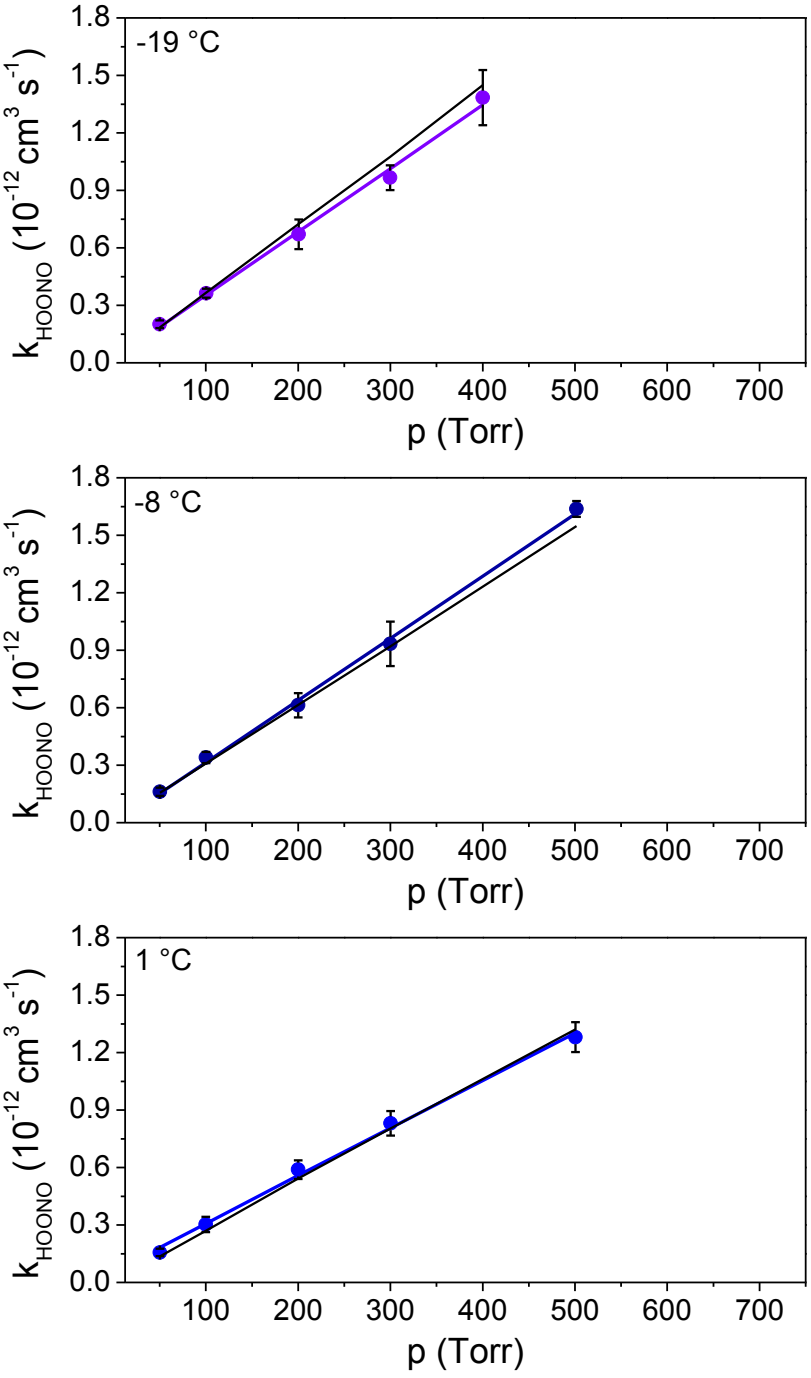
-19 °C
-8 °C
1 °C
k_{HOONO} (10^{-12} cm^3 s^{-1})
p (Torr)
0.0
0.3
0.6
0.9
1.2
1.5
1.8
100
200
300
400
500
600
700

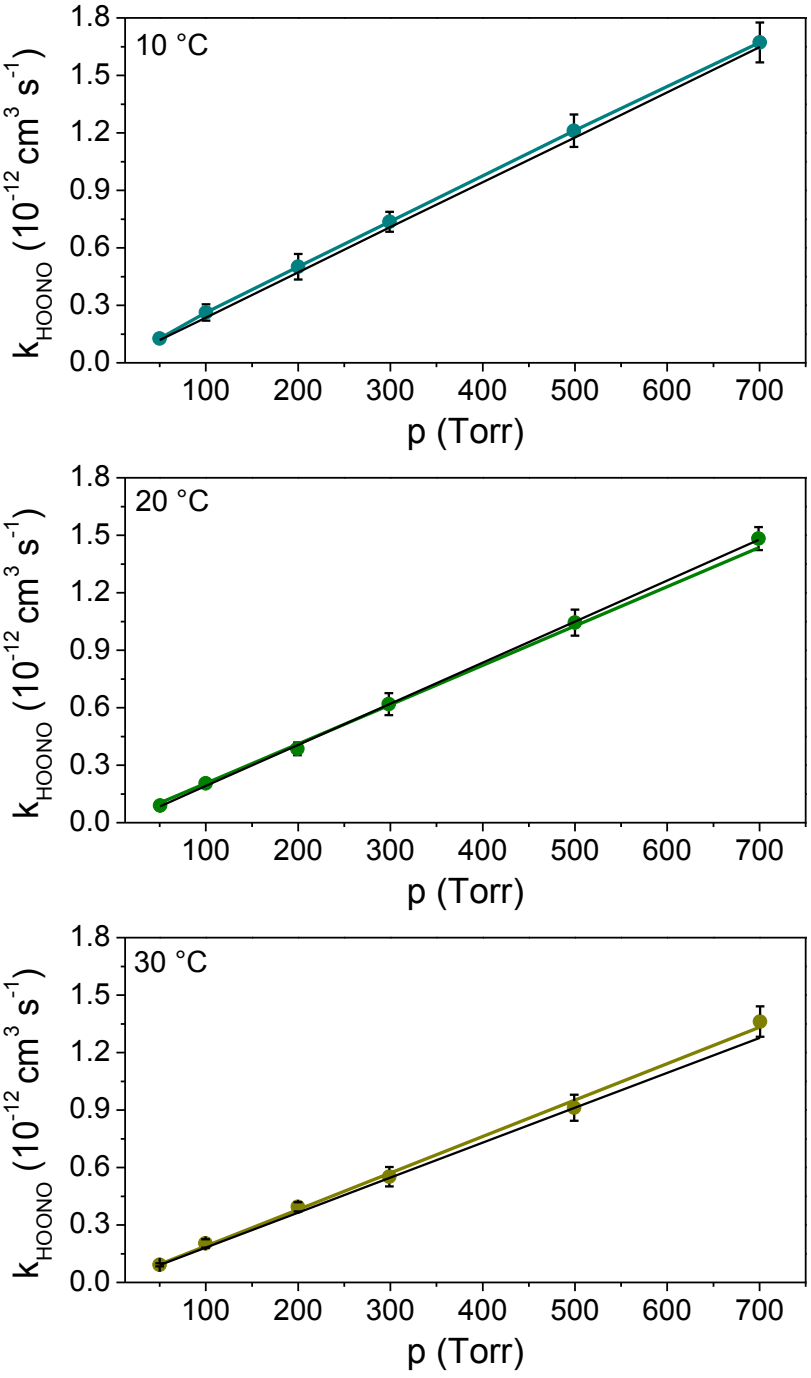
10 °C
20 °C
30 °C
k_{HOONO} (10^{-12} cm^3 s^{-1})
p (Torr)
0.0
0.3
0.6
0.9
1.2
1.5
1.8
100
200
300
400
500
600
700

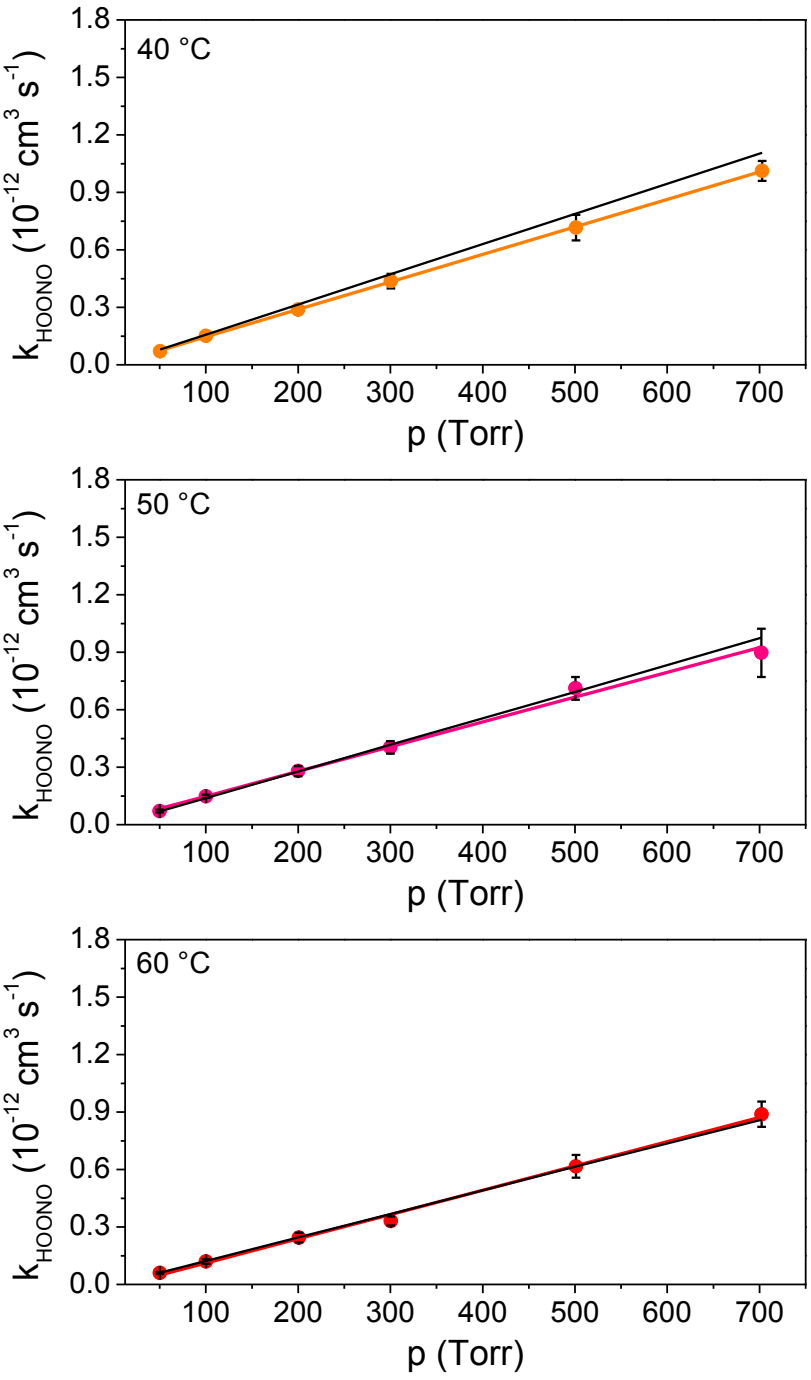

Figure 13. k_{HOONO} as a function of pressure at every temperature in this study. The error bars are from the 2σ standard error from the branching ratios. The colored lines are linear fit to the data just at a single temperature. The black lines are from a fit to the entire data assuming that the rate is still in its low pressure limit.

Table 4. Results from a simple linear fit of k_{HOONO} vs. pressure at each temperature in Figure 13. The slope is reported as $k_0(T)$, which is the slope when using cm^{-3} instead of Torr for the x axis. Errors, from the fit only, are 2σ.

T	$k_0(T)$ (10^{-32} cm^6 s^{-1})	Intercept (10^{-12} cm^3 s^{-1})
-19	9.3 ± 0.7	0.02 ±0.06
-8	9.5 ± 0.5	-0.01 ± 0.05
1	7.6 ± 0.5	0.06 ± 0.05
10	7.4 ± 0.1	0.02 ± 0.01
20	6.9 ± 0.1	-0.02 ± 0.02
30	6.3 ± 0.3	0.00 ± 0.04
40	4.9 ± 0.1	0.00 ± 0.01
50	4.6 ± 0.4	0.02 ± 0.04
60	4.6 ± 0.3	-0.01 ± 0.03

We also fit the entire data set to equations 6, 7 and 8 in order to get k_{HOONO} as a function of temperature (T) and number density (M) and find k_0^{300}, k_∞^{300}, n, and m. As described in the JPL[39] data evaluations, we set F_c to 0.6. This fit, performed using a Levenberg-Marquart algorithm, was performed in Matlab. It yielded the following constants for k_{HOONO}:

$$k_0^{300} = (6.9 \pm 0.6) \times 10^{-30}\ cm^6\ s^{-1}$$

$$k_\infty^{300} = (1.8 \pm 4.0) \times 10^{-10}\ cm^3\ s^{-1}$$

$$n = 2.4 \pm 0.4$$

$$m = 27.2 \pm 16.1$$

$$F_c = 0.6$$

The errors are all 2σ and include only uncertainty from the fit. The large errors of k_∞^{300} and m suggest that our function, equation 6, does not well constrain these values. In fact, they vary greatly based on the starting values inputted into the Levanberg-Marquart fit, again indicating that our data does not well constrain these constants.

A fit assuming a low pressure limit yields more reasonable errors than the full fit to equation 6. In the low pressure limit, the rate is approximately linear with pressure, so the total rate is given by:

$$k_0(T) = k_0^{300}\left(\frac{T}{300}\right)^{-n} \times M \quad (12)$$

This value yielded the following rate constants for k_{HOONO}:

$$k_0^{300} = (6.2 \pm 0.1) \times 10^{-30}\ \text{cm}^6\ \text{s}^{-1}$$

$$n = 3.0 \pm 0.2$$

These values are very close to the k_0^{300} and n found with the full model, except with less error. The above values only contain error from the fit (2σ) when the errors from the total rate constant (k_{total}(T)) they are:

$$k_0^{300} = (6.2 \pm 0.6) \times 10^{-30}\ \text{cm}^6\ \text{s}^{-1}$$

$$n = 3.0 \pm 0.8$$

To ensure that this value is linear, we performed additional fits on only data taken at pressures up to 300 Torr. If the rate constant was not in the low pressure limit, reducing the pressure range would lead to an increase in the fitted k_0^{300} due the negative curvature as it reaches k_∞. The rate constants are completely unchanged (but with slight higher error) if we only fit points up to 300 Torr:

$$k_0^{300} = (6.2 \pm 0.2) \times 10^{-30}\ \text{cm}^6\ \text{s}^{-1}\ \text{(fitted up to 300 Torr)}$$

$$n = 2.9 \pm 0.3\ \text{(fitted up to 300 Torr)}$$

Since this further ensures that we're in the low pressure limit, and more data at higher pressures is needed accurately quantify k_∞^{300} and m for R1b.

With k_{HOONO} and k_{total}, we can easily find the rate constant for $HONO_2$ formation based on equation (9). After calculation k_{HONO2} with equation 9 as a variety of different temperatures and pressures (-20 – 60 °C and 50 – 700 Torr of air) we fit those values to equation (6) to find k_{HONO2}:

$$k_0^{300} = (1.8 \pm 0.2) \times 10^{-30}\ cm^6\ s^{-1}$$

$$k_\infty^{300} = (2.4 \pm 0.5) \times 10^{-11}\ cm^3\ s^{-1}$$

$$n = 2.7 \pm 0.4$$

$$m = 0.4 \pm 0.8$$

$$F_c = 0.6$$

Discussion

While previous work has found the total rate (k_{total}) and has fit fall-off curves to back-out the rate constants for HOONO and $HONO_2$ formation, our group is the first to specifically look at the branching ratio of HOONO. By combining LIF measurements the find the total rate by watching the rate of OH decay in the presence of NO_2 and our branching ratio measurements, we have found the first temperature-dependent rate constants for both R1a and R1b.

Our values of k_{HOONO} and k_{HONO2} are compared to previous literature values and values from current atmospheric evaluations data in Table 5 and Table 6. Hippler *et al*. found the rate constants at 300 and 600 K from high pressure experiments with He (1500 – 375,000 Torr) and Ar (1500 – 3000 Torr) background gases and fit their results to fall-off curves (similar to equation 6) to find their rate constants presented in Table 5 and Table 6.[40] Troe fitted previous data (220 – 600 K) to equation 6 with asymmetric broadening factors, F_c to yield his rate constants in Table 5 and Table 6.[41] We also compare our values to those found by Mollner *et al*.,[1] who we are in excellent agreement with. Since the experiment was based on this previous

work we expect to have similar systematic errors as Mollner *et al*.[1] The nearly identical values suggest that both experiments were performed consistently.

Table 5. Our rates constant for k_{HOONO} compared to literature values.

	k_0^{300} (10^{-32} cm^6 s^{-1})	n	k_{inf}^{300} (10^{-11} cm^3 s^{-1})	m	F_c
This Work	6.2 ± 0.3	3.0 ± 0.8	-	-	-
JPL 2016[39]	9.1 *f*(298K) = 1.5**	3.9 (g = 200)**	4.2 *f*(298K) = 1.5**	0.5 (g = 200)**	0.6
IUPAC[42]	10 *f* = 1.26*	4.5 *f* = 3.2*	3.5 *f* = 2.0*	0 *f* = 3.2*	0.41
Mollner *et al.* 2011[1]	6.2	-	8.1	-	0.6
Hippler *et al.* 2006[40]	9.2	2.6	1.9	0	0.73
Troe 2012[41]	10	4.5	4.8	0	0.41

**f* is the uncertainty factor of the rate constant. The upper and lower limit of the rate constants from the JPL and IUPAC Data Evaluations are found by multiplying or dividing the rate by *f*.

**In the JPL data evaluation, the uncertainty factor, *f*(*T*), for in any rate constant k(T) is given by: $f(T) = f(298K)\exp\left|g\left(\frac{1}{T}-\frac{1}{298}\right)\right|$.

Table 6. Our rates constant for k_{HONO2} compared to literature values.

	k_0^{300} (10^{-30} cm^6 s^{-1})	n	k_{inf}^{300} (10^{-11} cm^3 s^{-1})	m	F_c
This Work	1.8 ± 0.2	3.4 ± 0.3	2.5 ± 0.2	-0.4 ± 0.9	0.6
JPL 2016[39]	1.8 *f*(298K) = 1.3**	3.0 (g = 100)**	2.8 *f*(298K) = 1.3**	0 (g = 100)**	0.6
IUPAC[42]	3.2 *f*(298K) = 1.12*	4.5 *f* = 3.2*	3.0 *f*(298K) = 2.0*	0 *f* = 3.2*	0.41
Mollner *et al.* 2011[1]	1.51	-	2.58	-	0.6
Hippler *et al.* 2006[40]	2.5	3.0	2.8	0	0.62
Troe 2012[41]	3.2	4.5	2.7	0	0.41

Our values do significantly differ from the current recommended values. This is demonstrated in Figure 14 and Figure 15, which plot the rate constants on Table 5 and Table 6, respectively. Our values of k_{HOONO} are significantly lower than the currently recommended values. The JPL data evaluation reports 9.1×10^{-32} cm^{-6} s^{-1} and IUPAC recommended 10×10^{-32} cm^{-6} s^{-1} for , values that are approximately 50% larger than our value of $(6.2 \pm 0.3) \times 10^{-32}$. This is seen in Figure 14, were our rate of HOONO formation is consistently lower than the other values at both 300 and 250 K. Our value of k_{HONO2} agrees very well many of the other previously reported values at 300 K as shown on Figure 15. However, at 250 K our value becomes significantly lower than the all literature values. This suggests current rate constants in the literautre might overestimate the real rate.

Yet our data agrees with commonly trends in this reaction. Firstly, previous data on the fall-off behavior of the reaction of OH with NO_2, suggest that the high-pressure limit, k_∞, of HOONO is much higher than the high-pressure limit, k_∞, of $HONO_2$. In fact, HOONO was proposed as the reason for unexpected fall-off behavior for the OH + NO_2 reaction, that the reaction reached its high pressure limit at very high pressures.[4,5,18-20] Since our data suggests that at atmospheric pressure and below that the reaction of OH with NO_2 to produce HOONO is still in at the low-pressure regime, it will only reach the high-pressure limit at very high pressures, leading to an extended fall-off region for the total OH + NO_2 reaction.

Secondly, due to the lower stability of HOONO compared to $HONO_2$, the lifetime of excited HOONO* is shorter than the lifetime of excited $HONO_2$*. When $HONO_2$* forms from the reaction of OH with NO_2, its long lifetime will make it the more favorable pathway compared to HOONO at low pressures and high temperatures. As the temperature decreases (so that collisions will be better at removing excess energy from nascent HOONO* and $HONO_2$*) or

the pressures increases, any excited molecule will be easily be collisionally stabilized. Thus, the short lifetime of HOONO* will become less important as temperature decreases and pressure increases, making the branching ratio of HOONO formation increase.

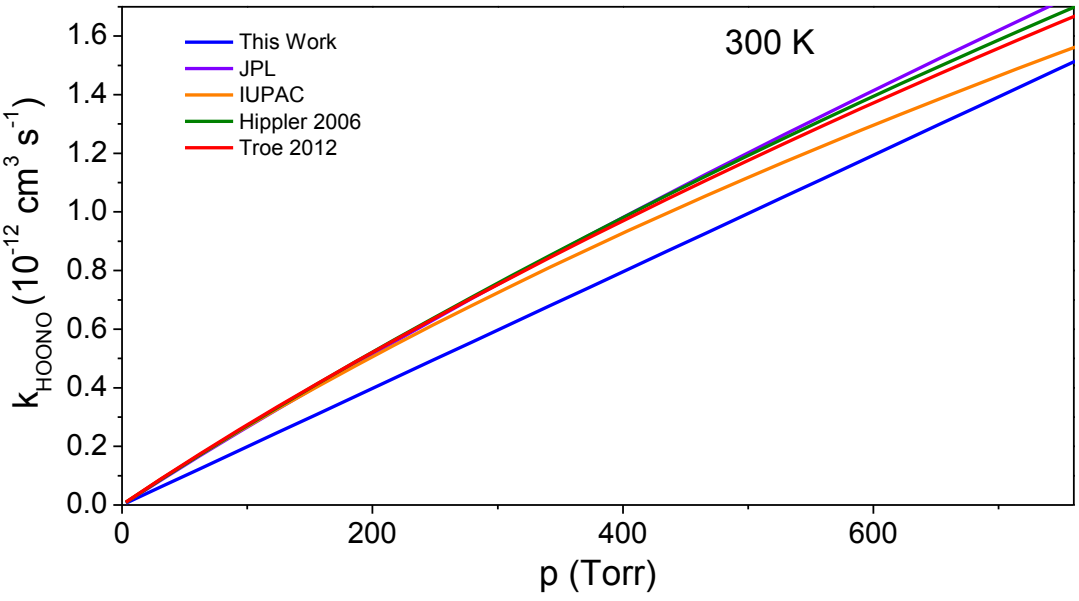

(a)

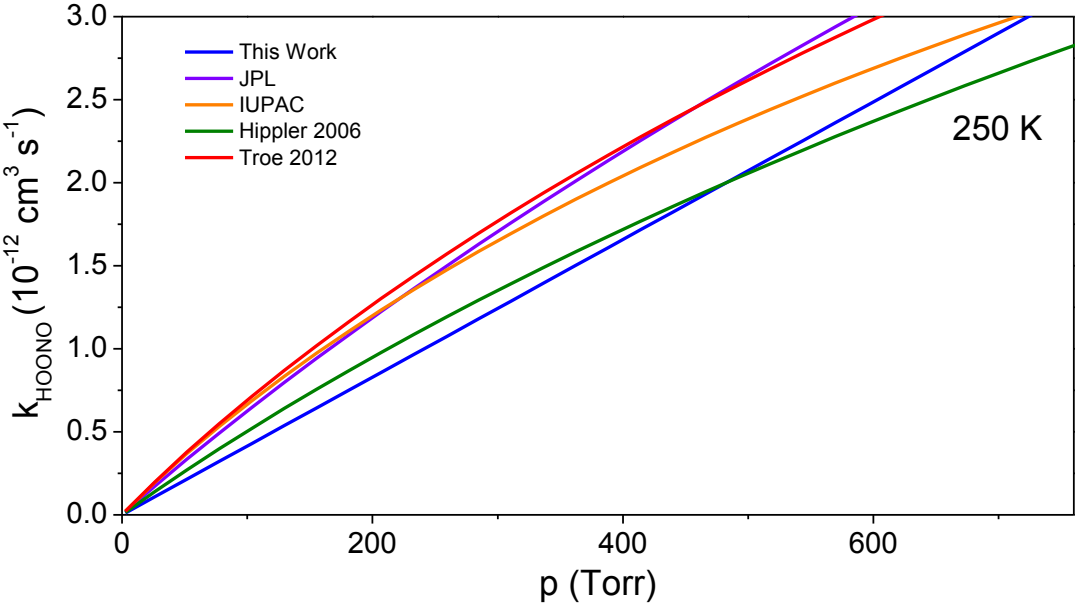

(b)

Figure 14. Our values for k_{HOONO} compared to the literature values from Table 5 at (top panel) 300 K and (bottom panel) 250 K.

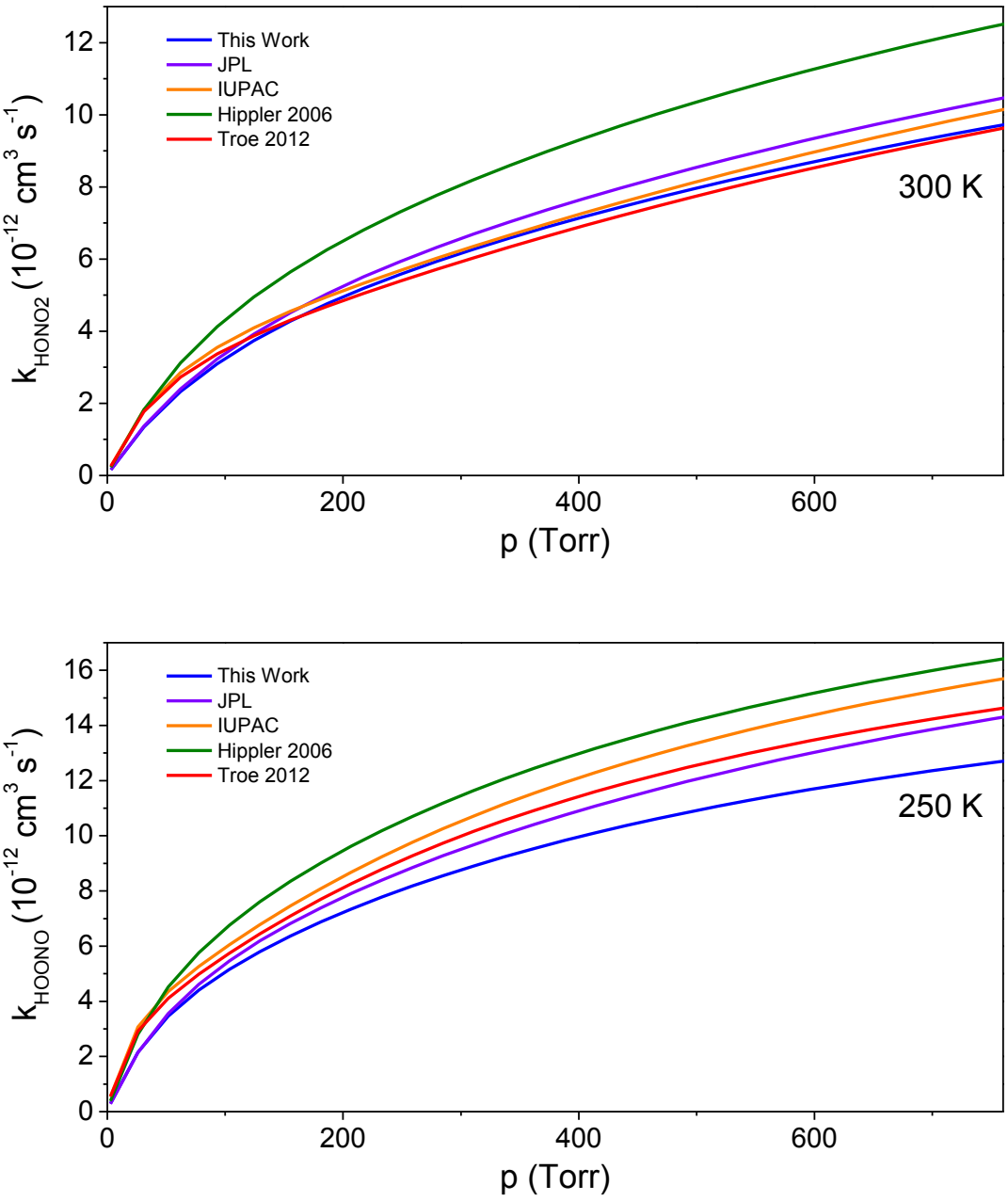

Figure 15. Our values for k_{HONO2} compared to the literature values from Table 6 at (top panel) 300 K and (bottom panel) 250 K.

Conclusions

We measured the branching ratios of HOONO and $HONO_2$ from the reaction of OH and NO_2 at temperatures from -19 to 60 °C and pressures from 50 – 700 Torr of N_2 with mid-IR CRDS. Data from collaborators at JPL measured total temperature and pressure dependent rate constants for the reaction of OH with NO_2 and, combined with our branching ratios, allowed calculations of both k_{HOONO} and k_{HONO2}. We fit this data to fall-off curves (equation 6), and the results of these fits and final rate constants are presented in Table 5 and Table 6. Our rate constants – which are slightly lower than the rate constants currently reported in the JPL[39] and IUPAC[42] data evaluations – are the first temperature and pressure dependent rate constants that directly measures both the total rate constants and the branching ratio between HOONO and $HONO_2$. These new rate constants can now be inputted into atmospheric models, allowing for better estimation of the total rate and the amount of HOONO produced from OH + NO_2.

References

(1) Mollner, A. K.; Valluvadasan, S.; Feng, L.; Sprague, M. K.; Okumura, M.; Milligan, D. B.; Bloss, W. J.; Sander, S. P.; Martien, P. T.; Harley, R. A.; McCoy, A. B.; Carter, W. P. L. *Science* **2010**, *330*, 646.

(2) " Predicting smoggiest days: Experiments improve accuracy of ozone predictions in air-quality models." In ScienceDaily. 2010. <www.sciencedaily.com/releases/2010/10/101028143946.htm>

(3) Seinfeld, J. H.; Pandis, S. N. *Atmospheric Chemistry and Physics: From Air Pollution to Climate Change*.

(4) Matheu, D. M.; Green, W. H. *International Journal of Chemical Kinetics* **2000**, *32*, 245.

(5) Golden, D. M.; Smith, G. P. *The Journal of Physical Chemistry A* **2000**, *104*, 3991.

(6) Sander, S. P., B. J. Finlayson-Pitts, D. M. Golden, R. E. Huie, C. E. Kolb, M. J. Kurylo, M. J. Molina, et al., Chemical Kinetics and Photochemical Data for Use in Atmospheric Studies, Evaluation Number 15. 2006, Jet Propulsion Laboratory: Pasadena, CA.

(7) Berces, T.; Forgeteg, S. *Transactions of the Faraday Society* **1970**, *66*, 640.

(8) Anderson, J. G.; Kaufman, F. *Chemical Physics Letters* **1972**, *16*, 375.

(9) Westenberg, A. A.; deHaas, N. *The Journal of Chemical Physics* **1972**, *57*, 5375.

(10) Anderson, J. G.; Margitan, J. J.; Kaufman, F. *The Journal of Chemical Physics* **1974**, *60*, 3310.

(11) Howard, C. J.; Evenson, K. M. *The Journal of Chemical Physics* **1974**, *61*, 1943.

(12) Anastasi, C.; Bemand, P. P.; Smith, I. W. M. *Chemical Physics Letters* **1976**, *37*, 370.

(13) Anastasi, C.; Smith, I. W. M. *Journal of the Chemical Society, Faraday Transactions 2: Molecular and Chemical Physics* **1976**, *72*, 1459.

(14) Atkinson, R.; Perry, R. A.; Pitts, J. N. *The Journal of Chemical Physics* **1976**, *65*, 306.

(15) Anderson, L. G. *The Journal of Physical Chemistry* **1980**, *84*, 2152.

(16) Burrows, J. P.; Wallington, T. J.; Wayne, R. P. *Journal of the Chemical Society, Faraday Transactions 2: Molecular and Chemical Physics* **1983**, *79*, 111.

(17) Burkholder, J. B.; Hammer, P. D.; Howard, C. J. *The Journal of Physical Chemistry* **1987**, *91*, 2136.

(18) Robertshaw, J. S.; Smith, I. W. M. *The Journal of Physical Chemistry* **1982**, *86*, 785.

(19) Donahue, N. M.; Mohrschladt, R.; Dransfield, T. J.; Anderson, J. G.; Dubey, M. K. *J. Phys. Chem. A* **2001**, *105*, 1515.

(20) Donahue, N. M.; Dubey, M. K.; Mohrschladt, R.; Demerjian, K. L.; Anderson, J. G. *Journal of Geophysical Research: Atmospheres* **1997**, *102*, 6159.

(21) Mollner, A. K. **2007**. Ph.D Thesis.

(22) *CRC Handbook of Chemistry and Physics*; 88 ed.; Linde, D. R., Ed.; CRC Press: Boca Raton, Fl, 2007.

(23) Hippler, H.; Nasterlack, S.; Striebel, F. *Physical Chemistry Chemical Physics* **2002**, *4*, 2959.

(24) Matthews, J.; Sinha, A. *The Journal of Chemical Physics* **2005**, *122*, 104313.

(25) Konen, I. M.; Pollack, I. B.; Li, E. X. J.; Lester, M. I.; Varner, M. E.; Stanton, J. F. *The Journal of Chemical Physics* **2005**, *122*, 094320.

(26) Fry, J. L.; Nizkorodov, S. A.; Okumura, M.; Roehl, C. M.; Francisco, J. S.; Wennberg, P. O. *The Journal of Chemical Physics* **2004**, *121*, 1432.

(27) Troe, J. *International Journal of Chemical Kinetics* **2001**, *33*, 878.

(28) Dransfield, T. J.; Donahue, N. M.; Anderson, J. G. *The Journal of Physical Chemistry A* **2000**, *105*, 1507.

(29) Nizkorodov, S. A.; Wennberg, P. O. *The Journal of Physical Chemistry A* **2002**, *106*, 855.

(30) Bean, B. D.; Mollner, A. K.; Nizkorodov, S. A.; Nair, G.; Okumura, M.; Sander, S. P.; Peterson, K. A.; Francisco, J. S. *The Journal of Physical Chemistry A* **2003**, *107*, 6974.

(31) Konen, I. M.; Pollack, I. B.; Li, E. X. J.; Lester, M. I.; Varner, M. E.; Stanton, J. F. *The Journal of Chemical Physics* **2005**, *122*.

(32) Aker, P. M.; Sloan, J. J. *The Journal of Chemical Physics* **1986**, *85*, 1412.

(33) Smith, I. W. M.; Williams, M. D. *Journal of the Chemical Society, Faraday Transactions 2: Molecular and Chemical Physics* **1985**, *81*, 1849.

(34) Rensberger, K. J.; Jeffries, J. B.; Crosley, D. R. *The Journal of Chemical Physics* **1989**, *90*, 2174.

(35) McCoy, A. B.; Sprague, M. K.; Okumura, M. *The Journal of Physical Chemistry A* **2010**, *114*, 1324.

(36) Pine, A. S. and A. Goldman. private communication.

(37) Sander, S.P. private communication.

(38) Brown, S. S.; Talukdar, R. K.; Ravishankara, A. R. *Chemical Physics Letters* **1999**, *299*, 277.

(39) J. B. Burkholder, S. P. Sander, J. Abbatt, J. R. Barker, R. E. Huie, C. E. Kolb, M. J. Kurylo, V. L. Orkin, D. M.Wilmouth, and P. H. Wine "Chemical Kinetics and Photochemical Data for Use in Atmospheric Studies, Evaluation No. 18," JPL Publication 15-10, Jet Propulsion Laboratory, Pasadena, 2015 http://jpldataeval.jpl.nasa.gov.

(40) Hippler, H.; Krasteva, N.; Nasterlack, S.; Striebel, F. T*he Journal of Physical Chemistry A* 2**006,** 1*10*, 6781.

(41) Troe, J. T*he Journal of Physical Chemistry A* 2**012,** 1*16*, 6387.

(42) Atkinson, R.; Baulch, D. L.; Cox, R. A.; Crowley, J. N.; Hampson, R. F.; Hynes, R. G.; Jenkin, M. E.; Rossi, M. J.; Troe, J. A*tmos. Chem. Phys.* 2**004,** 4, 1461.

Appendix A: Explanation of Variables and Programs in Multiexponential Ring-down Code Used to Simulate $HONO_2$ Spectra.

The code for simulating multexponential ring-downs is available in Andrew Mollner's thesis and in the Okumura group dropbox: Dropbox (Okumura Group)\17 Noyes\Matlab\Matlab ring-down simulations from Andrew. Here I give a summary of all the programs and all the variables used in the code.

Variables

Variable	Calculated by another program?	Description
fwhm	no	"Fwhm of Lorentzian profile you are convoluting"
regionwidth	no	"total width over which each spectral point will be 'spread'". Andrew suggests using a value of 4*fwhm
Spectrum	no	Spectrum to convolute. 2D matrix. First column is wavelength; second column is intensity
xi, xf	no	"range of simulated spectrum"
laserfwhm	no	Fwhm of laser
modespace	no	"spacing of modes for Gaussian laser profile. Generally assumed to be 0.00666cm^{-1} we expect from the YAG cavity" Is 0.00666cm^{-1} the spacing for the old YAG!?
centerwavenumber	no	"the frequency at which the laser is centered"
Times or fulltimes	no	"1D column array specifying the time axis of the ringdowns. Should reflect the number of points and sample rate of the experiment you are simulating"
combpattern	yes	Output of Gaussiancomb.m A simulated Gaussian laser profile.
cavitylifetimes	no	2D matrix. First column is wavenumber and the second is the values of 1/tau (not just mirror. Put in 1/tau for the cavity with the sample!)
Decay, or fulldecsignal	yes	Full simulated ringdown (at one wavelength, centerwavelength)

simpleavg	yes	Weighted average of the ringdown times. Weighted by the relative intensity at each wavelength.
fitparam	yes	Output of LMDecayFit (LMDecayFitModified.m) that gives information about the exponential ringdown fit. It's a matrix in this order: [amplitude, 1/tau, number of iterations, chi^2]
inita	no	Initial guess for the amplitude of the ringdown
initb	No	Initial guess for 1/tau
absspectrum	maybe	Like spectrum. Needed for RingSimFixedBatch.m and RingSimVarCutBatch.m can be spectrum or can be the output of Lorentzbroaden.m
Background	Yes	Background value of 1/tau (for empty cavity?)
scalefactor	yes	The different "concentrations" of the peak that you want. You need to look/modify the code to make sure that this is actually numerical concentration.
Scannedwavenumbers	yes	What wavenumbers you want it to simulate the spectrum with for the batch programs.
integrals	no	
summary	no	6 columns: 1. integral of simulated ringdown spectrum 2. integral of simple average spectrum 3. first point ringdown spectrum 4. first point simple average spectrum 5. last point ringdown spectrum 6. last point simple average spectrum

Programs

Program	"Sub" programs	Input Variables	Outputs	Description
Lorentzbroaden.m	none	Fwhm, regionwidth, spectrum	Just say ans, but this is the Lorentz broadened spectrum,	Convolutes input spectrum with Lorentzian lineshape to simulate pressure broadening

			Broadspec or abspectrum	
findindex.m	none	Spectrum, xi or xf	Index number of matrix (spectrum),	Finds index numbers for your matrix.
trapintegrate.m	findindex.m	xi,xf,spectrum	Value of integral, **trapintegrals**	Integrates your spectrum using rectangles
Gaussiancomb.m	none	Laserfwhm, regionwidth, modespace	**combpattern**	Creates a Gaussian shape to simulate laser profile.
CombDecay.m	Gaussiancomb (not directly, it needs its output, combpattern) Maybe: Lorentzbroaden (again, not directly, but if you want to put in the pressure broadened spectrum…)	centerwavenumber, times, combpattern, cavityinvlifetimes	Simulated multiexponential ringdown, **decay** weighted average of all the ringdown times, **simpleavg**	Was combdecay3.m in Andrew's thesis. Simulates the ringdown. Takes the ringdown of each part of the laser and combines them all into a multexponential. Also, will give an average of all the ringdown times weighted by the relative intensities of the laserbeam at each wavelength.
LMdecayfit.m	Need to get fulldecaysignal from combdecay	fulltimes,fulldecsignal,inita,initb	[amplitude, exponent, number of iterations, chi^2], **fitparam**	Fits the simulated decay from combdecay with a Lev-Mar algorithm. This program uses a set amount of ringdown to cut.

LMdecayfitVarCut.m	LMdecayfit.m	fulltimes,fulldecsignal,inita,initb	[amplitude, exponent, number of iterations, chi^2], **fitparam**	Just like Ldecayfit.m, but will fit the ringdown twice, once with LMdecayfit.m and a second time cutting a portion of the ringdown and refitting (much like we do on LabView).
RingSimFixedCutBatch.m Or RingSimVarCutBatch.m	Gaussiancomb., LMdecayfit.m or LMdecayfitVarCut.m, CombDecay.m	laserfwhm, regionwidth,modespace, times, scannedwavenumbers, background, scalefactor, absspectrum	**Ringspec**, all the fitted ringdowns from decay from combdecay **Simplespec**, all the simpleavg for each point	This program takes all the frequency values that you want and makes a simulated ringdown and a simple average tau for each frequency that you want
SFBatchFixCut.m or SFBatchVarCut.m	RingSimFixedCutBatch.m Or RingSimVarCutBatch.m (and therefore all the programs they need). Trapintegrate.m	scalefactors, xi,xf,absspectrum,background,scannedwavenumbers, times,laserfwhm,regionwidth,modespace	**Ringspec, simplespec, integrals, Summary,** first column	Repeats RingSimFixedCutBatch.m or RingSimVarCutBatch.m with different scale factors (concentrations)

Chapter 6: Rotational energy transfer in collisions between CO and Ar at temperatures from 293 to 30 K: Infrared-Vacuum Ultraviolet Double Resonance CRESU Experiments

Abstract

Intermolecular forces, including van der Waals forces, influence many chemical and physical properties, including collisional excitation, collisional relaxation, pressure broadening, thermal conduction, and diffusion. Due to argon's large polarizability and consequently its large van der Waals forces, the Ar-CO system has been studied extensively as a model for these long range forces. While many experiments have studied the pressure broadening of CO in Ar and found spectra of the CO-Ar complex, less work as explored the rate of collisional energy transfer between Ar and CO. We have found total and state-to-state rate constants for collisional energy transfer for CO in Ar with infrared-vacuum ultraviolet double resonance experiments at temperatures down to 30 K with the CRESU technique. Our results found trends similar to work on the CO/He system, but with larger rate constants for Ar, likely due to Ar's strong intermolecular forces. Our data is compared to theoretical calculations from the University of Bordeaux, and will be used to refine the theoretical potential energy surface of the CO/Ar system and deepen our understanding of van der Waals forces.

Introduction

Ar-CO is a model system for understanding intermolecular forces,[1] as owing to its large polarizability, van der Waals forces are stronger for Ar than for smaller atoms, such as He. Understanding these long-range forces is essential to calculating many properties of gases.[1-4] A reliable potential energy surface describing these intermolecular forces can be used to calculate bulk properties of gases including viscosity, diffusion, thermal conductivity, and virial coefficients.[5-9] These long range forces also influence pressure broadening of spectra; larger van der Vaals forces generally lead to more broadening. So, an understanding of long range forces is needed to accurately predict the spectra of atoms and molecules.[3,4,10-12]

Intermolecular forces also control the rate of collisional rotational energy transfer in gases. Rate constants for rotational energy transfer are needed to predict the lifetimes of energetically excited molecules – an important issue in physical chemistry because these "hot" reactants can react differently, leading to new product channels or non-thermal product distributions.[13] Unimolecular reactions require collisional excitation in order for reaction to occur;[14] calculating the reaction kinetics with methods like RRKM (Rice Rampsberger Kassel Marcus)[15] theory or the SACM model[16] requires a thorough understanding of rotational energy transfer and intermolecular forces. Rotational energy transfer is important to deriving CO column densities in the interstellar medium, because rotationally excited CO molecules emit microwave radiation detectable on Earth. This microwave signal is dependent on the number of rotationally excited molecules of CO which could emit radiation – an equilibrium that is greatly influenced by collisional excitation of CO from collisions with abundant interstellar species such as H, H_2, and He.[17,18]

While theoretical methods can calculate extensive matrices of state-to-state rate constants for rotational energy transfer a large variety of compounds, these calculations depend on the quality of the available potential energy surfaces, especially at low temperatures. In order to ensure accuracy of these computations, the theory must be benchmarked with experiments, especially with model systems like CO-Ar. In this way, theory can be refined to ensure accurate values for other systems and then can predict rate constants for rotational energy transfer, spectral linewidths of gases, and bulk properties of gases like viscosity.

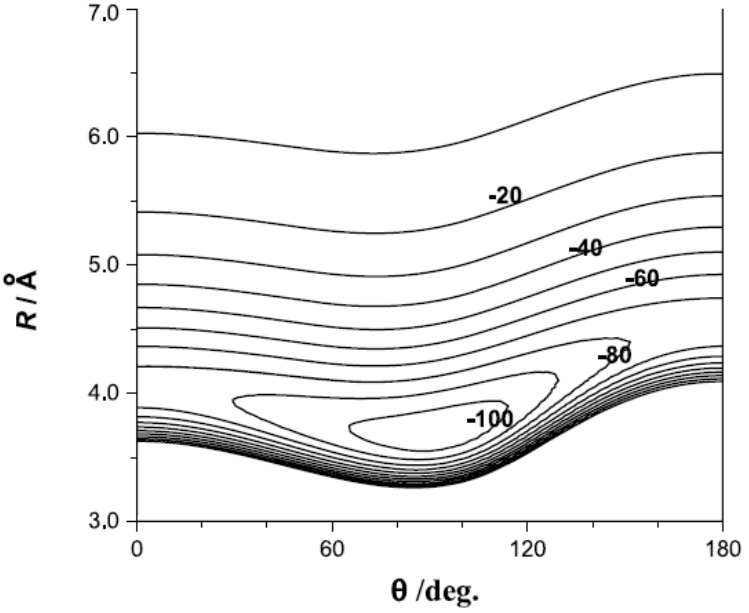

Figure 1. Potential energy surface calculated by Sumiyoshi and Endo.[19] θ=0° corresponds to Ar···OC and θ=180° corresponds to Ar···CO. R is the distance between Ar and the CO molecule.

The CO-Ar complex has been the subject of extensive experimental and theoretical studies as it serves as a prototype of weakly bound clusters. Several potential energy surfaces for Ar-CO have already been published[19-23] and compared to a variety of experimental methods, including studies on the collisional line broadening of CO in Ar[10-12,24,25] and spectroscopic

studies of the Ar-CO van der Waals complex.[26-29] Havenith and Schwaab have summarized many of these studies in their 2005 review article.[1] Very recently, Sumiyoshi and Endo[19] have provided an updated survey and a high quality 3D potential energy surface for the Ar-CO system using coupled cluster theory (CCSD(T)-F12b/aug-cc-pV5Z). They parameterized this potential energy surface to reproduce experimental spectra of the Ar-CO complex. State-to-state rate constants for rotational energy transfer would provide an additional test of this potential energy surface, especially at low temperatures where the collision energy is of the same order or less than the Ar-CO var der Waals well. While state-to-state rate constants for rotational energy transfer have been reported for CO in He, much less work is published on rates of rotational energy transfer between CO and Ar.[30-32] The most recent measurement, from 1999,[32] found state-to-state rate constants for rotational energy transfer of CO in Ar with a double resonance experiment, but they used a free jet expansion, which required complicated deconvolution since the beam was at multiple temperatures.

We found total and state-to-state rate constants for the rotational relaxation and of CO in Ar between 30 and 295 K using infrared-vacuum ultraviolet double resonance (IRVIVDR) in a CRESU (Cinétique de Réeaction en Ecoulement Supersonique Uniforme or Reaction Kinetics in a Uniform Supersonic Flow) apparatus. The CRESU technique produces supersonic expansions at uniform temperatures ideal for studying chemical kinetics.[33,34] The IRVUVDR technique allows us to obtain absolute state-to-state rate constants. By exciting the CO to $v = 2$, we can specifically choose the initial rotational energy level with the IR frequency, and by varying the delay between the IR and the VUV laser pulses, we can watch the rotational energy transfer in real time. VUV laser induced fluorescence (LIF) provides a sensitive detection method,

allowing us to work at very low [CO] (<0.5%). Nanosecond lasers gave us a time resolution of ca. 5 ns, enough to probe the fast kinetics of rotational energy transfer.

Experimental

The CRESU apparatus was built specifically for studying the kinetics of neutral-neutral reactions,[35,36] and has been successfully used to find state-to-state rate constants for collisional rotational energy transfer in diatomic molecules at temperatures as low as 7 K.[17,37] The CRESU and IRVUVDR techniques have been described in detail by James *et al.*[37] and Carty *et al.*[17] Briefly, gas from a reservoir is compressed through a specially-design laval nozzle to create a supersonic expansion into a large vacuum chamber (Figure 2). The laval nozzle's convergent, divergent design creates a nearly uniform temperature distribution in the supersonic jet, which is necessary for kinetics.

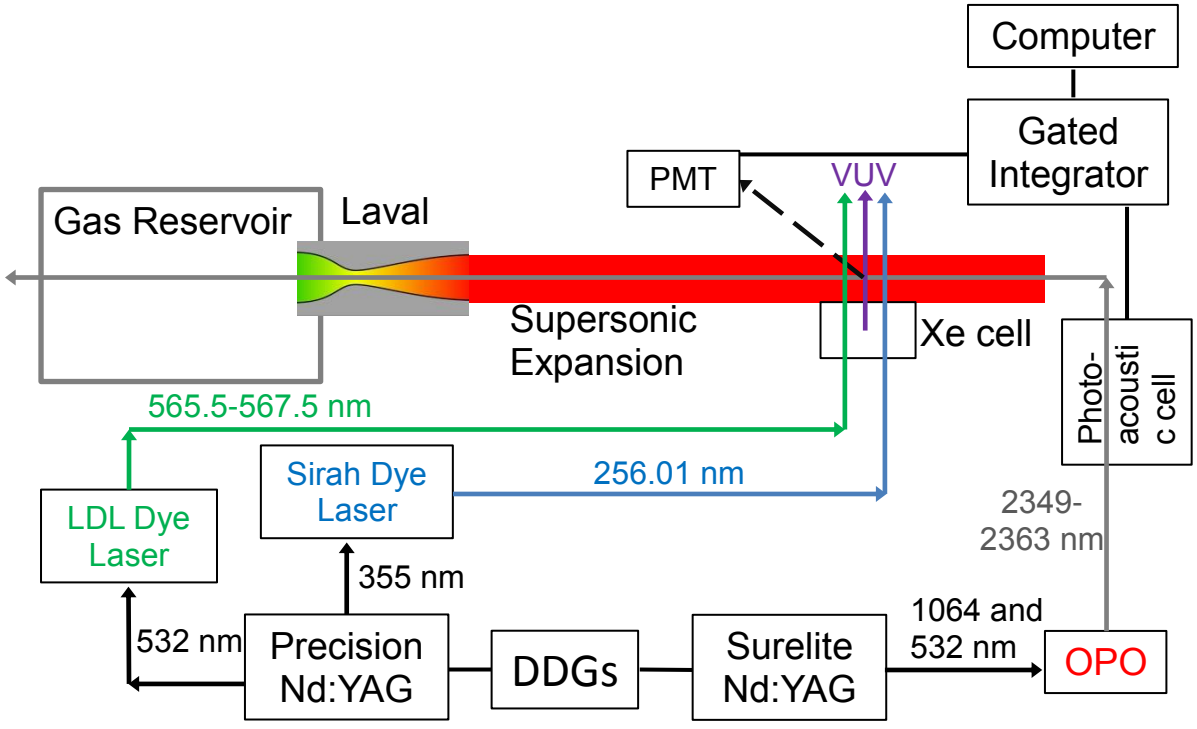

Figure 2. Schematic of the CRESU/ IRVUVDR experimental set-up.

In a typical experiment, CO molecules are excited to their second (v = 2) vibrational excited state by an infrared pulse that propagates anti-parallel to the supersonic expansion. By tuning the frequency of the IR laser, we can choose the exact rotational level in the excited state (for example, if we excite the P(1) IR transition, 100% of the initial population in the excited (v = 2) state will be in J = 0). Through collisions with the Ar bath gas, the CO molecules will relax to rotational equilibrium (vibrational relaxation is negligible on the timescales, 0 – 2 μs, of the experiments), and at any time the rotational state of the CO can be probed with laser induced fluorescence (LIF) by detecting the $A^1\Pi - X^1\Sigma^+$ (0,2) band of CO in the VUV.

IR light was produced by a LaserVision KTP OPO with OPA pumped by a Continuum Surelite EX injection seeded YAG laser operated at 10 Hz. 5-10 mJ pulses of IR light were produced at 2349.5, 2351.67, 2358.41, or 2363.12 nm to study J = 0, 1, 4 and 6, respectively. Vibrations in the room produced frequency and wavelength fluctuations from the OPO: power typically fluctuated between 5 and 10 mJ/pulse with frequency fluctuations of 0.04 nm (2σ standard deviation). To reduce noise from these fluctuations, we discriminated data points based upon signal received from a custom-built photoacoustic cell filled with 8 mbar of CO.[17] The photoacoustic signal from this cell was amplified with a Stanford Research SR560 low-noise voltage amplifier before being integrated with a Stanford Research SR250 gated integrator with a 15 μs gate. A custom LabView (National Instruments) program discarded points for which the photoacoustic signal was below a predetermined threshold (generally set at ~1.2 times the average photoacoustic signal).

VUV light needed for LIF detection of the vibrationally excited CO was produced through 4-wave frequency mixing in Xe gas as described by Hilbig and Wallenstein.[38] In this method, VUV light is produced using two 256.01 nm photons to excite the $5p^5 6p(5/2)_2 \leftarrow 5p^6$

$^1S_0$ transition of Xe. A visible photon at 565.5 – 567.5 nm stimulates the emission of photons at 565.5 – 567.5 nm and 165.29 – 165.45 nm. The 256.01 nm light is produced with a Sirah Lasertechnik Cobra-Stretch dye laser with Courmarin 503 dye (Exciton) pumped by a frequency tripled Continuum Precision II YAG laser (355 nm) operated at 10 Hz. The output of the dye laser (512.02 nm) was frequency doubled with a BBO crystal to produce ~1 mJ of the desired 256.01 nm light. A frequency doubled output of the Continuum Precision II YAG (532 nm) also pumped a Laser Analytical Systems LDL 20505 dye laser operated with Rhodamine 6G dye (Exciton) dye to produce ~8 mJ/pulse of 565.5 – 567.5 nm light. These two beams were focused through a fused silica window into a cell filled with 2.7 torr of Xe, producing VUV light which was recollimated by 7 cm focal length MgF_2 lens into the CRESU chamber perpendicular to the IR beam.

LIF signal was recorded with an ET Enterprises 9403B photomultiplier tube equipped with an Acton Research Ltd bandpass interference filter centered at 158.9 nm with a 23.4 nm bandwidth. The signal from the photomultiplier tube was sent to the Stanford Research SR250 gated integrator where the signal was integrated with a 16 ns gate and sent to the computer to be recorded with LabView software. Timing between the IR and the VUV pulses was controlled with two Stanford Research SR535 digital delay generators.

Three different nozzles were used to produce supersonic flows at 110.6 K (110.6 K. with a density of 2.7×10^{16} cm^{-3} with a flow of 44 standard liters per min (SLM) of Ar), 52.2 K (5.2×10^{16} cm^{-3} with a flow of 44 SLM or Ar), and 30.5 K (1.9×10^{16} cm^{-3} with a flow of 15.5 SLM of Ar) in addition to a laminar subsonic flow at room temperature, 293 K ($2 - 4 \times 10^{16}$ cm^{-3} with a flow of 2 - 3 SLM of Ar). The pressures in the chamber and the gas reservoir were measured using MKS Baratron absolute capacitance manometers (629F, heated to 45° C, 1Torr for the

chamber; 626C 100 Torr for the reservoir), and flows were controlled with MKS Mass-flow controllers (1179A and 1559A). In all experiments the CO concentration was kept at or below 0.6% of the Ar concentration, so we expect minimal interference from CO/CO collisions. Pressure and temperature in the supersonic expansion were measured by means of impact pressure measurements employing a Pitot probe.[35] An example of a beam profile measured with our Pitot Probe is shown in Figure 3. All pressures and flows during experiments were within 5% of the conditions for the Pitot measurements. Gases were evacuated from the chamber with a combination of five vacuum pumps (a mechanical primary pump and four roots pumps) with a combined pumping speed of about 29,000 m^3 hr^{-1}.

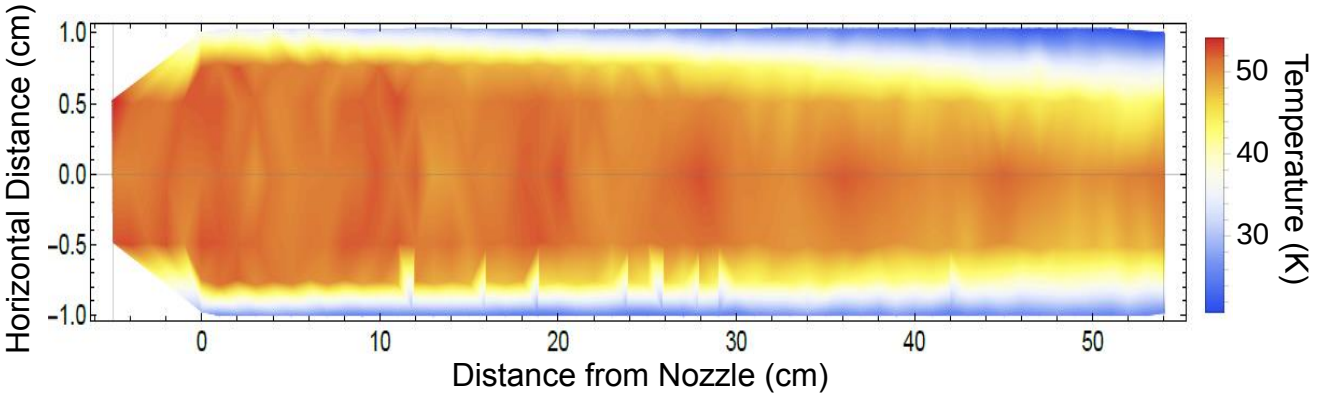

Figure 3. An example of a beam profile (Ar 52 K) from our pitot probe.

Analysis of Experimental Data

We performed two types of experiments: a total-removal experiment in which we watched the signal of the original rotational state decay with time (Figure 4) and state-to-state experiments by which we obtained state-to-state rate constants using spectra at very short delay times (Figure 5). These data analysis methods have been previously discussed in greater detail by Carty *et al.*[17] and James *et al.*[37]

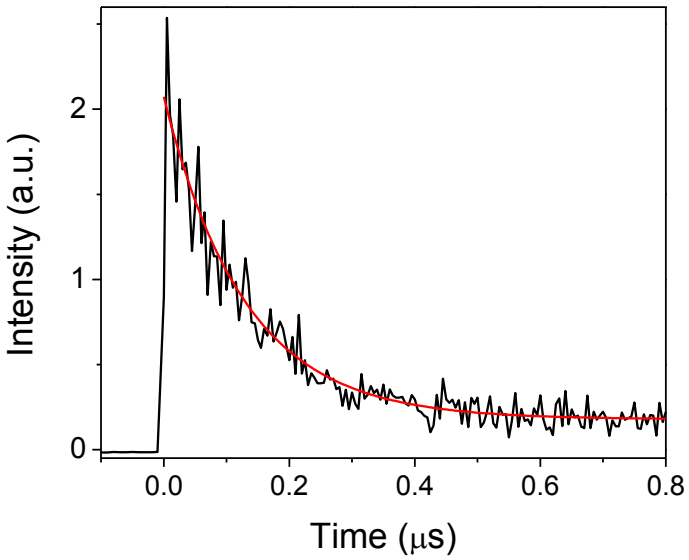

Figure 4. A typical LIF decay (black) used to find total removal rate constants, taken at 295 K with $J_i = 6$ (IR wavelength = 2363.122 nm) and detecting the LIF signal of the Q(6) branch in the excited state at 165.358 nm) with a 5 ns step size. The exponential fit is shown in red.

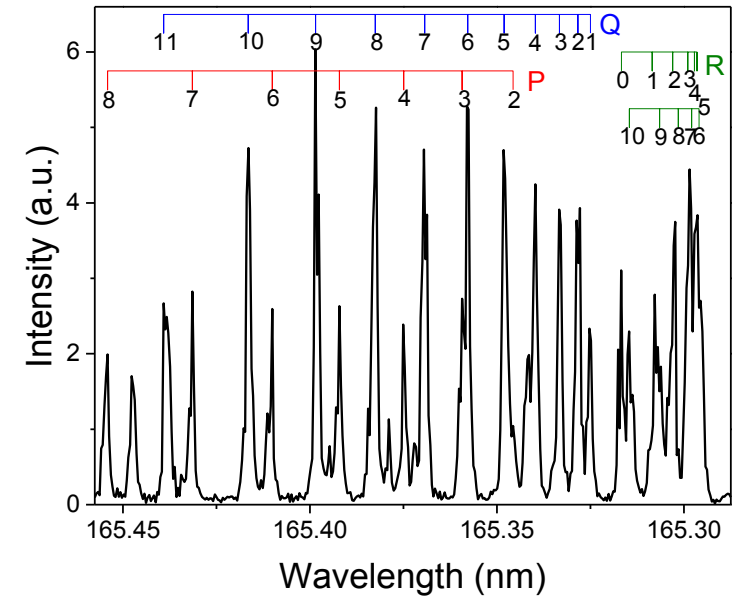

(a)

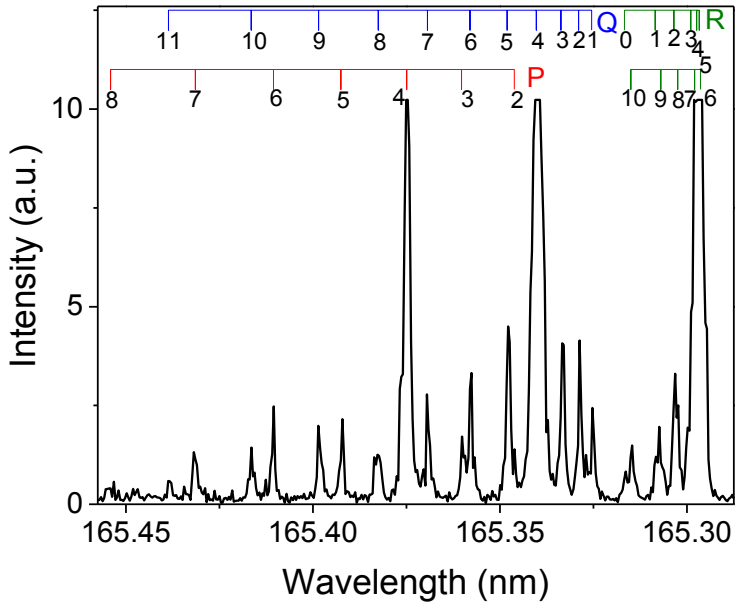

(b)

Figure 5. Double resonance spectra taken at room temperature at a (a) 1.5 μs delay, in which the CO is in rotational equilibrium and (b) 30 ns delay, in which most of the population is still in the initially excited rotational level, $J_i = 4$ in this case.

A. Total Removal Rate Constants and Cross Sections

The frequency of the IR laser selects a rotational state, J_i, in which the entire CO population in $v = 2$ starts out. Within ~1μs the population relaxes to rotational equilibrium. The total rate for collisional rotational relaxation from a given rotational level (we chose $J_i = 0$, 1, 4, and 6) can be found by recording the decay of the LIF signal of Q(J_i) as a function of time (Figure 4). We chose the Q branch of the $A^1\Pi - X^1\Sigma^+$ (0,2) band of CO because it is more intense than the P branch and its lines are more isolated than the R branch. A typical decay is shown in Figure 4. The decays were fit to a simple exponential model with a floating baseline using the Levenberg-Marquardt algorithm to find the exponential decay rate, $k_{exp,}$ which is the inverse of the exponential decay time, τ. Since there is significant reverse reaction from all of the other states, $J_{f,,}$ to the initial state, J_i, k_{exp}, must be corrected with the following equation in order to find the rate of total removal from $J_{i,}$ k_{tot}:

$$k_{tot} = \frac{k_{\exp}(1 - f_{J_i}^{eq})}{[Ar]} \quad (1)$$

where $f_{J_i}^{eq}$ is the Boltzmann factor of J_i at rotational equilibrium divided by the partition function, or simply the proportion of CO molecules in state J_i at equilibrium. This equation assumes that the rate of constant for the reverse reaction at any time is equal to the reverse rate constant from an equilibrium distribution of states. Thus, the kinetics model assumes a simple forward and reverse rate between two states: J_i and a fully rotationally relaxed equilibrium distribution.

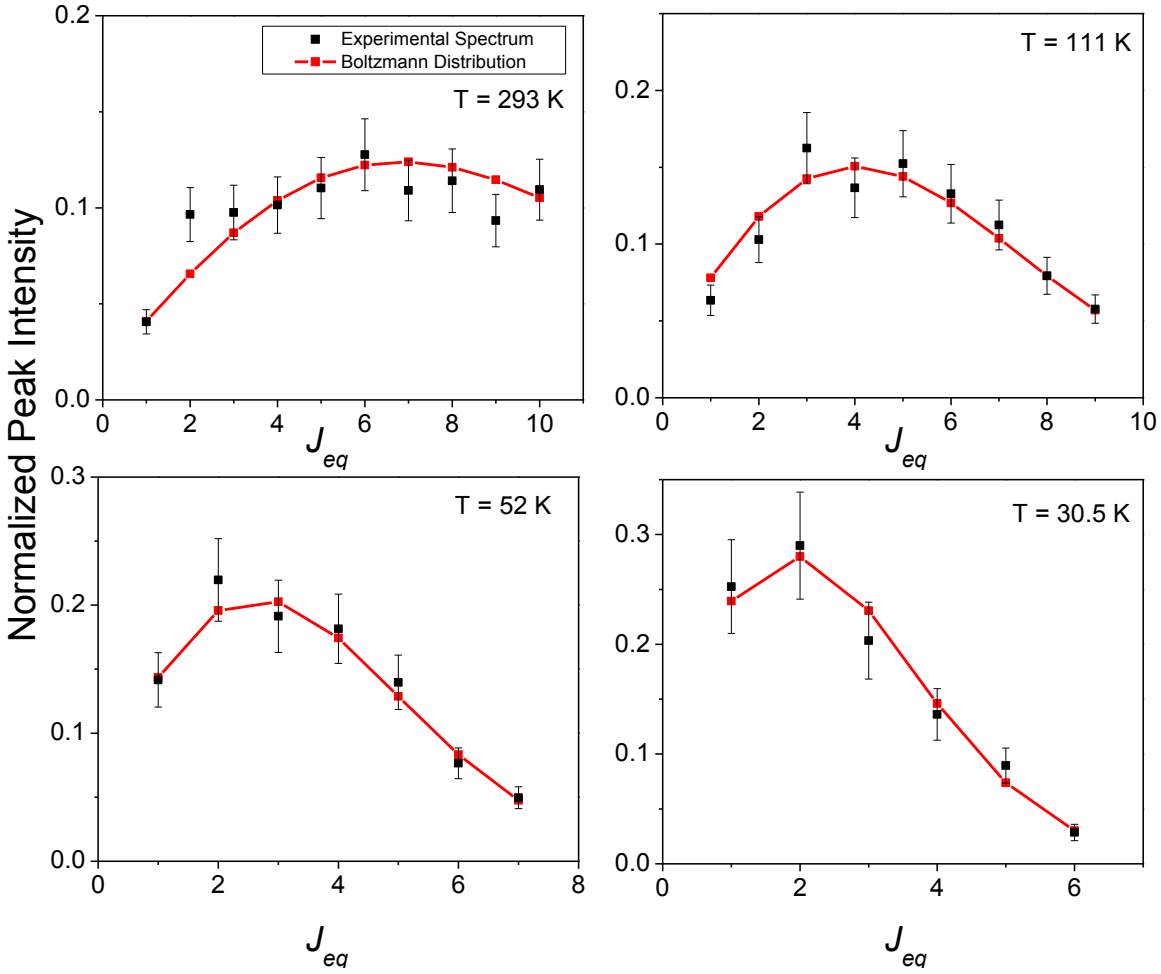

Figure 6. The normalized intensity of peaks from our double-resonance spectra at 293, 111, 52, and 30.5 K (black) compared to theoretical Boltzmann weights (red).

J_i will be populated at rotational equilibrium, so the exponential traces do not decay to zero, as shown in Figure 4. Since, the baseline is determined by the population in J_i at rotational equilibrium, we can calculate the rotational temperature by dividing the baseline by the maximum LIF intensity (which represents the total population of partition function). All values of rotational temperature calculated with this method were found to be within error (2σ) of the temperature measured by the Pitot probe. The temperature was also confirmed with the relative

intensities of peaks, which always followed a Boltzmann distribution for the expected temperature (Figure 6).

B. State-to-State Rate Constants

We also found individual state-to-state rate constants from J_i (again we chose J_i = 0, 1, 4, and 6) to J_f (for J_f = 0 – 10). To do this, we assume that at very short times there will be an approximately linear increase in the population of J_f, and we chose reaction times (15 – 50 ns) in which the "linear rate" would be off from the exponential rate by less than 10% (according to the total removal rate). If the increase in J_f is linear, the constant can be found simply by dividing the amount of CO in state J_f by the time delay (Δt) and the concentration of Ar ([Ar]). The amount of CO in state J_f at time Δt can be found from the intensity of J_f absorbance for the $A^1\Pi$ – $X^1\Sigma^+$ (0,2) band of CO, $I_{J_f}^{\Delta t}$. We also need to correct for the total population of CO that started in J_i, which is given by $I_{J_f}^{eq} * (f_{J_f}^{eq})^{-1}$. The total equation for the rotational relaxation rate constant from J_i to J_f is given by the following equation:

$$k_{J_i \to J_f} = \left(\frac{I_{J_f}^{\Delta t} f_{J_f}^{eq}}{I_{J_f}^{eq}} \right) \frac{1}{\Delta t [Ar]} \qquad (2)$$

In order to find values for $I_{J_f}^{\Delta t}$, we took a double resonance spectrum at Δt = 15-50 ns; to find values for $I_{J_f}^{eq}$ we took a spectrum at times long enough for the CO to achieve rotational equilibrium, Δt we set to 1.5 - 2 μs. Figure 5b shows a double resonance spectrum in rotational equilibrium at room temperature (295 K), and Figure 5a shows a spectrum taken only 30 ns after the IR pulse, in which the majority of the population is still in J_i = 4. Since we need the intensities of the small peaks (J_f = 0, 1, 2, 3, 5, 6, 7, 8, 9, and 10), we used a scale in which the J_i = 4 peaks were completely saturated. Peaks were assigned experimentally, by taking spectra 10

ns after the IR pulse; at these time scales the population is almost entirely in the initial rotational state J_i, determined by the wavelength of the IR light. We fit all peaks to Gaussians with deconvolution fitting using PeakFit (SyStat) software, and the amplitude of each peak was used to calculate the state-to-state rate constants according to the above equation.

Results

To obtain experimental state-to-state rate constants, we took two IRVUVDR spectra: one at short delays (15 - 50 ns) and one at long delays (1.5 - 2 μs), and used equation (2) to derive state-to-state rate constants. The procedure was repeated at four different temperatures (30.5, 52, 111, and 293 K) and four different values of J_i (0, 1, 4, and 6). We also recorded the decay of the double-resonance signal of J_i with time for these same temperatures by scanning the delay time between the IR and the VUV laser pulses. This decay was fit to a simple exponential to derive the rate constant using equation (1).

These experimental results are compared to the theoretical rates in Tables 1, Table 2, Table 3,and Table 4 for 110.6, 52.2, and 30.5 K, respectively. Rate constants were found for four values of J_i (0, 1, 4, and 6). The experimental values are given with 2σ errors, and the theoretical values are given without error in parentheses. In general, we find very good agreement between theory and experiment, as shown in Figure 7 – 10 which plot the state-to-state rate constants for theory and experiment for J_i = 0, 1, 4, and 6 at temperature 30.5, 52, 110.6 and 293 , respectively. Tables 1-4 compare the total removal rate constants found from fitting the first-order decay of the double resonance signal of J_i and the sum of the state-to-state rate constants. In all cases, except room temperature, these values are within combined errors, which means not only that are total removal and state-to-state experiments are consistent, but that the state-to-state rate constants include all the major rate pathways (i.e. there are no

significant contributions from J_f > 10). For ambient temperatures, the state-to-state rate constants will likely not agree exactly with the total removal, since we only found rate constants up to J_f = 10 when there are likely significant contributions from higher J values. Additionally, some of the total removal rates are less accurate at this temperature, notably J_i = 0, due to spectra interference.

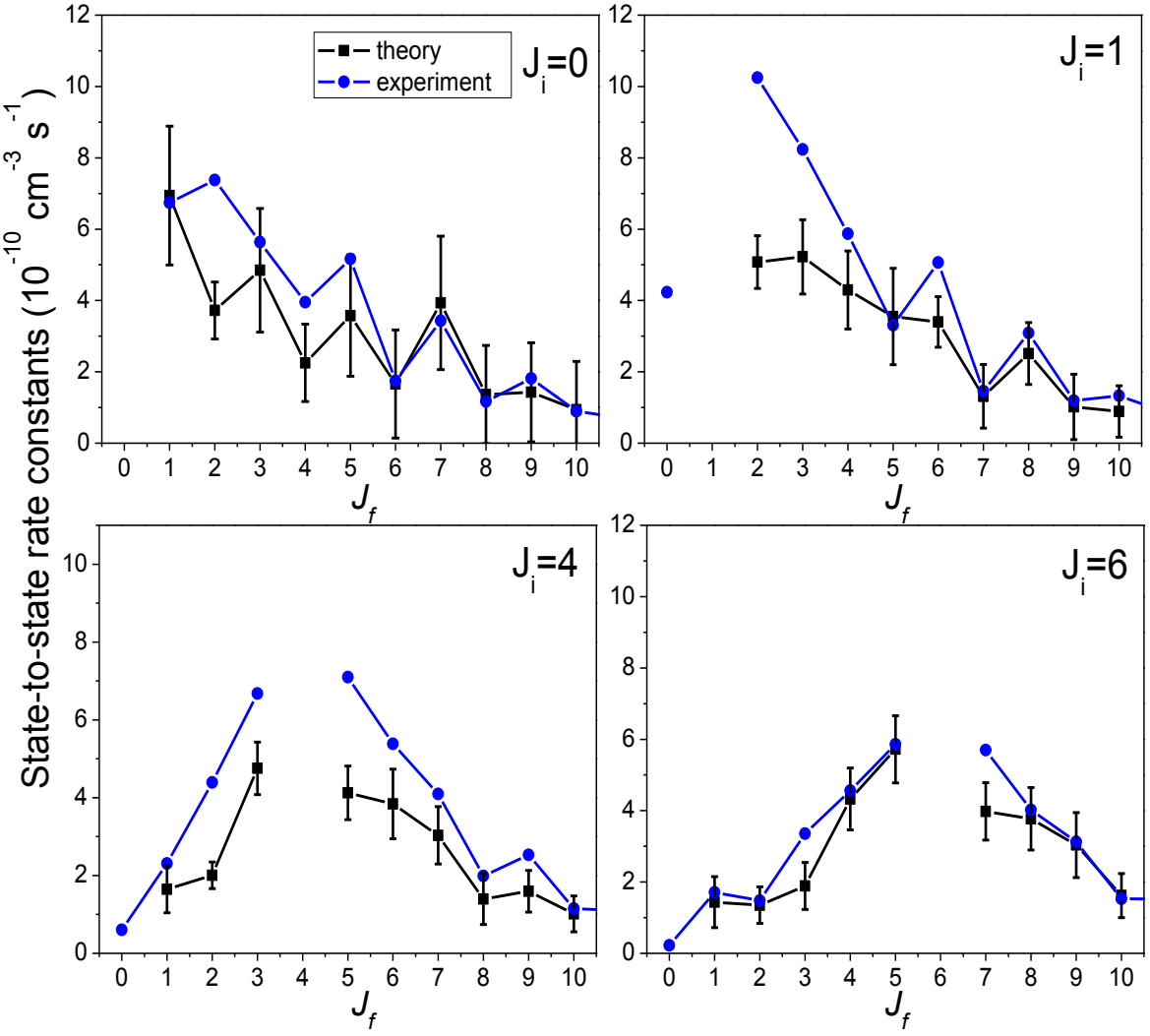

Figure 7 State-to-state rate constants for J_i =0, 1, 4, and 6 at ambient temperature, 293 K (black, 2σ error) compared to theory (blue).

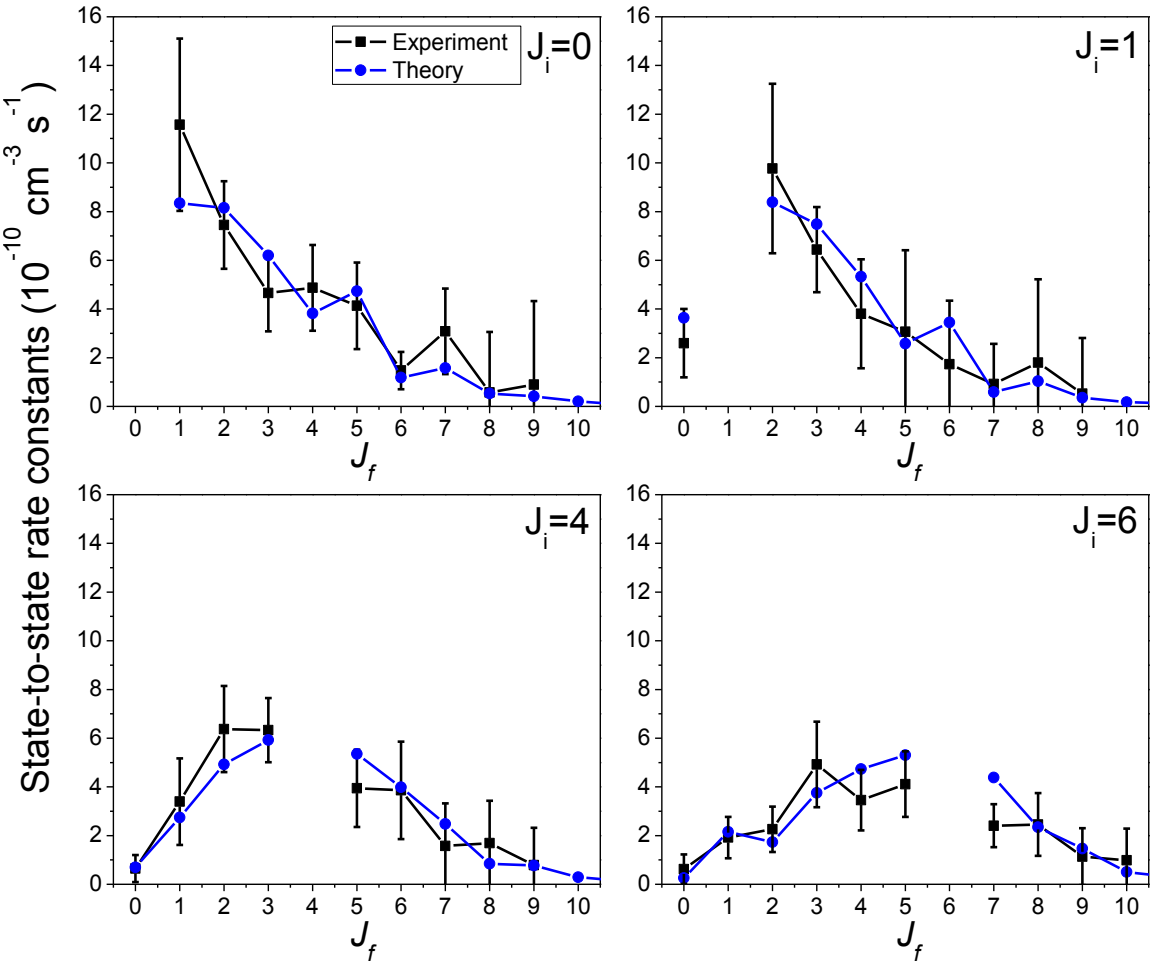

Figure 8. State-to-state rate constants for J_i =0, 1, 4, and 6 at 111 K (black, 2σ error) compared to theory (blue).

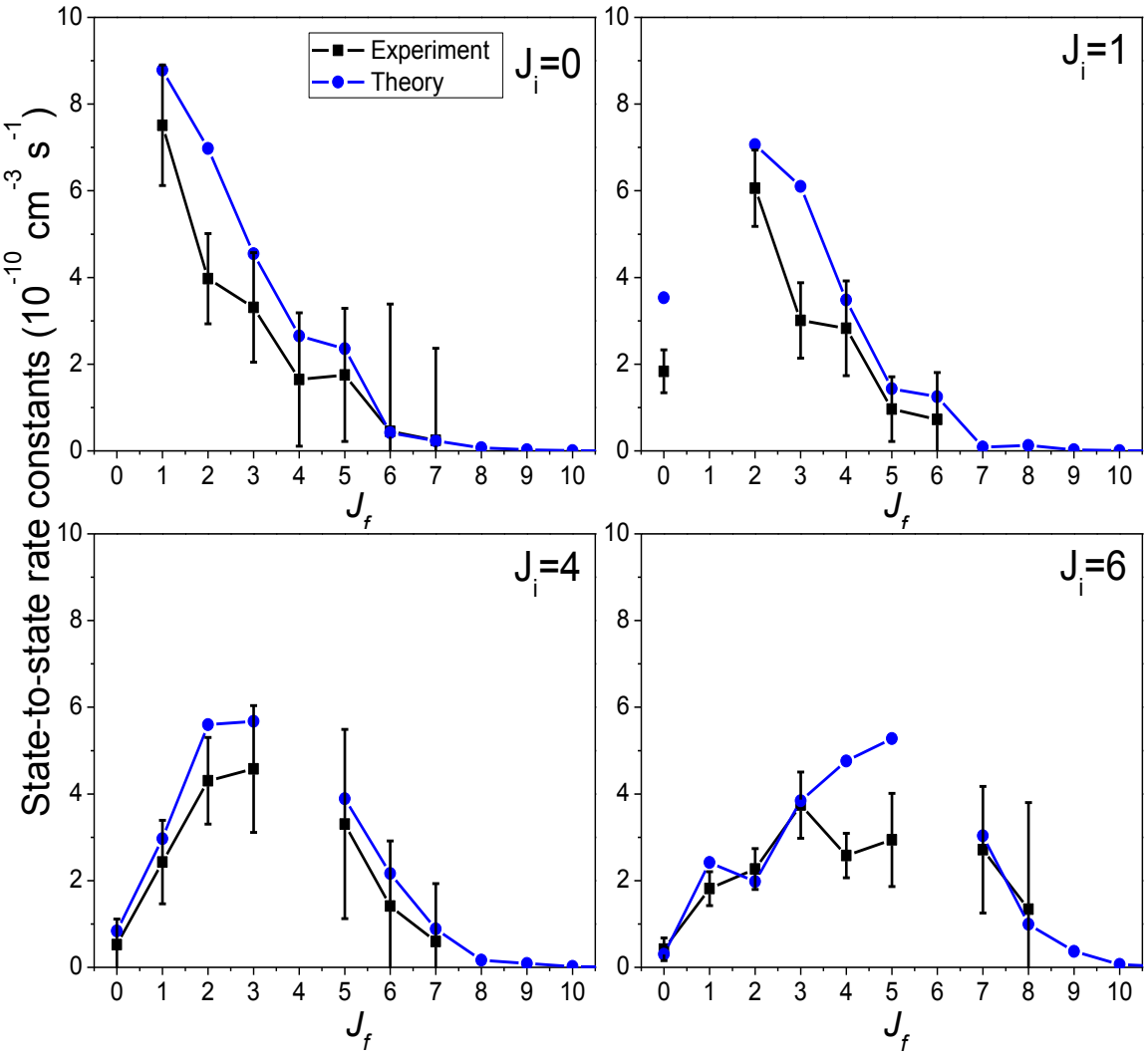

Figure 9. State-to-state rate constants for J_i =0, 1, 4, and 6 at 52 K (black, 2σ error) compared to theory (blue).

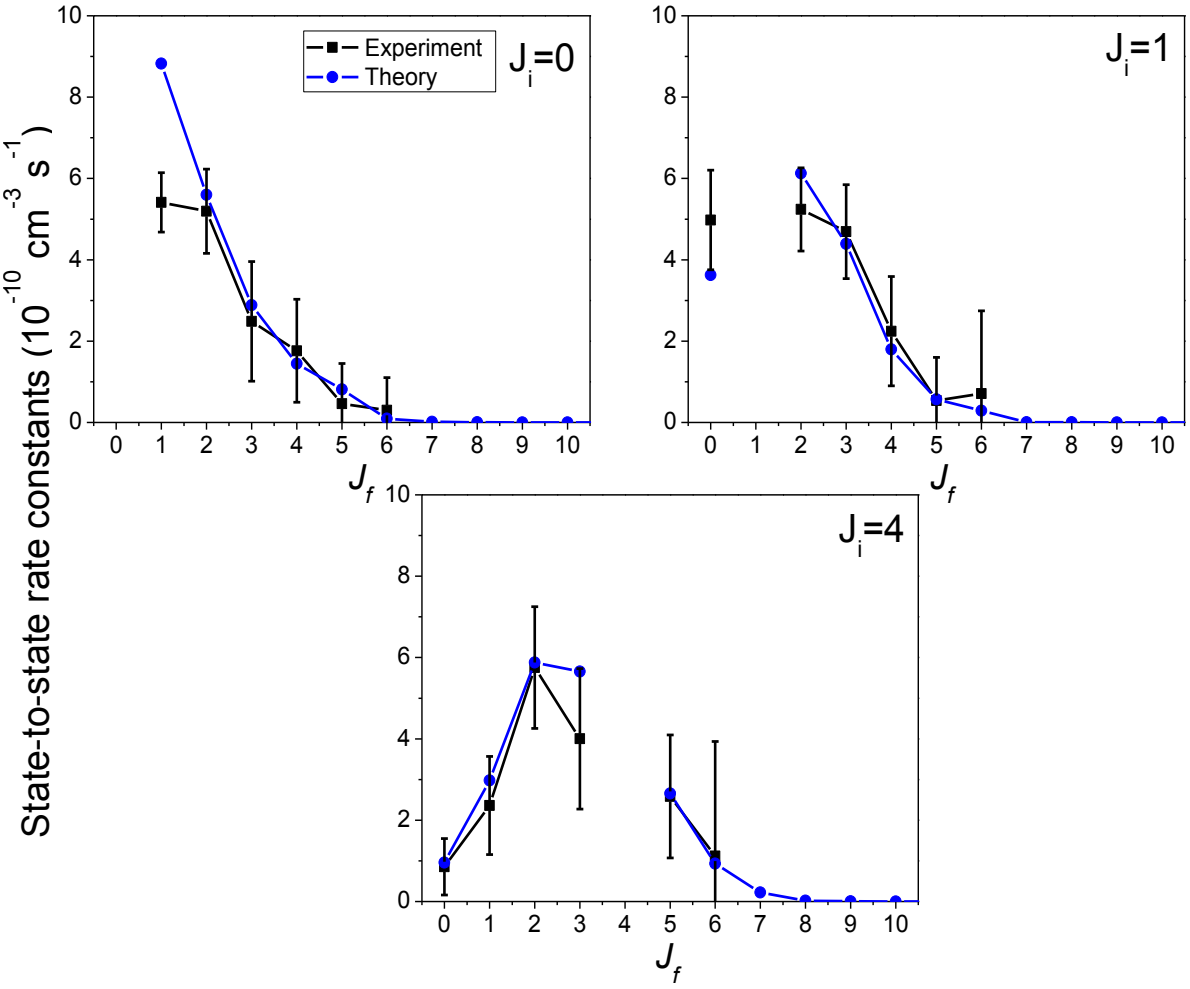

Figure 10. State-to-state rate constants for J_i =0, 1, 4, and 6 at 30.5 K (black, 2σ error) compared to theory (blue).

Figure 11 plots the total removal cross section with the sum of the theoretical state-to-state rate constants for J_f = 0 - 20. As with the state-to-state rate constants, most experimental values are within error of the theoretical values. For J_i = 1, 4, and 6 the total removal cross section increases with decreasing temperature, with larger increases for J_i = 4 and 6 than for J_i = 1. While the total removal cross section for J_i = 0 initial increases, it begins to decrease at 52 K.

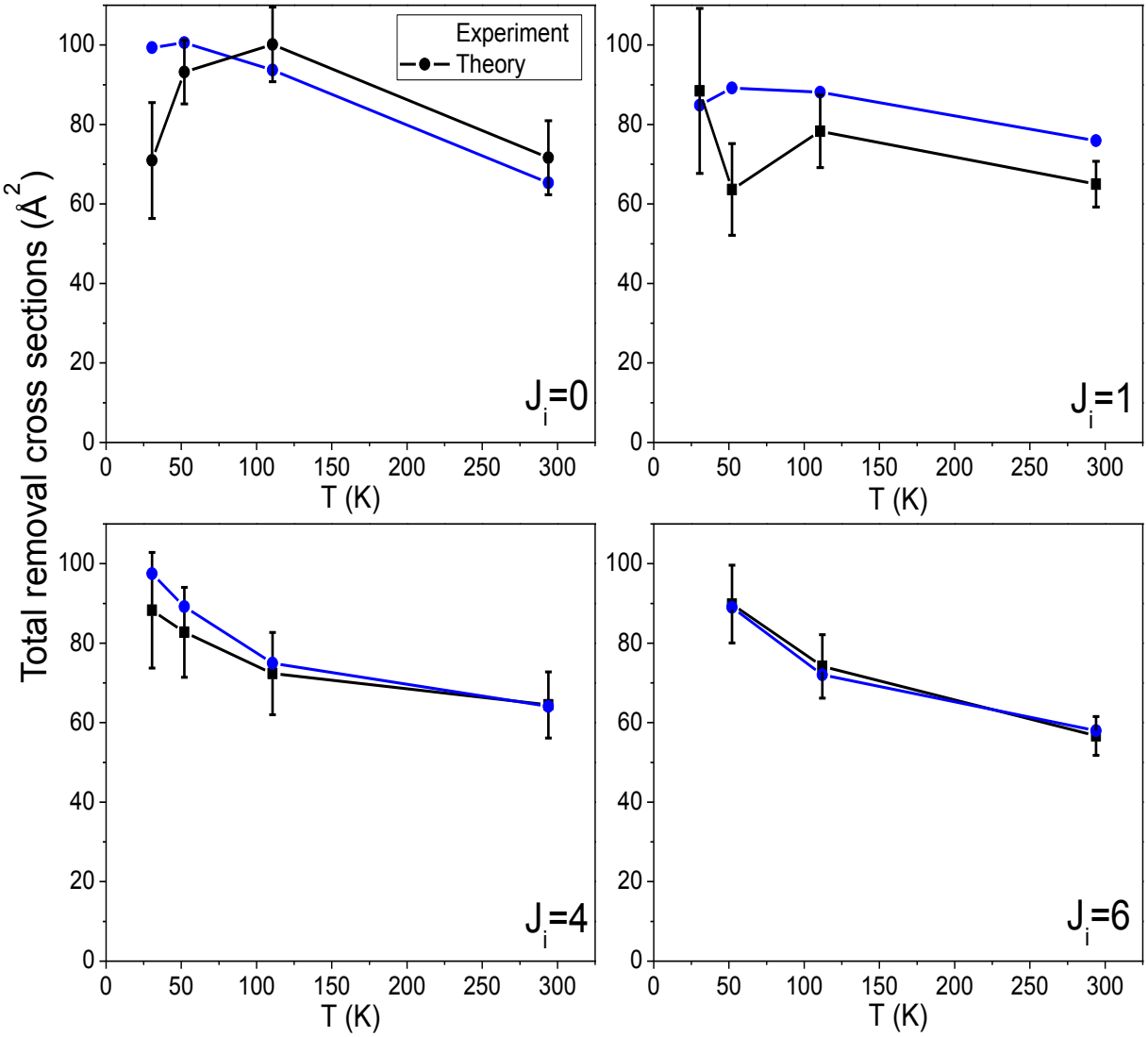

Figure 11. Experimental total experimental removal cross sections (Å^2) for J_i = 0, 1, 4 and 6 at T = 295, 111, 52, and 30.5 K (black, 2σ error) compared to the total theoretical cross sections, found by summing the theoretical state-to-state rate constants for J_f = 0-20 (blue).

Table 1. State-to-state rate constants for transfer between initial and final rotational states of CO in collision with Ar at ambient temperature (293 K) in units of 10^{-11} cm^{-3} s^{-1}. Experimental values are given with 2σ statistical errors and compared to theoretical values which are given in parentheses.

J_{final}	$J_{Initial}$			
	0	1	4	6
0	$J_{Initial}$	-	-	-
1	6.9 ± 1.9 (6.7)	$J_{Initial}$	1.7 ± 0.6 (2.3)	1.4 ± 0.7 (1.7)
2	3.7 ± 0.8 (7.4)	5.1 ± 0.7 (10.2)	2.0 ± 0.3 (4.4)	1.4 ± 0.5 (1.5)
3	4.8 ± 1.7 (5.6)	5.2 ± 1.0 (8.2)	4.8 ± 0.7 (6.7)	1.9 ± 0.7 (3.4)
4	2.3 ± 1.1 (4.0)	4.3 ± 1.1 (5.9)	$J_{Initial}$	4.3 ± 0.9 (4.6)
5	3.6 ± 1.7 (5.2)	3.6 ± 1.4 (3.3)	4.1 ± 0.7 (7.1)	5.7 ± 0.9 (5.9)
6	1.7 ± 1.5 (1.7)	3.4 ± 0.7 (5.1)	3.8 ± 0.9 (5.4)	J_{Initia}
7	3.9 ± 1.9 (3.4)	1.3 ± 0.9 (1.5)	3.0 ± 0.7 (4.1)	4.0 ± 0.8 (5.7)
8	1.4 ± 1.4 (1.2)	2.5 ± 0.9 (3.1)	1.4 ± 0.7 (2.0)	3.8 ± 0.9 (4.0)
9	1.4 ± 1.4 (1.8)	1.0 ± 0.9 (1.2)	1.6 ± 0.5 (2.5)	3.0 ± 0.9 (3.1)
10	0.9 ± 1.4 (0.9)	0.9 ± 0.7 (1.3)	1.0 ± 0.5 (1.1)	1.6 ± 0.6 (1.5)
$\Sigma k_{st\text{-}to\text{-}st}$	30.7 ± 4.8 (37.9)	27.3 ± 2.8 (39.8)	23.4 ± 1.9 (35.6)	27.1 ± 2.3 (31.3)
k_{Total}	50.8 ± 4.1 (40.2)	40.0 ± 3.5 (46.7)	39.8 ± 2.7 (39.4)	34.8 ± 3.0 (35.6)

Table 2. State-to-state rate constants for transfer between initial and final rotational states of CO in collision with Ar at 111 K in units of 10^{-11} cm^{-3} s^{-1}. Experimental values are given with 2σ statistical errors and compared to theoretical values which are given in parentheses.

J_{final}	$J_{Initial}$			
	0	1	4	6
0	$J_{Initial}$	2.6 ± 1.4 (3.6)	6.5 ± 0.6 (6.9)	0.6 ± 0.6 (0.3)
1	11.2 ± 3.5 (8.3)	$J_{Initial}$	3.4 ± 1.8 (2.7)	1.9 ± 0.8 (2.2)
2	7.5 ± 1.8 (8.2)	9.8 ± 3.5 (8.4)	6.4 ± 1.8 (4.9)	2.3 ± 0.9 (1.7)
3	4.7 ± 1.6 (6.2)	6.4 ± 1.8 (7.5)	6.3 ± 1.3 (5.9)	4.9 ± 1.8 (3.8)
4	4.9 ± 1.8 (3.8)	3.8 ± 2.2 (5.3)	$J_{Initial}$	3.5 ± 1.2 (4.7)
5	4.1 ± 1.8 (4.7)	3.1 ± 3.4 (2.6)	3.9 ± 1.6 (5.4)	4.1 ± 1.4 (5.3)
6	1.5 ± 0.8 (1.2)	1.7 ± 2.6 (3.4)	3.9 ± 2.0 (4.0)	$J_{Initial}$
7	3.1 ± 1.8 (1.6)	0.9 ± 1.6 (0.6)	1.6 ± 1.8 (2.5)	2.4 ± 0.9 (4.4)
8	0.6 ± 2.5 (0.5)	1.8 ± 3.4 (1.0)	1.7 ± 1.7 (0.8)	2.5 ± 1.3 (2.3)
9	0.9 ± 3.4 (0.4)	0.5 ± 2.3 (0.4)	0.8 ± 1.5 (0.8)	1.1 ± 1.2 (1.5)
10	-	-	-	1.0 ± 1.3 (0.5)
$\Sigma k_{st\text{-}to\text{-}st}$	38.7 ± 6.8 (35.0)	30.6 ± 7.7 (32.8)	28.6 ± 4.8 (27.7)	27.8 ± 3.7 (26.6)
k_{Total}	38.0 ± 3.6 (35.3)	29.7 ± 3.5 (33.2)	27.3 ± 3.9 (28.3)	25.7 ± 3.0 (27.2)

Table 3. State-to-state rate constants for transfer between initial and final rotational states of CO in collision with Ar at 52 K in units of 10^{-11} cm^{-3} s^{-1}. Experimental values are given with 2σ statistical errors and compared to theoretical values which are given in parentheses.

J_{final}	$J_{Initial}$			
	0	1	4	6
0	$J_{Initial}$	1.8 ± 1.4 (3.5)	0.5 ± 0.6 (0.8)	0.4 ± 0.3 (0.3)
1	7.5 ± 1.4 (8.8)	$J_{Initial}$	2.4 ± 1.8 (3.0)	1.8 ± 0.4 (2.4)
2	4.0 ± 1.0 (7.0)	6.1 ± 3.5 (7.1)	4.3 ± 1.8 (5.6)	2.3 ± 0.5 (2.0)
3	3.3 ± 1.3 (4.6)	3.0 ± 1.8 (6.1)	4.6 ± 1.3 (5.7)	3.7 ± 0.8 (3.8)
4	1.7 ± 1.5 (2.7)	2.8 ± 2.2 (3.5)	$J_{Initial}$	2.6 ± 0.5 (4.7)
5	1.8 ± 1.5 (2.4)	1.0 ± 3.4 (1.4)	3.3 ± 1.6 (3.9)	2.9 ± 1.1 (5.2)
6	0.5 ± 2.9 (0.4)	0.7 ± 2.6 (1.3)	1.4 ± 2.0 (2.2)	$J_{Initial}$
7	0.2 ± 2.1 (0.2)	-	0.6 ± 1.8 (0.9)	2.7 ± 1.5 (3.0)
8	-	-	-	1.3 ± 2.5 (1.0)
$\Sigma k_{st\text{-}to\text{-}st}$	18.9 ± 4.7 (26.0)	15.4 ± 2.2 (22.9)	17.1 ± 3.6 (22.0)	17.8 ± 3.3 (22.6)
k_{Total}	24.1 ± 2.3 (26.0)	18.1 ± 3.2 (23.1)	21.4 ± 2.9 (22.3)	23.2 ± 2.5 (23.1)

Table 4. State-to-state rate constants for transfer between initial and final rotational states of CO in collision with Ar at 30.5 K in units of 10^{-11} cm^{-3} s^{-1}. Experimental values are given with 2σ statistical errors and compared to theoretical values which are given in parentheses.

J_{final}	$J_{Initial}$		
	0	1	4
0	$J_{Initial}$	5.0 ± 1.2 (3.6)	0.9 ± 0.7 (1.0)
1	5.4 ± 0.7 (8.8)	$J_{Initial}$	2.4 ± 1.2 (3.0)
2	5.2 ± 1.0 (5.6)	5.2 ± 1.0 (6.1)	5.8 ± 1.5 (5.8)
3	2.5 ± 1.5 (2.9)	4.7 ± 1.2 (4.4)	4.0 ± 1.7 (5.7)
4	1.8 ± 1.3 (1.5)	2.2 ± 1.4 (1.8)	$J_{Initial}$
5	0.5 ± 1.0 (0.8)	0.5 ± 1.1 (0.6)	2.6 ± 1.5 (2.7)
6	0.3 ± 0.8 (0.1)	0.7 ± 2.0 (0.3)	1.1 ± 2.8 (0.9)
$\Sigma k_{st\text{-}to\text{-}st}$	15.6 ± 2.6 (19.7)	18.4 ± 3.3 (16.8)	16.7 ± 4.2 (19.1)
k_{Total}	14.0 ± 2.9 (19.7)	17.5 ± 4.1 (16.8)	17.5 ± 2.9 (19.3)

Discussion

The temperature dependent rate constants and cross sections for collisional rotational energy transfer between Ar and CO can be explained by a few factors. The first is the strength of the polarizability and long range forces of the gases. According to Sumiyoshi and Endo the CO-Ar van der Waals well is deep: 107.1 cm^{-1} or 103 K.[19] As the energy of the gas decreases to below this level, we would expect Ar and CO molecules to spend more time in the van der Waals complex, leading to more inelastic collisions and higher cross sections. Second, as the temperature of the gas decreases, collisions will also have less energy, potentially decreasing the cross sections, especially for endothermic pathways which rely on collisional excitation of CO molecules to overcome the endothermicity of the reaction. The number of available exothermic pathways is different for different J values; $J = 0$ has none ($\Delta J > 0$ for all transitions) whereas $J = 6$ has six exothermic pathways ($J_f = 0$, 1, 2, 3, 4, and 5).

Total Removal Cross Sections

The total removal cross sections (Figure 11) were large compared to those of smaller rare gases. Carty *et al*.[17] report a total removal cross section from $J_i = 1$ at ambient temperature of (22.3 ± 0.6) $Å^2$ for the rotational relaxation of CO in He, and Hostutler *et al*.[39] report a total removal cross section of 29.2 $Å^2$ for the rotational relaxation of CO in Ne. Both these values are significantly lower than the value of 65.0 ± 5.7 $Å^2$ for CO in Ar. For every temperature the cross sections from Carty *et al*. taken in a He bath gas are 2 - 3 times smaller than those reported here with an Ar bath gas. This trend follows the relative magnitudes of the CO-He, CO-Ne and CO-Ar van der Waals wells, which are calculated to be 107.1,[19] 49.4,[40] and 22.34 cm^{-1},[41] respectively. A larger van der Waals well increases the strength of the interaction between CO and the noble gas and the likelihood of inelastic collisions. This trend agrees with long known

trends for collisional broadening; the larger rare gases with strong polarizability and deep van der Waals wells lead to more collisional broadening. For example, the FWHM of the J 1 ← 0 microwave transition at 77 K of CO is 3.9 ± 0.4 for He, 4.8 ± 0.5 for Ne and 7.3 ± 0.7 for Ar.[10]

While the absolute cross sections were bigger for CO rotational energy transfer in Ar than compared to He, the general trends of the total cross sections with temperature are very similar to those found by Carty *et al*.[17] for CO-He. For the larger values of J_i, there are many exothermic pathways available, so the decreasing energy of the bath gas has only a small effect on the total cross section. Consequently, the total removal cross sections for $J_i = 4$ and 6 decrease with temperature due to an increase in the strength of long range forces as the temperature decreases below the depth of the van der Waals well at 103 K.

The temperature dependence is more complicated for $J_i = 0$ and 1, which have no or only one exothermic ($\Delta J < 0$) pathways available. While long range forces still play a larger role at lower temperatures, this is offset by the decreased energy of the Ar bath gas which disfavors endothermic reactions. While Carty *et al*.[17] found that the temperature dependence of the total removal cross section of $J_i = 1$ was essentially temperature independent with these two effects essentially counteracting each other, we see a small increase of the cross section of $J_i = 1$ with decreasing temperature. This discrepancy is likely because the long range forces are larger for Ar than for He, making them more important than decreasing bath gas energy at the temperatures studied. Like Carty *et al.*, we did see a noticeable decrease in the cross section at lower temperatures for $J_i = 0$.[17] This is expected given that there are no available exothermic channels available, meaning that the decreasing energy of the Ar bath should be most important for $J = 0$.

State-to-State Rate Constants

Like the general trends in the total removal cross sections, we see many trends in the state-to-state rate constants that are similar to those found by Carty *et al*.[17] Firstly, rate constants are largest when J_f is close to J_i (ΔJ is small), and the rate decreases as ΔJ increases. This is explained by the larger collision energy or larger number of collisions needed to transfer the larger amounts of energy of high ΔJ transitions. We also observe narrower distributions of the state-to-state rate constants as the temperature decreases, because a lower energy bath gas will disfavor transitions that require large energy transfers. This effect favors low ΔJ transitions and narrows distribution of state-to-state rate constants.

Finally, we do see a slight propensity for ΔJ = odd transitions, most clearly seen in the data for $J_i = 0$ at room temperature, since at lower temperatures this effect is washed out by the steep decrease in rate as ΔJ increases. As previously described by McCurdy and Miller,[42] this effect arises from resonances in the quantum trajectories. The selection rule for homonuclear atoms is ΔJ = even. If the molecule is quasihomonuclear, then ΔJ = even transitions will be more intense. Some heteronuclear molecules, like CO, even show the reverse trend, which is seen both in this work and in Carty *et al*.'s data.[17]

Comparison with Scattering Calculations

Our experimental data is currently being analyzed by Thierry Stoecklin's theory group at the University of Bordeaux to test the potential energy surface by comparing their scattering calculations to our experimental cross sections. Using the Newmat computational package[43,44] and the potential energy surface for the Ar-CO complex presented by Sumiyoshi and Endo,[19] Stoeklin and coworkers have performed quantum scattering calculations in order to find theoretical total and state-to-state rate constants. They describe their methods as follows: [45]

[The] code solves the close coupling equations in the space fixed frame. The vibration of the diatomic molecule is treated following the procedure described by Colbert and Miller.[46] *We used the log-derivative propagator to solve the close coupling equations. The maximum propagation distance used was 60* a_0. *The basis set includes 21 rotational states in each of the three vibrational levels analyzed. The convergence of the quenching cross section as a function of the step size and total angular momentum was checked for each collision energy. The state to state rate coefficients at temperature T were computed by Boltzmann averaging the corresponding cross sections* $\sigma_{J,v \rightarrow J',v'}$.[44]

Calculations were also performed to ensure that rate constants found in the excited vibrational state $v = 2$ applied to the ground state. Theoretical calculations from Stoeklin and coworkers show that our rate constants should be applicable to $v = 0$, by checking that the theoretical rates in the two vibrational states $v = 2$ and 0 are essentially identical.[44]

These calculations provide a way to test our knowledge the CO/Ar potential energy surface (Figure 1) and to compare our experimental data to what is previously known about the CO/Ar system. As shown in Figures 7 -11, the experimental data and the theory values are almost always within error of the experiment, an outstanding agreement, indicating that the potential energy surface is likely very accurate.

Conclusions

We have explored the state-to-state collisional rotational energy transfer for CO in an Ar bath gas with CRESU and IRVUVDR. We found rate constants that were larger, as expected, than previous work on collisional relaxation of CO in He and Ne. Our data also follow many

similar trends seen in the state-to-state cross sections for CO rotational relaxation in He. This work provides a valuable look into the Ar/CO system, which is a model system for understanding long range van der Waals forces. Our data can now be compared to theoretical values in order to even further characterize the Ar/CO potential energy surface and to further sharpen our understand of fundamental molecular forces.

References

(1) Havenith, M.; Schwaab, G. W. *Z. Phys. Chemie-Int. J. Res. Phys. Chem. Chem. Phys.* **2005**, *219*, 1053.

(2) Dham, A. K.; Gupta, S. C. *J. Phys. B-At. Mol. Opt. Phys.* **1976**, *9*, L127.

(3) Dham, A. K.; McBane, G. C.; McCourt, F. R. W.; Meath, W. J. *The Journal of Chemical Physics* **2010**, *132*, 024308.

(4) Dham, A. K.; McCourt, F. R. W.; Meath, W. J. *J. Chem. Phys.* **2009**, *130*.

(5) Dickinson, A. S.; Lee, M. S. *J. Phys. B-At. Mol. Opt. Phys.* **1985**, *18*, 4177.

(6) Heck, E. L.; Dickinson, A. S. *Physica A* **1995**, *217*, 107.

(7) Moszynski, R.; Korona, T.; Wormer, P. E. S.; Vanderavoird, A. *J. Chem. Phys.* **1995**, *103*, 321.

(8) McCourt, F. R. W.; ter Horst, M. A.; Heck, E. L.; Dickinson, A. S. *Mol. Phys.* **2002**, *100*, 3893.

(9) McCourt, F. R. W.; Weir, D.; Clark, G. B.; Thachuk, M. *Mol. Phys.* **2005**, *103*, 17.

(10) Nerf, R. B.; Sonnenberg, M. A. *Journal of Molecular Spectroscopy* **1975**, *58*, 474.

(11) Thibault, F.; Calil, B.; Buldyreva, J.; Chrysos, M.; Hartmann, J. M.; Bouanich, J. P. *Physical Chemistry Chemical Physics* **2001**, *3*, 3924.

(12) Thibault, F.; Martinez, R. Z.; Domenech, J. L.; Bermejo, D.; Bouanich, J. P. *J. Chem. Phys.* **2002**, *117*, 2523.

(13) Andrews, D. U.; Heazlewood, B. R.; Maccarone, A. T.; Conroy, T.; Payne, R. J.; Jordan, M. J. T.; Kable, S. H. *Science* **2012**, *337*, 1203.

(14) Forst, W. (2003). Unimolecular reactions : a concise introduction. New York : Cambridge University Press.

(15) Steinfeld, J. I.; Francisco, J. S.; Hase, W. L. *Chemical Kinetics and Dynamics*; 2 ed.; Prentice Hall: Upper Saddle River, New Jersey

1999.

(16) Troe, J. *The Journal of Chemical Physics* **1987**, *87*, 2773.

(17) Carty, D.; Goddard, A.; Sims, I. R.; Smith, I. W. M. *The Journal of Chemical Physics* **2004**, *121*, 4671.

(18) Roueff, E.; Lique, F. *Chemical Reviews* **2013**, *113*, 8906.

(19) Sumiyoshi, Y.; Endo, Y. *J. Chem. Phys.* **2015**, *142*.

(20) Salazar, M. C.; Paz, J. L.; Hernandez, A. J. *Mol. Simul.* **2003**, *29*, 413.

(21) Pedersen, T. B.; Cacheiro, J. L.; Fernandez, B.; Koch, H. *J. Chem. Phys.* **2002**, *117*, 6562.

(22) Gianturco, F. A.; Paesani, F. *J. Chem. Phys.* **2001**, *115*, 249.

(23) Toczylowski, R. R.; Cybulski, S. M. *J. Chem. Phys.* **2000**, *112*, 4604.

(24) Wehr, R.; Vitcu, A.; Thibault, F.; Drummond, J. R.; May, A. D. *Journal of Molecular Spectroscopy* **2006**, *235*, 69.

(25) Coudert, L. H.; Pak, I.; Surin, L. *J. Chem. Phys.* **2004**, *121*, 4691.

(26) Scheele, I.; Havenith, M. *Mol. Phys.* **2003**, *101*, 1423.

(27) Melnik, D. G.; Gopalakrishnan, S.; Miller, T. A.; De Lucia, F. C.; Belov, S. *J. Chem. Phys.* **2001**, *114*, 6100.

(28) McKellar, A. R. W. *Mol. Phys.* **2000**, *98*, 111.

(29) Hepp, M.; Gendriesch, R.; Pak, I.; Kuritsyn, Y. A.; Lewen, F.; Winnewisser, G.; Brookes, M.; McKellar, A. R. W.; Watson, J. K. G.; Amano, T. *Mol. Phys.* **1997**, *92*, 229.

(30) Dimov, S. S.; Vidal, C. R. *Chem. Phys.* **1992**, *164*, 107.

(31) Kruus, E. J. *J. Phys. Chem.* **1994**, *98*, 3099.

(32) Belikov, A. E.; Smith, M. A. *J. Chem. Phys.* **1999**, *110*, 8513.

(33) Rowe, B. R.; Dupeyrat, G.; Marquette, J. B.; Gaucherel, P. *J. Chem. Phys.* **1984**, *80*, 4915.

(34) Rowe, B. R.; Marquette, J. B. *Int. J. Mass Spectrom. Ion Process.* **1987**, *80*, 239.

(35) Sims, I. R.; Queffelec, J. L.; Defrance, A.; Rebrionrowe, C.; Travers, D.; Bocherel, P.; Rowe, B. R.; Smith, I. W. M. *J. Chem. Phys.* **1994**, *100*, 4229.

(36) Sims, I. R.; Queffelec, J. L.; Defrance, A.; Rebrionrowe, C.; Travers, D.; Rowe, B. R.; Smith, I. W. M. *J. Chem. Phys.* **1992**, *97*, 8798.

(37) James, P. L.; Sims, I. R.; Smith, I. W. M.; Alexander, M. H.; Yang, M. B. *J. Chem. Phys.* **1998**, *109*, 3882.

(38) Hilbig, R.; Wallenstein, R. *IEEE J. Quantum Electron.* **1983**, *19*, 194.

(39) Hostutler, D. A.; Smith, T. C.; Hager, G. D.; McBane, G. C.; Heaven, M. C. *The Journal of Chemical Physics* **2004**, *120*, 7483.

(40) Wang, Z. Q.; Feng, E. Y.; Yu, H. J.; Zhang, C. Z.; Du, J. M. *J. Chem. Phys.* **2011**, *134*.

(41) Peterson, K. A.; McBane, G. C. *J. Chem. Phys.* **2005**, *123*.

(42) McCurdy, C. W.; Miller, W. H. *The Journal of Chemical Physics* **1977**, *67*, 463.

(43) Stoecklin, T.; Voronin, A.; Rayez, J. C. *Phys. Rev. A* **2002**, *66*.

(44) Denis-Alpizar, O.; Stoecklin, T. *Mon. Not. Roy. Astron. Soc.* **2015**, *451*, 2986.

(45) Stoecklin, T. private communication.

(46) Colbert, D. T.; Miller, W. H. *J. Chem. Phys.* **1992**, *96*, 1982.